MESHFREE SIMULATION OF FRACTURE MECHANICS PROBLEMS UNDER THERMO-MECHANICAL LOADING

A THESIS

Submitted in partial fulfilment of the requirements for the award of the degree of

DOCTOR OF PHILOSOPHY

in

MECHANICAL ENGINEERING

by

MOHIT PANT

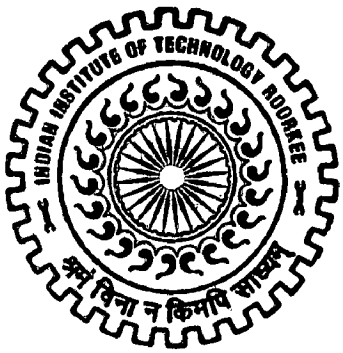

DEPARTMENT OF MECHANICAL AND INDUSTRIAL ENGINEERING
INDIAN INSTITUTE OF TECHNOLOGY ROORKEE
ROORKEE-247 667 (INDIA)

SEPTEMBER, 2010

INDIAN INSTITUTE OF TECHNOLOGY ROORKEE, ROORKEE

CANDIDATE'S DECLARATION

I hereby certify that the work which is being presented in the thesis entitled **MESHFREE SIMULATION OF FRACTURE MECHANICS PROBLEMS UNDER THERMO-MECHANICAL LOADING** in partial fulfilment of the requirements for the award of the Degree of Doctor of Philosophy and submitted in the Department of Mechanical and Industrial Engineering of the Indian Institute of Technology Roorkee, Roorkee is an authentic record of my own work carried out during a period from January 2008 to September 2010 under the supervision of Dr. I. V. Singh, Assistant Professor and Dr. B. K. Mishra, Professor, Department of Mechanical and Industrial Engineering, Indian Institute of Technology Roorkee, Roorkee.

The matter presented in this thesis has not been submitted by me for the award of any other degree of this or any other Institute.

MOHIT PANT

This is to certify that the above statement made by the candidate is correct to the best of our knowledge.

(B. K. Mishra)
Supervisor

(I. V. Singh)
Supervisor

Date: Sept 22, 2010

The Ph.D. Viva-Voce Examination of Mr. **Mohit Pant**, Research Scholar, has been held on 20/12/2010

Signature of Supervisors

Signature of External Examiner

ABSTRACT

The quest for perfection has led us to all the scientific developments and technological advancements. In spite of all the scientific developments, the flaws and imperfection in materials often leads to catastrophic consequences. Fracture is one of the most prevalent damage phenomena that society has faced for as long as there have been man-made structures. Over the past few decades, greater understanding of fracture mechanics has prevented a substantial number of structural failures. Cracks are inevitable in all engineering components. External loadings may result in either the propagation of pre-existing cracks or may initiate new cracks in the structures. This may finally lead to catastrophic failure of the components resulting in loss of property and lives.

Due to the scarcity of analytical solutions and also due to the versatility of the numerical methods in handling complex practical problems, research efforts continue to focus on improving the numerical schemes.

A new class of numerical methods known as meshfree method has been developed over the past 15 years. The meshfree method is a rather interesting complement to the traditional finite element method. The first advantage of a meshfree method is that it is possible to construct arbitrarily high order approximation for higher order problems. Secondly, the numerical integration can be performed on arbitrary cells covering the computational domain so that the expensive meshing and remeshing process can be avoided. Moreover, the mesh distortion insensitivity makes them a boon for the problems involving large deformation. These characteristics together, proffer the potential of meshfree methods in simplifying adaptive analysis and crack growth modeling in fracture mechanics.

Present research work focuses on the implementation and extension of the most popular meshfree method known as the element free Galerkin method (EFGM) to analyze a variety of fracture mechanics problems under thermal/mechanical loads. The versatility and the effectiveness of EFGM have been demonstrated through the solution of various problems. Moreover, few modifications have been proposed and implemented to enhance the proficiency of EFGM.

Simulating the problem of fracture mechanics requires some suitable crack modeling criterion. A comparison of various crack modeling techniques in EFGM unveiled the advantages of intrinsic enrichment criterion. Owing to its accuracy, convergence, ease of implementation and modifications, the intrinsic enrichment criterion was further exploited to accomplish the remaining research work.

Weak discontinuities in EFGM were modeled and compared using different existing criteria. The Jump function approach proved to be best among the available techniques for the modeling of material discontinuities. A new criterion for modeling bi-material interfacial crack using Jump function has been proposed. The proposed method involves only four enrichment functions in the basis instead of the usual twelve. Thus, computational complexity is significantly reduced.

In an attempt to simulate and analyze the effect of multiple cracks interaction in both convex and non-convex domains, a new intrinsic enrichment based criterion has been proposed, and implemented. Apart from accurate simulation, the proposed criterion effectively reduces the computational cost of the EFGM.

The EFGM has also been extended to simulate two-dimensional thermo-elastic fracture problems in isotropic material. Both temperature and mechanical fields were enriched intrinsically in order to represent the discontinuous temperature, heat flux, displacement and traction across the crack surface. Some example problems of fracture in functionally graded materials were tackled by EFGM under thermal/mechanical loads.

Motivated by the wide applicability of EFGM and to establish it as a robust tool for solving problems of fracture mechanics, the simulation of elasto-plastic fracture problems has been carried out for two dimensional cracked bodies. The enriched basis functions were used in order to capture the HRR (Hutchinson-Rice-Rosengren) singularity.

Finally, a new enrichment based EFGM criterion has been developed for modeling the kinked cracks. The proposed criterion was used for the simulation of quasi-static crack growth problems under mixed-mode loading conditions. The ease of modeling quasi-static crack growth highlights the strength of the proposed criterion. Moreover, the crack growth simulation also demonstrates the modeling capability of EFGM without any requirement of re-meshing.

ACKNOWLEDGEMENT

The tenure of human life in this world is supported by many others. Acknowledgement for a few might be just a trifle thing written on a piece of paper. Nevertheless, in the true essence, it gives us an opportunity to remember and express our feelings for those, whom we love, revere and share our secrets. Here I got a great chance to express my token of thanks to the people who in a way helped and supported me to complete this academic work.

First of all, I express profound sense of obligations to the almighty God for showing immense blessing upon me, which made me to accomplish this academic task. Words fail to express the noble sacrifice of my parents who brought me to this position.

My deepest sense of reverence, gratitude and indebtedness to Prof. B. K. Mishra, Professor, Department of Mechanical and Industrial Engineering and Dr. I. V. Singh, Assistant Professor, Department of Mechanical and Industrial Engineering, Indian Institute of Technology, Roorkee for their immaculate guidance, prudent suggestions, abundant interest and above all cooperative attitude during the course of my research work which bore the fruit in the form of this dissertation.

I wish to express my gratitude and fervent thanks to the members of my research committee, Dr. R. R. Bhargava (Professor, Department of Mathematics), Dr. S. C. Sharma (Professor & Head, Department of Mechanical and Industrial Engineering), Dr. Pradeep Kumar (Professor & Chairman DRC, Department of Mechanical and Industrial Engineering) and Dr. V.H. Saran (Assistant Professor, Department of Mechanical and Industrial Engineering) for their careful examination of the work and their invaluable comments and insights, which made a deep impact on my research.

Thanks to Ministry of Human Resource and Development (MHRD) for providing me the financial assistantship during the research. It is a pleasure to acknowledge the support extended by all my fellow research scholars. Thanks to all the staff of Ravindra Bhawan which made my stay quite comfortable and enjoyable during the research period. Last but not the least, I would like to convey thanks to all my beloved juniors for their love and respect.

This list is obviously incomplete, but let me submit that omissions are inadvertent and once again I record my deep felt gratitude to all those who cooperated, either directly or indirectly, with me in this endeavor. I dedicate this thesis to my parents, to whom I owe everything in my life.

MOHIT PANT

TABLE OF CONTENTS

LIST OF FIGURES

LIST OF TABLES

NOMENCLATURE

Notation	Definition
$a_j(\mathbf{x})$	Non constant coefficients
a	Crack length
Δa	Increment in crack length
$\mathbf{A}(\mathbf{x})$	Moment matrix
$\mathbf{b}$	Body force vector
$\overline{c}$	Domain parameter
$\widetilde{C}$	Predefined constant
C_{ep}	Elastoplastic stiffness matrix
$\mathbf{C}$	Fourth order Hooks tensor
d_{ml}	Influence domain of a node
$d_{\max}$	Scaling parameter
d_I^d	Modified distance between node and evaluation point
$\overline{d}_I$	Weight function distance
d_i	Normalized crack tip distance
d	Distance between two parallel crack
$\mathbf{D}$	Constitutive matrix
E	Modulus of elasticity
$\overline{E}$	Equivalent Young's modulus
E_{tip}^*	Young's modulus evaluated at crack tip
E_t	Equivalent plastic modulus
$\mathbf{f}$	Force vector
$\overline{F}$	Normalized stress intensity factor
F	Yield function
$\mathbf{G}$	Displacement matrix
h	Nodal spacing

h'	Normal distance between crack and evaluation point
$\overline{h}$	Offset
$H(\mathbf{x})$	Heaviside function
H	Height of plate
$\overline{H}$	Equivalent Young's modulus for bi-material
H'	Plastic modulus of material
I_n	Dimensionless constant
$\overline{\mathbf{I}}$	Second order identity matrix
J	J-integral
J_2	Second deviatoric stress invariant
k	Thermal conductivity
k'	Degree of polynomial
$\hat{k}$	Work hardening parameter
$\mathbf{K}$	Stiffness matrix
K_T	Thermal stress intensity factor
K_{Ieq}	Equivalent mode-I stress intensity factor
K_I	Mode-I stress intensity factor
K_{II}	Mode-II stress intensity factor
L_2	Error norm
m	Number of terms in basis function
m_e	Length of extrinsic basis
M	Interaction integral
n	Number of nodes in domain of influence
$\overline{\mathrm{n}}$	Unit normal to domain
n_j	jth component of outward normal to contour Γ
N^c	Enriched nodes for Heaviside function
N^f	Enriched nodes for branch function
N	Number of cracks present in domain
$N_I(s)$	One dimensional shape function

n'	Ramberg-Osgood parameter
$p_j(\mathbf{x})$	Basis function
P	Applied traction
$\overline{q}$	Crack tip weight function
$q_i(\mathbf{x})$	Extrinsic basis
q^J	Amplitude parameter for jump function
$\mathbf{q}$	Heat flux vector
$\overline{Q}$	Heat source
r	Distance of evaluation point from crack tip
r_g	Distance of an evaluation point from crack tip
r_J	Distance to jth point of discontinuity
$\bar{r}$	Normalized radius
$R_p(\theta)$	Angular ramp function
$\bar{\mathbf{t}}$	Prescribed traction
T	Temperature field
T_0	Reference temperature
ΔT	Temperature change
$u^{EFGM}(\mathbf{x})$	Standard EFGM approximation
$\mathbf{u}$	Displacement vector
$\bar{\mathbf{u}}$	Prescribed displacement
$u^h(\mathbf{x})$	Approximate solution
U_x	Displacement in x-direction
U_y	Displacement in y-direction
W	Width of plate
$\widetilde{W}$	Strain energy density
$\mathbf{x}_{tip}$	Crack tip coordinates

Greek Letters

$\Phi_I(\mathbf{x})$	Shape function
δ_{ij}	Kronecker delta
Γ_t	Traction boundary
Γ_u	Displacement boundary
Ω	Two dimensional domain
∇_s	Symmetric gradient operator
λ	Lagrange multiplier enforcing essential boundary condition
δ	Variational operator
$\boldsymbol{\varepsilon}$	Strain tensor
$\boldsymbol{\varepsilon}_T$	Thermal strain
ε_{ij}^m	Mechanical strain
ε_{ij}^t	Total strain
ε^e	Elastic strain
ε^p	Plastic strain
γ_{xy}	Shear strain
$\tilde{\varepsilon}$	Bi-material constant
θ	Orientation of an evaluation point w.r.t. crack
θ'	Modified angle for kinked crack
θ_m	Crack propagation angle
μ	Shear modulus
κ	Kolosov constant
$\boldsymbol{\sigma}$	Stress tensor
σ_o	Applied far field stress
σ_e	Von-Mises stress
σ_{xx}	Stress in x-direction
σ_{yy}	Stress in y-direction

σ_{zz}	Stress in z -direction
σ_{xy}	Shear stress in xy direction
σ_s	Yield strength of material in pure shear
σ_Y	Yield strength of material in uniaxial tension
$\overline{\sigma}$	Effective stress
σ'_{ij}	Deviatoric stress
σ_m	Mean stress
γ	Lagrange multiplier enforcing displacement discontinuity
$\Psi_J(r)$	Jump shape function
β	Coefficient of thermal expansion
α	Angular orientation of crack
Γ_T	Temperature boundary
Γ_q	Heat flux boundary
Γ_c	Crack surface
Γ	Path surrounding crack tip
Θ	Reference temperature
$d\lambda$	Proportionality factor
α'	Ramberg-Osgood parameter
~~$\tilde{\sigma}_{ij}, \tilde{\varepsilon}_{ij}, \tilde{u}_i$~~	~~Dimensionless angular functions~~

Chapter 1

INTRODUCTION AND LITERATURE REVIEW

1.1 INTRODUCTION

Understanding fracture was important for us even in the stone-age when the primitive men tried to make stone tools and weapons. Time has changed from stone-age to space-age but the phenomenon of fracture is still being studied. The quest for perfection has led us to many scientific developments and technological advancements. In spite of all the scientific developments, the flaws and imperfection in materials often leads to catastrophic consequences. Fracture is one of the most prevalent damage phenomena. It can be observed right from withering of rocks in nature to crash of an aero-plane. Loosely speaking, fracture can be defined as the separation of an object or material into two or more pieces under the action of stress. A crack/flaw is the basic entity which leads to fracture of component/structure when subjected to external loads.

Cracks are inevitable in all engineering components. Thermo-mechanical loading may result in either the propagation of pre-existing cracks or may initiate new cracks in the structures. Fatigue and quasi-static fracture are two forms of crack growth phenomenon. Fatigue fracture refers to the slow propagation of cracks under cyclic loading conditions where the stress intensity factors are below the fracture toughness of the material. Quasi-static fracture is common near the end of the fatigue life when the increased crack length leads to stress intensity factors which are above the fracture toughness (Chowdhury and Narasimhan 2000; Sasikala and Ray 2008; Partheepan *et al.* 2008).

Fracture is characterized by unstable and extremely fast crack growth. This may finally lead to failure of the components resulting in the loss of property and lives. Several experimental (Nurse and Patterson, 1990; Khanna and Shukla, 1995; Maiti and Patil, 2003; Guagliano *et al.* 2006; Singh and Gope 2009) and simulation techniques (Choubey *et al.* 2006; Zhong and Oyadiji 2007; Lam and Ng 2008) are dedicated to crack detection at an early stage. Research efforts have been made to predict, and retard the effect of fatigue on the structures (Adrov 1993; Gope 1999; Shang *et al.* 2001; Liu and Mahadevan 2005).

In many cases, multiple cracks may exist in the components. These cracks interact with each other resulting in the variation of stress distribution, stress intensity factor and propagation direction of the main crack. As such, all important failure phenomena such as stress corrosion cracking, hydrogen embrittlement, and creep micro cracking are directly linked to the crack interactions. In past, some efforts have been made using analytical, experimental and simulation techniques to analyze the effect of interaction among multiple cracks (Cheung *et al.* 1992; Ang and Gumel 1996; Ang and Park 1996; Denda *et al.* 1997; Muravin and Turkel 2006a).

Although, a plenty of analytical (Rice 1968; Agarwal *et al.* 1986; Rao and Rahman 2003; Sills and Dolev 2004) and experimental methods (Khanna and Shukla, 1993; Chattopadhyay *et al.*, 2005) have been exploited for the calculation of fracture parameters even then the drawbacks associated with experimental investigation and scarcity of analytical solution have impelled the analysts towards alternative techniques. Numerical methods hold the promise in this regard.

Numerical methods along with high-fidelity mathematical models are able to predict the behavior of an engineering system before the physical system has been built. The

majority of such models take the form of partial differential equations (PDEs) which relate variables whose values are confined to a given domain. Except for the simplest cases, the PDE and/or the domain under consideration are complex enough to rule out the possibility of finding an exact solution, and a suitable numerical approach is needed to simulate the modeled phenomenon. Loosely speaking, numerical methods transform a PDE defined over a continuum into a finite set of equations which are later solved (exactly or approximately) by using matrix algebra. In many situations, numerical simulation effectively reduces or replaces expensive experimental studies as an alternative investigation tool for the engineers.

Due to advances in the computational technologies over past two decades, many numerical simulation tasks, which were once considered computationally formidable or could be addressed only by a supercomputer, can now be carried out by a normal desktop computer. Due to the scarcity of analytical solutions for most of the practical cases, and also due to the versatility of computational procedures in handling such problems, research efforts continue to focus on improving such numerical schemes.

Over past fifty five years, finite element method (FEM) has been used for solving a wide variety of engineering and industrial problems (Giudice *et al.* 1978; Reddy and Chao 1980; Corvi 1990; Kant and Menon 1993; Sze and Wang 2000; Chattopadhyay *et al.* 2005; Armentani and Citarella 2006; Kant *et al.* 2007; Goo *et al.* 2006, 2008a, Yoon et al. 2010). The method has achieved remarkable success in solving many linear and non-linear problems (Deodatis 1989; Kant *et al.* 1992; Yoon *et al.* 1999; Andreev and Harmuth 2003; Cardoso *et al.* 2007; Huang 2007; Dias *et al.* 2007; Goo *et al.* 2008b; Coda 2009). Although FEM is quite successful, the discretization of complex three-dimensional geometries and re-meshing of the domain changing with time is a very daunting and time-consuming task. Assembly and solution of the finite element equations

also often lead to numerical errors (Umar *et al.* 1996; Prathap 1999; Meric 2001; Kikuchi and Liu 2003; Cardoso and Yoon 2007). Despite its numerous advantages and unparalleled success, FEM is not well suited for certain classes of problems such as crack propagation and moving discontinuities, moving phase boundaries, continuous casting, phase transformation, free surface flow, fluid structure interaction, large deformations, solution of higher order partial differential equations, multi-scale analysis. Difficulties arise due to the inherent structure of finite element method, i.e. the connectivity defined through the use of elements.

In the fracture mechanics problems, for instance, element edges provide natural lines along which a crack can grow. This is advantageous if the crack path is known a *priori,* but in most complex fracture phenomenon, the crack path is unknown. Thus, the finite element method requires remeshing to ensure that element boundaries coincide with moving discontinuities. Therefore, a method is needed which may be somewhat more expensive from the viewpoint of computational time but requires less time in the preparation of data.

To cope with these problems, a class of new methods has been developed over the past thirty years. These methods are known as meshfree (meshless) method. The common feature of the meshfree methods is that they do not require any connectivity information i.e. a elemental mesh is not required. In meshfree methods, interpolants (strictly speaking approximants) are constructed solely on the basis of a set of scattered nodes whereas in case of finite element method, interpolants are constructed using a number of small elements known as finite elements. The meshfree method is a rather interesting complement to the traditional finite element method. The first advantage of meshfree method is that it is possible to construct higher order approximation. Secondly, the numerical integration can be performed on simple cells covering the computational

domain so that the expensive meshing and remeshing process can be avoided. The mesh distortion insensitivity makes them a boon for the problems involving large deformation. Moreover, these properties make them ideally suited for adaptive analysis, and crack growth modeling.

1.2 LITERATURE REVIEW

In the past, a number of meshfree methods have been developed to tackle the problems faced by FEM. These include smooth particle hydrodynamics (Monaghan, 1988; Monaghan, 1992; Bonet and Kulasegaram 2002; Kulasegaram *et al.* 2004; Chen and Kulasegaram 2009), diffuse element method (Nayroles *et al.*, 1992, 1994; Marechal *et al.*, 1993), element-free Galerkin method (Belytschko *et al.*, 1994; Lu *et al.*, 1994), reproducing kernel particle method (Liu *et al.*, 1995a,b,1996; Chen *et al.*, 1997; Jun *et al.*, 1998; Aluru, 1998), finite point method (Onate *et al.*, 2001), partition of unity method (Melenk and Babuska, 1996; Babuska and Melenk, 1997), *H-p* cloud method (Durate and Oden, 1996), free mesh method (Yagawa and Yamada, 1996; Yagawa and Furukawa, 2000), boundary node method (Mukherjee and Mukherjee, 1997), natural element method (Sukumar, 1998a,b), local boundary integral equation method (Zhu *et al.*, 1998a,b; Atluri *et al.*, 2000; Long and Zhang, 2002,), meshless local Petrov-Galerkin method (Atluri and Zhu, 1998; Cho and Atluri, 2001; Atluiri and Shen, 2002; Xiao and McCarthy, 2003), the method of finite spheres (De and Bathe, 2000, 2001a,b), regular hybrid boundary node method (Zhang *et al.*, 2003; Zhang and Yao, 2004; Zhang *et al.*, 2004), local point interpolation method (Liu and Gu, 2001a; Gu and Liu, 2001) and local radial point interpolation method (Liu and Gu, 2001b).

All these meshfree methods have a common feature that only nodal data is required to describe the interpolation of field variables. Although, in most of the meshfree methods, Galerkin formulation is utilized to develop the discrete equations, the major

difference among these methods lies in the interpolation (approximation) techniques. Generally, three different interpolation (approximation) techniques have been used in meshfree methods, kernel approximation, moving least square approximation and partition of unity. In meshfree methods, one uses the term approximation rather than interpolation since the meshfree shape functions do not satisfy the Kronecker-delta property. This entails certain difficulties in imposing essential boundary conditions. Probably the simplest way to impose essential boundary conditions is the boundary collocation methods. Other alternatives are to use the penalty method, Lagrange multipliers, full transformation technique, and Nitsche's method. The most important advantages of meshfree methods compared to finite elements are their higher order continuous shape functions that can be exploited e.g. for thin shells or gradient-enhanced constitutive models; higher smoothness; simpler incorporation of h and p-adaptivity and few advantages in crack problems (no mesh alignment sensitivity; some methods do not need to enforce crack path continuity). The main drawback of all meshfree methods is probably their higher computational cost.

Based on an idea of Lancaster and Salkauskas (1981) and probably motivated by the purpose to model arbitrary crack propagation without computationally expensive remeshing, Belytschko and his co-workers developed the element free Galerkin method (EFGM) in 1994.

In 1994, Belytschko *et al.* first used EFGM for arbitrary shape elasticity problems and a simple heat conduction problem. The trial and test functions were selected from moving least square interpolants. They found that the method does not exhibit volumetric locking, and a higher rate of convergence was achieved. In the same year, Belytschko *et al.* implemented EFGM for quasi-static crack growth problems using the visibility criterion. Moving least square interpolant was used along with Gelarkin method.

Accurate stress intensity factors were obtained with very irregular arrangement of nodes and without using any enrichment function to model a near crack tip singularity.

Belytschko *et al.* (1995a) applied EFGM for static and dynamic fracture problems. They modeled a growing crack by extending its free boundary. The results were found quite close to the analytical solution. The need of remeshing during crack propagation was eliminated but the computational time was increased by almost 50% as compared to FEM.

Belytschko *et al.* (1995b) used EFGM to solve the problems of mixed mode dynamic fracture in concrete. They suggested that crack tip velocity leads to significant differences in the crack path, especially in later stages of fracture. Though, the running time for these calculations were found to be more as compared to finite element procedure but when viewed in terms of interactive remeshing by user , the increase in computer cost were quite modest.

Organ *et al.* (1996) developed continuous meshless approximation for the domains with non-convex boundaries. Two techniques namely diffraction and transparency were compared to the original visibility criterion. Moderate improvement in accuracy over the discontinuous approximation was obtained but significant improvements were obtained for the case with enriched basis with crack tip singular functions.

Belytschko and Tabbara (1996a) used the EFGM to solve the problems of dynamic crack propagation. The essential boundary conditions were imposed by collocation method and the discrete equations were obtained by Hamilton's principle. They tested and applied this method to solve elasto-dynamic non-linear crack growth problems.

Belytschko and Tabbara (1996b) suggested the use of EFGM to solve several problems involving dynamic crack propagation. The crack growth was modeled using the concept of dynamic stress intensity factor. A comparison with analytical and other

numerical solution for linear crack growth showed that the method is capable of modeling crack growth without re-meshing.

Belytschko *et al.* (1996) used the EFGM for smoothing the approximation near concave boundaries, and increased the efficiency of EFGM by computing the approximation functions and their derivatives by a new methodology. A moderate improvement in the accuracy of smoothed interpolant was achieved. A comparison with the original formulation of the method showed a two fold increase in speed in the computation of derivatives.

Krongauz (1996) in his doctoral thesis proposed a technique for incorporating the discontinuous derivatives in EFGM for both one and two-dimensional problems. An approximation function was introduced which has discontinuous first derivative at the point of discontinuity. The approximation possesses a compact support. In comparison to standard meshless approximation, oscillations were avoided at the surface of the discontinuity.

Organ (1996) in his PhD thesis implemented the EFGM for the numerical solution of dynamic fracture problem. A procedure was developed for coupling of meshless methods with finite element methods. Dynamic fracture problems were solved ranging from stationary crack under impact loading to multiple cracks growing in arbitrary directions. The EFGM solutions compared well with experimental results for both constant and variable crack velocities.

Sukumar *et al.* (1997) used EFGM for three dimensional fracture mechanics problems by coupling it with finite element method. The method allowed the use of EFGM in crack region and finite element method in the rest of the domain. The stress

intensity factors obtained for two benchmark problems were found in good agreement with the reference solution.

Fleming *et al.* (1997) proposed an enriched EFGM for crack tip fields by adding asymptotic fields to the trial function and by augmenting the basis with asymptotic fields. A local mapping for the enriched fields for curved cracks was also described. This enrichment greatly reduced the stress oscillations and allowed the accurate calculation of stress intensity factors with fewer degrees of freedom.

Fleming (1997) in his PhD thesis applied the EFGM for fatigue and quasi-static fracture. Crack growth was modeled by adding an additional segment at the crack tip. Techniques for enriching and smoothing meshless approximation for linear elastic fracture were also presented. The method was found to perform well for arbitrary crack growth in complicated geometries.

Tabbara and Stone (1998) applied the EFGM in quasi-static mixed mode fracture problems. The expression for normalized critical traction was derived in terms of fracture resistance (*R*-curve) and a crack dependent function. This method provided a direct procedure to resolve an arbitrary crack extension without any change to the original geometry. Predictions agreed quite well with the experimental results.

Combe (1998) suggested an automatic mesh adaption approach using EFGM which can be applied for several linear and physically non-linear problems with high stress-strain gradients. The adaption criterion was based on strain gradients and a strategy for node refinement. Continuous mesh refinement in areas of high gradient was used. The convergence was investigated for the problems having analytical solutions.

Xu and Saigal (1998a) established a discrete formulation for stable crack growth in elastic solid using EFGM. Inertia force term in the momentum equation was converted into a spatial gradient term by employing the steady state condition. A good

approximation of the near tip stress field was achieved. These calculations suggested that the quality of numerical results was not affected much by the crack tip speed.

Ponthot and Belytschko (1998) presented an arbitrary Lagrangian–Eulerian (ALE) formulation for EFGM, which continuously relocates the nodes in the computational domain. By combining EFGM with ALE, the spatial discretization in the neighborhood of a propagating crack tip was refined locally. The new formulation can be easily implemented in a pre-existing mesh-free code.

Xu and Saigal (1998b) established an EFGM based formulation for the quasi-static crack growth in an elastic-plastic material undergoing small scale yielding. A mode-I crack under plane strain condition is considered in an elastic-perfectly plastic material. The computed near tip stress distribution and crack opening displacement were found in good agreement with the analytical solutions.

Xu and Saigal (1999) developed an EFGM based formulation for dynamic crack growth in an elastic-plastic material. Both rate independent and rate dependent materials were considered. Von-Mises yielding criterion along with an associated flow rule was used. Crack propagation speed showed a great influence on the results for rate independent materials.

Dolbow and Belytschko (1999) suggested some improvements in numerical integration of Gelarkin weak form for meshfree methods. Construction of quadrature cells without local support to weight function was found to be a source of integration error. A new structure of integration cells was proposed which reduced the quadrature error.

Krysl and Belytschko (1999) proposed a technique for modeling three-dimensional dynamically propagating cracks in elastic bodies by EFGM. The crack surface was defined by a set of triangular elements. Surface updating techniques were also described.

Stress intensity factor was calculated using interaction integral approach. This approach was only applicable to non-interacting cracks.

Belytschko and Fleming (1999) compared three different methods for smoothing meshfree approximation near non-convex boundaries. Two different techniques for enriching the EFGM approximation near the crack tip were also summarized and compared against each other. The extrinsic enrichment criterion was found to be more suitable for the simulation of multiple cracks.

Barry (1999) formulated a small strain, three-dimensional elasto-plastic EFGM. Singular weight functions were used in moving least square approximation. Elasto-plastic formulations were done on the basis of consistent tangent operator approach and incremental theory. The computational efficiency was improved by using variable domain of influence.

Rao and Rahman (2000) developed an efficient meshless method for the analysis of linear elastic cracked structure subjected to single or mixed mode loading condition. The method involves an EFGM formulation in conjunction with an exact implementation of essential boundary condition and a new weight function. The predicted crack trajectories were found in good agreement with experimental data.

Belytschko *et al.* (2000) further used EFGM to study the mixed mode dynamic crack propagation in concrete. The essential boundary conditions were imposed by explicit time integration scheme and coupling with finite elements. The discrete equations were obtained using variational approach. Fracture process zone model was used to replicate the salient features of dynamic crack growth with arbitrary path.

Yagawa and Furukawa (2000) reviewed recent developments in mesh free methods, and analyzed the computing efficiency for these methods. A good parallel computing efficiency was achieved but there was a sudden decrease in computing efficiency with

the increase in number of processors. Parallel computing efficiency was found to be dependent on the ratio of number of processors to degrees of freedom.

Rao and Rahman (2002) developed a Gelarkin based meshless method for predicting the first order derivative of stress intensity factor with respect to crack size in a linear elastic structure. For mode-I loading, the first order derivative of SIF was found quite close to analytical solution, whereas for mixed mode loading, the maximum error was found to be 7%.

Gavete (2000) proposed a new way of imposing essential boundary condition in EFGM. A penalty function was used along with a constrained variational principle. The method was tested for the case of a complex domain with irregular grid of nodes. The formulation exhibited very high accuracy and stability when appropriate weighting function were used.

Pannachet and Askes (2000) come up with some observations on the enforcement of constraint equations. Both Lagrange's multiplier and penalty approach were used to solve two benchmark problems. Inaccuracies such as oscillations were observed due to abrupt change in the boundary conditions. Instead of Gauss integration, nodal integration was found to eliminate these deficiencies.

Rao and Rahman (2001) developed a technique for coupling of EFGM method with traditional finite element method for the analysis of linear elastic crack problems subjected to mode-I and mixed mode loading conditions. A significant saving in computational efforts was achieved by coupling the two methods. The calculated stress intensity factors compared very well with the existing solution.

Gavete and Ruiz (2001) presented an error indicator for EFGM which can be easily implemented in existing EFGM codes. The calculation was performed on a cell by cell basis. Performance of error indicator was demonstrated for two different problems with

known analytical solutions. This method allowed a global energy norm to be estimated with good estimation of local errors.

Ventura *et al.* (2001) proposed a new level set method for the description of a propagating crack in EFGM. This approach helps to model a crack on the basis of nodal data only without introducing any geometrical entity. The nodal data gets updated with crack propagation. The method finds a promising application for three dimensional entities where the geometrical description of a crack surface is a computationally expensive task.

Yavari *et al.* (2001) studied the topological aspects of EFGM and compared them with finite element method. They suggested that EFGM requires large domain of influence to satisfy the basis. Appropriate size of domain of influence is configuration dependent. No conclusive result was obtained for node ordering.

Hazama *et al.* (2001) suggested an EFGM approach for two-dimensional elasto-plastic problems. Computer aided engineering seamless systems and digital analysis procedures were developed for extraction of domain data for practical problems. Infinitesimal deformation involving material non-linearity was examined. The method predicted the deformation state as competently as the finite element method.

Belytschko *et al.* (2002) proposed a new technique for modeling discontinuities. Jump function was used to model material discontinuity and Westergard's solution (Gdoutos, 2005) was used for near crack tip enrichment. Being extrinsic in nature, these enrichments were only limited to nodes surrounding cracks. Use of vector level set method in crack modeling requires only nodal data for crack description.

Duflot and Dang (2002) suggested a new body integration technique for the evaluation of stiffness matrix and body load vector. The new integration technique does

not require the partition of integration domain into small cells. Numerical results demonstrated that the method is especially useful when nodes are irregularly scattered.

Xuan *et al.* (2002) proposed an EFGM for non destructive testing (NDT) applications. This method eliminated the requirement of remeshing with probe motion. The method was validated and applied for two-dimensional magneto-static and eddy current NDT problems. Results clearly demonstrated the feasibility of using EFGM for modeling non destructive evaluation problems.

Lee *et al.* (2003) proposed an adaptive analysis for crack propagation based on error estimation. Nodes were added or removed from the background integration cell according to error estimator. The proposed adaptive scheme showed the good validity and efficiency for several numerical problems.

Lee *et al.* (2003) proposed an improved crack analysis technique with auxiliary support. A singular basis function, which varies only on the auxiliary support, was added to enrich the standard EFGM approximation. A discontinuous shape function was used in the vicinity of a crack. Higher accuracy was obtained as compared to standard EFGM solution.

Rao and Rahman (2003) proposed a technique for calculating the stress intensity factors for a stationary crack in two-dimensional functionally graded materials of arbitrary geometry. Material properties were considered to be smooth functions of spatial coordinates. Two new interaction integrals were developed for mixed mode fracture analysis. A good agreement was obtained between EFGM solution and reference solutions.

Muravin (2003) in his PhD thesis proposed a multiple crack weight method for the solution of strongly interacting cracks. The interaction effect was found to be dependent on the position of cracks, their orientation, and distance from each other. A satisfactory

accuracy was achieved when numerical solutions were compared with the analytical results.

Hagihara (2003) modified an EFGM with Delaunay triangulation for searching the nodes and divisions of integral domain. The incremental formulation of EFGM was used to deal with several time dependent non-linear problems. CPU time was greatly reduced by this approach.

Duflot and Dang (2004) developed a new enriched weight function for the simulation of fatigue crack growth in two dimensional bodies. A constant amplitude cyclic loading was used along with Paris law. Numerical results showed good agreement with results obtained using boundary element method even with lesser degree of freedom.

Rao and Rahman (2004) proposed an enriched meshless method for the fracture analysis of cracks in homogeneous, isotropic, non-linear, two dimensional solid subjected to mode-I loading. Two new basis functions were introduced to capture the crack tip singularity. Both the crack tip field and crack mouth opening displacements were found in excellent agreement with the experimental and finite element method results.

Rabczuk and Belytschko (2004) suggested a new approach for modeling the discrete cracks in meshfree method. The crack was modeled using local enrichment of trial and test function. No representation of crack topology was needed in this approach. The results were found to be in good agreement with the experimental data.

Chen *et al.* (2004) implemented EFGM for the classical rate-independent plasticity problems. Both plane stress and plane strain conditions were chosen for the analysis of crack growth in elastic-plastic solids.

Lee and Yoon (2004) proposed an enhanced EFGM to improve the solution accuracy for linear elastic fracture problems. The enhancement functions were added to the conventional EFGM approximation for the implicit description of near-tip fields. The discontinuity of crack surface was efficiently modeled by introducing a discontinuous function. Crack growth was modeled with initial node arrangement only. The robustness of the enhanced EFGM was established by examining the stress intensity factor for various crack problems.

Kargarnovin (2004) extended EFGM for elasto-plastic stress analysis. A system of elasto-plastic EFGM relations were derived using incremental relations of plastic deformation. A non-linear solution technique was selected to examine the stress field near the crack tip. Power law work hardening was employed in the formulation. Results were obtained for two different plates, with crack and without crack.

Brighenti (2005) implemented EFGM for the solution of three-dimensional elastic fracture mechanics problems. The geometrical description of the body was performed by employing triangles in space to describe edges and by generating grid of internal points. Visibility criterion (Belytschko *et al.,1994*) was used along with Gauss type weight function. The values of SIF's were found in good agreement with the reference solution.

Chen (2005) extended the EFGM to determine the stress intensity factor for an interface crack in a graded orthotropic coating and a homogeneous substrate structure. Analytical results were obtained using integral transform and singular integral equation technique. To evaluate thermal SIF, an interaction integral was developed. A good agreement between analytical and numerical results was obtained.

Duflot (2006) proposed a meshless method with enriched weight function for three-dimensional crack propagation. Cracks were modeled by a set of triangles. New triangles

were added as the crack propagated. Crack singularity along crack front was obtained by enrichment of shape functions by means of appropriate weight function.

Muravin and Turkel (2006a) devised a multiple crack weight method for the solution of strongly interacting cracks by meshless method. Weight functions were constructed so as to simultaneously characterize the presence of all the cracks in the domain of influence of a single crack. Sufficiently accurate solutions were obtained with less number of nodes. The computational cost of the method was reduced by 14% in comparison to conventional EFGM.

Muravin and Turkel (2006b) also developed spiral weight for modeling crack in EFGM. These weights preserved all the discontinuities along the entire crack length even with a linear basis. The need of additional array of nodes at the crack tip was eliminated. The results were found more accurate than the diffraction technique.

Li and Simonsen (2007) used EFGM to simulate ductile crack growth and propagation under finite deformation and large scale yielding conditions. A parametric visibility condition was developed to automatically adapt fracture configuration for arbitrary crack growth in ductile material. The proposed method was found to be versatile in simulating arbitrary crack propagation.

Rabczuk and Belytschko (2007) suggested a new approach for modeling discrete cracks. The crack growth was represented discretely by activation of crack surfaces at individual particles. The method was formulated for large deformations and arbitrary non linear and rate dependent materials. Cohesive crack laws were used to govern the traction-crack opening relations. Rabczuk *et al.* (2007) proposed a three-dimensional meshfree method for arbitrary crack initiation and propagation in non-linear material models. Extrinsic enrichment criterion was used to model a crack. Numerical results precisely replicated the available experimental data.

Zhang *et al.* (2008) established an improved EFGM for the analysis of two-dimensional fracture problems. An improved moving least square approximation was proposed which has a greater computational efficiency and did not lead to ill-conditioned system of equations. Crack tip singularity was captured in a better way with the use of enriched basis.

Gu and Zhang (2008) developed a new simulation technique to couple the meshfree method with finite element method for the analysis of crack tip fields. Meshfree method was applied to a sub-domain around the crack tip while the rest of the domain was treated with finite element method. Lagrange multiplier method was used to ensure the compatibility of displacements and their gradients in the transition region. The method showed a promising potential in solving complicated crack problems.

Zhang *et al.* (2008) developed an adaptive element free Gelarkin-finite element (EFGM-FE) coupling model for a thermal elasto-plastic coupling problem. Influence of steady state frictional heating between two contacting bodies was studied. The method was verified through the contact analysis of a cylinder with an elasto-plastic plane. Adaptive refinement reduced the computational time, and achieved a satisfactory level of accuracy when compared with uniform refinement.

Nguyen *et al.* (2008) reviewed the EFGM from the viewpoint of computer implementation. Well structured algorithms were proposed for several one and two-dimensional problems of elastostatics. Techniques for incorporating weak and strong discontinuities were also discussed along with the different ways of enforcing essential boundary conditions.

On the basis of the literature review, it is observed that a lot of research work has been carried out over past fifteen years in the area of fracture mechanics using EFGM

under mechanical loading conditions. Both quasi-static and propagating cracks have been analyzed under static and dynamic loading conditions. A number of EFGM formulations have been developed for the analysis of brittle and ductile fracture under large scale yielding. Various techniques have been developed to incorporate the effect of weak and strong discontinuities. Although, the results obtained by EFGM are found to be more accurate than conventional FEM (Lu, 1994; Beytschko *et al.*, 1996a; Bouillard and Suleau, 1998; Dolbow and Belytschko, 1998; Singh *et al*, 2005; 2006). The only draw back of this method is its high computational cost in comparison to FEM (Belytschko *et al.*, 1996b, c; Dolbow and Belytschko, 1998; Singh *et al*, 2003, Singh, 2004). A good agreement between EFGM and analytical results has been achieved for different fracture modes. However, the failure of engineering components is not only due to the mechanical loads but also due to the thermal stresses/thermal fatigue. Some of the practical applications where thermal loads play a significant role are as follows:

- Turbine nozzles, blades and other components are exposed to cyclic thermal load.
- Aerospace components are exposed to extreme thermal shocks due to varying operating conditions.
- Satellite components are subjected to thermal cycles when they are exposed to sun for some duration of time and go under the shadow for the remaining period of time.
- Internal combustion engine, components are subjected to mechanical as well as thermal loads.
- In military applications, the components are exposed to varying thermal loads e.g. the gun chamber is subjected to very high temperature and high pressure during the shell firing and cools down to nominal temperature after that.
- Creep failure in industrial boilers is due to high pressure and temperature.

- ❖ Alternate heating and cooling of the die during die casting process causes thermal fatigue.
- ❖ Cyclic heating and cooling of electronic circuit causes thermal fatigue in solder joints.

Besides these, there are many other structures/components which fail either due to pre-existing cracks or thermal/mechanical loading may initiate a crack, causing catastrophic failure. In this regard, some efforts have already been made to analyze the cracked structures under thermal loading. In 1976, Chell and Ewing suggested that the thermally induced stresses can behave like primary or mechanical stresses (redistributed but not relieved by introduction of a crack) in linear elastic regime. For identical geometry, the stress intensity factor due to secondary loading is less as compared to primary loading. In elastic-plastic regime, it is not safe to ignore thermal stresses. Rao (1976) presented a solution for stresses around the tip of an insulated arbitrary crack in a thin plate subjected to uniform heat flow. The stress at the crack tip exhibit inverse square root singularity. Stern (1977) developed a contour integral method for calculating the stress intensity factor for a crack at the interface of two dissimilar materials subjected to thermal stresses. Lam *et al.* (1992) suggested that the presence of crack in a steady heat flow gives rise to local intensification of temperature gradient, resulting in large thermal stresses at the crack tip. Prasad *et al.* (1996) suggested that cracked bodies under thermal loading exhibit a thermal singularity which may be measured in the same way as the stress singularity. A quarter-point crack tip element was developed in FEM to accurately measure these thermal singularities. Zohar (1996) computed the generalized thermal stress intensity factor for a two-dimensional thermo-elastic problem. Singular behavior of flux was obtained near the crack tip. Thermal loads thus obtained were used to obtain displacement. Ang and Clements (1999) considered a problem of calculating

the thermo-elastic stress around an arbitrarily located planar crack in an infinite anisotropic medium. Hyper-singular integral equations were derived, and solved numerically to compute the crack tip stress intensity factor. Bruno (2004) presented a numerical method for the evaluation of stress intensity factors in two dimensional homogeneous materials under thermal and mechanical loads. The results were found to be in good agreement with those available in the literature. Simkins and Li (2005) simulated thermo-mechanical ductile fracture using meshfree Gelarkin method. Johnson-Cook damage model was implemented in the numerical formulation for large scale yielding. Visibility criterion was used to modify particle connectivity based on evolving crack morphology. The proposed model predicted the effect of thermo-mechanical loading on ductile fracture in an efficient manner.

Dai *et al.* (2005) presented a meshfree model for the thermo mechanical analysis of functionally graded material plates. Shape functions were derived using moving least square method with C^1 consistency. First order shear deformation theory was used to establish the weak form, and a variational principle approach was used for thermo-electro-mechanical coupling. The effect of volume fraction, loading type and control gains were discussed in detail.

Dag (2006) proposed a new equivalent domain integral technique for thermal fracture analysis of orthotropic functionally graded material subjected to thermal stresses. All the thermo-mechanical properties were assumed to have continuous spatial variations through the functionally graded medium. The in-plane component of the coefficient of thermal expansion has the most significant effect on the mode-I stress intensity factor.

1.3 SCOPE OF PRESENT WORK

From the literature review, it is clearly seen that both analytical and numerical methods have been explored to a great extent, but not much work has been reported under thermo-mechanical fracture using EFGM. Therefore, this gives us an opportunity to explore the wide field of thermo-mechanical fracture. Therefore, in the present work, EFGM has been exploited to simulate two-dimensional fracture problems under thermal/mechanical loads. The broad objectives of present thesis work are as follows:

- ❖ To study and compare the different crack modeling techniques.
- ❖ To simulate the weak/strong discontinuity under thermal/mechanical loads.
- ❖ To study the effect of multiple cracks interaction under thermal/mechanical loads.
- ❖ To simulate two-dimensional thermo-elastic fracture problems.
- ❖ To study the fracture in FGMs under thermal/mechanical loads.
- ❖ To perform elastic-plastic analysis of fracture mechanics problems.
- ❖ To simulate the quasi-static crack growth under thermal/mechanical loads.
- ❖ To develop the meshfree codes for the above work.

1.4 THESIS ORGANIZATION

A chapter wise breakup of the present thesis work is as follows:

Chapter 1: Introduction and Literature Review

This chapter presents a brief introduction to the various meshfree methods and their characteristic features which secludes them from conventional mesh-based numerical methods. Exhaustive literature review of EFGM applied in the area of fracture mechanics is also presented in this chapter. The gaps in the application of EFGM were indentified, and then the objectives of thesis are presented.

Chapter 2: EFGM and Crack Modeling Techniques

This chapter elucidates the EFGM starting from the variational form of governing equation in elastostatics. Techniques to enforce essential boundary conditions and numerical integration are also explained. Different crack modeling techniques in EFGM are implemented and compared against each other. A comparison of various crack modeling techniques has been presented, and it was found that the intrinsic enrichment technique performs well for the fracture mechanics problems, and thereby further endorsed in the present thesis work.

Chapter 3: Modeling of Weak and Strong Discontinuities

In this chapter, EFGM has been extended to simulate the problems involving weak and strong discontinuities. Different techniques of modeling the derivative discontinuity viz. domain decomposition method, Lagrange multiplier approach, and jump function criterion have been implemented and compared against each other. The jump function criterion proved to be the best among these techniques. Therefore, the jump function is exploited to model cracks in bi-material (combination of weak and strong discontinuity) under thermal/mechanical loads. A new criterion for modeling bi-material interfacial crack has been suggested, which involves only four enrichment functions in the basis instead of twelve enrichment functions.

Chapter 4: Simulation of Multiple Interacting Cracks

The numerical simulation of multiple interacting cracks under both mechanical and thermal loading is carried out in this chapter. A new criterion based on intrinsic enrichment is proposed to simulate the interaction effect of multiple cracks in both convex and non-convex domains. The proposed criterion was found to be quite effective in reducing the computational cost of EFGM.

Chapter 5: Cracks under Thermoelastic Loading

In this chapter, the EFGM has been extended to simulate two-dimensional thermo-elastic fracture problem in isotropic material. The problem is decoupled in such a way that the temperature distribution is obtained first. Temperature field thus obtained is employed then as input for determining the displacement and stress fields. Both temperature and mechanical fields are enriched intrinsically in order to represent the discontinuous temperature, heat flux, displacement and traction across the crack surface. The crack surface is modeled with isothermal or adiabatic boundary conditions.

Chapter 6: Cracks in Functionally Graded Materials

This chapter covers a brief introduction to fracture in functionally graded materials (FGMs) along with the modifications in the interaction integral to capture the mixed-mode stress intensity factor. The EFGM has been applied to simulate the problems of fracture in FGMs under both mechanical and thermal loads.

Chapter 7: Simulation of Elasto-Plastic Fracture

An application of EFGM to the problems of non-linear fracture mechanics has been presented in this chapter. Ramberg-Osgood hardening rule has been used for modeling the non-linearity in the constitutive relations. Temperature dependent material properties were considered as another source of non-linearity. Enriched basis functions were used in order to capture the HRR (Hutchinson-Rice-Rosengren) singularity. The values of *J*-integral obtained by EFGM were found in good agreement with the FEM solution.

Chapter 8: Crack Growth Modeling

This chapter focuses on the modeling of kinked cracks using intrinsic enriched EFGM. A new criterion for modeling kinked crack has been proposed and implemented. This technique is later exploited for the modeling of a crack growth.

Chapter 9: Conclusions and Future Scope

In this chapter, the key findings of the present work are summarized along with a future scope of the work.

1.5 MAJOR FINDINGS AND CONCLUSIONS

In the present work, EFGM has been successfully extended to simulate the various fracture mechanics problems subjected to thermal/mechanical loads. The major findings of the present thesis work are as follows:

Initially, a comparison of various crack modeling techniques has been presented, and it was found that intrinsic enrichment criterion gives quite accurate results for cracks simulations. Owing to its simplicity and accuracy, the intrinsic enrichment criterion was further exploited to accomplish the remaining research work.

The weak discontinuities in EFGM were modeled using different criteria. The jump function approach was found most suitable for the modeling of material discontinuity. A new criterion for modeling bi-material interfacial crack using Jump function has been proposed. The proposed method involves only four enrichment functions in the basis function instead of the usual twelve.

A new intrinsic enrichment based criterion has been proposed, and implemented to simulate the interaction effect of multiple cracks in both convex and non-convex domains. The results were found in good agreement with the FEM solutions. Moreover, it was found that the proposed criterion also reduces the computational cost of the EFGM.

The EFGM has also been extended to simulate two-dimensional thermo-elastic fracture problems in isotropic material. Both temperature and mechanical fields were enriched intrinsically in order to represent the discontinuous temperature, heat flux,

displacement and traction across the crack surface. Some example problems of fracture in functionally graded materials under thermal/mechanical loads were tackled by EFGM. The results were found quite close to the available analytical solutions.

Next, the simulation of a non-linear fracture mechanics problem has been carried out using EFGM. The enriched basis functions were used in order to capture the HRR (Hutchinson-Rice-Rosengren) singularity. The values of *J*-integral were found to be in good agreement with the FEM solution.

Finally, a new EFGM criterion has been developed for the modeling the kinked cracks. This criterion was used for the simulation of quasi-static crack growth. The crack path obtained using the proposed technique was found to be almost same as that obtained by other techniques.

Chapter 2

EFGM AND CRACK MODELING TECHNIQUES

2.1 INTRODUCTION

The element free Galerkin method (EFM) is a recently developed meshfree method (Belytschko *et al.*, 1994) which has been extensively used for simulating various problems of solid mechanics. The EFGM is considered a meshfree method as it only requires a set of nodes and description of boundaries to construct an approximate solution. The connectivity among data points and shape functions are constructed without any requirement of elements. A Galerkin scheme is used for approximating the solution to partial differential equation with an approximant written in terms of nodes. This method has been extensively used for simulating cracks growth problems as it does not require remeshing for crack growth simulation. In this method, both trial and test functions are constructed from the same space using moving least square (MLS) approximants. The MLS approximation consists of three elements: a compact support weight function associated with each node, a polynomial basis and a set of coefficient that depends on node position. The nodal connectivity is ensured by overlapping nodal domain of influence.

The advantage of MLS approximation is that a highly continuous approximation can be easily generated by the appropriate choice of weight function. Thus, the post processing required to generate smooth stress fields becomes unnecessary in EFGM. Although, EFGM is considered to be a meshfree method with respect to construction of shape function, a background mesh/cell is still required for the evaluation of integrals in Galerkin weak form.

2.2 OVERVIEW OF EFGM

In this section, some basic concepts are discussed along with a general procedure for the construction of EFGM approximations.

2.2.1 Moving Least Square (MLS) Approximation

The moving least square approximation scheme was introduced by Lancaster and Salkauskas (1981) for the interpolation/approximation of data points. Later, it was used for the construction of meshfree shape functions. Initially, MLS approximation scheme was used by Nayroles *et al* (1992) to construct the shape functions for diffuse element method, which was later used in EFGM for generating the shape functions (Belytschko *et al.*, 1994).

In EFGM, a field variable u is approximated by MLS approximation, $u^h(\mathbf{x})$ which is given as

$$u^h(\mathbf{x}) = \sum_{j=1}^{m} p_j(\mathbf{x}) a_j(\mathbf{x}) = \mathbf{p}^T(\mathbf{x})\mathbf{a}(\mathbf{x}) \tag{2.1}$$

where, $\mathbf{p(x)}$ is a vector of complete basis functions (usually a polynomial), which is given as

$$\mathbf{p}^T(\mathbf{x}) = [1,\ x,\ y,\ z,\ xy,\ yz,\ zx, \ldots\ x^{k'},\ y^{k'},\ z^{k'}] \tag{2.2}$$

and $\mathbf{a(x)}$ is a vector of unknown coefficients

$$\mathbf{a}^T(\mathbf{x}) = [a_1(\mathbf{x}),\ a_2(\mathbf{x}),\ a_3(\mathbf{x}),\ \ldots a_m(\mathbf{x})] \tag{2.3}$$

where, $\mathbf{x}^T = [x \quad y \quad z]$, k' is degree of the polynomial and m is the number of terms in the basis.

In 2D, the complete polynomial basis functions and corresponding coefficient vectors are given as:

Linear basis

$$\mathbf{p}^T(\mathbf{x}) = [1, x, y] \qquad (m = 3, \text{linear}) \tag{2.4}$$

$$\mathbf{a}^T(\mathbf{x}) = [a_1(\mathbf{x}),\ a_2(\mathbf{x}),\ a_3(\mathbf{x})]$$

Quadratic basis

$$\mathbf{p}^T(\mathbf{x}) = [1, x, y, xy, x^2, y^2], \qquad (m = 6, \text{ quadratic}) \tag{2.5}$$

$$\mathbf{a}^T(\mathbf{x}) = [a_1(\mathbf{x}),\ a_2(\mathbf{x}),\ a_3(\mathbf{x}), a_4(\mathbf{x}),\ a_5(\mathbf{x}),\ a_6(\mathbf{x})]$$

The unknown coefficients $\mathbf{a}(\mathbf{x})$ are obtained by minimizing a weighted least square sum of the difference between local approximation, $u^h(\mathbf{x})$ and field function nodal parameter u_I. The weighted least square sum denoted by $L(\mathbf{x})$ can be written in following quadratic form:

$$L(\mathbf{x}) = \sum_{I=1}^{n} w(\mathbf{x} - \mathbf{x}_I)[\mathbf{p}^T(\mathbf{x})\mathbf{a}(\mathbf{x}) - u_I]^2 \tag{2.6}$$

where, u_I is the nodal parameter associated with node I at $\mathbf{x} = \mathbf{x}_I$. However, u_I are not the nodal values of $u^h(\mathbf{x} = \mathbf{x}_I)$ because $u^h(\mathbf{x})$ is an approximant and not an interpolant. The difference between u_I and $u^h(\mathbf{x} = \mathbf{x}_I)$ is shown in Fig. 2.1. $w(\mathbf{x} - \mathbf{x}_I)$ is the weight function having compact support associated with node I, and n is the number of nodes with domain of influence containing the point $\mathbf{x}$, i.e. $w(\mathbf{x} - \mathbf{x}_I) \neq 0$.

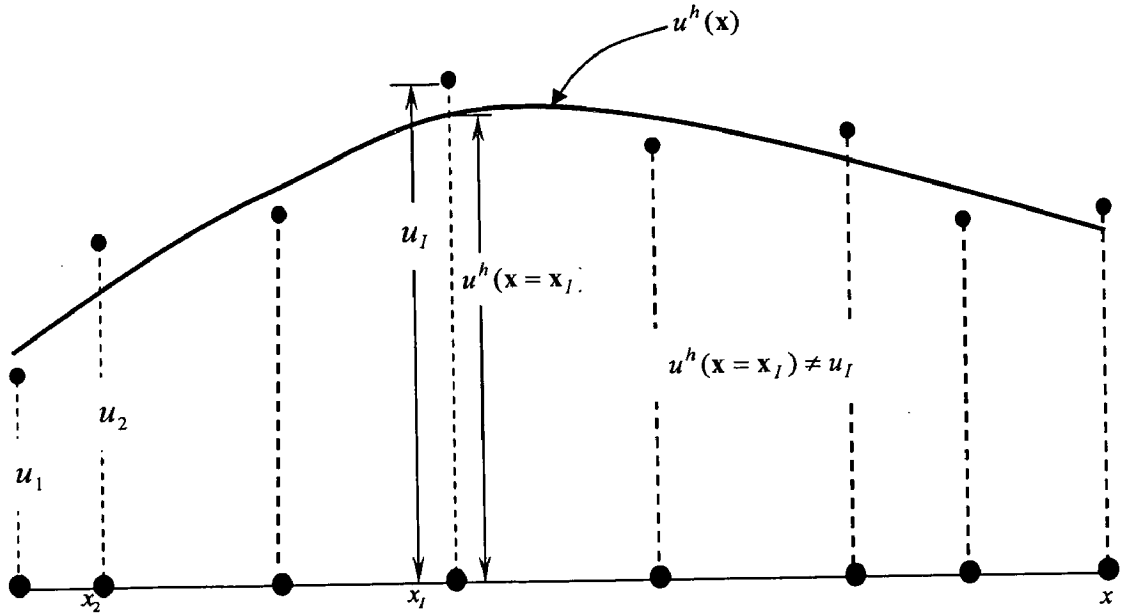

Fig. 2.1: Difference between u_I and $u^h(\mathbf{x})$

By setting $\frac{\partial L}{\partial \mathbf{a}} = 0$, a following set of linear equation is obtained

$$\mathbf{A}(\mathbf{x})\mathbf{a}(\mathbf{x}) = \mathbf{B}(\mathbf{x})\mathbf{u} \tag{2.7}$$

or

$$\mathbf{a}(\mathbf{x}) = \mathbf{A}^{-1}(\mathbf{x})\mathbf{B}(\mathbf{x})\mathbf{u} \tag{2.8}$$

where, $\mathbf{A}(\mathbf{x})$ and $\mathbf{B}(\mathbf{x})$ are given as:

$$\mathbf{A}(\mathbf{x}) = \sum_{I=1}^{n} w(\mathbf{x}-\mathbf{x}_I)\mathbf{p}(\mathbf{x}_I)\mathbf{p}^T(\mathbf{x}_I) \tag{2.9}$$

$$\mathbf{B}(\mathbf{x}) = \{w(\mathbf{x}-\mathbf{x}_1)\mathbf{p}(\mathbf{x}_1), w(\mathbf{x}-\mathbf{x}_2)\mathbf{p}(\mathbf{x}_2), \ldots\ldots\ldots\ldots, w(\mathbf{x}-\mathbf{x}_n)\mathbf{p}(\mathbf{x}_n)\} \tag{2.10}$$

By substituting Eq. (2.8) in Eq. (2.1), the MLS approximation is obtained as:

$$u^h(\mathbf{x}) = \sum_{I=1}^{n} \Phi_I(\mathbf{x})u_I = \mathbf{\Phi}^T(\mathbf{x})\mathbf{u} \tag{2.11}$$

where,

$$\mathbf{\Phi}^T(\mathbf{x}) = \{\Phi_1(\mathbf{x}),\ \Phi_2(\mathbf{x}),\ \Phi_3(\mathbf{x}),\ \ldots\ \Phi_n(\mathbf{x})\} \tag{2.12}$$

$$\mathbf{u}^T = [u_1,\ u_2,\ u_3,\ \ldots\ u_n] \tag{2.13}$$

The mesh free shape function $\Phi_I(\mathbf{x})$ is defined as:

$$\Phi_I(\mathbf{x}) = \sum_{j=}^{m} p_j(\mathbf{x})(\mathbf{A}^{-1}(\mathbf{x})\mathbf{B}(\mathbf{x}))_{jI} = \mathbf{p}^T\mathbf{A}^{-1}\mathbf{B}_I \tag{2.14}$$

The linear consistency requirements for the shape function $\Phi_I(\mathbf{x})$ (Belytschko *et al.*, 1996b) are given as:

$$\sum_{I=1}^{n} \Phi_I(\mathbf{x}) = 1, \qquad \sum_{I=1}^{n} \Phi_I(\mathbf{x})x_I = x \qquad \sum_{I=1}^{n} \Phi_I(\mathbf{x})y_I = y$$

The derivatives of MLS shape function are computed as:

$$\Phi_{I,\mathbf{x}}(\mathbf{x}) = (\mathbf{p}^T\mathbf{A}^{-1}\mathbf{B}_I)_{,\mathbf{x}} = \mathbf{p}^T{}_{,\mathbf{x}}\,\mathbf{A}^{-1}\,\mathbf{B}_I + \mathbf{p}^T(\mathbf{A}^{-1})_{,\mathbf{x}}\mathbf{B}_I + \mathbf{p}^T\mathbf{A}^{-1}\mathbf{B}_{I,\mathbf{x}} \tag{2.15}$$

where, $\mathbf{B}_{I,\mathbf{x}}(\mathbf{x}) = \frac{dw}{d\mathbf{x}}(\mathbf{x}-\mathbf{x}_I)\mathbf{p}(\mathbf{x}_I)$

and $\mathbf{A}^{-1}{}_{,x}$ is computed by

$$\mathbf{A}^{-1}{}_{,x} = -\mathbf{A}^{-1}\mathbf{A}_{,x}\mathbf{A}^{-1} \tag{2.16}$$

where,

$$\mathbf{A}_{,x} = \sum_{I=1}^{n} \frac{dw}{d\mathbf{x}}(\mathbf{x}-\mathbf{x}_I)\mathbf{p}(\mathbf{x}_I)\mathbf{p}^T(\mathbf{x}_I)$$

2.2.2 Domain of Influence

The domain of influence (influence domain) is defined as a domain in which a node exerts its influence. It is related to a node, in contrast to the support domain, which is linked with an evaluation point. The influence domain is predefined for each node in the problem domain, and it can vary from one node to another. The concept of influence domain is a way to select nodes for the interpolation and it works well with highly non-regular nodal distribution. Different types of influence domain (Fig. 2.2) are used in practice but among them, circular and rectangular influence domains are most widely used.

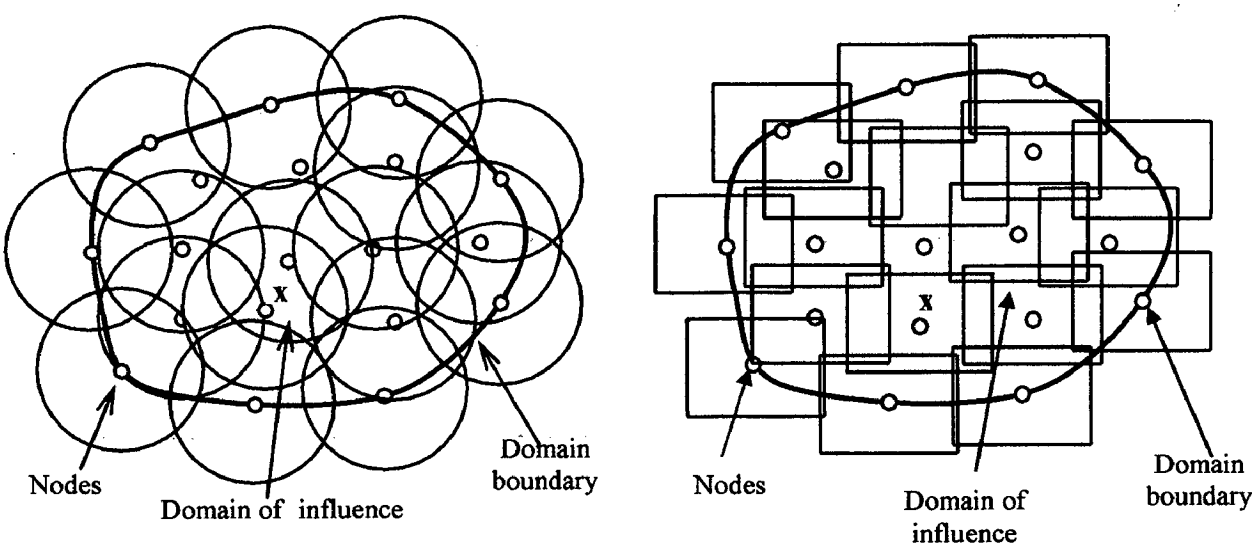

(a) Circular influence domain **(b) Rectangular influence domain**

Fig. 2.2: A schematic model for meshfree method showing the domain boundary, nodes and domain of influence (Nguyen *et al.*, 2008)

2.2.3 Weight Functions

The choice of weight function $w(\mathbf{x}-\mathbf{x}_I)$ affects the resulting approximation $u^h(\mathbf{x}_I)$ in EFGM. Therefore, the selection of appropriate weight function becomes quite essential. The weight function is non-zero only over a small neighborhood of a node $\mathbf{x}_I$, called the support or domain of influence of node I. The smoothness and continuity of the shape function $\Phi_I(\mathbf{x})$ depends on the smoothness and continuity of the weight function $w(\mathbf{x}-\mathbf{x}_I)$. If a weight function is C^1 continuous then the shape function will also have C^1 continuity (Fig. 2.3).

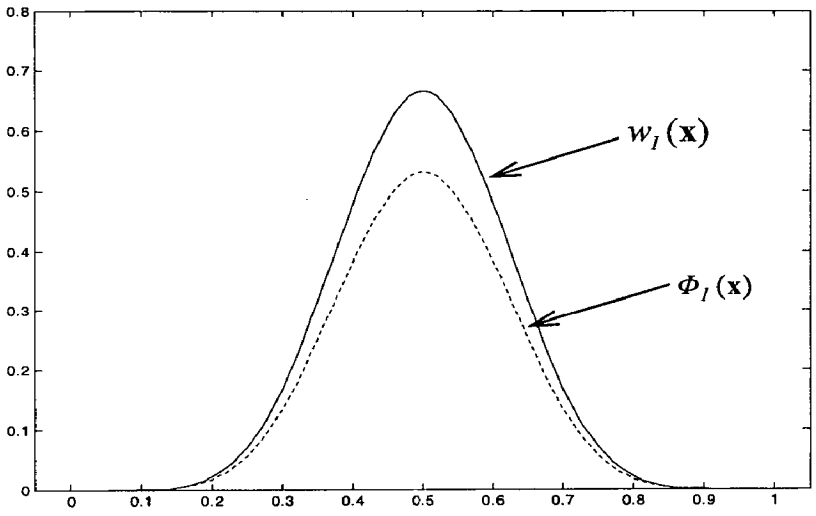

Fig. 2.3: A plot of weight function and corresponding shape function

A typical weight function must satisfy the following conditions (Singh, 2004):

- ❖ It must be positive, continuous and differentiable in the domain of influence.
- ❖ It should decrease in magnitude as the distance from $\mathbf{x}$ to $\mathbf{x}_I$ increases, so that local character of MLS approximation is maintained.
- ❖ It should be zero outside the domain of influence.
- ❖ It should have a relatively large value for a node, which is closer to the evaluation point.

❖ The nodes in the domain of influence should not be collinear (except 1-D) and the number of nodes must be larger than the number of terms in the basis function $(n > m)$.

The different weight functions used in literature can be written as a function of normalized radius $\bar{r}$ as follow:

Quartic spline weight function (Belytschko et al., 1996b)

$$w(\mathbf{x}-\mathbf{x}_I) = w(\bar{r}) = \begin{cases} 1-6\bar{r}^2+8\bar{r}^3-3\bar{r}^4 & 0 \le \bar{r} \le 1 \\ 0 & \bar{r} > 1 \end{cases} \tag{2.17}$$

Cubic spline weight function (Belytschko et al., 1996b)

$$w(\mathbf{x}-\mathbf{x}_I) = w(\bar{r}) = \begin{cases} \frac{2}{3}-4\bar{r}^2+4\bar{r}^3 & \bar{r} \le \frac{1}{2} \\ \frac{4}{3}-4\bar{r}+4\bar{r}^2-\frac{4}{3}\bar{r}^3 & \frac{1}{2} < \bar{r} \le 1 \\ 0 & \bar{r} > 1 \end{cases} \tag{2.18}$$

Gaussian weight function (Belytschko et al., 1996b)

$$w(\mathbf{x}-\mathbf{x}_I) = w(\bar{r}) = \begin{cases} e^{-(2.5\bar{r})^2} & 0 \le \bar{r} \le 1 \\ 0 & \bar{r} > 1 \end{cases} \tag{2.19}$$

Exponential weight function (Belytschko et al., 1996b)

$$w(\mathbf{x}-\mathbf{x}_I) = w(\bar{r}) = \begin{cases} 100^{-\bar{r}} & 0 \le \bar{r} \le 1 \\ 0 & \bar{r} > 1 \end{cases} \tag{2.20}$$

where, $\bar{r} = \dfrac{\| \mathbf{x}-\mathbf{x}_I \|}{\mathrm{d}_{mI}}$, $\| \mathbf{x}-\mathbf{x}_I \|$ is the distance from a sampling point $\mathbf{x}$ to a node $\mathbf{x}_I$ and d_{mI} is the influence domain of node I, $\bar{r} = \dfrac{\| \mathbf{x}-\mathbf{x}_I \|}{d_{mI}}$, $d_{mI} = d_{\max} c_I$, $d_{\max}$ = scaling parameter which defines size of the domain of influence and c_I at node I is the distances

to the nearest neighbors. d_{mI} is chosen such that the matrix is non-singular at every point in the domain. The cubic-spline weight function has been most commonly used in the present research work.

2.2.4 EFGM Shape Functions

To compute the meshfree shape functions Φ_I, it is necessary to calculate $\mathbf{A}^{-1}$. In one dimensional problem, the operation of inverting $\mathbf{A}$ matrix is not very difficult and time consuming but in two-dimensional and three-dimensional problems, this inversion becomes quite expensive. To overcome this situation, Dolbow and Belytschko (1998) proposed a computationally inexpensive alternative approach. This approach involves the LU decomposition of the $\mathbf{A}$ matrix. A brief description of this approach is given below. At any point $\mathbf{x}$, the shape function is given as

$$\Phi_I(\mathbf{x}) = \mathbf{P}^T(\mathbf{x})\mathbf{A}^{-1}(\mathbf{x})\mathbf{B}_I(\mathbf{x}) = \gamma^T(\mathbf{x})\mathbf{B}_I(\mathbf{x}) \tag{2.21}$$

where,

$\gamma^T(\mathbf{x}) = \mathbf{p}^T(\mathbf{x})\mathbf{A}^{-1}(\mathbf{x})$.

This leads to the relationship

$$\mathbf{A}(\mathbf{x})\gamma(\mathbf{x}) = \mathbf{p}(\mathbf{x}) \tag{2.22}$$

$$\Phi_I(\mathbf{x}) = \mathbf{P}^T(\mathbf{x})\mathbf{A}^{-1}(\mathbf{x})\mathbf{B}_I(\mathbf{x}) = \gamma^T(\mathbf{x})\mathbf{B}_I(\mathbf{x})$$

The vector $\gamma(\mathbf{x})$ is to be calculated using **LU** decomposition of the matrix $\mathbf{A}$ followed by back substitution.

The partial derivatives of $\gamma(\mathbf{x})$ can be recursively calculated as

$$\mathbf{A}(\mathbf{x})\gamma_{,x}(\mathbf{x}) = \mathbf{p}_{,x}(\mathbf{x}) - \mathbf{A}_{,x}(\mathbf{x})\gamma(\mathbf{x}) \tag{2.23}$$

$$\mathbf{A}(\mathbf{x})\gamma_{,y}(\mathbf{x}) = \mathbf{p}_{,y}(\mathbf{x}) - \mathbf{A}_{,y}(\mathbf{x})\gamma(\mathbf{x}) \tag{2.24}$$

The derivatives of shape function are given as

$$\Phi_{I,x}(\mathbf{x}) = \gamma^T{}_x(\mathbf{x})\mathbf{B}_I(\mathbf{x}) + \gamma^T(\mathbf{x})\mathbf{B}_{I,x}(\mathbf{x}) \tag{2.25}$$

$$\Phi_{I,y}(\mathbf{x}) = \gamma^T{}_y(\mathbf{x})\mathbf{B}_I(\mathbf{x}) + \gamma^T(\mathbf{x})\mathbf{B}_{I,y}(\mathbf{x}) \tag{2.26}$$

2.2.5 Enforcement of Essential Boundary Conditions

The proper imposition of essential boundary condition is quite difficult in EFGM since MLS approximation does not satisfy the Kronecker delta function property i.e. $\Phi_I(\mathbf{x}_J) \neq \delta_{IJ}$. Many numerical techniques have been proposed to enforce the essential boundary conditions in EFGM. Lagrange multiplier method was first proposed by Belytschko *et al.*, (1994). This technique is quite accurate but its imposition creates problems such as the system matrix does not remain positive definite and banded. Lu *et al.* (1994) proposed a modified variational principle approach, in which Lagrange multipliers were replaced by their physical meaning. As a result, banded sets of equations were obtained but the results were not found as accurate as obtained by Lagrange multiplier approach. Another approach named as coupling with finite element method was proposed by Krongauz and Belytschko (1996) for the imposition of essential boundary conditions. In this approach, EFGM domain was necklaced by FEM domain and then essential boundary conditions were applied. This method simplified the enforcement of boundary conditions but the numerical integration became more tedious. Gavete *et al.* (2000) used the penalty approach, which is quite easy for enforcing the essential boundary conditions, and it gives discrete equations in simple form similar to FEM. Although, system matrix obtained by this method is positive and posses the bandedness property but improper selection of penalty parameter can lead to wrong results. Rao and Rehman (2000) presented an efficient full transformation technique to enforce the essential boundary conditions, but this technique was found difficult from the implementation point of view. In the present work, Lagrange multiplier technique has been used due to its accuracy.

2.3 ELASTOSTATICS

2.3.1 Governing Equations

Consider small displacement elastostatics, which is governed by the equation of equilibrium (Ottosen and Petersson, 1992)

$$\nabla \cdot \sigma + \mathbf{b} = 0 \quad \text{in} \quad \Omega \tag{2.27}$$

along with the following boundary conditions

(Natural boundary condition) $\boldsymbol{\sigma}.\bar{\mathbf{n}} = \bar{\mathbf{t}}$ on Γ_t

(Essential boundary condition) $\mathbf{u} = \bar{\mathbf{u}}$ on Γ_u

where, σ is the stress tensor, which corresponds to the displacement field $\mathbf{u}$, $\mathbf{b}$ is a body force vector, ∇ is the divergence operator, superposed bar denotes prescribed boundary values, and $\bar{\mathbf{n}}$ is the unit normal to the domain Ω .

The variational (or weak) form of the equilibrium Eq. (2.27) can be written

$$\int_\Omega \delta\boldsymbol{\varepsilon} : \boldsymbol{\sigma}\, d\Omega - \int_\Omega \delta\mathbf{u}.\mathbf{b}\, d\Omega - \int_{\Gamma_t} \delta\mathbf{u}.\bar{\mathbf{t}}\, d\Gamma - \delta\mathbf{W}_u(\mathbf{u},\boldsymbol{\lambda}) = 0 \tag{2.28}$$

where, $\delta\boldsymbol{\varepsilon} = \nabla_s(\delta\mathbf{u})$, ∇_s is the symmetric gradient operator, $\delta\mathbf{W}_u$ is used to enforce the essential boundary conditions. Several forms of $\mathbf{W}_u$ are possible, in the present work, Lagrange multiplier method has been used as

$$\mathbf{W}_u(\mathbf{u},\boldsymbol{\lambda}) = \int_{\Gamma_u} \boldsymbol{\lambda}(\mathbf{u} - \bar{\mathbf{u}})\, d\Gamma \tag{2.29}$$

$$\delta\mathbf{W}_u(\mathbf{u},\boldsymbol{\lambda}) = \int_{\Gamma_u} \delta\boldsymbol{\lambda}\,(\mathbf{u} - \bar{\mathbf{u}})\, d\Gamma + \int_{\Gamma_u} \delta\mathbf{u}\,\boldsymbol{\lambda}\, d\Gamma \tag{2.30}$$

2.3.2 Discrete Equations

Considering linear elastic relations

$$\boldsymbol{\varepsilon} = \nabla_s \mathbf{u} \tag{2.31}$$

$$\boldsymbol{\sigma} = \mathbf{D}\boldsymbol{\varepsilon} \tag{2.32}$$

where, $\boldsymbol{\varepsilon}$ is the strain and $\mathbf{D}$ is a constitutive matrix.

For the case of plane stress in an isotropic material with coefficient of thermal expansion β subjected to a temperature change ΔT, the thermal strain matrix is given by

$$\varepsilon_T = \begin{Bmatrix} \beta \Delta T \\ \beta \Delta T \\ 0 \end{Bmatrix}$$

Lagrange multiplier λ used in Eq. (2.29) is expressed as

$$\lambda(\mathbf{x}) = N_I(s)\boldsymbol{\lambda}_I, \qquad \mathbf{x} \in u \tag{2.33a}$$

$$\delta\lambda(\mathbf{x}) = N_I(s)\delta\boldsymbol{\lambda}_I \qquad \mathbf{x} \in u \tag{2.33b}$$

where, $N_I(s)$ is a Lagrange interpolant and s is the arc length along the boundary; the repeated indices indicate summations.

In the variational form of equilibrium Eq. (2.28), $u(\mathbf{x})$ is replaced by EFGM approximation $u^h(\mathbf{x})$, and the variation $\delta u(\mathbf{x})$ is replaced by $\delta u^h(\mathbf{x})$.

$$u^h(\mathbf{x}) = \sum_{I=1}^{n} \Phi_I(\mathbf{x}) u_I \tag{2.34}$$

$$\delta u^h(\mathbf{x}) = \sum_{I=1}^{n} \Phi_I(\mathbf{x}) \delta u_I \tag{2.35}$$

The nodal test function values δu_I are arbitrary, except on Γ_u, and can be eliminated from the equations. Substituting Eq. (2.33) into the weak form Eq. (2.28) yields:

$$\begin{bmatrix} \mathbf{K} & \mathbf{G} \\ \mathbf{G}^T & 0 \end{bmatrix} \begin{Bmatrix} \mathbf{u} \\ \lambda \end{Bmatrix} = \begin{Bmatrix} \mathbf{f} \\ \mathbf{q} \end{Bmatrix} \tag{2.36}$$

where,

$$\mathbf{K}_{IJ} = \int_{\Omega} \mathbf{B}^T \mathbf{D}\, \mathbf{B}\, d\Omega \tag{2.37}$$

$$G_{IK} = -\int_{\Gamma_u} \Phi_I \mathbf{N}_K \, d\Gamma \tag{2.38}$$

$$\mathbf{f}_I = \int_{\Gamma_t} \bar{\mathbf{t}} \Phi_I \, d\Omega + \int_{\Gamma_u} \mathbf{b} \Phi_I \, d\Omega \tag{2.39}$$

$$\mathbf{q}_K = -\int_{\Gamma_u} \mathbf{N}_K \, \bar{\mathbf{u}} \, d\Gamma \tag{2.40}$$

$\mathbf{B}_I = \begin{bmatrix} \Phi_{I,x} & 0 \\ 0 & \Phi_{I,y} \\ \Phi_{I,y} & \Phi_{I,x} \end{bmatrix}$, $\mathbf{N}_k = \begin{bmatrix} N_k & 0 \\ 0 & N_k \end{bmatrix}$, $\mathbf{D} = \dfrac{E}{(1+\nu)(1-2\nu)} \begin{bmatrix} 1-\nu & \nu & 0 \\ \nu & 1-\nu & 0 \\ 0 & 0 & \dfrac{1-2\nu}{2} \end{bmatrix}$ for plane strain, $\mathbf{D} = \dfrac{E}{1-\nu^2} \begin{bmatrix} 1 & \nu & 0 \\ \nu & 1 & 0 \\ 0 & 0 & \dfrac{1-\nu}{2} \end{bmatrix}$ for plane stress, comma denotes partial derivative with respect to the indicated spatial variable, E and ν are Young's modulus and Poisson's ratio respectively.

2.3.3 Integration Issues

Computation of stiffness matrix ($\mathbf{K}$), displacement matrix ($\mathbf{G}$) and force vector ($\mathbf{f}$) in Eqs. (2.37–2.40) requires the integration over the domain, which corresponds to area integration in two dimensions. Stiffness matrix and force vector computation requires a numerical integration scheme such as Gauss quadrature, which in turn, requires a subdivision of the domain. Unlike finite elements, meshfree methods have no inherent subdivision of the domain. Hence, it is necessary to introduce a subdivision of the domain for purpose of integration. Two different types of subdivisions are shown in Fig. 2.4. The quadrature shown in Fig. 2.4a is the most common. It uses a finite element mesh generator to create a cell structure which matches with the problem domain; this technique is often called an element quadrature. The vertices of this background mesh are often used as the initial array of nodes for the EFGM model; however, additional nodes

may be added where desired such as the nodes at the crack tip in the model shown in Fig. 2.4a. The second integration technique, which is often called cell quadrature, uses background cells, which is independent of the problem domain as shown in Fig. 2.4b. During integration over the problem domain, a particular quadrature point is checked whether it lies inside the domain or not. This technique is not widely used because it does not yield accurate results along curved boundaries. A nodal integration technique, proposed by Beissel and Belytschko (1996), was an effort to make EFGM a completely meshfree method. However, in this technique, additional terms are required for stability purpose. Moreover, the accuracy of this scheme is not as good as cell based integration schemes. Hence, element quadrature scheme has been adopted in the present work.

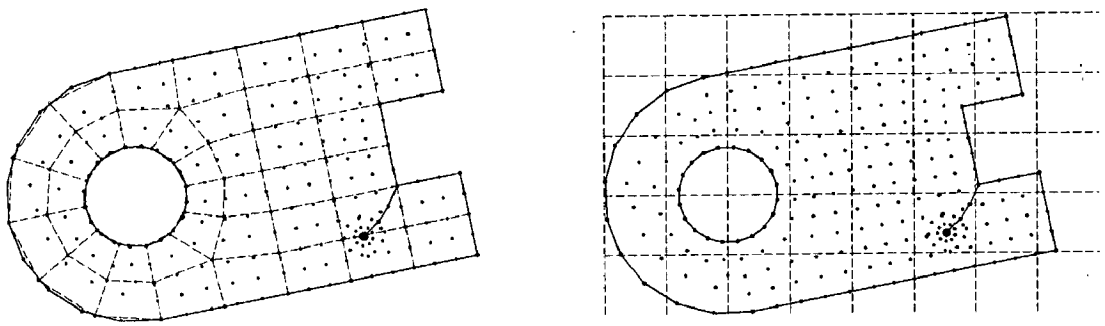

(a) Element quadrature **(b)** Cell quadrature

Fig. 2.4: Integration techniques for EFGM (Belytschko *et al.*, 1996c)

The smoothness which is inherent in meshfree methods not only provides the smooth approximation functions but also provides smooth derivatives. These approximation functions possess same continuity as that of the weight functions. This higher order smoothness leads to difficulties where a discontinuity is present either in the geometry or in the material. These discontinuities include cases where a boundary of the geometry can be non-convex e.g. a plate with a hole or a crack. Because of the aforementioned smoothness of meshfree methods, special procedure is required to simulate the presence of crack.

As the present work deals with application of EFGM to fracture mechanics problems, thereby a discussion on crack modeling techniques is needed. Moreover, before discussing crack modeling techniques, a brief introduction of linear elastic fracture mechanics is also presented in the next section.

2.4 LINEAR ELASTIC FRACTURE MECHANICS

The concept of linear elastic fracture mechanics is based on the assumption that the plastic zone is significantly small when compared with the dimensions of body. Based on this assumption stress field near the crack tip is calculated using theory of elasticity. Analytical expressions derived for plane stress or plane strain depends on the associated mode of loading/fracture.

2.4.1 Modes of Fracture

The displacement field around a crack can be categorized by three different modes as shown in Fig. 2.5. The arrow indicates the direction of crack surface displacement. Mode-I is called the opening mode, and is characterized by the displacements of the crack normal to the crack plane. Mode-II is called the shearing or sliding mode, and is characterized by in-plane displacements of the crack faces. Mode-III is called the tearing or antiplane mode, and is characterized by out of plane shear.

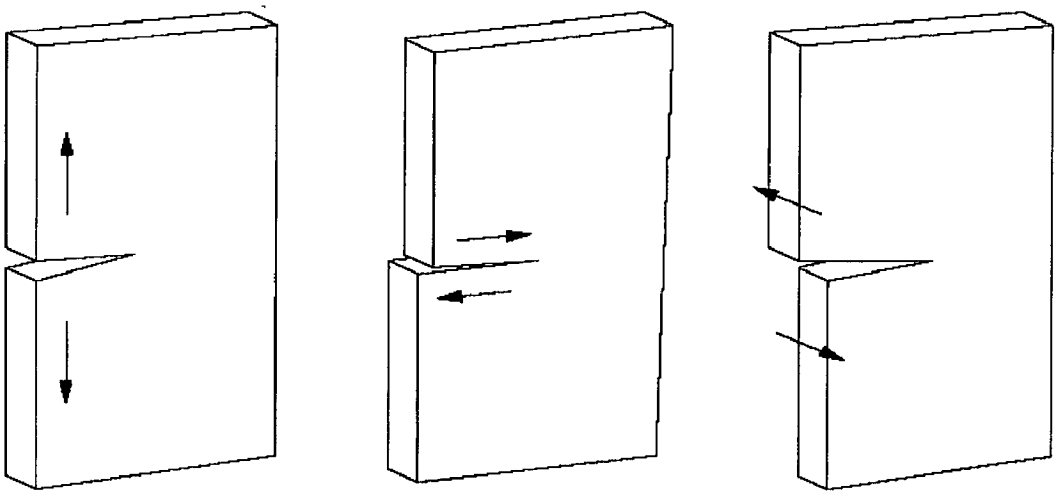

(a) Opening mode **(b)** Shearing mode **(c)** Tearing mode

Fig. 2.5: Schematic representation of the different fracture modes

2.4.2 Stress Intensity Factors

The stress at a point in the vicinity of crack tip exhibits $1/\sqrt{r}$ singularity, where r is the distance from the crack tip. The stress field near the crack tip is dominated by the first term in the asymptotic expansion (Williams, 1957). For mode-I crack (displacement perpendicular to the crack faces), the stresses can be written as (Tada *et al.*, 1997)

$$\sigma_{xx} \approx \frac{k_1}{\sqrt{2\pi r}} \cos\frac{\theta}{2}\left(1-\sin\frac{\theta}{2}\sin\frac{3\theta}{2}\right) \tag{2.41}$$

$$\sigma_{yy} \approx \frac{k_1}{\sqrt{2\pi r}} \cos\frac{\theta}{2}\left(1+\sin\frac{\theta}{2}\sin\frac{3\theta}{2}\right) \tag{2.42}$$

$$\sigma_{xy} \approx \frac{k_1}{2\sqrt{2\pi r}} \sin\theta\cos\frac{3\theta}{2} \tag{2.43}$$

The associated compatible displacement fields are as follows

$$u_x \approx \frac{k_1}{2\mu}\sqrt{\frac{r}{2\pi}}\cos\frac{\theta}{2}(\kappa-\cos\theta) \tag{2.44}$$

$$u_y \approx \frac{k_1}{2\mu}\sqrt{\frac{r}{2\pi}}\sin\frac{\theta}{2}(\kappa-\cos\theta) \tag{2.45}$$

For a mode-II crack (displacement parallel to the crack faces), the stresses can be written as

$$\sigma_{xx} \approx -\frac{k_2}{\sqrt{2\pi r}} \sin\frac{\theta}{2}\left(2+\cos\frac{\theta}{2}\cos\frac{3\theta}{2}\right) \tag{2.46}$$

$$\sigma_{yy} \approx \frac{k_2}{2\sqrt{2\pi r}} \sin\theta\cos\frac{3\theta}{2} \tag{2.47}$$

$$\sigma_{xy} \approx \frac{k_2}{\sqrt{2\pi r}} \cos\frac{\theta}{2}\left(1-\sin\frac{\theta}{2}\sin\frac{3\theta}{2}\right) \tag{2.48}$$

the associated compatible displacement fields are as follows

$$u_x \approx \frac{k_2}{2\mu}\sqrt{\frac{r}{2\pi}}\sin\frac{\theta}{2}(2+\kappa+\cos\theta) \tag{2.49}$$

$$u_y \approx \frac{k_2}{2\mu}\sqrt{\frac{r}{2\pi}}\cos\frac{\theta}{2}(2-\kappa-\cos\theta) \tag{2.50}$$

The variables r and θ denote the distance of an evaluation point from the crack tip and the angle measured from local coordinate system, respectively (see Fig. 2.6); μ is the

shear modulus and κ is the Kolosov constant defined in terms of Poisson's ratio ν as

$\kappa = (3-4\nu)$ plane stress

$\kappa = \frac{(3-\nu)}{(1+\nu)}$ plane strain

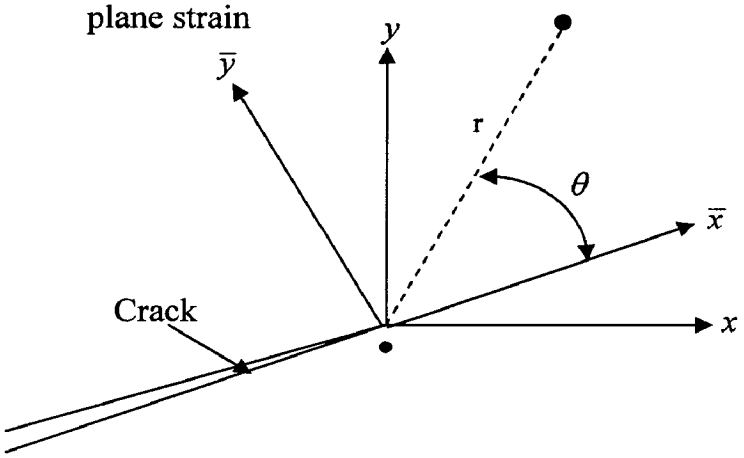

Fig. 2.6: Local coordinate system ($\bar{x}$, $\bar{y}$) at crack tip

The mode-I and mode-II stress intensity factors, k_1 and k_2, depend on the crack length, specimen geometry and applied loading. It is significant to note that the determination of these constants completely determines the asymptotic stress and displacement fields around the crack tip. For this reason, a great deal of analytical and numerical effort has gone into finding the solutions and techniques for calculating stress intensity factors.

2.4.3 Integration Integral

The interaction integral method is an effective tool for evaluating the mixed-mode fracture parameters. For a homogenous cracked body, the path independent *J*-integral is given as (Rice, 1968)

$$J = \int_{\Gamma} \left(\tilde{W}\delta_{1j} - \sigma_{ij} \frac{\partial u_i}{\partial x_1} \right) \bar{n}_j d\Gamma \tag{2.51}$$

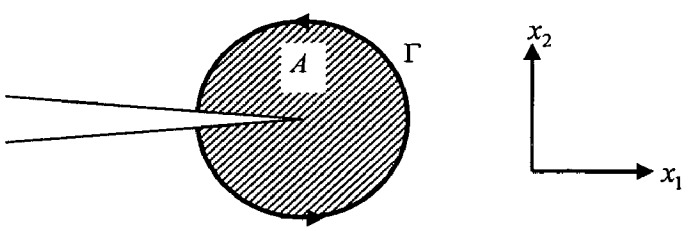

Fig. 2.7: Path Γ surrounding a crack with an enclosed area *A*

where, $\widetilde{W} = \int \sigma_{ij} d\varepsilon_{ij}$ is the strain energy density and $\overline{n}_j$ is the jth component of the outward unit vector normal to an arbitrary contour Γ enclosing the crack tip (Fig. 2.7). For linear elastic materials, it can be shown that $\widetilde{W} = \sigma_{ij}\varepsilon_{ij}/2$.

The path independence property allows the J-integral to be evaluated using far field information which is generally more accurate than near tip solution. In order to enhance its usefulness, the contour integral in Eq. (2.51) is converted into an equivalent domain form using divergence theorem (Rice, 1968).

$$J = \int_A \left(\sigma_{ij} \frac{\partial u_i}{\partial x_1} - \widetilde{W}\delta_{1j} \right) \frac{\partial \overline{q}}{\partial x_j} dA + \int_A \frac{\partial}{\partial x_j} \left(\sigma_{ij} \frac{\partial u_i}{\partial x_1} - \widetilde{W}\delta_{1j} \right) \overline{q} dA \tag{2.52}$$

where, A is the area inside the contour and $\overline{q}$ is a weight function chosen such that it has a value of *unity* at the crack tip, *zero* along the boundary of the domain, and arbitrary elsewhere. By expanding the second integrand, Eq. (2.52) reduces to

$$J = \int_A \left(\sigma_{ij} \frac{\partial u_i}{\partial x_1} - \widetilde{W}\delta_{1j} \right) \frac{\partial \overline{q}}{\partial x_j} dA + \int_A \left(\frac{\partial \sigma_{ij}}{\partial x_j} \frac{\partial u_i}{\partial x_1} + \sigma_{ij} \frac{\partial^2 u_i}{\partial x_j \partial x_1} - \sigma_{ij} \frac{\partial \varepsilon_{ij}}{\partial x_1} \right) \overline{q} dA \tag{2.53}$$

Using equilibrium $\partial \sigma_{ij}/\partial x_j = 0$ and compatibility $\varepsilon_{ij} = \frac{1}{2}\left(\frac{\partial u_i}{\partial x_j} + \frac{\partial u_j}{\partial x_i} \right)$ conditions, the second integrand of Eq. (2.53) vanishes, which results in the following equation

$$J = \int_A \left(\sigma_{ij} \frac{\partial u_i}{\partial x_1} - \widetilde{W}\delta_{1j} \right) \frac{\partial \overline{q}}{\partial x_j} dA \tag{2.54}$$

This is the classical domain form of J-integral for homogenous materials.

For calculating the interaction integral, two equilibrium states of a cracked body are considered. State 1 corresponds to be the actual state along with the given boundary conditions while state 2 is defined as an auxiliary state. The superposition of these two

states leads to another equilibrium state (state S) for which the domain form of the J-integral is

$$J^{(S)} = \int_A \left(\left(\sigma_{ij}^{(1)} + \sigma_{ij}^{(2)}\right) \frac{\partial\left(u_i^{(1)} + u_i^{(2)}\right)}{\partial x_1} - \tilde{W}^{(S)} \delta_{1j} \right) \frac{\partial \overline{q}}{\partial x_j} dA \tag{2.55}$$

where, superscript i=1, 2, and S indicates fields and quantities associated with state i. Also the strain energy density for the superimposed state is given as

$$\tilde{W}^{(S)} = \frac{1}{2}\left(\sigma_{ij}^{(1)} + \sigma_{ij}^{(2)}\right)\left(\varepsilon_{ij}^{(1)} + \varepsilon_{ij}^{(2)}\right) \tag{2.56}$$

By expanding Eq. (2.55),

$$J^{(S)} = J^{(1)} + J^{(2)} + M^{(1,2)} \tag{2.57}$$

where,

$$J^{(1)} = \int_A \left(\sigma_{ij}^{(1)} \frac{\partial u_i^{(1)}}{\partial x_1} - \tilde{W}^{(1)} \delta_{1j} \right) \frac{\partial \overline{q}}{\partial x_j} dA \tag{2.58}$$

and

$$J^{(2)} = \int_A \left(\sigma_{ij}^{(2)} \frac{\partial u_i^{(2)}}{\partial x_1} - \tilde{W}^{(2)} \delta_{1j} \right) \frac{\partial \overline{q}}{\partial x_j} dA \tag{2.59}$$

are the J-integral for states 1 and 2 respectively, and

$$M^{(1,2)} = \int_A \left(\sigma_{ij}^{(1)} \frac{\partial u_i^{(2)}}{\partial x_1} + \sigma_{ij}^{(2)} \frac{\partial u_i^{(1)}}{\partial x_1} - \tilde{W}^{(1,2)} \delta_{1j} \right) \frac{\partial \overline{q}}{\partial x_j} dA \tag{2.60}$$

is expression for the interaction integral.

In Eq. (2.57), Eq. (2.58) and Eq. (2.59), $\tilde{W}^{(1)} = \frac{1}{2}\sigma_{ij}^{(1)}\,\varepsilon_{ij}^{(1)}$, $\tilde{W}^{(2)} = \frac{1}{2}\sigma_{ij}^{(2)}\,\varepsilon_{ij}^{(2)}$, and $\tilde{W}^{(1,2)} = \frac{1}{2}\left(\sigma_{ij}^{(1)}\,\varepsilon_{ij}^{(2)} + \sigma_{ij}^{(2)}\,\varepsilon_{ij}^{(1)}\right)$ represent various strain energy densities, which satisfy

$$\widetilde{W}^{(S)} = \widetilde{W}^{(1)} + \widetilde{W}^{(2)} + \widetilde{W}^{(1,2)} \tag{2.61}$$

For linear elastic solid under mixed-mode loading conditions, the J-integral is also equal to the energy release rate and hence, the J -integral can be written as

$$J = \frac{1}{E^*}\left(K_I^2 + K_{II}^2\right) \tag{2.62}$$

where, $E^* = \left\{ \dfrac{E}{1-\nu^2} \right\}$ Plane strain

$E^* = E$ Plane stress

Applying Eq. (2.62) to states 1, 2, and the superimposed state S gives

$$J^{(1)} = \frac{1}{E^*}\left(K_I^{(1)^2} + K_{II}^{(1)^2}\right) \tag{2.63}$$

$$J^{(2)} = \frac{1}{E^*}\left(K_I^{(2)^2} + K_{II}^{(2)^2}\right) \tag{2.64}$$

and

$$\begin{aligned} J^{(S)} &= \frac{1}{E^*}\left[\left(K_I^{(1)} + K_I^{(2)}\right)^2 + \left(K_{II}^{(1)} + K_{II}^{(2)}\right)^2\right] \\ &= \frac{1}{E^*}\left[\left(K_I^{(1)^2} + K_{II}^{(1)^2}\right) + \left(K_I^{(1)^2} + K_{II}^{(2)^2}\right) + 2\left(K_I^{(1)}K_I^{(2)} + K_{II}^{(1)}K_{II}^{(2)}\right)\right] \\ &= J^{(1)} + J^{(2)} + \frac{2}{E^*}\left(K_I^{(1)}K_I^{(2)} + K_{II}^{(1)}K_{II}^{(2)}\right) \end{aligned} \tag{2.65}$$

Comparing Eq. (2.57) and Eq. (2.65),

$$M^{(1,2)} = \frac{2}{E^*}\left[\left(K_I^{(1)}K_I^{(2)} + K_{II}^{(1)}K_{II}^{(2)}\right)\right] \tag{2.66}$$

The individual SIFs for the actual state can be obtained by judiciously choosing the auxiliary state (state 2). For example, if state 2 corresponds to Mode-I loading i.e. the mode-I near tip displacement and stress field is chosen as the auxiliary state, then $K_I^{(2)} = 1$ and $K_{II}^{(2)} = 0$. Hence, Eq. (2.66) can be reduced to

$$M^{(1,I)} = \frac{2K_I^{(1)}}{E^*} \tag{2.67}$$

From above equation, we get

$$K_I^{(1)} = \frac{M^{(1,I)}E^*}{2} \tag{2.68}$$

Similarly, if state 2 is chosen to corresponds to pure Mode-II loading, i.e. the mode-II near tip displacement and stress field is chosen as the auxiliary state, then $K_I^{(2)} = 0$, $K_{II}^{(2)} = 1$ and following the similar considerations,

$$K_{II}^{(1)} = \frac{M^{(1,II)}E^*}{2} \tag{2.69}$$

Thus, numerical evaluation of interaction integral from Eq. (2.60) allows us to calculate the mixed mode stress intensity factors.

2.5 CRACK MODELING TECHNIQUES

In EFGM, special techniques have been developed for incorporating the singular functions associated with elastostatic fracture rather than employing a high nodal density near the crack tip. The latter can be expensive and awkward for problems with complex geometry. It was found that the incorporation of the singular fields in a meshfree method is substantially simpler and more trouble-free than in finite element methods. An enrichment of a meshfree method may be carried out extrinsically or intrinsically. In EFGM, the crack modeling techniques are broadly classified in two categories

(a) Enrichment Techniques

(b) Smoothening Techniques

2.5.1 Enrichment Techniques

As the name suggests, enrichment theoretically means increasing the order of completeness. With respect to crack modeling, enrichment techniques involve inclusion of additional information regarding crack tip fields in the standard EFGM solution. Few important enrichment techniques are described below.

2.5.1.1 Extrinsic PU Enrichment

Extrinsic enrichment of meshfree methods can be carried out using partition of unity (PU) technique (Duarte and Oden, 1996; Melenk and Babuska, 1996; Belytschko *et al.*, 1996c). In this technique, the approximation is augmented by enrichment functions added extrinsically to the existing EFGM approximation. The enrichment term is smoothly added to the existing approximation by multiplying it with a factor based on a partition of unity. The essential element of this technique is the construction of a partition of unity, which can be obtained by MLS methodology. A partition of unity $\Phi_I(\mathbf{x})^{k'}$ is constructed from a complete polynomial basis of order k', and is a local approximation for which

$$\sum_{I=1}^{n} \Phi_I(\mathbf{x}) = 1 \tag{2.70}$$

It can easily be seen that MLS approximation builds partition of unity since Eq. (2.70) possesses the reproducing condition for a constant, which must be satisfied (Belytschko *et al.* 1996b) by an approximation. The enriched approximation of an unknown function can be written as

$$u^h(\mathbf{x}) = \sum_{I=1}^{n} \Phi_I^{k'}(\mathbf{x}) u_I + \sum_{I=1}^{n} \sum_{i=1}^{m_e} \Phi_I(\mathbf{x}) b_{Ii}\, q_i(\mathbf{x}) \tag{2.71}$$

where u_I and b_{Ii} are nodal coefficients, and n is the number of neighbors of a point x. The vector $q_i(\mathbf{x})$ is called the extrinsic basis of length m_e. For linear elastic fracture problems, this basis can contain radial ($\sqrt{r}$) dependence or radial ($\sqrt{r}$) as well as angular (θ) dependence. A superscript k' is added to the shape functions (Φ_I) in the approximation to denote the polynomial order of the basis used in forming the partition of unity.

PU technique appears to provide a vehicle for local enrichment. The partition of unity, $\Phi_I(\mathbf{x})^{k'}$ can be formed from a linear basis (k'=2), which yields linear consistency.

Enrichment of the approximation may be carried out locally by adding the known form of the solution to the extrinsic basis $q_i(\mathbf{x})$, at nodes in the region where it is required. It should be noted that the enrichment is to be added to each node whose domain of influence extends into the region to be enriched (Sukumar *et al.* 2000, Ventura *et al.* 2002).

$$\mathbf{u}^h(\mathbf{x}) = \sum_{I\in \mathrm{N}} \Phi_I(\mathbf{x})\, u_I + \sum_{J\in \mathrm{N}^c} \Phi_J(\mathbf{x})\, H(\mathbf{x})\, a_J + \sum_{K\in \mathrm{N}^f} \Phi_K(\mathbf{x}) \sum_{\alpha=1}^{4} \Psi_K^\alpha b_K^\alpha \tag{2.72}$$

where, $\Phi_I(\mathbf{x})$ are MLS shape functions, Heaviside function, $H(\mathbf{x})$ and the branch functions, Ψ_K^α are given as

$$H(\mathbf{x}) = \begin{cases} +1 & if (\mathbf{x}-\mathbf{x}^*).n \geq 0 \\ -1 & otherwise \end{cases} \tag{2.73}$$

$$\Psi_K^\alpha = \left[\Psi_K^1, \Psi_K^1, \Psi_K^1, \Psi_K^1\right] = \left[\sqrt{r}\sin\frac{\theta}{2}, \sqrt{r}\cos\frac{\theta}{2}, \sqrt{r}\sin\frac{\theta}{2}\cos\theta, \sqrt{r}\cos\frac{\theta}{2}\cos\theta\right] \tag{2.74}$$

where, r and θ are polar coordinates in the local crack tip coordinate system, a_J and b_K^α are the additional unknowns, $\mathbf{x}^*$ is the point nearest to crack segment. The set N^c includes the nodes whose support contains point x and are cut by the crack, see Fig. 2.8, whereas the set N^f are nodes whose support contains point x as well as crack tip $\mathbf{x}_{tip}$, see Fig. 2.9.

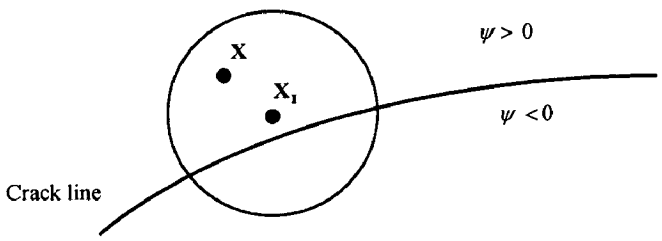

Fig. 2.8: Nodes whose support contains point **x** and cut by the crack (Nguyen *et al.*, 2008)

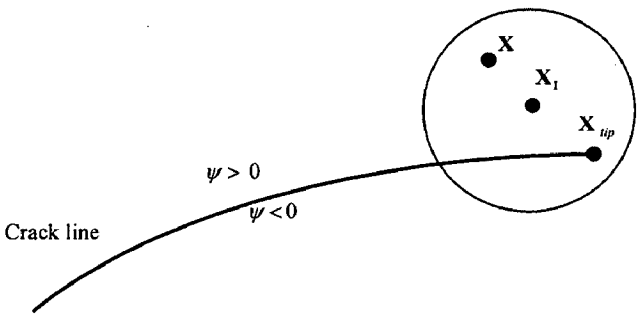

Fig. 2.9: Nodes whose support contains point **x** and the crack tip $\mathbf{x}_{tip}$ (Nguyen *et al,*. 2008)

Using standard Galerkin procedure as described in previous sections, the discrete equations are obtained with only one difference in **B** matrix which now becomes

$$\mathrm{B} = \left[\mathrm{B}^{EFGM} \mid \mathrm{B}^{enr}\right] \tag{2.75}$$

where B^{EFGM} is the standard **B** matrix, which can be written as

$$\mathrm{B}_I^{EFGM} = \begin{bmatrix} \Phi_{I,x} & 0 \\ 0 & \Phi_{I,y} \\ \Phi_{I,y} & \Phi_{I,x} \end{bmatrix} \tag{2.76}$$

and B^{enr} is the enriched **B** matrix

$$\mathrm{B}_I^{enr} = \begin{bmatrix} (\Phi_I)_{,x}\Psi_I + \Phi_I(\Psi_I)_{,x} & 0 \\ 0 & (\Phi_I)_{,y}\Psi_I + \Phi_I(\Psi_I)_{,y} \\ (\Phi_I)_{,y}\Psi_I + \Phi_I(\Psi_I)_{,y} & (\Phi_I)_{,x}\Psi_I + \Phi_I(\Psi_I)_{,x} \end{bmatrix} \tag{2.77}$$

where, enrichment function can be either the Heaviside function $H(\mathbf{x})$, or the branch functions $\Psi_I(\mathbf{x})$.

2.5.1.2 Intrinsic Enrichment

Meshfree approximations can be intrinsically enriched by including a special function in the basis (Fleming *et al.*, 1997). For example, in fracture mechanics, one can include the asymptotic near-tip displacement field, or an important ingredient such as $\sqrt{r}$. The choice of functions depends on the coarse mesh accuracy desired. For higher accuracy, the full asymptotic field can be included, while for higher computational speed but at some cost of accuracy, only the $\sqrt{r}$ function can be included in the basis. These techniques are described in the subsequent sections.

Full Enrichment

In case of linear elastic fracture problems for full intrinsic enrichment, all terms of near-tip asymptotic displacement field are included in the basis. After some trigonometric

manipulation, it can be shown that all the functions in Eqs. (2.44–2.45, 2.49–2.50) are spanned by the basis as

$$\mathbf{P}^T(\mathbf{x}) = \left[1, x, y, \sqrt{r}\cos\frac{\theta}{2}, \sqrt{r}\sin\frac{\theta}{2}, \sqrt{r}\sin\frac{\theta}{2}\sin\theta, \sqrt{r}\cos\frac{\theta}{2}\sin\theta\right] \tag{2.78}$$

First three terms in above equation are not related to the near-tip fields, and are only used for linear completeness of the EFGM approximation. This basis when used in Eq. (2.1) leads the approximations of the form

$$u^h(\mathbf{x}) = \sum_{I=1}^{n} \underbrace{\mathbf{p}^T(\mathbf{x})\mathbf{A}^{-1}(\mathbf{x})\mathbf{C}_I(\mathbf{x})}_{\Phi_I(\mathbf{x})} u_I \tag{2.79}$$

where, $\Phi_I(\mathbf{x})$ is the enriched EFGM shape function.

In contrast to the extrinsic techniques, this technique involves no additional unknowns. However, because of the increased size of the basis, additional computational effort is required to invert the moment matrix $\mathbf{A}(\mathbf{x})$. Moreover, for multiple cracks, four additional terms needs to be added in the basis for each crack.

2.5.2 Smoothening Techniques

In EFGM, the choice of weight function affects the resulting approximation. The smoothness and continuity of the shape function depends on the smoothness and continuity of the weight function. The presence of crack results in the discontinuity in displacement fields along the crack surface while the stresses become singular at the crack tip. Smoothening techniques refers to the methods involving modifications of weight functions so as to simulate the presence of a crack. A brief description of some smoothening techniques is given below:

2.5.2.1 Visibility Criterion

The first technique for dealing with non-convex boundaries is the visibility criterion

(Belytschko *et al.*, 1994). In this approach, the domain of influence is considered as the field of vision at a node. All boundaries, internal and external are considered to be opaque so that the field of vision is interrupted as soon as such a boundary is encountered. Consider node *J* in Fig. 2.10, where the surface of the crack is within its domain of influence and is therefore truncated. This truncation will create a discontinuity in the shape function for node *J* which will lead to the desired discontinuity in the solution across the crack (see Fig. 11a, c).

The difficulty with the visibility criterion arises for nodes near the end of a discontinuity, i.e. near a crack tip. Consider node *I* in Fig. 2.10, the field of vision is cut by the crack, leading to a discontinuity along line *AC*, i.e. the line of the crack. However, the field of vision is also truncated along line AB, which extends into the domain. This leads to an undesirable discontinuity in the weight function as well as the shape function along this line as shown in Fig. 2.11b and Fig. 2.11d. Since, the shape functions are created from the weight functions, thereby discontinuities arise in the shape functions from other nodes which are having discontinuous weight functions due to the presence of crack tip.

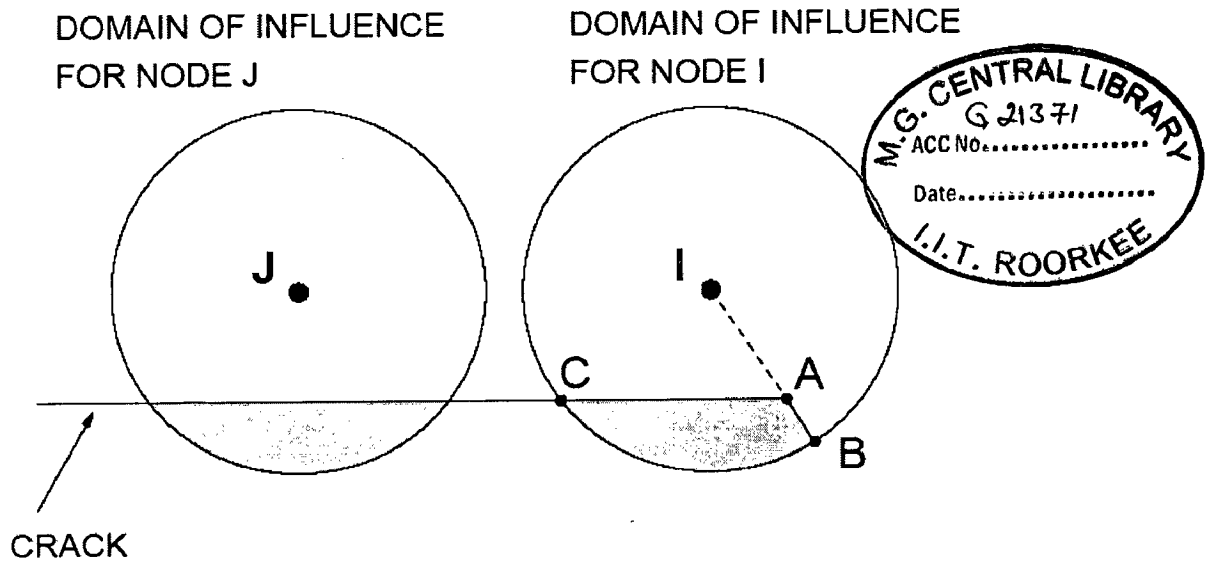

Fig. 2.10: Domain of influence by visibility criterion near a crack (Belytschko *et al.*, 1994)

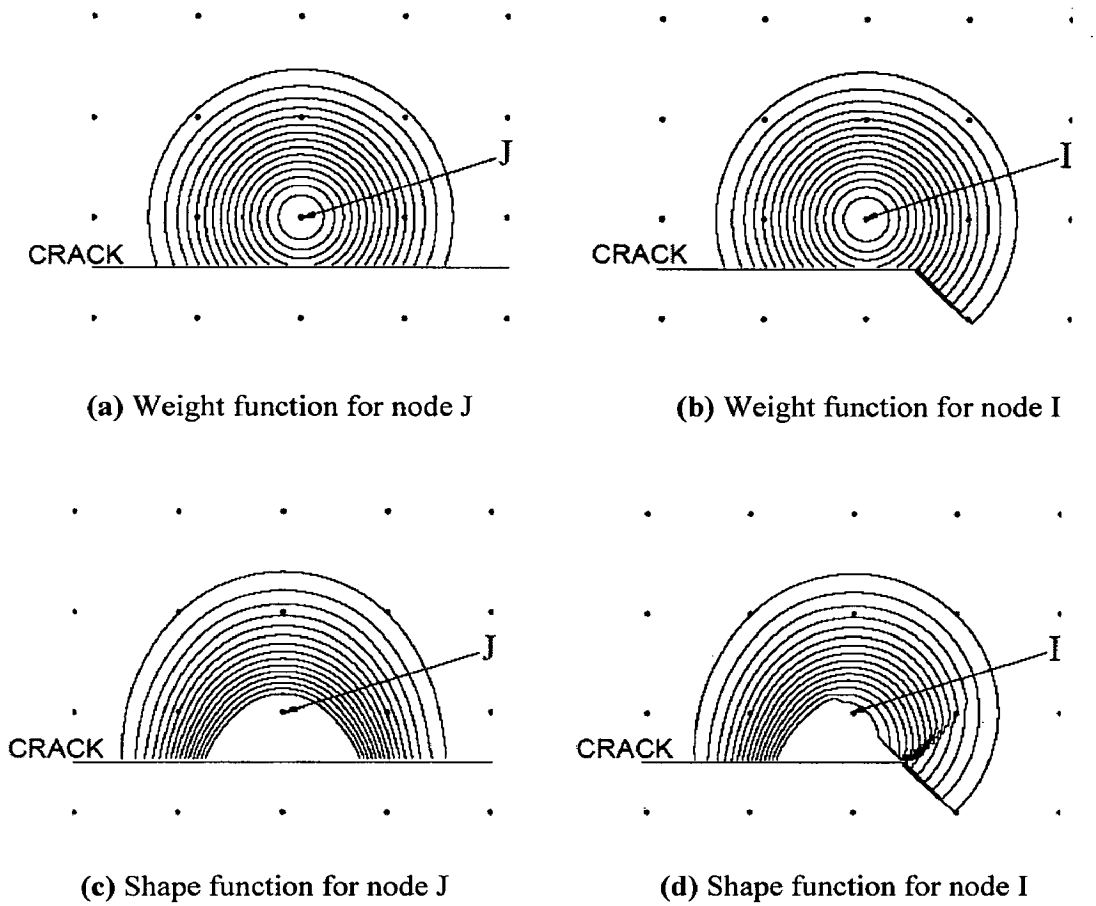

(a) Weight function for node J

(b) Weight function for node I

(c) Shape function for node J

(d) Shape function for node I

Fig. 2.11: Contour plots of weight function $w(\mathbf{x}-\mathbf{x}_I)$ and shape function $\Phi_I(\mathbf{x})$ by visibility criterion for nodes adjacent to a line of discontinuity due to a crack (Belytschko *et al.*, 1994)

2.5.2.2 Diffraction Criterion

Continuous and smooth approximations near non-convex boundaries can be constructed quite easily by the diffraction technique (Organ *et al.*, 1996; Organ, 1996; Belytschko *et al.*, 1996c). In diffraction criteria, the nodal support is wrapped around non-convex boundaries similar to the way light diffracts around sharp corners. This technique, which is also called the wrap-around technique, is quite general, and can be used for cracks or smooth boundaries such as interior holes.

Consider Fig. 2.12, where a line between the node $\mathbf{x}_I$, and a sampling point $\mathbf{x}$ intersects a crack and the tip is within the domain of influence of the node. The weight function distance $\bar{d}_I$, is modified (lengthened) by

$$\bar{d}_I = \left(\frac{s_1 + s_2(\mathbf{x})}{s_0(\mathbf{x})} \right)^{\bar{\lambda}} s_0(\mathbf{x}) \tag{2.80}$$

where, $s_1 = \|\mathbf{x}_I - \mathbf{x}_c\|$, $s_2(\mathbf{x}) = \|\mathbf{x} - \mathbf{x}_c\|$, $s_0(\mathbf{x}) = \|\mathbf{x} - \mathbf{x}_I\|$

and $\mathbf{x}_I$ is the node, $\mathbf{x}$ is the sampling point, and $\mathbf{x}_c$ is the crack tip. The parameter $\bar{\lambda}$ is used to adjust the distance of the support on the opposite side of the crack. It was found that $\bar{\lambda}$ =1, 2 perform well. Surface plots of the weight and shape functions obtained by the diffraction technique are shown in Fig. 2.13.

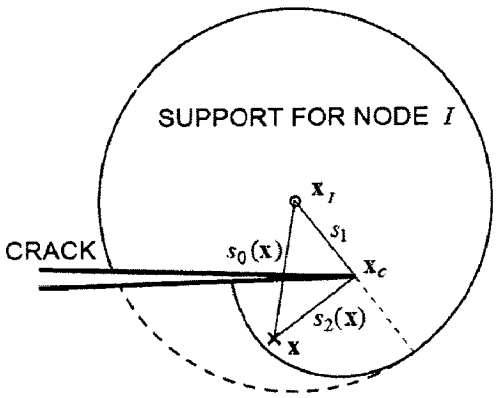

Fig. 2.12: Diffraction (wrap-around) technique for constructing smooth weight functions around non-convex boundaries (Organ *et al.*, 1996)

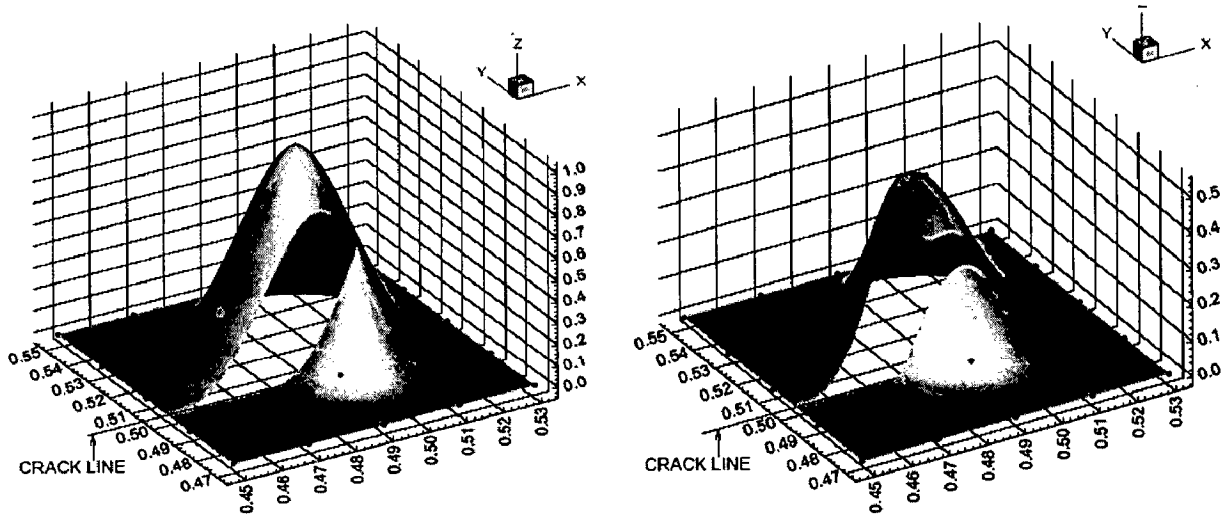

(a) weight function **(b) shape function**

Fig. 2.13: Surface plots of **(a)** weight function and **(b)** shape function associated with node near crack tip constructed by diffraction technique (Organ *et al.*, 1996)

The spatial derivatives of the weight function are computed using the chain rule as

$$\frac{dw}{d\mathbf{x}_i} = \frac{\partial w}{\partial \bar{d}_I}\frac{\partial \bar{d}_I}{\partial \mathbf{x}_i} \tag{2.81}$$

Since $\partial w / \partial \bar{d}_I$ is unchanged, that is necessary are expressions for $\partial \bar{d}_I / \partial \mathbf{x}_i$

$$\frac{\partial \bar{d}_I}{\partial x_i} = \bar{\lambda}\left(\frac{s_1 + s_2}{s_0}\right)^{\bar{\lambda}-1}\frac{\partial s_2}{\partial x_i} + (1-\bar{\lambda})\left(\frac{s_1 + s_2}{s_0}\right)^{\bar{\lambda}}\frac{\partial s_0}{\partial x_i} \tag{2.82}$$

where,

$$\frac{\partial s_0}{\partial \mathbf{x}_i} = \frac{\mathbf{x} - \mathbf{x}_{Ii}}{s_0}, \quad \frac{\partial s_2}{\partial \mathbf{x}_i} = \frac{\mathbf{x}_i - \mathbf{x}_{ci}}{s_2}$$

The diffraction technique works well for general non-convex boundaries as well. The tangent point between the node and the non-convex boundary is used as the wrap-around point $\mathbf{x}_c$.

2.5.2.3 Transparency Criterion

Another technique for constructing continuous approximations is the transparency technique (Organ *et al.*, 1996; Belytschko *et al.*, 1996c), which will be described here for cracks. The underlying concept of this technique is to endow the crack tip with a varying measure of transparency such that it is completely transparent at the tip and becomes completely opaque at a short distance behind the tip. In this way, the field of vision for a node near the crack tip is not abruptly truncated when it reaches the crack tip, but rather diminishes smoothly to zero a short distance behind the crack tip.

When a ray passes between a node $\mathbf{x}_I$ and a sampling point $\mathbf{x}$, and crosses the crack as shown in Fig. 2.14, the distance parameter $\bar{d}_I$ in the weight function is modified (lengthened) by the following:

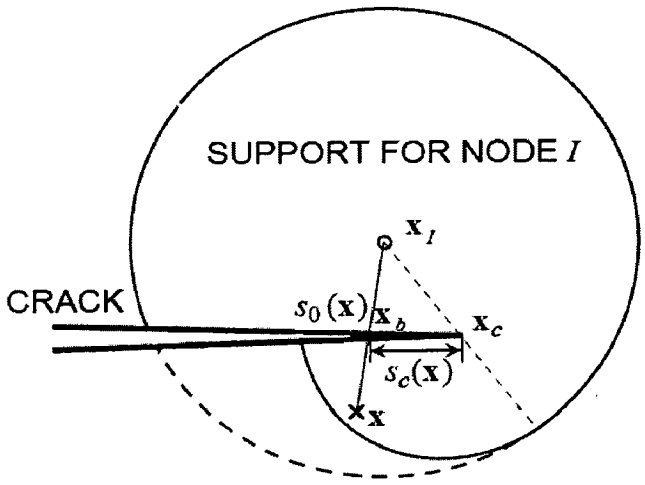

Fig. 2.14: Transparency technique for computing smooth weight functions (Organ *et al.*, 1996)

$$\bar{d}_I(\mathbf{x}) = s_0(\mathbf{x}) + d_{mI}\left(\frac{s_c(\mathbf{x})}{\bar{s}_c}\right)^{\bar{\lambda}} \qquad \lambda \geq 2 \tag{2.83}$$

where, $s_0(\mathbf{x}) = \|\mathbf{x} - \mathbf{x}_I\|$, d_{mI} is the radius of support for node I, and $s_c(\mathbf{x})$ is the intersection distance behind the crack tip. The parameter $\bar{s}_c$ sets the distance behind the crack tip at which complete opacity occurs

$$\bar{s}_c = \bar{k}\, h \tag{2.84}$$

where, h is the nodal spacing and $\bar{k}$ is a constant, usually $0 < \bar{k} < 1$.

The spatial derivatives of the distance parameter, d_I obtained by chain rule, are

$$\frac{\partial \bar{d}_I}{\partial \mathrm{x}_i} = \frac{\partial s_0}{\partial \mathbf{x}_i} + \bar{\lambda} d_{mI} \frac{s_c^{\bar{\lambda}-1}}{s_c^{-\bar{\lambda}}} \frac{\partial s_c}{\partial \mathbf{x}_i} \tag{2.85}$$

where, $\frac{\partial s_0}{\partial \mathbf{x}_i} = \frac{\mathrm{x}_i - \mathrm{x}_I}{s_0}$, $\frac{\partial s_c}{\partial \mathrm{x}_I} = -\cos\theta = \frac{\mathrm{x}_b - \mathrm{x}_c}{s_c}$, $\frac{\partial s_c}{\partial \mathrm{x}_I} = -\sin\theta = \frac{y_b - y_c}{s_c}$, θ is the angle between the crack and x-axis and x_b is the intersection point behind the crack tip. Surface plots of the weight and shape functions near a crack tip constructed by the transparency technique are shown in Fig. 2.15.

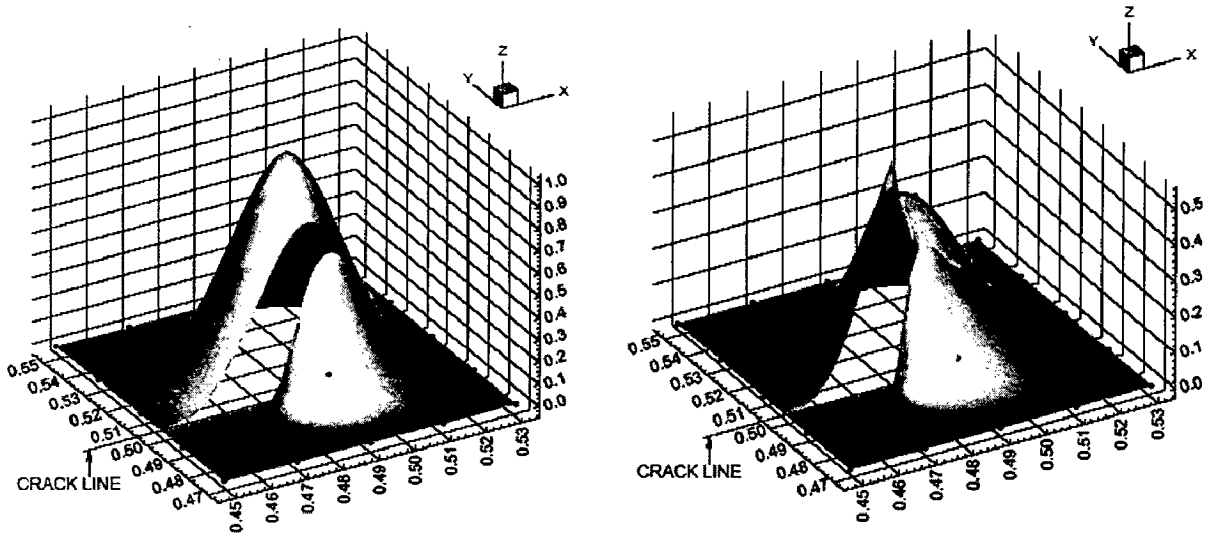

(a) Weight function **(b) Shape function**

Fig. 2.15: Surface plots of **(a)** weight function and **(b)** shape function associated with node near crack tip constructed using the transparency technique (Organ *et al.*, 1996)

One drawback of the transparency technique is that it does not work well when nodes are placed too close to the crack surface. A trough appears in the shape function ahead of the crack tip because although the crack tip is transparent for this node, the change in the degree of transparency with respect to the change in angle is very sharp. There is no discontinuity in the shape function is observed, only a small dip appears in the shape function. To circumvent this problem in the transparency technique, a restriction has been placed on the position of the nodes. All nodes should be placed such that the normal distance from the node to the crack surface is greater than roughly by $1/4h$, where h is the nodal spacing.

2.5.2.4 Spiral Weight Criterion

According to spiral weight criterion (Muravin and Turkel, 2006), the distance d_I between node $\mathbf{x}_I$ and sampling point $\mathbf{x}$ is modified when the line segment between $\mathbf{x}$ and $\mathbf{x}_I$ crosses the crack. The modification is done as follows

$$d_I = \bar{d}_I + (1 - R_P) d_{mI} \tag{2.86}$$

where, $\bar{d}_I$ is initially modified distance between node $\mathbf{x}_I$ and sampling point $\mathbf{x}$, d_{mI} is the size of nodal domain of influence and R_P is an angular ramp function. The initially modified distance $\bar{d}_I$ can be calculated either by diffraction or transparency criterion. The area around the crack tip $\mathbf{x}_c$ is divided into four quarters Q_i for $i = 1...4$.

$$Q_i : (i-1)\frac{\pi}{2} \le \theta < i\frac{\pi}{2} \tag{2.87}$$

Let $\mathbf{x}_v$ be a point that belongs to visibility ray and is located at a distance d_{mI} from the crack tip. The visibility angle θ_v is the angle between the visibility ray and the crack line Fig. 2.16a. The angle θ_m is given as:

$$\theta_m = \begin{Bmatrix} \pi/2 \ , \theta_v \in Q_1 \\ -\pi/2 \ , \theta_v \in Q_3 \\ \theta_v , otherwise \end{Bmatrix} \tag{2.88}$$

The ramp area is the part of invisible area between the ray at angle θ_m and the crack line Fig. 2.16b, c.

The angular ramp function $R_P(\theta)$ is constructed in such a manner that it satisfies the following conditions:

- The function $R_P(\theta)$ is smooth and monotonically decreasing from 1 to 0.
- For angle θ_m, $R_P(\theta_m) = 1$
- For the crack surface $R_P(\pm\pi) = 0$

The ramp function which satisfies the above condition is

$$R_p(\tilde{\theta}) = c \sin^{\tilde{n}} \tilde{\theta} \tag{2.89}$$

where, $\tilde{k} = 0...4$, $c = \begin{Bmatrix} 1, & \tilde{\theta} \in Q_{1,2} \\ -1, & \tilde{\theta} \in Q_{3,4} \end{Bmatrix}$ and $\tilde{\theta} = \dfrac{(\theta - \theta_a)(\theta_d - \theta_c)}{\theta_b - \theta_a} + \theta_c$

The values of θ_a, θ_b, θ_c and θ_d depends on parameter c and are presented below.

	θ_a	θ_b	θ_c	θ_d
$c=1$	θ_m	π	$\pi/2$	π
$c=-1$	$-\pi$	θ_m	$-\pi$	$-\pi/2$

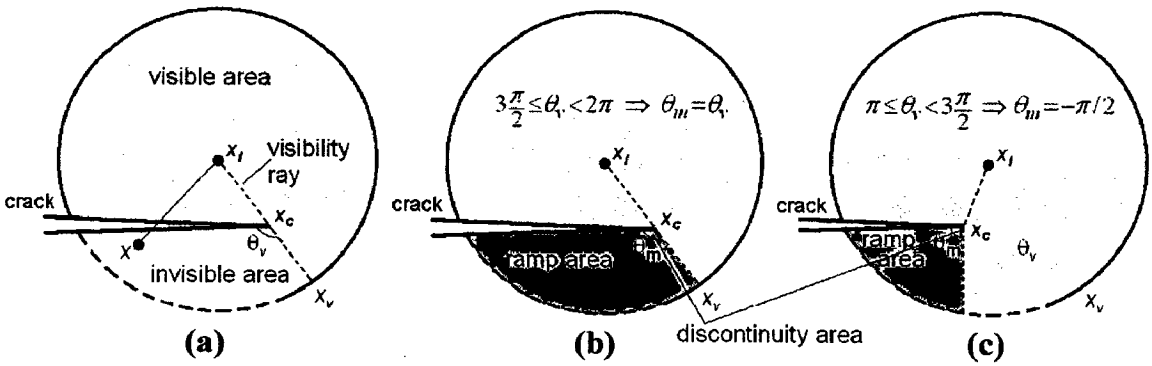

Fig. 2.16: Definition of spiral weight function parameters (Muravin and Turkel, 2006)

It should be noted that ramp functions and its derivatives are discontinuous at the crack tip. However, this does not pose any problem since no quadrature points are placed at the crack tip. For nodes which are located ahead of the crack tip, the visibility angle and consequently θ_m are smaller than 90°. For small visibility angle, the ramp function has large gradients. The power n in Eq. 2.89 is used as a parameter to adjust the rate of ramp function which changes in accordance with the value of angle θ_m. For $\theta_m = \pm\pi/2$, the value of parameter $\tilde{n} = 1$, while for other values of θ_m smaller than 90°, a larger value of $\tilde{n}$ should be considered. The value $\tilde{n} = 5$ has been found to work well with all such cases. Figure 2.17 presents the weight and shape functions and their x derivatives calculated by the spiral weight method. The nodal distribution is equally spaced with additional nodes around the crack line and at the crack tip. A linear basis is used for the shape function and its x derivative calculations.

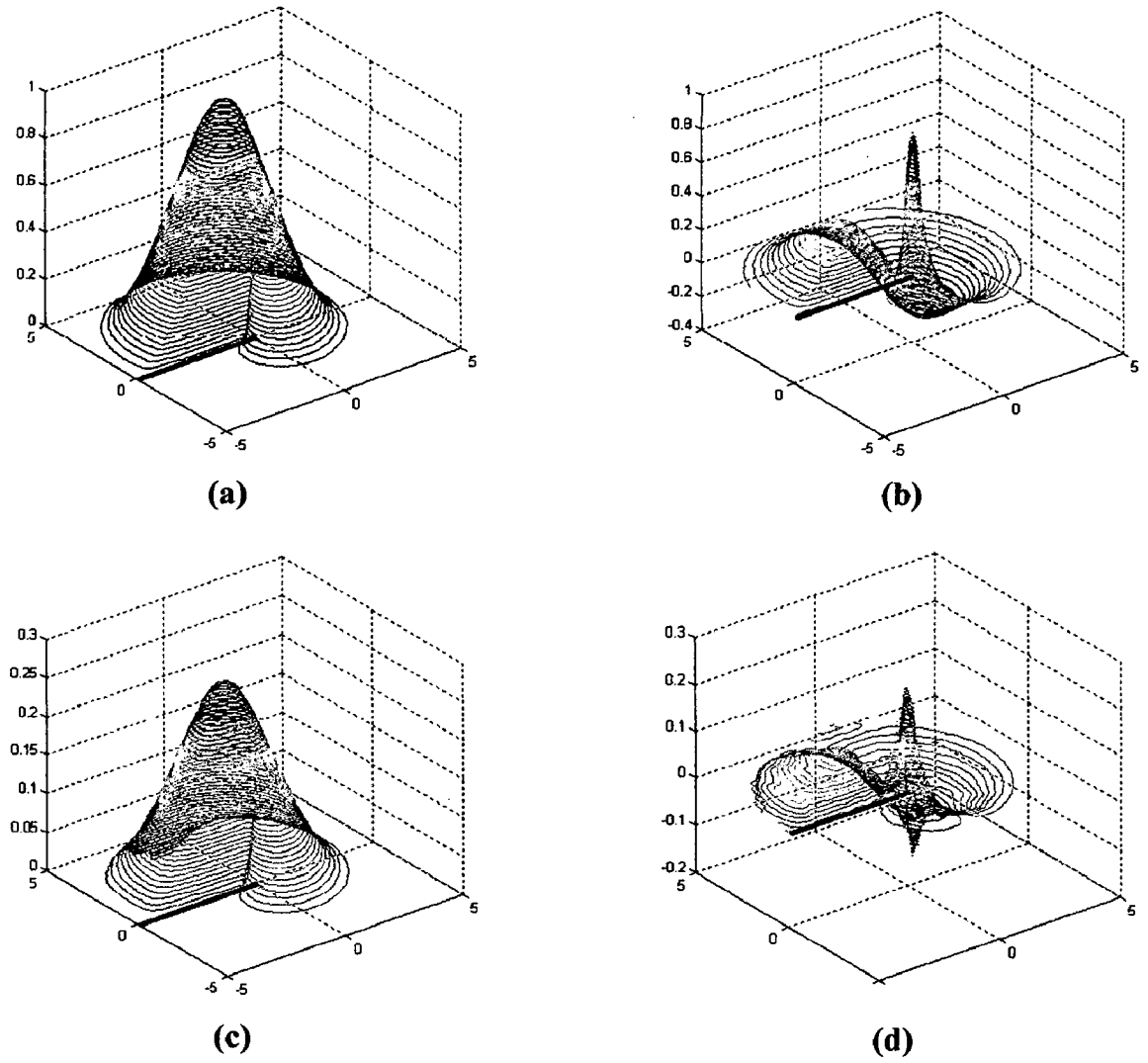

Fig. 2.17: (a) Spline weight function, (b) its x-spatial derivative, (c) shape function, (d) its x-spatial derivative by the spiral method near the crack tip (Muravin and Turkel, 2006)

2.6 COMPARISON OF CRACK MODELING TECHNIQUES

In order to check the accuracy and efficiency of various crack modeling techniques, a comparative study of these techniques has been performed in this section. For this purpose, a single edge cracked plate is considered as shown in Fig. 2.18. The dimensions of the cracked body are taken as $H = 200$ mm, $W = 100$ mm. ASTM 36 steel is taken as a material with modulus of elasticity, $E = 200$ GPa, Poisson's ratio (ν) = 0.3. A far field stress, σ_o = 100 MPa is applied. The bottom edge has been constrained along y-direction, and an external far field stress is applied at the top edge. The problem domain has been discretized using 800 nodes in intrinsic enrichment criterion while in diffraction

criterion, 66 additional nodes are defined at the crack surface and crack tip. A regular nodal distribution has been considered in both simulations having $d_{max} = 1.5$. Six point Gauss quadrature has been used for the numerical integration of the Galerkin weak form. A plane stress condition is assumed. The values of mode-I stress intensity factors i.e. K_I are calculated using domain based interaction integral approach using a square domain of having edge length of $a/3$.

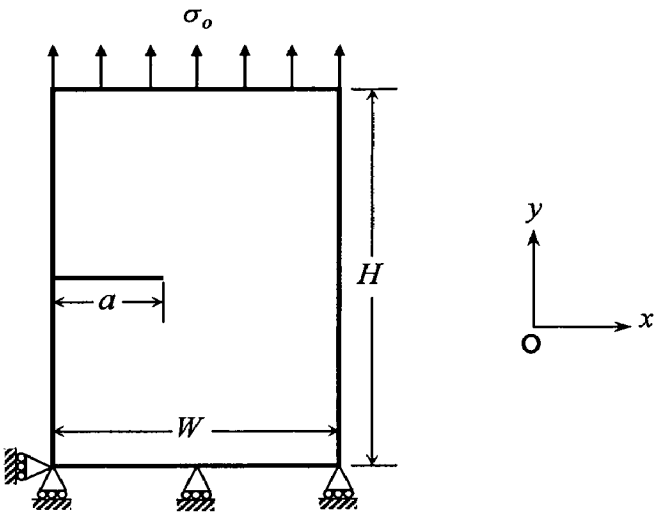

Fig. 2.18: Problem geometry along with dimensions and boundary conditions

2.7 RESULTS AND DISCUSSIONS

The value of mode-I stress intensity factors i.e. K_I for the above problem, are calculated using various crack modeling techniques, and the results obtained using these techniques are compared with the analytical solutions. Figure 2.19 shows the variation of normalized mode-I stress intensity factor with varying nodal density over the domain. The numerical values of stress intensity factors are normalized with standard analytical solutions. The simulation is performed for a constant crack length of $a = 40\,\text{mm}$. A comparison of different crack modeling techniques revealed that the intrinsic basis enrichment is found quite promising as it gives results quite close to the analytical solution even with small number of nodes. Moreover, the convergence of intrinsic enrichment criterion is also found good as compared to other crack modeling techniques which can be clearly seen

from Fig. 2.19. A problem is solved for a fixed nodal density of 800 nodes by intrinsic enrichment while in diffraction criterion, 66 additional nodes are used at the crack surface and crack tip. The variation of normalized mode-I stress intensity factor with varying crack length are plotted in Fig. 2.20. Again a comparative study of different crack modeling techniques shows that the efficiency of intrinsic enrichment criterion is good in solving cracks of varying length. The numerical values of stress intensity factor obtained by intrinsic enrichment for different crack lengths are relatively closer to the analytical solution as can be clearly observed from Fig. 2.20.

A comparison of various crack modeling techniques has demonstrated the advantages of intrinsic enrichment criterion over other crack modeling techniques. Owing to its accuracy and convergence, the intrinsic enrichment criterion has been used in the present research work. The various factors which motivated the use of intrinsic enrichment in the present research work are summarized as

- ❖ Good convergence and accuracy.
- ❖ No need of crack tip refinement.
- ❖ Easy implementation (basis modification only).
- ❖ No additional unknowns are required for solving a problem.

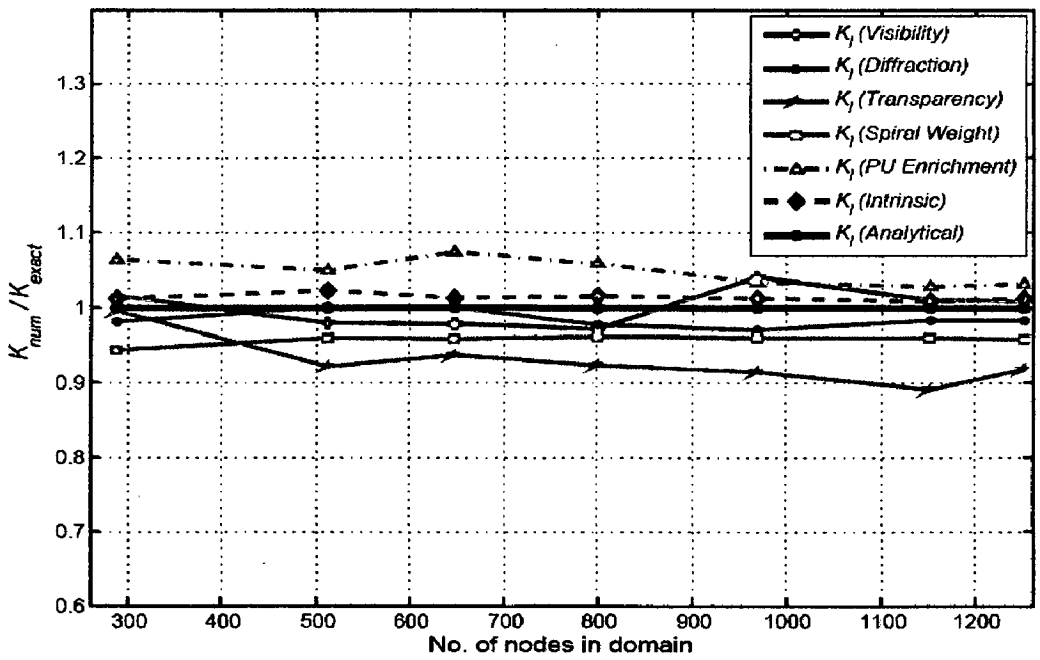

Fig. 2.19: Variation of normalized stress intensity factor vs. nodal density

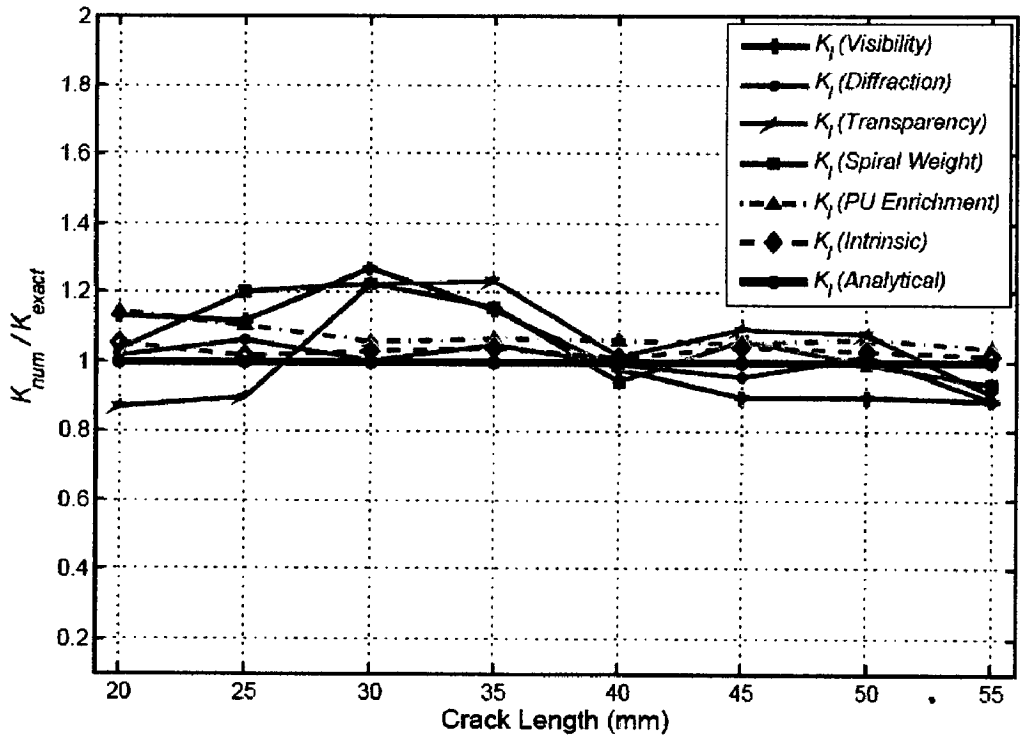

Fig. 2.20: Variation of normalized stress intensity factor vs. crack length

2.8 CONCLUSION

A brief introduction of EFGM along with its application to fracture mechanics has been presented in this chapter. Different crack modeling techniques have been discussed and implemented for a standard mode-I edge crack problem. A comparison of these crack modeling techniques shows that the intrinsic enrichment criterion is found quite appealing owing to its simplicity, accuracy and convergence. Moreover, the intrinsic enrichment criterion is easy to implement as it only requires modification in the basis function. Lack of additional unknowns and crack tip refinement add to the proficiency of intrinsic enrichment criterion. Motivated by the advantages of intrinsic enrichment criterion along with its ease in implementation and scope for further modification, we decided to exploit this crack modeling criterion for the present research work.

Chapter 3

MODELING OF WEAK AND STRONG DISCONTINUITIES

3.1 INTRODUCTION

The element free Galerkin method (EFGM) is quite attractive as compared to standard finite element methods as it avoids the need for tedious and time consuming element based mesh. The EFGM utilizes the moving least-square interpolants which require only nodes unencumbered by elements and elemental connectivity to construct the shape functions. Furthermore this method leads to the continuous differentiable approximations so that the derivatives involved in field quantities such as strains in the elastic problems are smooth, and require no post-processing. This method has been mainly applied to solve the problems of cracks growth (Belytschko *et al.*, 1995a; Li and Simonsen, 2007; Belytschko *et al.*, 1996b), where nodes continuously move or even get added so as to follow the crack tip. It has also been established that the convergence rate for EFGM is higher than the finite element method. However, the continuity of meshfree approximations becomes a drawback for such problems where the solution inherently possesses discontinuities (Cordes and Moran, 1996; Batra *et al.*, 2004; Belytschko and Gracie, 2007; MacKinnon and Carey, 1987) in the derivatives. Smooth solution then exhibit the well known Gibb's phenomenon (Arfken and Weber, 1985) at the line (or surface) of discontinuity. These situations are quite common in many engineering and science problems. For example, the first derivative of displacement becomes discontinuous at the bi-material interfaces (Belytschko and Gracie, 2007) in a continuum mechanics problem.

To model these discontinuities in meshfree methods, few techniques have been developed over the years namely Domain Partitioning (Liu, 2003), Lagrange Multiplier (Cordes and Moran, 1996) and Jump Function (Krongauz and Belytschko, 1998). The first two methods are based on the modifications at the variational level for the treatment of material discontinuity, while the last technique enriches the EFGM approximation by the addition of special shape function i.e. Jump function that contains the discontinuity in the derivative. In the present work, all the three approaches have been explored. These have been compared among themselves to select the most efficient technique. Moreover, a new criterion has been proposed to model weak as well as strong discontinuities such as cracks in bi-materials under thermal/mechanical loads.

3.2 MODELING OF MATERIAL DISCONTINUITY

3.2.1 Governing Equations for Bi-Material

The treatment of material discontinuity in EFGM is demonstrated by considering a two dimensional linear elastostatic problem in plane stress. For simplicity, two distinguishable materials represented by domains Ω^- and Ω^+ is considered. The two domains are separated by a single interface, Γ_s as shown in Fig. 3.1. This interface is defined by n_s^-, the unit outward normal of Ω^- along the material interface. The governing equilibrium equation is given by

$$\nabla.\boldsymbol{\sigma}+\mathbf{b}=0 \quad \text{on} \quad \Omega \tag{3.1}$$

along with associated boundary conditions

$$\boldsymbol{\sigma}.\bar{\mathbf{n}}=\bar{\mathbf{t}} \quad \text{on} \quad \Gamma_t \tag{3.2}$$

$$\mathbf{u}=\bar{\mathbf{u}} \quad \text{on} \quad \Gamma_u \tag{3.3}$$

where, $\boldsymbol{\sigma}$ is the Cauchy stress tensor and $\mathbf{b}$ is a body force vector, $\bar{\mathbf{t}}$ is the specified traction, $\bar{\mathbf{u}}$ is the specified displacement field and $\bar{\mathbf{n}}$ is the unit normal. A perfect

interface has been assumed, and hence the traction and displacement are assumed to be continuous across the interface Γ_s.

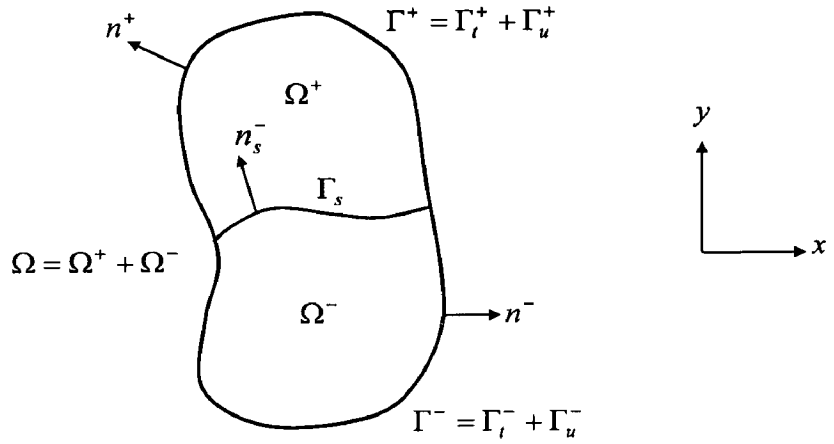

Fig. 3.1: Two-dimensional inhomogeneous body

3.2.2 Modifications for Material Discontinuity

Few modifications and additions are introduced in EFGM to solve the bi-material problems. These changes give EFGM an ability to solve the problems involving material discontinuities. The modifications in the approaches are discussed below:

3.2.2.1 Domain partitioning approach

In domain partitioning approach (Liu, 2003), the following weak/variational form of $\nabla.\boldsymbol{\sigma}+\mathbf{b}=0$ is considered in Ω along with associated boundary constraint applied using Lagrange multipliers λ (Cordes and Moran, 1996; Dolbow and Belytschko, 1998; Krongauz and Belytschko, 1998)

$$\int_\Omega \nabla_s \delta \mathbf{u} : \boldsymbol{\sigma}\, d\Omega - \int_\Omega \delta \mathbf{u}\mathbf{b}\, d\Omega - \int_{\Gamma_t} \delta \mathbf{u}\bar{\mathbf{t}}\, d\Gamma - \int_{\Gamma_u} \delta\lambda(\mathbf{u}-\bar{\mathbf{u}})d\Gamma - \int_{\Gamma_u} \delta \mathbf{u}\lambda\, d\Gamma = 0 \qquad (3.4)$$

Corresponding to the satisfaction of the equilibrium equation $\nabla.\boldsymbol{\sigma}+\mathbf{b}=0$ on Ω in both Ω^+ and Ω^-; the traction and displacement boundary conditions, $\boldsymbol{\sigma}.\bar{\mathbf{n}} = \bar{\mathbf{t}}$ on Γ_t in both

Γ_t^+ and Γ_t^-, $\mathbf{u} = \bar{\mathbf{u}}$ on Γ_u in both Γ_u^- and Γ_u^+. The discretization of the above Eq. (3.4) after imposing boundary conditions leads to the following set of linear equations:

$$\begin{bmatrix} \mathbf{K} & \mathbf{G} \\ \mathbf{G}^T & 0 \end{bmatrix} \begin{Bmatrix} \mathbf{u} \\ \boldsymbol{\lambda} \end{Bmatrix} = \begin{Bmatrix} \mathbf{f} \\ \mathbf{q} \end{Bmatrix} \tag{3.5}$$

where,

$$K_{IJ} = \int_\Omega \mathbf{B}_I^T \mathbf{D} \mathbf{B}_J \, d\Omega, \qquad f_I = \int_\Omega \Phi_I \mathbf{b} \, d\Gamma + \int_{\Gamma_t} \Phi_I \bar{\mathbf{t}} \, d\Gamma, \qquad G_{JK} = \int_{\Gamma_u} \Phi_I \mathbf{N}_K \, d\Gamma,$$

$$q_K = \int_{\Gamma_u} \mathbf{N}_K \bar{\mathbf{u}} \, d\Gamma, \quad \mathbf{B}_I = \begin{bmatrix} \Phi_{I,x} & 0 \\ 0 & \Phi_{I,y} \\ \Phi_{I,y} & \Phi_{I,x} \end{bmatrix}, \quad N_K = \begin{bmatrix} N_K & 0 \\ 0 & N_K \end{bmatrix}, \quad \mathbf{D} = \frac{E}{1-\nu^2} \begin{bmatrix} 1 & \nu & 0 \\ \nu & 1 & 0 \\ 0 & 0 & \frac{1-\nu}{2} \end{bmatrix}$$

$\Omega = \Omega^+ + \Omega^-$, $\Gamma_u = \Gamma_u^- + \Gamma_u^+$ and $\Gamma_t = \Gamma_t^- + \Gamma_t^+$

This method involves considering the inhomogeneous medium as separate homogeneous bodies, and then some modifications are applied at the interface. The separation of the body into its homogeneous parts is accomplished through the weight function, and specifically the neighbors are decided on the basis of the domain of influence. For a homogeneous part, the neighbors at a point $\mathbf{x}$ are the nodes which contain $\mathbf{x}$ in their domain of influence (Belytschko *et al.*, 1996c). The neighbors for inhomogeneous bodies are determined by defining the interface by a set of nodes which belong to both materials. The line drawn by connecting these nodes is considered as the interface Γ_s between two materials (material-1 and material-2). Therefore, the points contained in material-1 can only be influenced by the nodes in material-1 plus interface nodes; and points contained in material-2 can only be influenced by nodes contained in material-2 plus interface nodes. Figs. 3.2 and 3.3 illustrate the selection of the neighbors for homogeneous and inhomogeneous materials respectively. The domains of influence are drawn for nodes labeled 1 through 5 in each figure to determine the neighbors for the points ***a***, ***b*** and ***c***.

The domain of influence for each node is a circle centered at the node. For the homogeneous case (Fig. 3.2), point *a* is contained in the domain of influence of both nodes 4 and 5; therefore, nodes 4 and 5 are considered the neighbors of the point *a*. Similarly, point *b* has nodes 3 and 5 as neighbors, and point *c* has nodes 1 and 2 as neighbors. However, when an interface separating two materials is added as in Fig. 3.3, the neighbors of the points *a*, *b* and *c* change.

The domains of influence for node 4 and node 5 are unaffected by the interface. The domain of influence for node 4 does not intersect the interface, and node 5 is an interface node belonging to both materials. Therefore, point *a* still contains nodes 4 and 5 as neighbors. The domains of influence for nodes 1, 2 and 3 are truncated at the interface. The neighbors of point *b* still include nodes 3 and 5 since each pertain to material-1; however, point *c* is not included in the domain of influence of node 2 due to the truncation of the domain of influence of node 2 at the interface. Similarly, point *c* has only one neighbor labeled in Fig. 3.3 i.e. node 1.

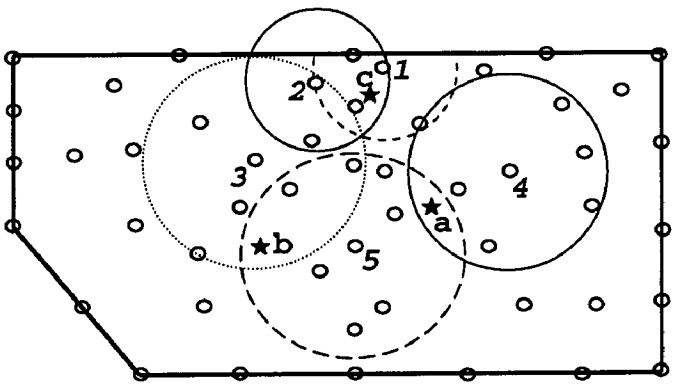

Fig. 3.2: Domains of influence and nearest neighbors in homogeneous bodies

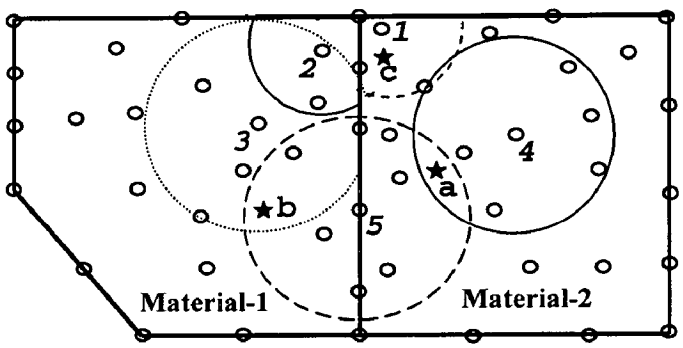

Fig. 3.3: Domains of influence and nearest neighbors for inhomogeneous bodies

3.2.2.2 Lagrange multiplier approach

In this approach, the following interface constraint is applied apart from essential and traction boundary conditions (Cordes and Moran, 1996):

$$\int_{\Gamma_z} (\mathbf{u}^+ - \mathbf{u}^-) d\Gamma = 0 \tag{3.6}$$

Hence, the following weak form of $\nabla . \boldsymbol{\sigma} + \mathbf{b} = 0$ is used on Ω using interface condition:

$$\begin{aligned} &\int_\Omega \nabla_s \delta \mathbf{u} : \boldsymbol{\sigma} d\Omega - \int_\Omega \delta \mathbf{u}\, \mathbf{b}\, d\Omega - \int_{\Gamma_t} \delta \mathbf{u}\, \bar{\mathbf{t}}\, d\Gamma - \int_{\Gamma_u} \delta\lambda (\mathbf{u} - \bar{\mathbf{u}}) d\Gamma - \int_{\Gamma_u} \lambda\, \delta \mathbf{u}\, d\Gamma - \\ &\int_{\Gamma_s} (\mathbf{u}^+ - \mathbf{u}^-) \delta\gamma\, d\Gamma - \int_{\Gamma_s} \gamma (\delta\mathbf{u}^+ - \delta\mathbf{u}^-) d\Gamma = 0 \end{aligned} \tag{3.7}$$

The Lagrange multipliers λ, enforce the essential boundary constraint on Γ_u, while the Lagrange multiplier γ enforce the displacement discontinuity. The associated Euler equations are as follows:

$$\nabla . \boldsymbol{\sigma} + \mathbf{b} = 0 \text{ in } \Omega^+ \text{ and } \Omega^-, \tag{3.8}$$

$$\mathbf{t} - \bar{\mathbf{t}} = 0 \quad \text{on} \quad \Gamma_t^+ \text{ and } \Gamma_t^-, \tag{3.9}$$

$$\mathbf{u} - \bar{\mathbf{u}} = 0 \quad \text{on} \quad \Gamma_u^+ \text{ and } \Gamma_u^-, \tag{3.10}$$

$$\lambda - \bar{\mathbf{t}} = 0 \quad \text{on} \quad \Gamma_u^+ \text{ and } \Gamma_u^-, \tag{3.11}$$

$$\mathbf{u}^+ - \mathbf{u}^- = 0 \quad \text{on} \quad \Gamma_s \tag{3.12}$$

$$\gamma + \mathbf{t}^+ = 0 \quad \text{on} \quad \Gamma_s \tag{3.13}$$

$$\gamma + \mathbf{t}^- = 0 \quad \text{on} \quad \Gamma_s \tag{3.14}$$

corresponding to the satisfaction of the equilibrium equation $\nabla . \boldsymbol{\sigma} + \mathbf{b} = 0$ on Ω in both Ω^+ and Ω^-; the traction and displacement boundary conditions, $\boldsymbol{\sigma} . \bar{\mathbf{n}} = \bar{\mathbf{t}}$ on Γ_t and $\mathbf{u} = \bar{\mathbf{u}}$ on Γ_u on both Γ^+ and Γ^-, and, the physical interpretation of the Lagrange multipliers $\lambda = \mathbf{t}$, $\gamma = -\mathbf{t}^+ = -\mathbf{t}^-$. Substituting Eq. (3.11) and Eq. (3.13) into Eq. (3.7), the following equations are obtained:

$$\int_\Omega \nabla_s \delta \mathbf{u} : \boldsymbol{\sigma}\, d\Omega - \int_\Omega \delta \mathbf{u}\, \mathbf{b}\, d\Omega - \int_{\Gamma_t} \delta \mathbf{u}\, \bar{\mathbf{t}}\, d\Gamma - \int_{\Gamma_u} \delta \mathbf{t}(\mathbf{u} - \bar{\mathbf{u}}) d\Gamma - \int_{\Gamma_u} \mathbf{t}\, \delta \mathbf{u}\, d\Gamma - \int_{\Gamma_s} (\mathbf{u}^+ - \mathbf{u}^-) \delta \mathbf{t}^- d\Gamma - \int_{\Gamma_s} \mathbf{t}^- (\delta \mathbf{u}^+ - \delta \mathbf{u}^-) d\Gamma = 0 \tag{3.15}$$

The discretization of the above Eq. (3.15), leads to the following set of linear equations:

$$\mathbf{K}\,\mathbf{u} = \mathbf{f} \tag{3.16}$$

where, the matrices $\boldsymbol{K}$ and $\mathbf{f}$ are defined as

$$K_{IJ} = \int_\Omega B_I^T D\, B_J d\Omega - \int_{\Gamma_u} \Phi_I S\, N\, D\, B_J d\Gamma + \int_{\Gamma_u} B_I^T D^T N^T S\, \Phi_J d\Gamma - \int_{\Gamma_s} (\Phi_I^+ - \Phi_I^-) N^- D^- B_J^- d\Gamma + \int_{\Gamma_s} (B_I^-)^T (D^-)^T (N^-)^T (\Phi_J^+ - \Phi_J^-) d\Gamma \tag{3.17}$$

$$f_I = \int_{\Gamma_t} \Phi_I \bar{\mathbf{t}}\, d\Gamma - \int_{\Gamma_u} B_I^T D^T N^T S\, \bar{\mathbf{u}} d\Gamma + \int_\Omega \mathbf{b}\, \Phi_I d\Omega \tag{3.18}$$

$$\mathbf{D} = \frac{E}{1-\nu^2} \begin{bmatrix} 1 & \nu & 0 \\ \nu & 1 & 0 \\ 0 & 0 & \frac{1-\nu}{2} \end{bmatrix} \text{ for plane stress} \tag{3.19}$$

$$\mathbf{B}_I = \begin{bmatrix} \Phi_{I,x} & 0 \\ 0 & \Phi_{I,y} \\ \Phi_{I,y} & \Phi_{I,x} \end{bmatrix} \tag{3.20}$$

$$\mathbf{N} = \begin{bmatrix} n_x & 0 & n_y \\ 0 & n_y & n_x \end{bmatrix} \quad \mathbf{S} = \begin{bmatrix} s_x & 0 \\ 0 & s_y \end{bmatrix} \tag{3.21}$$

$$s_x = \begin{Bmatrix} 1, \text{ if the prescribed } u_x \text{ on } \Gamma_u \\ 0, \text{ if the prescribed } u_y \text{ on } \Gamma_u \end{Bmatrix} \tag{3.22}$$

$$s_y = \begin{Bmatrix} 0, \text{ if the prescribed } u_x \text{ on } \Gamma_u \\ 1, \text{ if the prescribed } u_y \text{ on } \Gamma_u \end{Bmatrix} \tag{3.23}$$

3.2.2.3 Jump function approach

In this approach, the discontinuities in derivatives are incorporated by using a Jump function in the solution (Krongauz and Belytschko, 1998). The enrichment of EFGM approximations is done by adding special shape functions i.e. Jump functions that contain

discontinuities in derivative (Batra *et al.*, 2004) to the approximate solution. The Jump shape functions have compact support which results in banded stiffness matrix.

Consider a two dimensional model (Fig. 3.1) having a line of derivative discontinuity. The approximation with Jump function becomes

$$u^h(\mathbf{x}) = u^{EFGM}(\mathbf{x}) + q^J(s)\Psi_J(\mathbf{r}) \tag{3.24}$$

where, u^{EFGM} is the standard EFGM approximation, which is given as:

$$u^{EFGM}(\mathbf{x}) = \sum_{I=1}^{n} \Phi_I(\mathbf{x}) u_I \tag{3.25}$$

q^J are amplitude parameters of the jumps, and $\Psi_J(r)$ are the Jump shape functions. s provides parameterization of the line of discontinuity, and q^J is discretized as follows:

$$q^J(s) = \sum_I N_I(s) q_I^J \tag{3.26}$$

where, $N_I(s)$ are one dimensional shape functions which need to be C^1 continuous so that they do not introduce any discontinuities in derivatives other than across the discontinuity line.

From Eq. (3.24), it is clear that constant and linear fields will still be reproduced exactly when $q^J = 0$. The distance to the closest point on the line of discontinuity is denoted by r (positive on one side of the discontinuity and negative on the other side). The Jump shape function is constructed from polynomials with a built-in discontinuity in the derivatives. Let Ψ_J be equal to $\Psi_J(\bar{r}_J)$, where $\bar{r}_J = r_J / d_{mI}$; r_J is the distance to the J^{th} point of discontinuity and d_{mI} is the domain of influence. A cubicspline Jump function used in the present work is given as

$$\Psi_J(\bar{r}_J) = \begin{cases} \frac{-1}{6}\bar{r}_J^{\,3} + \frac{1}{2}\bar{r}_J^{\,2} - \frac{1}{2}\bar{r}_J + \frac{1}{6} & \bar{r}_J \le 1 \\ 0 & \bar{r}_J \ge 1 \end{cases} \tag{3.27}$$

A discontinuity in two dimensions is shown in Fig. 3.4. The distance r from the node to the line of discontinuity is taken as positive for the nodes lying on the right side of the line of discontinuity while for the nodes on left side r is taken as negative. For example r_I and r_J are positive while r_K and r_L are negative.

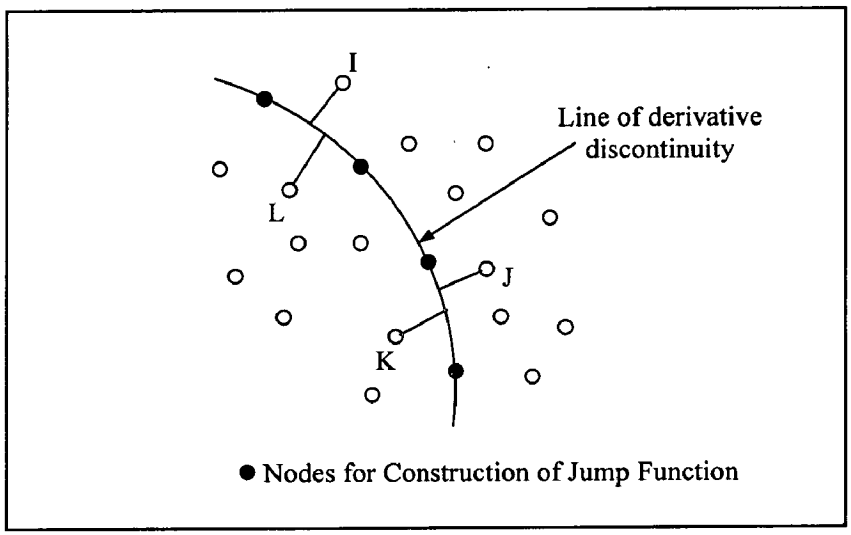

Fig. 3.4: Discontinuity and sign convention for r in two dimensions

In order to make a comparative study of the above techniques, the results have been obtained for two different cases of a bi-material beam. In the first case, the interface has been kept normal to the length of the beam while in the second case; the interface has been kept parallel to the length of the beam.

3.2.3 Bi-material Beam with Vertical Interface

A beam of dimensions $W \times H$ subjected to traction at the free end is shown in Fig. 3.5. The problem has been solved for a plane stress condition with the following material properties: $E_1 = 4\text{x}10^5$ units, ν_1=0.2, $E_2 = 2\text{x}10^5$ units, $\nu_2 = 0.1$. The dimensions of the beam are $W = 8$ units, $H = 1$ unit. The material constants are chosen in such a way that $E_1 / \nu_1 = E_2 / \nu_2$, so that the magnitude of strain along the interface remains equal for both material. This ensures that there is no singularity in field variables at the interface.

The material interface is vertical (parallel to y-axis) and is halfway along the length of the beam. The applied traction (P) is 1 unit. The beam has been discretized using 41 uniformly distributed nodes in x-direction and 11 uniformly distributed nodes in y-direction for both EFGM and FEM. Four point Gauss quadrature (Dolbow and Belytschko, 1999) i.e. 16 Gauss points are used in each cell to evaluate the stiffness matrix. The solutions were obtained using a linear basis function (Belytschko *et al.*, 1994) with cubic-spline weight function with $d_{\max} = 1.5$.

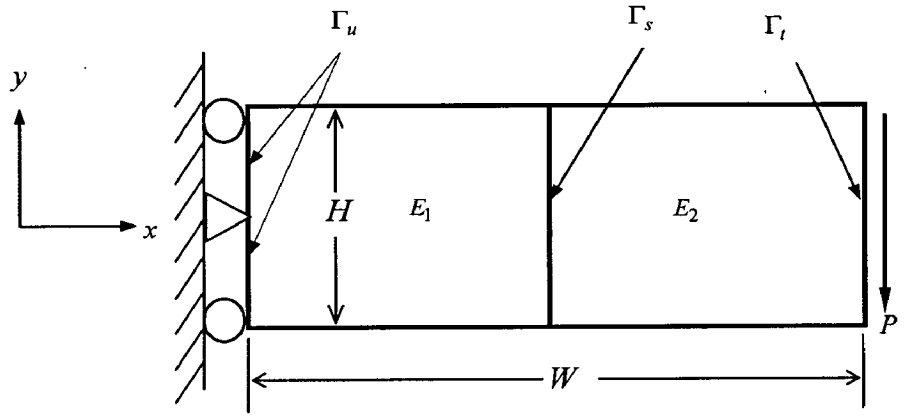

Fig. 3.5: A two dimensional bi-material beam with vertical interface

Numerical results obtained by three different EFGM approaches are compared with those obtained by FEM. Figure 3.6 shows the results obtained using domain partitioning approach. The variation of stress component σ_{xx} and strain component ε_{xx} is presented in this figure along the length of the beam at the top surface. It shows that the stress values exhibit a linear variation along the length of the beam, while a sudden jump is noticed in strain at the material interface, which is expected. A similar variation of σ_{xx} and ε_{xx} along the length of the beam have been obtained using the Lagrange multiplier and Jump function approaches as can be seen in Figs. 3.7 and 3.8 respectively. Except the Jump function approach, all other methods including the FEM solution shows a slight

kink in the linear variation of stress σ_{xx} at the material interface. Also, the magnitude of Jump in strain ε_{xx} values is more for the Jump function approach as compared with FEM solution as can be seen from Fig. 3.8 (b).

The variations of σ_{yy} and ε_{yy} along the length of beam at the top surface is shown in Figs. 3.9-3.11 for domain partitioning, Largrange multiplier and Jump function approaches respectively. The results obtained by these approaches are compared with FEM solution as shown in Figs. 3.9 - 3.11. From these plots, it is seen that σ_{yy} remains nearly zero along the length of beam as expected from the theoretical calculations. In order to check the effectiveness of these methods, L_2 error has been calculated for different parameters ($\sigma_{xx}, \sigma_{yy}, \varepsilon_{xx}, \varepsilon_{yy}, U_x, U_y$), and is presented in Table 3.1. From the results in Table 3.1, it is found that the error in solutions obtained by Jump function approach is minimum as compared to other two approaches. The error in results obtained by domain partitioning and Lagrange multiplier methods are almost similar.

For a better understanding of the results, the stress/strain contours have been plotted over the domain of the problem using jump function technique. Figure 3.5 shows the schematic diagram of the vertical interface bi-material beam problem subjected to traction on the right edge. The stress and strain contours, generated due to applied traction, are shown in Fig. 3.12 and Fig. 3.13 respectively. The stress (σ_{xx}) and strain (ε_{yy}) are smooth and continuous along the interface as expected while a jump in the strain field (ε_{yy}) across the interface can be clearly seen from Fig. 3.12b. Moreover, the stresses along y-axis (σ_{xx}) are nearly zero in magnitude as observed from Fig. 3.13a. Thus, the stress/strain contours show a good modeling capability of Jump function criterion.

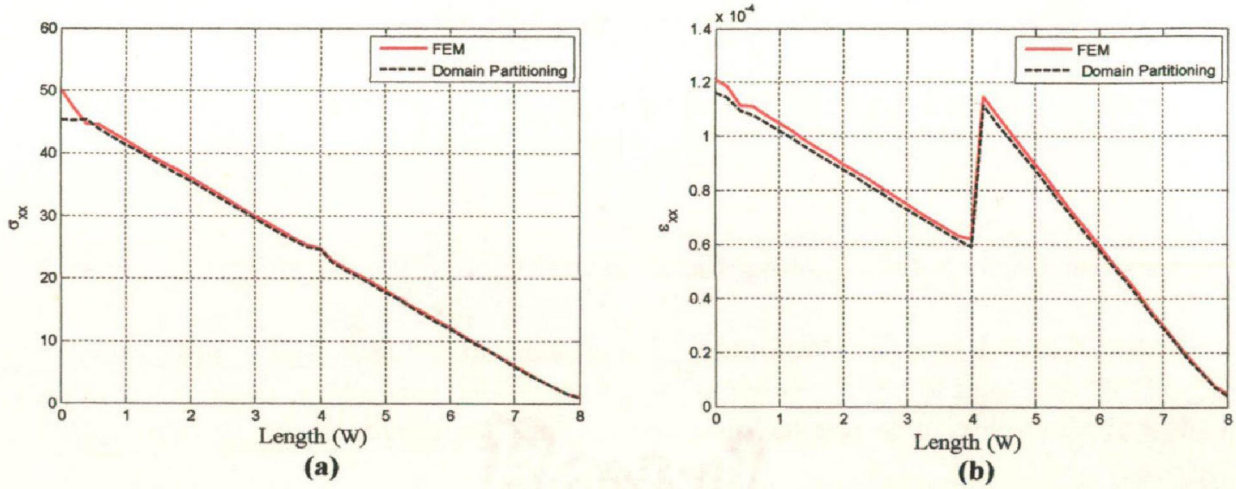

Fig. 3.6: σ_{xx} and ε_{xx} variation along length of beam at top nodes (Domain partitioning)

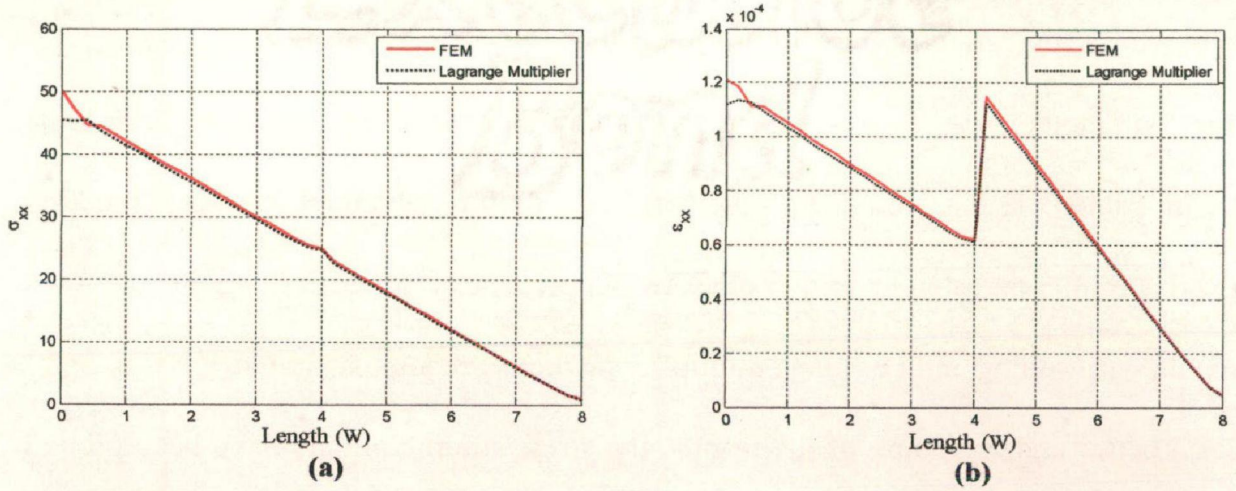

Fig. 3.7: σ_{xx} and ε_{xx} variation along length of beam at top nodes (Lagrange multiplier)

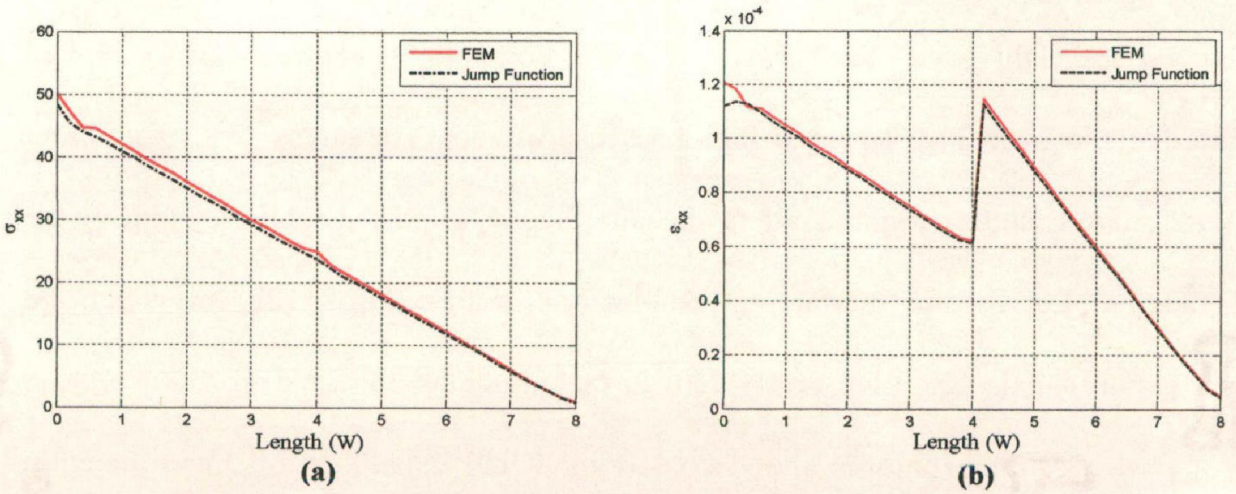

Fig. 3.8: σ_{xx} and ε_{xx} variation along length of beam at top nodes (Jump function)

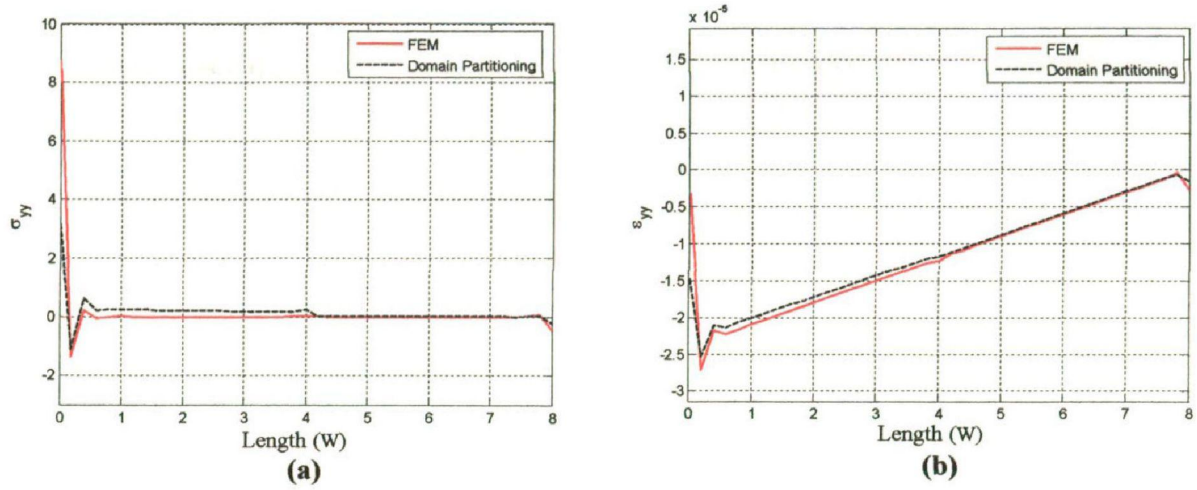

Fig. 3.9: σ_{yy} and ε_{yy} variation along length of beam at top nodes (Domain partitioning)

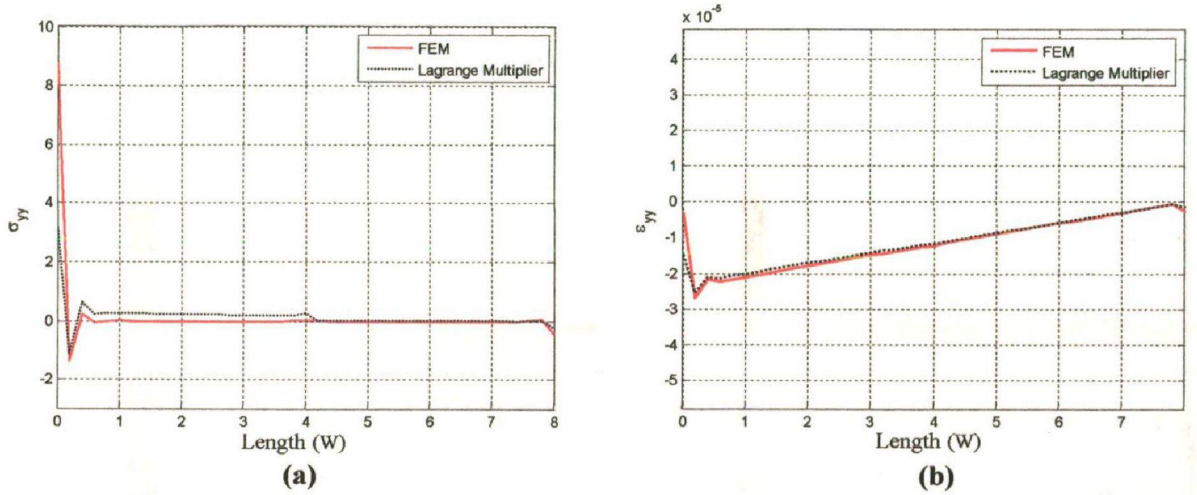

Fig. 3.10: σ_{yy} and ε_{yy} variation along length of beam at top nodes (Lagrange multiplier)

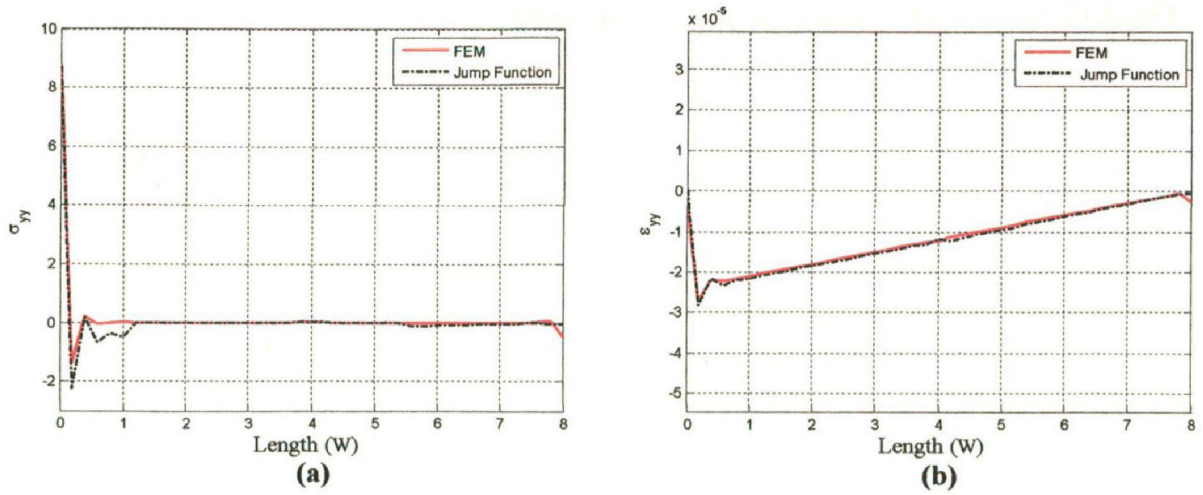

Fig. 3.11: σ_{yy} and ε_{yy} variation along length of beam at top nodes (Jump function)

Table 3.1: L_2-error norms for bi-material beam having a vertical interface

Parameter	Domain Partitioning	Lagrange Multiplier	Jump Function
σ_{xx}	1.4177	1.4084	**1.0970**
σ_{yy}	1.7256	1.7256	**0.4520**
ε_{xx}	1.1996e-005	1.1996e-005	**1.0188e-005**
ε_{yy}	4.2719e-006	4.2589e-006	**1.1119e-006**
U_x	9.5176e-006	9.5176e-006	**4.0670e-006**
U_y	9.8266e-005	9.8266e-005	**4.2033e-005**

$$L_2 = \sqrt{\sum_{i=1}^{n}\left(X_{EFG} - X_{FEM}\right)} \times \sqrt{\frac{Domain\ Area}{no.of\ cells}}$$ where X is any field parameter.

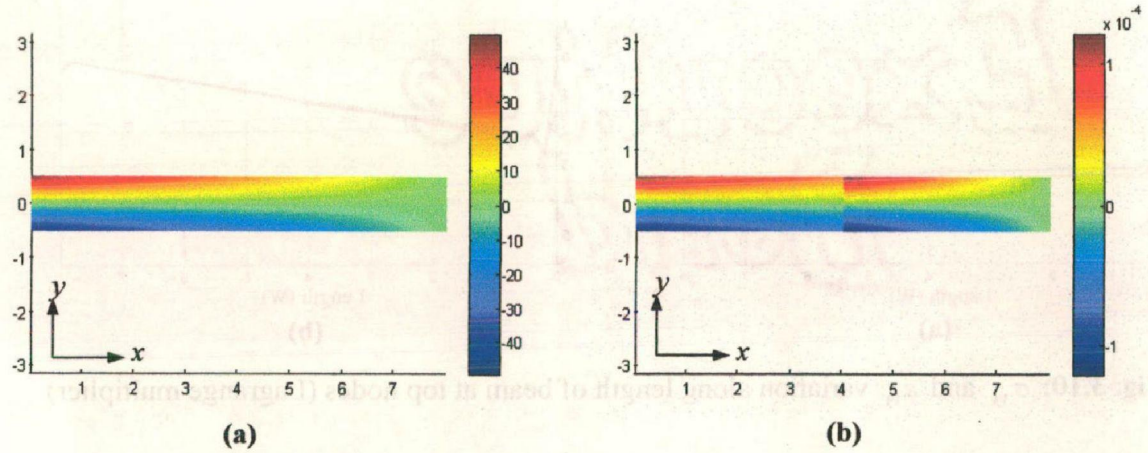

Fig. 3.12: Contour plots using Jump Function **(a)** Stress (σ_{xx}) **(b)** Strain (ε_{xx})

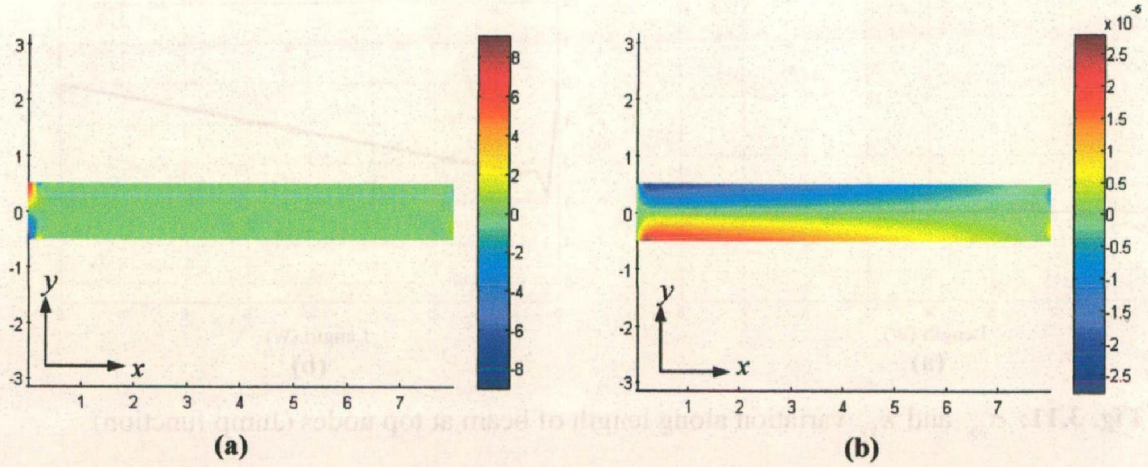

Fig. 3.13: Contour plots using Jump Function **(a):** Stress (σ_{yy}) **(b):** Strain (ε_{yy})

3.2.4 Bi-material Beam with Horizontal Interface

A bi-material beam of dimensions $W \times H$ is subjected to traction P at the free end as shown in Fig. 3.14. The problem has been solved for a plane stress condition with the following material properties: $E_1 = 9\text{x}10^5$ units, $\nu_1 = 0.45$, $E_2 = 1\text{x}10^5$ units, $\nu_2 = 0.05$, and beam dimensions $W = 8$ units, $H = 1$ unit. One end of the beam is fixed whereas traction (P) of 1 unit is applied at the other end of the beam. The material interface is kept horizontal (parallel to x-axis) and is made to coincide with the neutral axis of beam. The neutral axis of the beam is obtained at $H/4$ by using the compatibility condition for bi-material i.e $E_1/E_2 = Z_2/Z_1$ where Z denotes the section modulus. A regular arrangement of (35×9) nodes has been used for domain discretization. In each integration cell, 4×4 Gauss quadrature is utilized to evaluate the stiffness matrix. The EFGM simulations are performed using a linear basis function with the cubic-spline weight function for $d_{\max} = 1.5$.

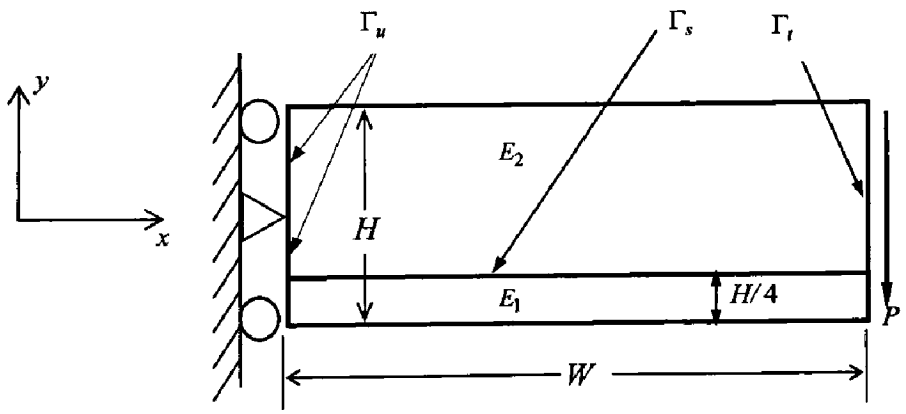

Fig. 3.14: A two dimensional bi-material beam with horizontal interface

Numerical results obtained using three different EFGM approaches namely domain partitioning, Lagrange multiplier, and Jump function approaches, are compared with FEM solution. Figure 3.15 shows the variation of σ_{xx} and ε_{xx} along a line normal to the material interface at $x = W/2$ for domain partitioning approach. Figure 3.15(a) shows

that σ_{xx} values exhibit a linear variation in both the materials but the slopes are different. At the interface the value of σ_{xx} becomes zero. The zero value of σ_{xx} is due to the fact that the material interface coincides with the neutral axis of beam where all the stresses are zero. The variation of strain component ε_{xx} along a line normal to material interface shows a linear variation as can be seen from Fig. 3.15(b). A similar variation of σ_{xx} and ε_{xx} has been obtained using the Lagrange multiplier and Jump function approaches as can be seen in Fig. 3.16 and Fig. 3.17 respectively. From these plots, it is seen that the results obtained by Jump function technique are more close to the FEM solutions.

The variation of σ_{yy} and ε_{yy} obtained by the above three approaches along a line normal to the interface at $x = W/2$ is shown in Figs. 3.18 - 3.20. The magnitude of σ_{yy} remain nearly zero along a line normal to material interface. The variation of strain component ε_{yy} again shows a linear variation on both sides of interface with different slopes. At the material interface, the value of ε_{yy} becomes zero as it is the neutral axis of the beam.

The results obtained by all three techniques are compared with those obtained by FEM as shown in Figs. 3.15-3.20. L_2-error norm are obtained for $\sigma_{xx}, \varepsilon_{xx}\ \sigma_{yy}, \varepsilon_{yy}, U_x$, U_y, and are presented in Table 3.2. From Table 3.2, it is found that Jump function technique possess the least error for all parameters. Due to better accuracy, Jump function has been used to generate stress/strain contours for the horizontal interface problem as shown in Fig. 3.21 and Fig. 3.22. The contour plots reveal that Jump function has got good modeling capability as the results are found to be quite at par with those expected analytically.

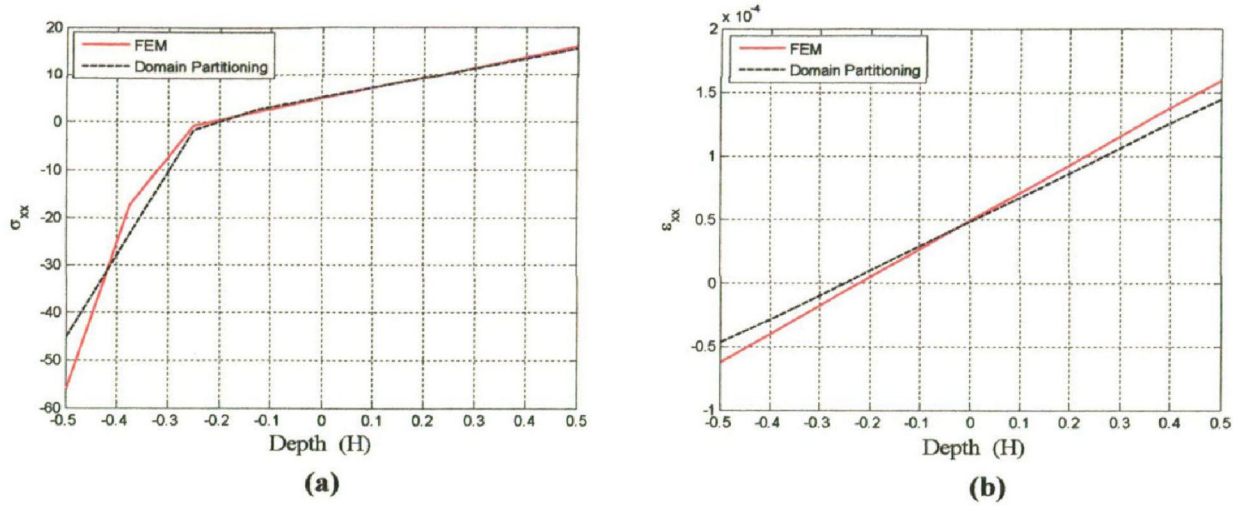

(a) (b)

Fig. 3.15: σ_{xx} and ε_{xx} variation along depth of beam (Domain partitioning)

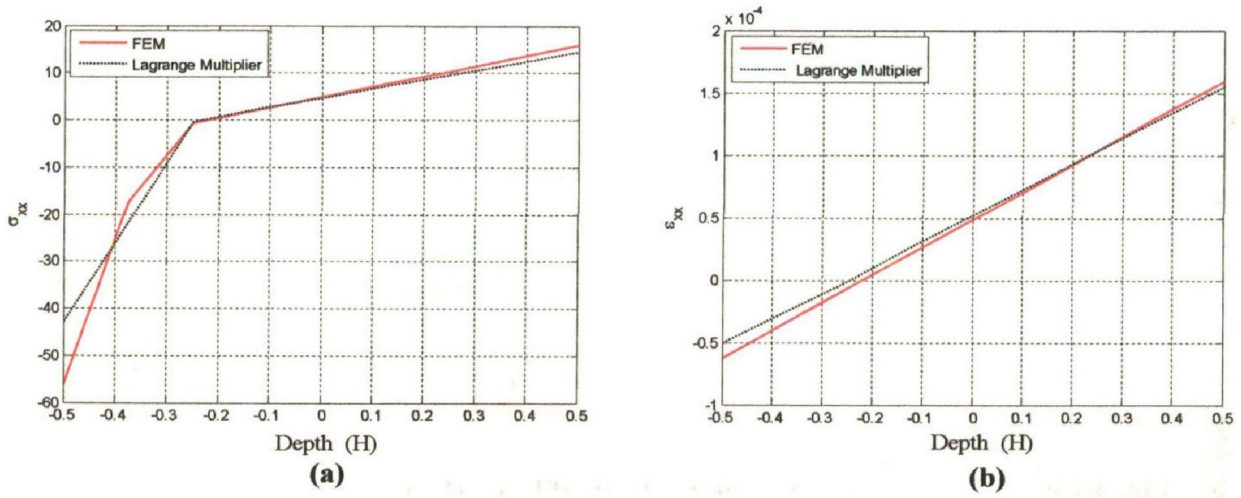

(a) (b)

Fig. 3.16: σ_{xx} and ε_{xx} variation along depth of beam (Lagrange multiplier)

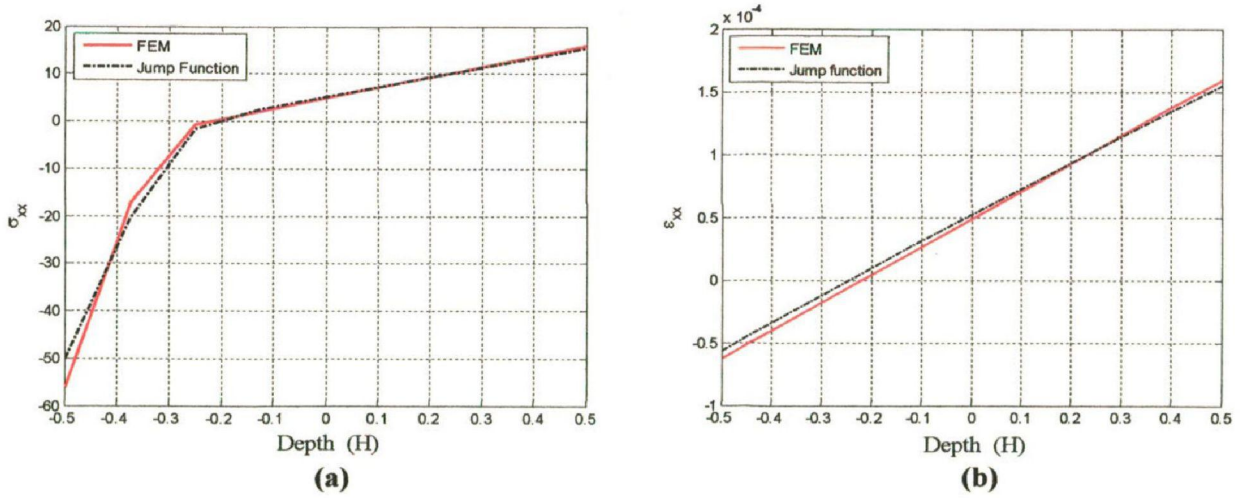

(a) (b)

Fig. 3.17: σ_{xx} and ε_{xx} variation along depth of beam (Jump function)

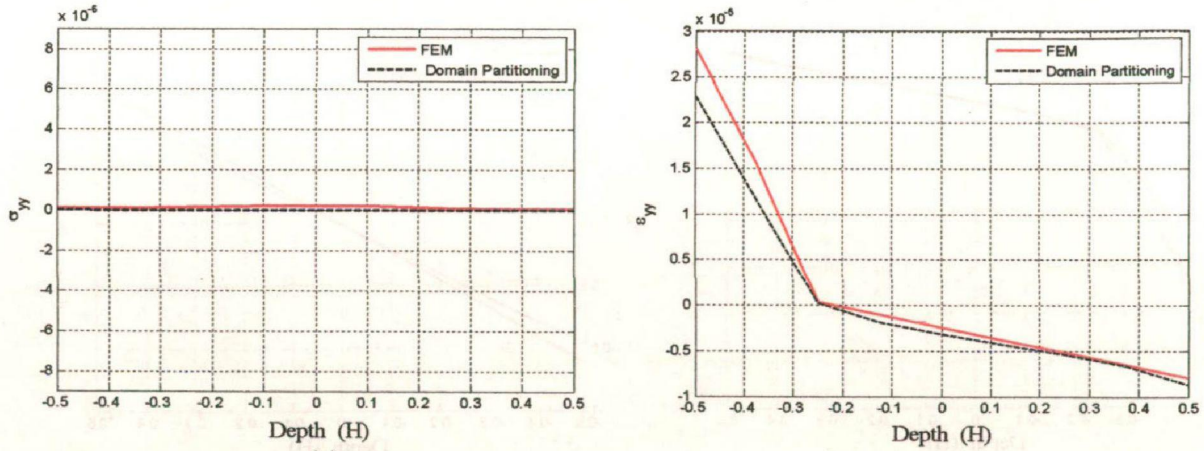

Fig. 3.18: σ_{yy} and ε_{yy} variation along depth of beam (Domain partitioning)

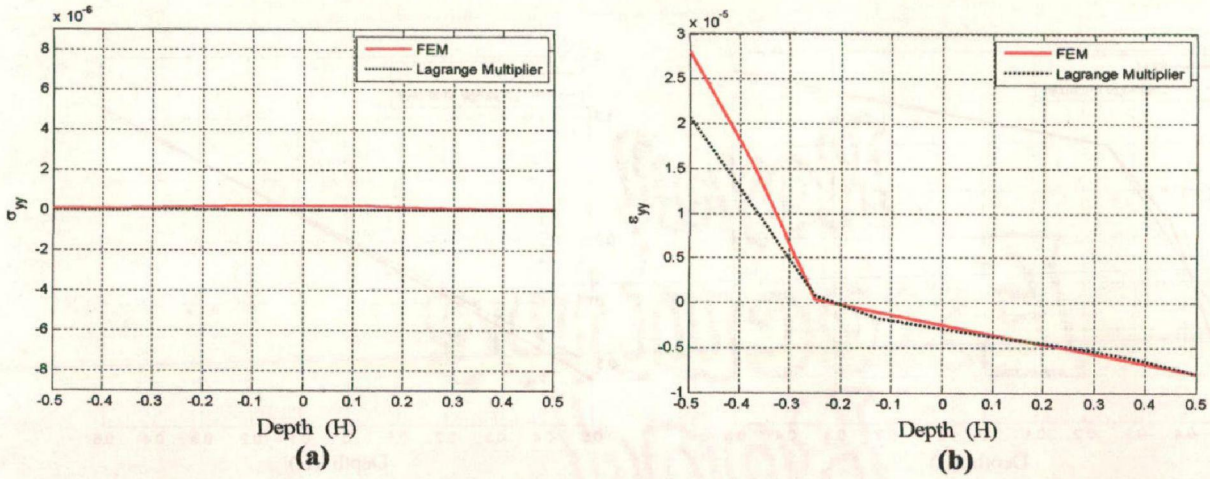

Fig. 3.19: σ_{yy} and ε_{yy} variation along depth of beam (Lagrange multiplier)

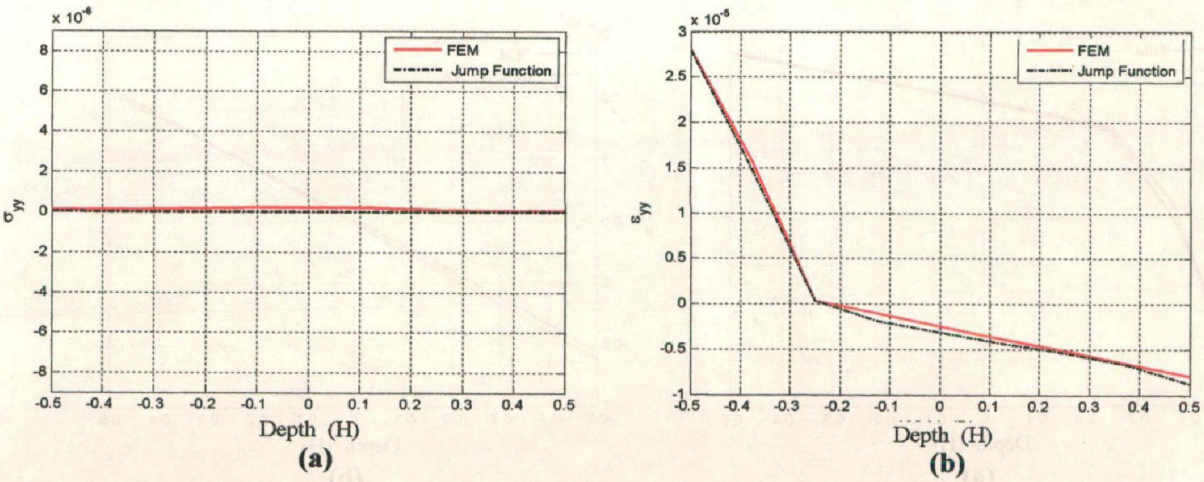

Fig. 3.20: σ_{yy} and ε_{yy} variation along depth of beam (Jump function)

Table 3.2: L_2-error norms for bi-material beam having a horizontal interface

Parameter	Domain. Partitioning	Lagrange Multiplier	Jump Function
σ_{xx}	92.82176	93.42694	**92.68715**
σ_{yy}	10.34732	10.97538	**10.08384**
ε_{xx}	3.2547e-004	3.2548e-004	**2.8378e-004**
ε_{yy}	4.847e-005	4.8275e-005	**4.6998e-005**
U_x	0.0016866	0.0016867	**0.001485**
U_y	0.01016618	0.01016641	**0.009575**

$$L_2 = \sqrt{\sum_{i=1}^{n}\left(X_{EFG} - X_{FEM}\right)} \times \sqrt{\frac{Domain\ Area}{no.of\ cells}} \quad \text{where } X \text{ is any field parameter}$$

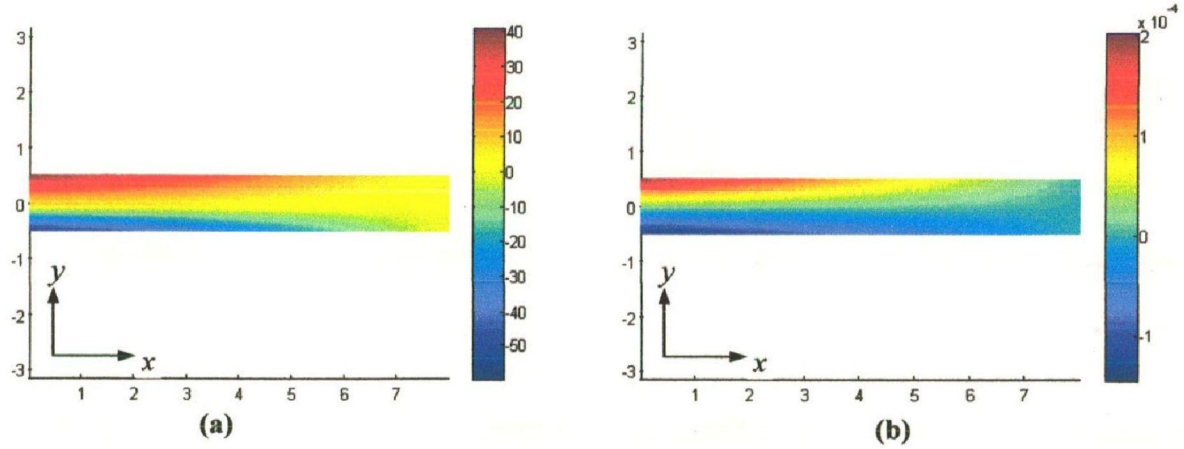

Fig. 3.21: Contour plots using Jump Function **(a):** Stress (σ_{xx}) **(b):** Strain (ε_{xx})

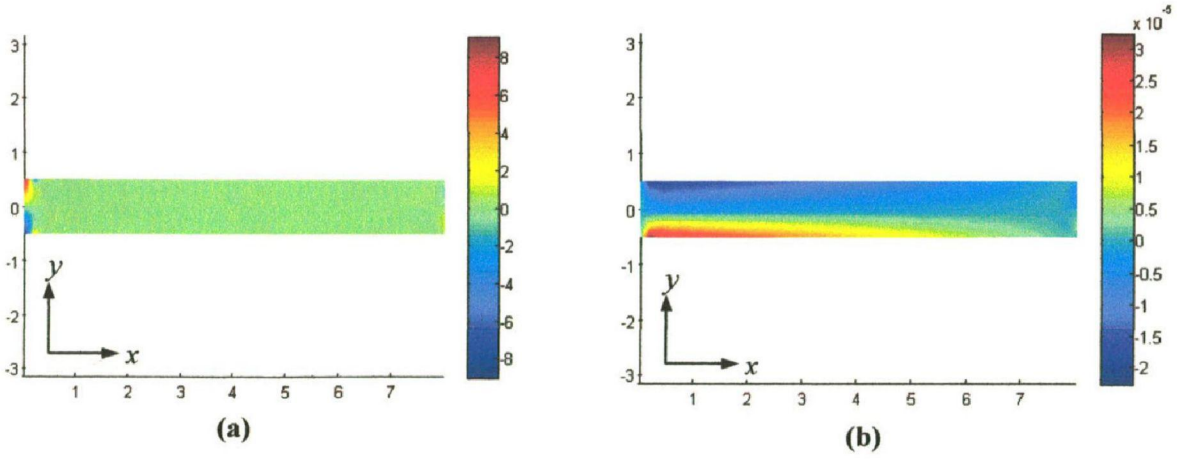

Fig. 3.22: Contour plots using Jump Function **(a):** Stress (σ_{yy}) **(b):** Strain (ε_{yy})

3.3 MODELING OF MATERIAL AND GEOMETRIC DISCONTINUITIES

The increasing demand of multifunctional materials (having resistance to corrosion, wear, thermal and chemical environment) in mechanical, aerospace and biomedical applications has imparted the layered materials, a coveted place in the world of engineering materials. Layered materials are found in a variety of important structures such as adhesive joints, composite laminates, and various electronics components. The overall mechanical behavior and response of layered systems depend on the mechanical properties and fracture behavior of the interface. The interaction between materials results in local load distribution, which determines the overall strength and fracture behavior. The abrupt change in properties at the interface of layered materials is a source of failure. A problem of great practical importance in composite laminate is a crack lying along the interface of two layers with different elastic properties. Unlike crack problems in homogeneous bodies, the bi-material interface crack always induces both opening and shearing under mode-I loading. This coupling of stress intensification was first demonstrated by Williams (1959) who used an Eigen function expansion approach, and it was found that the stress singularity in the vicinity of a crack tip of a bi-material interface crack is oscillatory in nature along with the presence of $1/\sqrt{r}$ singularity.

Various numerical methods for evaluating the stress intensity factors of bi-material interface cracks have been developed including FEM and BEM. Yau and Wang (1984) applied the *M*- integral approach in conjunction with FEM. Matos *et al.* (1989) used the virtual crack extension method in conjunction with the superposition method and FEM. Miyazaki *et al.* (1993a,b) applied the virtual crack extension technique and *M*- integral approach along with BEM. Ikeda and Sun (2001) presented an efficient numerical

procedure in conjunction with FEM for the analysis of an interface crack under thermal stresses. Some studies on bi-material interface cracks have also been performed using extended finite element method (Nagashima *et al.*, 2003).

At first, FEM appears to be an ideal method for the stress analysis of cracked components. Unfortunately, FEM solution converges very slowly if the conventional elements, which do not include stress singularities, are used. The high accuracy elements using higher order polynomials as interpolation functions cannot improve the rate of convergence. The error from the element immediately adjacent to the point of singularity is found to be the same order as that obtained from the remaining elements. Also, the use of small size elements cannot improve the situation either. The preparation of finite element meshes for effective product analysis usually requires considerable amount of labour and time as many products are composed of complex parts. To overcome these problems, a number of meshfree methods have been developed over past 15 years. Element free Galerkin method (Belytschko *et al.*, 1994; Krongauz, 1996, Lu *et al.*, 1994; Phu *et al.*, 2008; Liu, 2003) is one of them, which is found quite attractive in comparison to standard finite element method as it avoids the need for tedious and time consuming finite element mesh.

3.3.1 Modeling of Bi-material Interfacial Cracks

In this work, a simplified approach for modeling bi-material interface crack has been proposed. Material discontinuity i.e. weak discontinuity has been modeled by a Jump function (Batra *et al.*, 2004) and geometric discontinuity (crack) i.e. strong discontinuity has been modeled by intrinsic enrichment criterion (Li and Simonsen, 2007). In this approach, the crack lying at the interface of two materials has been modeled by using

same enrichment functions as were used for modeling the cracks in homogeneous materials. Only four standard enrichment functions are used for modeling an interfacial crack rather than the twelve enrichment functions used by Sukumar *et al.*, 2004. Thus, the use of four enrichment terms along with Jump function provides us a simplified approach to solve bi-material interface crack problem. At the same time it reduces the computational cost significantly. The mixed mode stress intensity factors K_I and K_{II} are evaluated using the modified domain form of interaction integral (Sukumar *et al.*, 2004).

3.3.1.1 Modeling of geometric discontinuity by intrinsic enrichment

In enrichment criterion (Li and Simonsen, 2007), the presence of a crack i.e. geometric discontinuity is modeled by adding extra terms either in the basis function or in the approximation function. According to this criterion, physically there is no crack in the domain. The meshfree standard basis functions are intrinsically enriched by the near-tip asymptotic field functions to solve the problems involving strong discontinuities. The number of enrichment functions depends on the coarse mesh accuracy desired. For higher accuracy, full asymptotic field functions can be included in the basis, whereas for higher speed at some cost of accuracy, only $\sqrt{r}$ can be included in the basis. An enriched basis function used in the present work is given as:

$$\mathbf{P}^T(\mathbf{x}) = \left[\underbrace{1,\ x,\ y}_{\substack{\text{standard} \\ \text{basis}}},\ \underbrace{\sqrt{r}\cos\frac{\theta}{2}, \sqrt{r}\sin\frac{\theta}{2}, \sqrt{r}\sin\frac{\theta}{2}\sin\theta, \sqrt{r}\cos\frac{\theta}{2}\sin\theta}_{\text{enrichment terms}} \right] \tag{3.32}$$

where, **P(x)** is the enriched basis function, r and θ are the local crack tip parameters. The first three terms of Eq. (3.32) represent the standard basis function $(1, x, y)$ while the remaining four terms obtained from the crack tip solution makes up the enrichment part.

3.3.1.2 Interaction integral approach for an interfacial crack

The J-integral remains globally path independent for bi-material interface crack problems when no material inhomogenity exists in the direction parallel to the crack (Smelser, 1977). In this case, the mixed mode stress intensity factors K_I and K_{II} can be readily evaluated using the domain form of the interaction integral (Moran and Shih, 1987). This is a well established technique for determining the mixed mode stress intensity factors for two-dimensional interfacial cracks (Nahta and Moran, 1993). In the interaction integral approach, the two dimensional auxiliary fields are introduced and superposed on the actual fields that arise from the solution of the boundary value problem. By judicious choice of auxiliary fields, the stress intensity factors can be directly linked to the interaction integral. The domain form of interaction integral (Sukumar *et al.*, 2004; Yau *et al.*, 1980) can be written as:

$$M = -\int_A (\sigma_{ik}\varepsilon_{ik}^{aux}\delta_{1j} - \sigma_{ij}u_{i,1}^{aux} - \sigma_{ij}^{aux}u_{i,1})\bar{q}_{,j}\,dA \tag{3.33}$$

where, $\bar{q}$ is an arbitrarily smooth scalar weighting function which is unity at the crack tip and zero on the contour C (Fig. 3.23). The auxiliary displacement fields for an interfacial crack can be extracted using stated equations, and the interaction integral is related to the stress intensity factors through the following relation (Sukumar *et al.*, 2004).

$$M_i = \frac{2}{\bar{E}\cosh^2(\pi\tilde{\varepsilon})}(K_I K_{II}^{aux} + K_I K_{II}^{aux}) \quad \text{with } i = 1, 2 \tag{3.34}$$

K_I^{aux} and K_{II}^{aux} are local auxiliary stress intensity factors for the auxiliary fields and $\overline{E}$ is the equivalent Young's modulus given as $2E_1E_2/(E_1+E_2)$ and $\widetilde{\varepsilon}$ is the bi-material constant (Sukumar *et al.*, 2004) of the bi-material system. K_I can be computed by taking $K_I^{aux}=1$ and $K_{II}^{aux}=0$ from I_1, and K_{II} can be computed in a similar fashion.

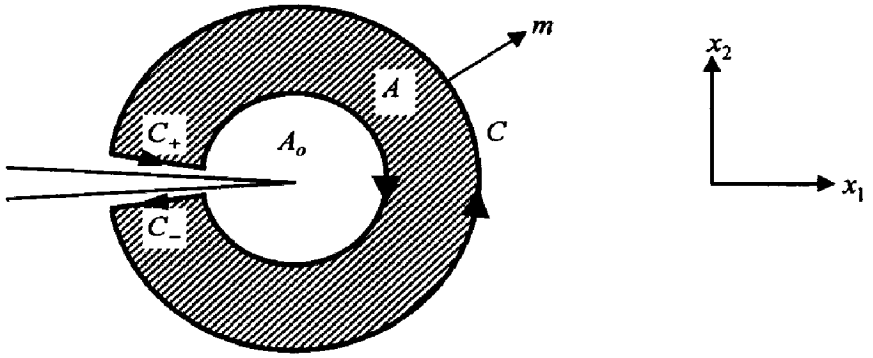

Fig. 3.23: Domain integral representation (Domain A is enclosed by C^+, C^- and C)

3.3.2 Bi-metallic Plate with an Interfacial Edge Crack

A bi-metallic plate having an edge crack of length a, is subjected to a tensile load on upper and lower boundaries as shown in Fig. 3.24. The plate dimensions are scaled with $W=3$ units, $H=9$ units, and far field applied stress $\sigma_o=1$ unit. The values of Poisson's ratios are taken as $\nu_1=\nu_2=0.3$. In order to demonstrate the validity of the proposed method for interface crack problems, the results are obtained for several ratios of Young's moduli $E_2/E_1=2,\ 3,\ 10,\ 100$, where E_1 is kept constant at 100 units and crack lengths $a/W=0.2,\ 0.3,\ 0.4,\ 0.5,\ 0.6$. Normalized stress intensity factors are shown in Fig. 3.25-3.28 where the results marked as Ref.1 and Ref.2 are taken from Matsumoto *et al.*, (2000) and Liu *et al.*, (2004) respectively.

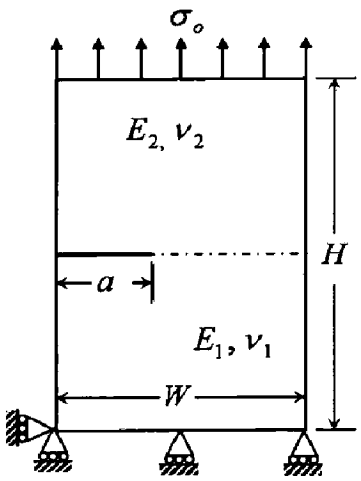

Fig. 3.24: A bi-metallic interface edge crack

Figure 3.25 shows the variation of normalized stress intensity factors i.e. K_I and K_{II} with varying crack length for $E_2/E_1 = 2$. The results show that with increase in crack length, K_I is increasing while K_{II} goes on decreasing. Next, the EFGM results are obtained for $E_2/E_1 = 3, 10$ and 100 as shown in Fig. 3.26-3.28 respectively. It can be clearly seen from Figs. 3.25-3.28 that the values obtained by EFGM are quite close to the reference values, and the maximum percentage difference in EFGM results with reference solutions is less than 5%.

In order to have a clear visualization of the crack tip fields, the contours of stress component (σ_{YY}) and strain component (ε_{YY}) have been generated for different ratios of E_2/E_1 with $a/W = 0.4$. Figure 3.29a and Figure 3.29b show the stress and strain contours respectively for $E_2/E_1 = 1$ i.e. for homogeneous plate. It can be clearly seen that both stress and strain fields are continuous and symmetric about x-axis as expected.

For non-homogeneous cases, the contours have been plotted for $E_2/E_1 = 2, 10, 100$. For $E_2/E_1 = 2$, the stress field σ_{YY} is nearly symmetric with a very small distortion as can be seen in Fig. 3.30a, but the strain contours for this case shows a small discontinuity

at the interface. Next, the stress contours have been plotted for the ratio of $E_2/E_1 = 10$, and a small variation in σ_{YY} from the homogeneous case is obtained as can be seen in Fig. 3.31a, while a strong discontinuity in the strain field is observed in Fig. 3.31b. The contours have also been plotted for a higher material mismatch ratio of $E_2/E_1 = 100$ which again shows a nearly continuous and symmetric stress field for σ_{YY} as shown in Fig. 3.32a, 3.33a while the strain field is highly discontinuous as can be seen in Fig. 3.32b, 3.33b. From these simulations, it is noticed that the discontinuity in strain field i.e. first derivative has been clearly observed due to the change in material property i.e. Young's moduli at the interface.

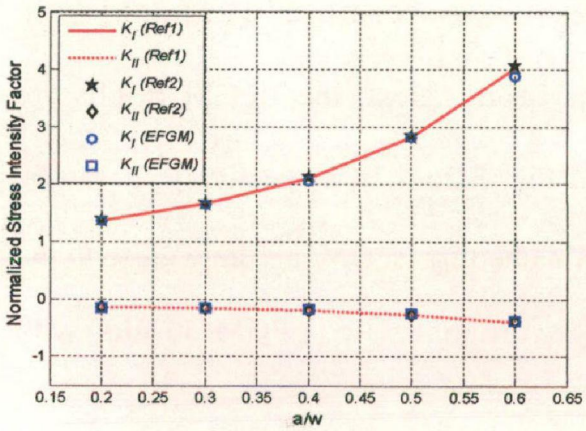

Fig. 3.25: SIFs variation for $E_2/E_1 = 2$

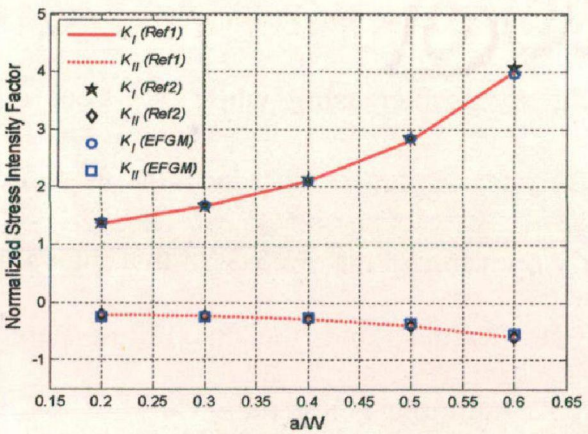

Fig. 3.26: SIFs variation for $E_2/E_1 = 3$

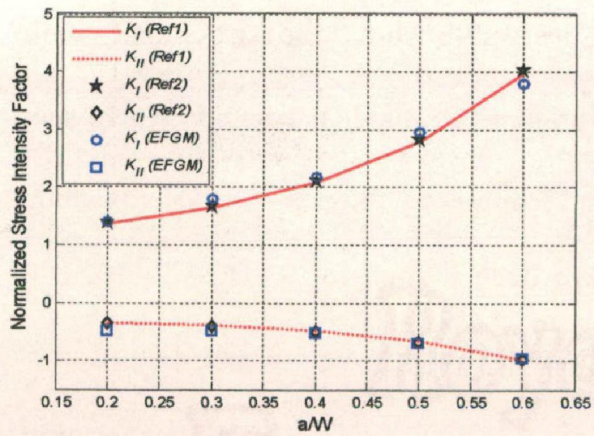

Fig. 3.27: SIFs variation for $E_2/E_1 = 10$

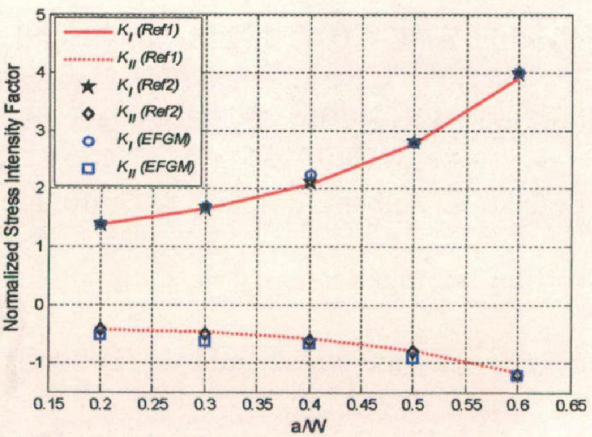

Fig. 3.28: SIFs variation for $E_2/E_1 = 100$

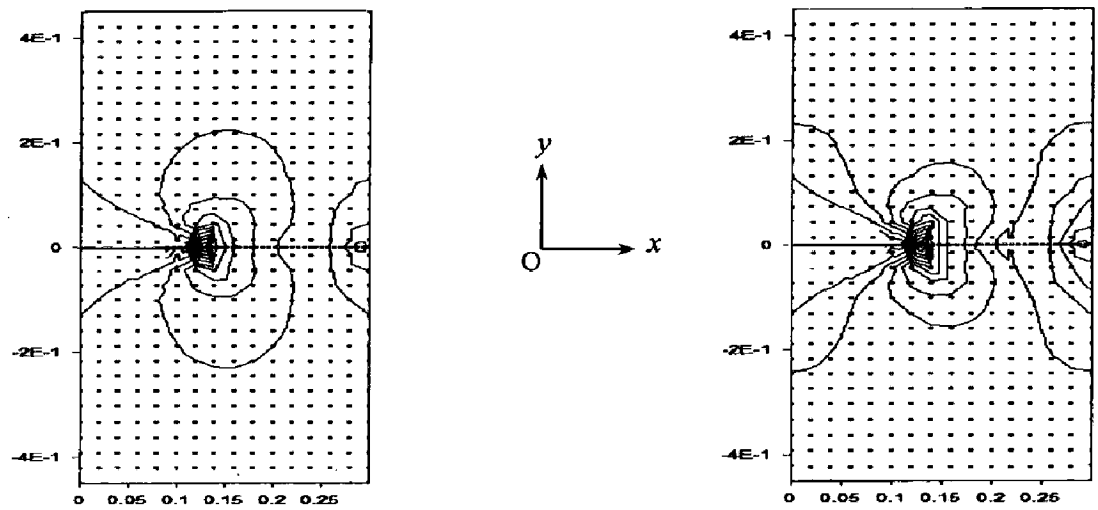

Fig. 3.29: σ_{xx} and ε_{xx} contours for $E_2/E_1 = 1$

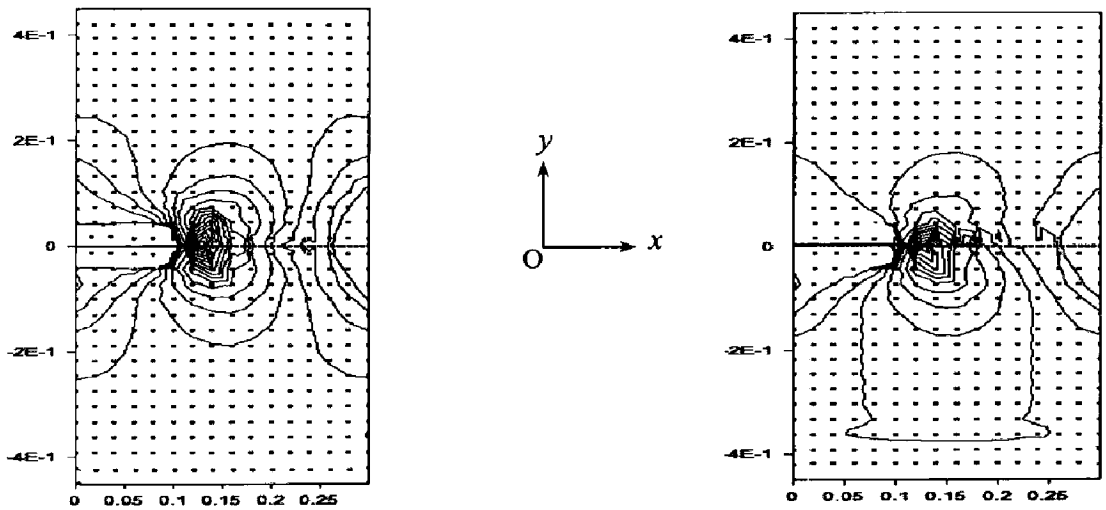

Fig. 3.30: σ_{xx} and ε_{xx} contours for $E_2/E_1 = 2$

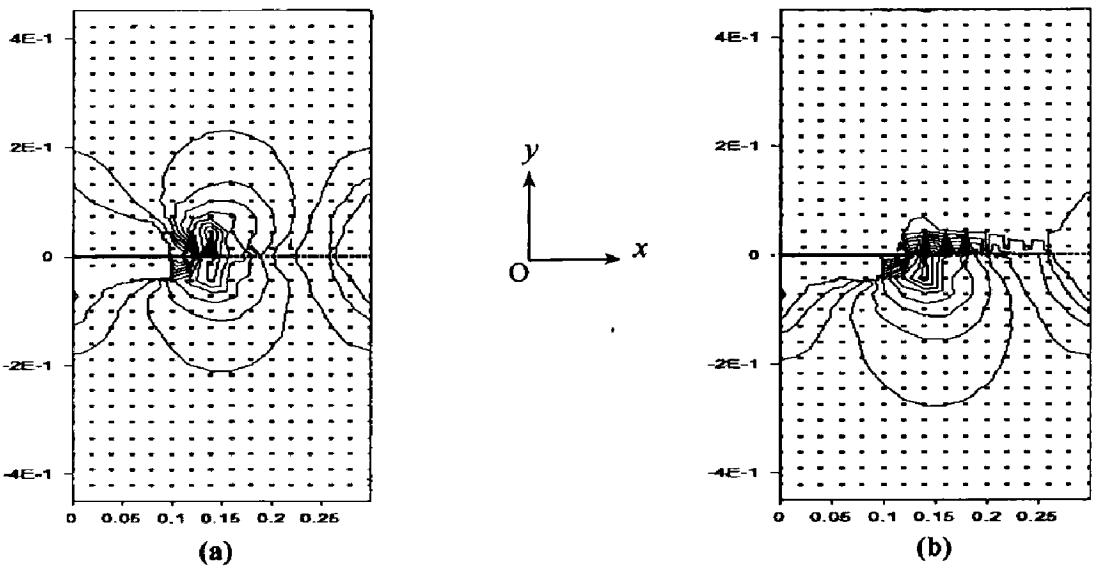

Fig. 3.31: σ_{xx} and ε_{xx} contours for $E_2/E_1 = 10$

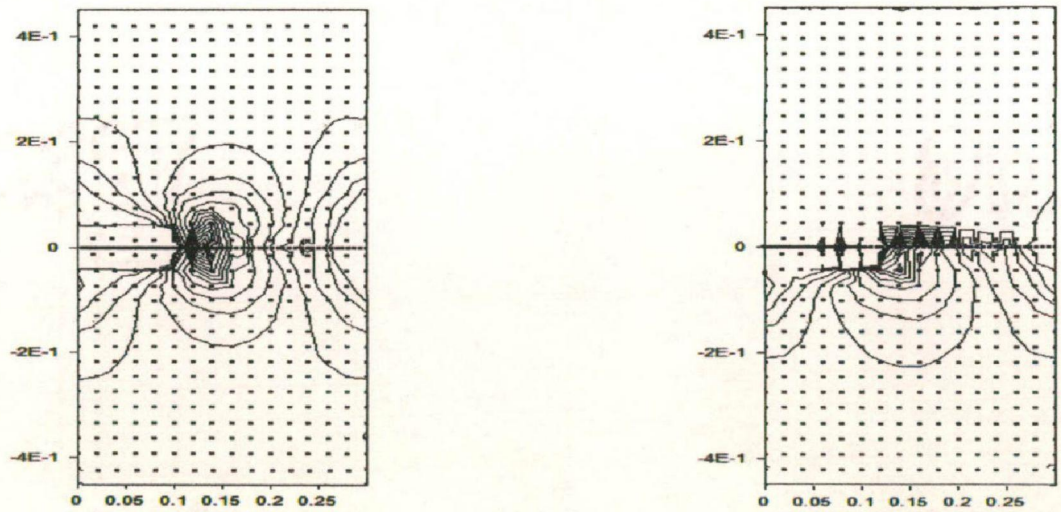

Fig. 3.32: σ_{xx} and ε_{xx} contours for $E_2/E_1 = 100$

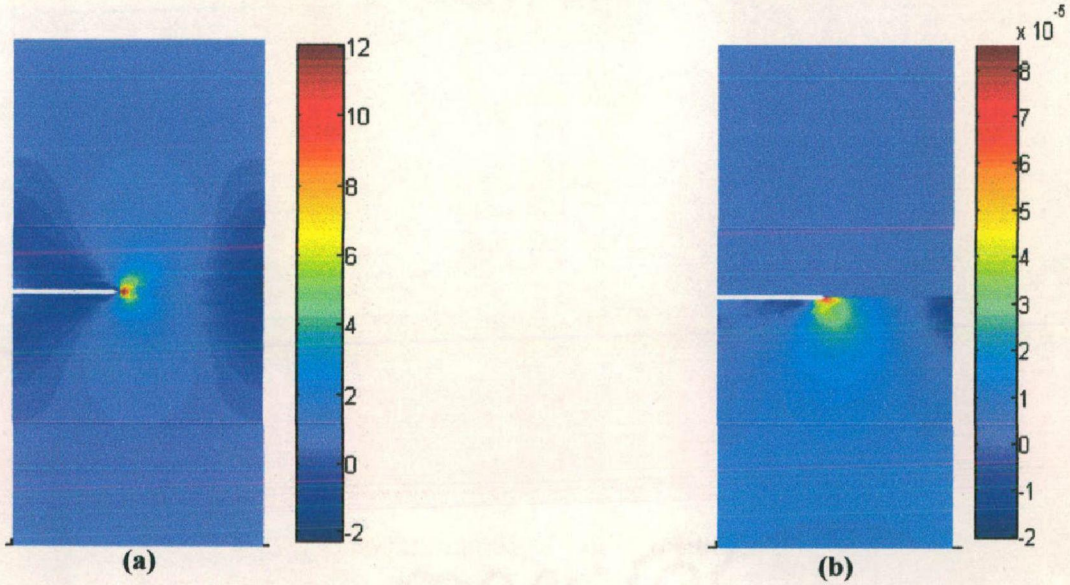

Fig. 3.33: σ_{xx} and ε_{xx} contours for $E_2/E_1 = 100$

3.3.3 Bi-metallic Plate with an Interfacial Center Crack

A bi-metallic rectangular plate with an interface crack at the center has been considered as shown in Fig. 3.34. The width (W) and height (H) of the plate are taken as 100 mm and 200 mm respectively. The material interface is kept horizontal at a distance of $H/2$ from the bottom of plate. A tensile load of 9.8 MPa is applied in a direction normal to the interface.

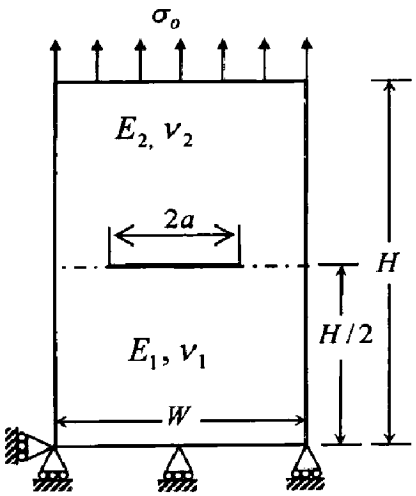

Fig. 3.34: Bi-metallic plate with an interface centre crack

Three different crack length$(2a)$, i.e. 40, 60 and 80 mm are considered. Young's modulus of the lower material (E_1) is kept constant at 205.8 GPa. For both materials, the values of Poisson's ratio are taken as 0.3. The results are obtained for different ratios of Young's modulus E_2 / E_1= 1, 2, 3, 4, 10, 100. The normalized stress intensity factor is defined as $K_i/\sigma\sqrt{\pi a}$ (i=1, 2) so as to obtain non-dimensional values corresponding to both mode-I and mode-II stress intensity factors. The EFGM results are compared with those obtained by BEM (Ref.1 (Miyakazi et al., 1993)) and X-FEM (Ref.2 (Nagashima et al., 2003)). Figure 3.35 shows the variation of normalized stress intensity factors with the variation of E_2 / E_1 for a crack length of 40 mm. The values of stress intensity factors have been evaluated at the right tip of the center crack. The analysis shows that the normalized values of K_I and K_{II} show a decreasing trend with the increase in E_2 / E_1. Moreover, the results obtained by EFGM are found to be quite close to the reference solutions. Another simulation is performed for a crack length of 60 mm, and the results are plotted in Fig. 3.36. From the results presented in Fig. 3.36, it can be clearly seen that the EFGM results are in good agreement with the reference solutions available in the

literature. The simulations are also performed for a crack length of 80 mm, and the normalized values of K_I and K_{II} are plotted for different ratios of E_2/E_1. The EFGM results are plotted along with the reference solution as shown in Fig. 3.37. The values of K_I are found to be quite close to Ref.1 solution with a maximum error of 4% for $E_2/E_1 = 100$.

The contours of σ_{YY} and ε_{YY} are also plotted in order to have a clear visualization of stress and strain fields. A centre crack of length $2a$ = 40 mm is considered for generating the contours with different ratios of Young' moduli. In the first case, the ratio E_2/E_1 is unity i.e. a case of homogeneous material, and the stress and strain contours are plotted as shown in Fig. 3.38a and Fig. 3.38b respectively. Both σ_{YY} and ε_{YY} are found to be continuous and symmetric about x-axis as expected. In non-homogeneous case, a bi-material plate with $E_2/E_1 = 2$ is considered as shown in Fig. 3.39. From the stress contour presented in Fig. 3.39a, a continuity of stress component σ_{YY} is noticed with a small distortion at the interface, while the strain contour for this case shows a clear deviation from the symmetry about x-axis as can be seen in Fig. 3.39b. The third set of contours is generated for a higher ratio of Young's moduli i.e. $E_2/E_1 = 10$, again the contours show a continuous nature of stress component σ_{YY} as shown in Fig. 3.40a, while the strain exhibits a high degree of discontinuity across the bi-material interface as can be seen in Fig. 3.40b. In order to fully validate the technique, a large material mismatch at the interface is considered i.e. $E_2/E_1 = 100$. In this case also, the stress contour of σ_{YY} is almost continuous as shown in Fig. 3.41a and Fig. 3.42a, while strain contour of ε_{YY} shows a discontinuity at the interface as shown in Fig. 3.41b and Fig. 3.42b.

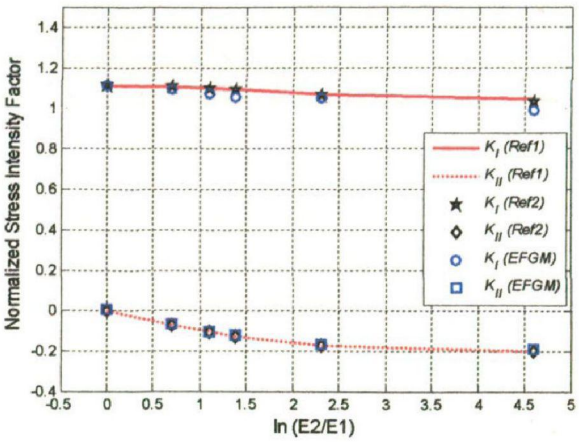

Fig. 3.35: SIFs variation for $2a = 40$ mm

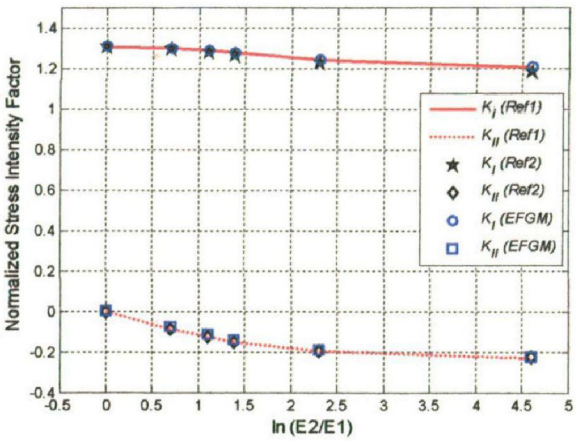

Fig. 3.36: SIFs variation for $2a = 60$ mm

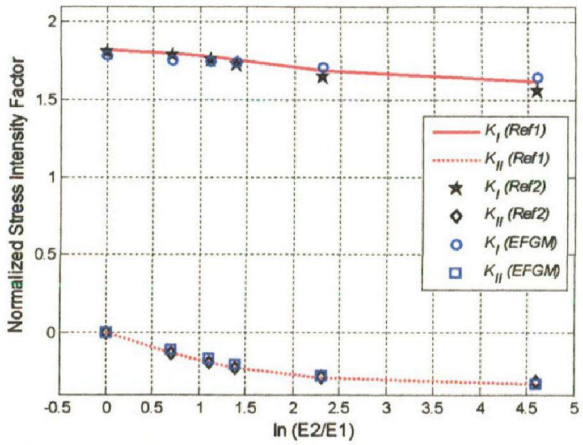

Fig. 3.37: SIFs variation for $2a = 80$ mm

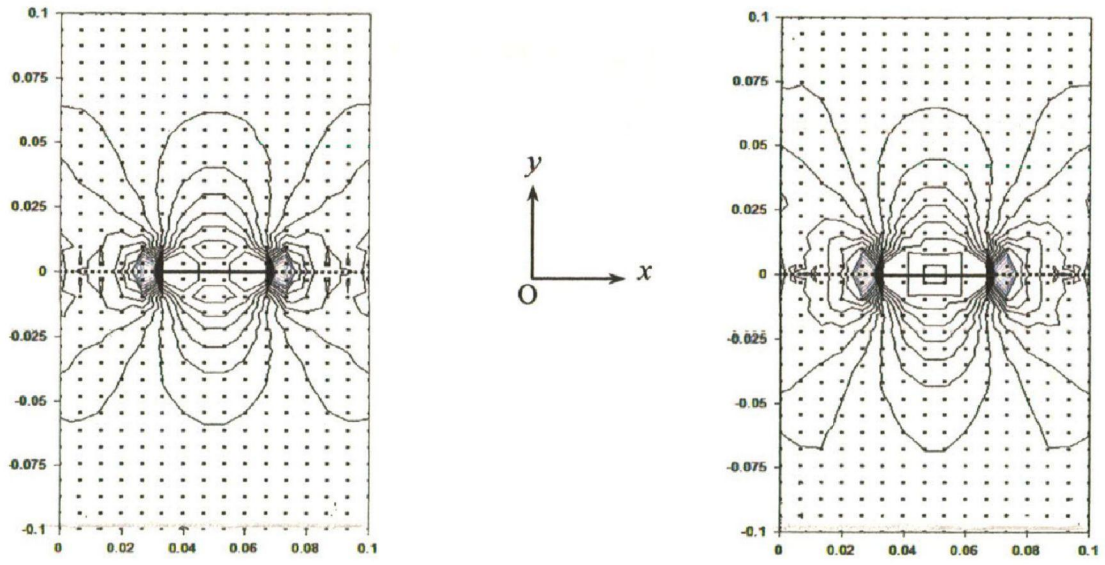

(a) **(b)**

Fig. 3.38: σ_{xx} and ε_{xx} contours for $E_2/E_1 = 1$

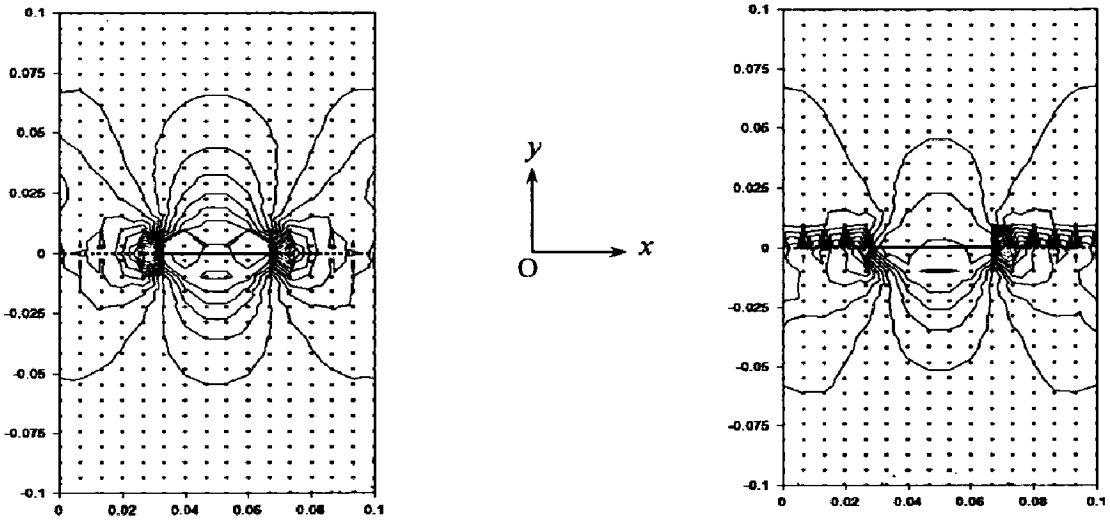

Fig. 3.39: σ_{xx} and ε_{xx} contours for $E_2/E_1 = 2$

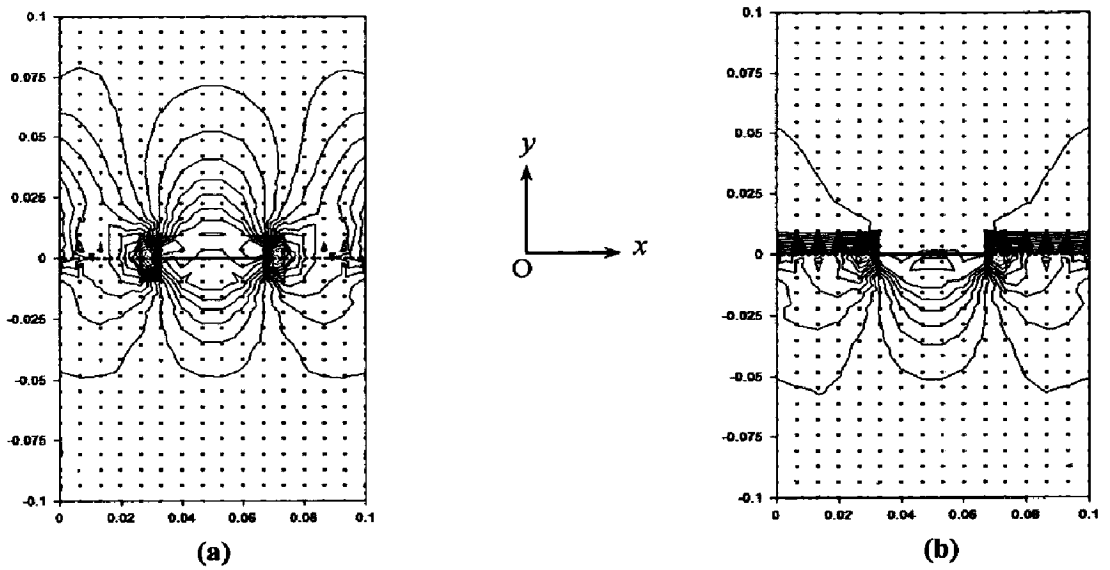

Fig. 3.40: σ_{xx} and ε_{xx} contours for $E_2/E_1 = 10$

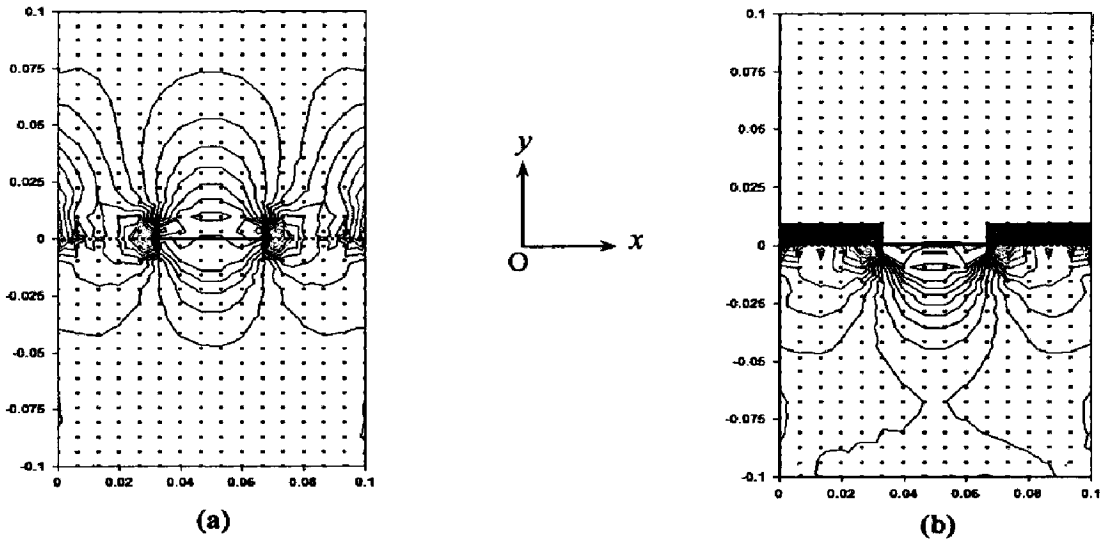

Fig. 3.41: σ_{xx} and ε_{xx} contours for $E_2/E_1 = 100$

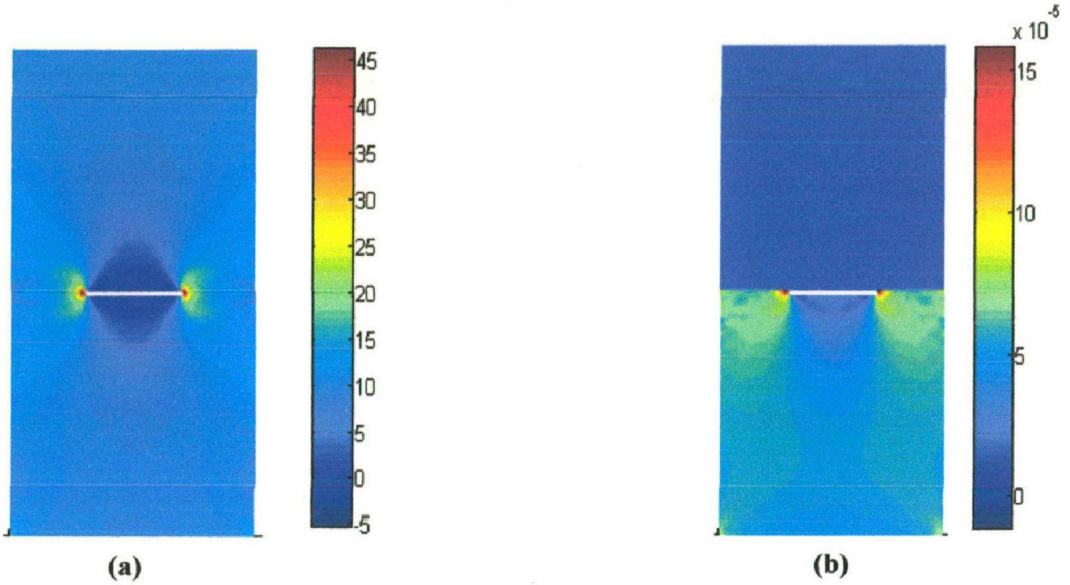

Fig. 3.42: σ_{xx} and ε_{xx} contours for $E_2/E_1 = 100$

3.3.4 Crack-Interfacial Crack Interaction in Bi-material

Fracture usually starts at a defect in the interface, especially at an interface or an edge of the microcrack. The interaction effect of interfacial crack-microcrack plays an important role in determining the fracture behaviour of bi-material. The present problem aims at studying the interaction effect between an interfacial crack and a microcrack parallel to the interface. The effect of transverse and longitudinal interaction distances between interfacial crack and the microcrack is investigated. A two dimensional bi-metallic rectangular plate is considered. The width (W) and height (H) of the plate are taken as 152.4 mm and 203.2 mm respectively as shown in Fig. 3.43a. The length of the interfacial crack (a) and the microcrack (a_1) are taken as 20 mm and 5 mm respectively. The bi-material assembly comprises of two elastic materials. The material properties are listed in Table 3.3. The plate is subjected to a far field tensile stress (σ) of 100 MPa. A plane stress condition is assumed. The domain has been discretized by taking 34 uniformly distributed nodes along both x and y-directions. A 4x4 Gauss quadrature has

been used in each integration cell to evaluate the stiffness matrix. The simulation is performed with an enriched basis function and cubicspline weight function for $d_{max} = 1.5$.

The variation of mode-I stress intensity factor (K_I) of an interfacial crack is shown in Fig. 3.43b as a function of offset $(\bar{h})$. For all values of offset $(\bar{h})$, the tip 1 of the microcrack lies on a line normal to the interfacial crack passing through tip 3. It was observed that for $\bar{h}$ =1.27 mm, K_I has got a maximum value of 32.5 MPa. Increasing the offset value results in a gradual decrease of the stress intensity factor until the offset reaches a value of $\bar{h}$ =5.1mm. Beyond this value of $\bar{h}$, the SIF becomes constant as can be clearly seen from Fig. 3.43b. Thus, one can say that the interaction effect almost disappear beyond a critical distance i.e. $\bar{h}$ =5.1 mm. It was also observed that a larger difference in mechanical properties of bi-materials results in greater interaction effect.

Next, the variation of mode-I stress intensity factor (K_I) of an interfacial crack is studied as a function of a longitudinal movement of the microcrack. For this study, the movement of microcrack is made parallel to x-axis while the interfacial crack remains fixed as shown in Fig. 3.44a. The transverse distance between interfacial crack and microcrack is kept constant at $\bar{h}$ = 1.27 mm. Figure 3.44b represents the variation of K_I with distance, d where, d is distance between the left edge of the plate and centre of microcrack). From the results presented in Fig. 3.44b, it is observed that for $d < 10$ mm, the interaction effect between interfacial crack and microcrack remains constant as can be seen from nearly constant values of K_I. For $d > 10$ mm, the shielding effect of microcrack over the interfacial crack goes on increasing, and reaches its maximum for $d = 20$ mm. Physically this happens when the tip 3 and tip 2 lies in the same vertical line. This configuration leads to a minimum value of $K_I = 11.023$ MPa$\sqrt{\text{m}}$ for the interfacial crack. With further increase in the longitudinal distance d, the value of K_I

gradually increases and reaches a maximum value of 32.50 MPa$\sqrt{\text{m}}$. This happens when the tip3 and tip1 lie in the same vertical line. This becomes a case of nearly collinear crack which causes the well known stress amplification effect. The interaction effect of microcrack over the interfacial crack tends to become smaller with further increase of distance d as can be seen from Fig. 3.44b. For $d > 30$ mm, the value of K_I becomes nearly constant at 26 MPa$\sqrt{\text{m}}$ as the interaction effect between the stress field of microcrack and interfacial crack becomes negligible. In order to check the modeling capability of EFGM and for a clear visualization of crack tip stress field of both interfacial crack and microcrack, the stress and strain contours of σ_{xx}, ε_{xx}, σ_{yy}, ε_{yy} have been generated over the problem domain as can be seen in Figs. 3.45-3.46.

Table 3.3: Bi-material properties

Material No.	Material Name	E (GPa)	ν
1	**Silicon Nitride** (Si_3N_4)	304	0.27
2	**Steel** (S45C)	206	0.30

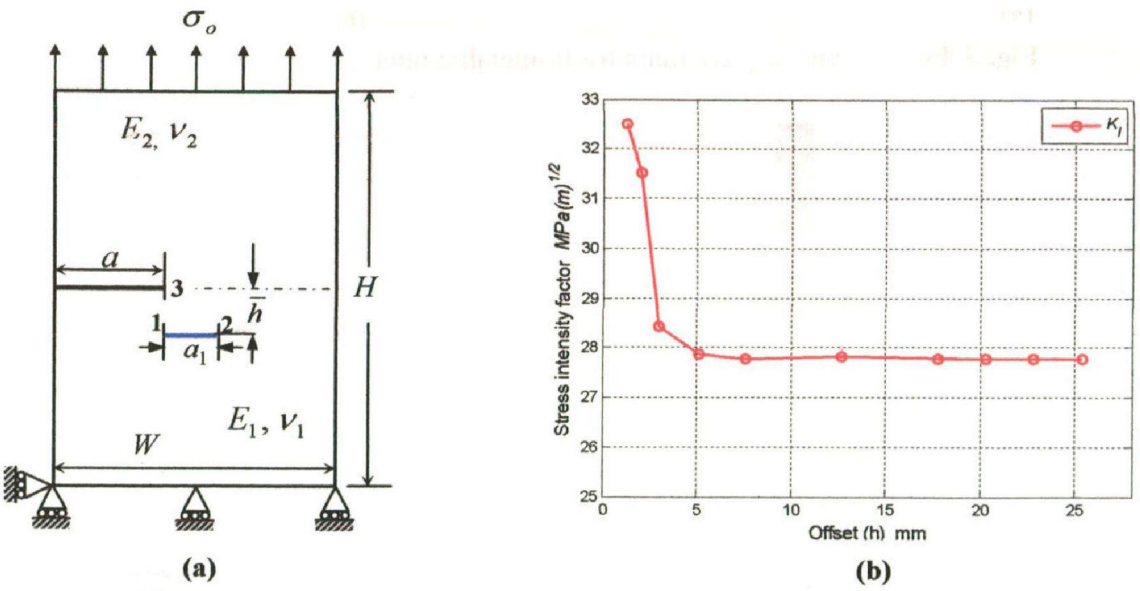

Fig. 3.43: Geometry description and SIF variation with offset ($\bar{h}$)

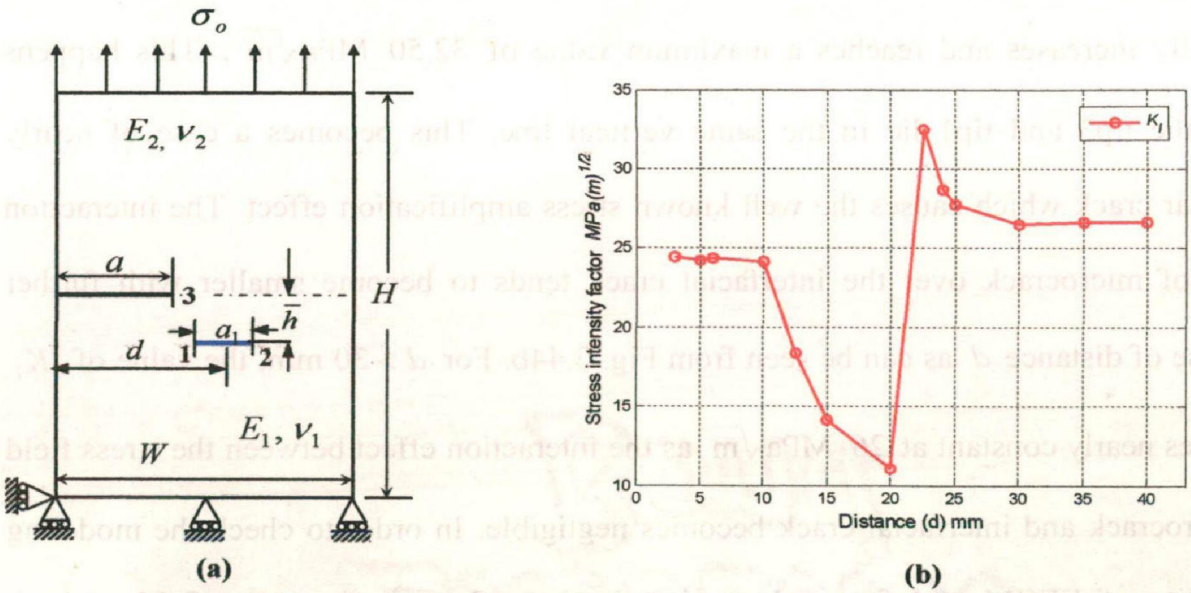

Fig. 3.44: Geometry description and SIF variation with distance (d)

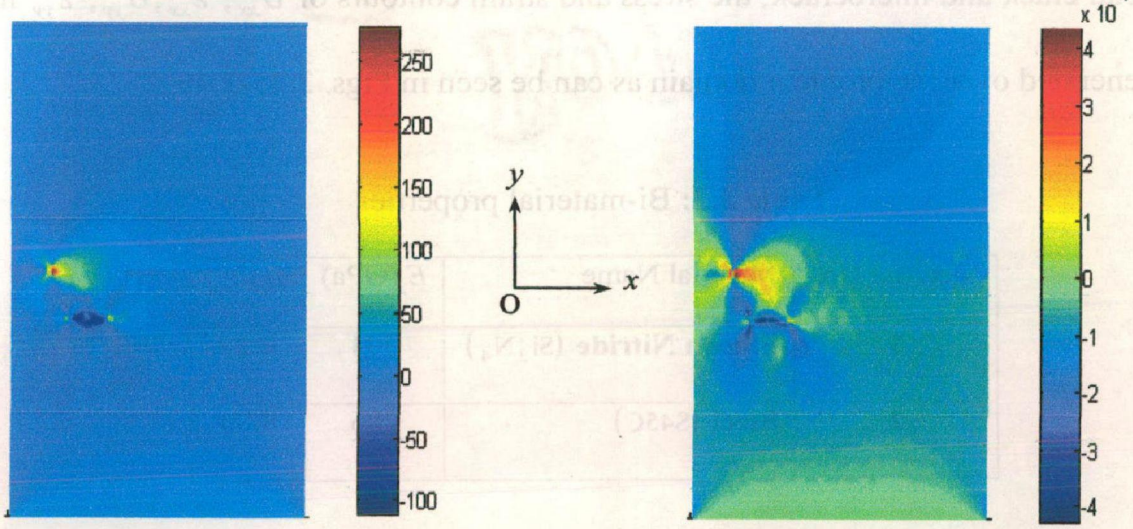

Fig. 3.45: σ_{xx} and ε_{xx} contours for bi-metallic interacting cracks

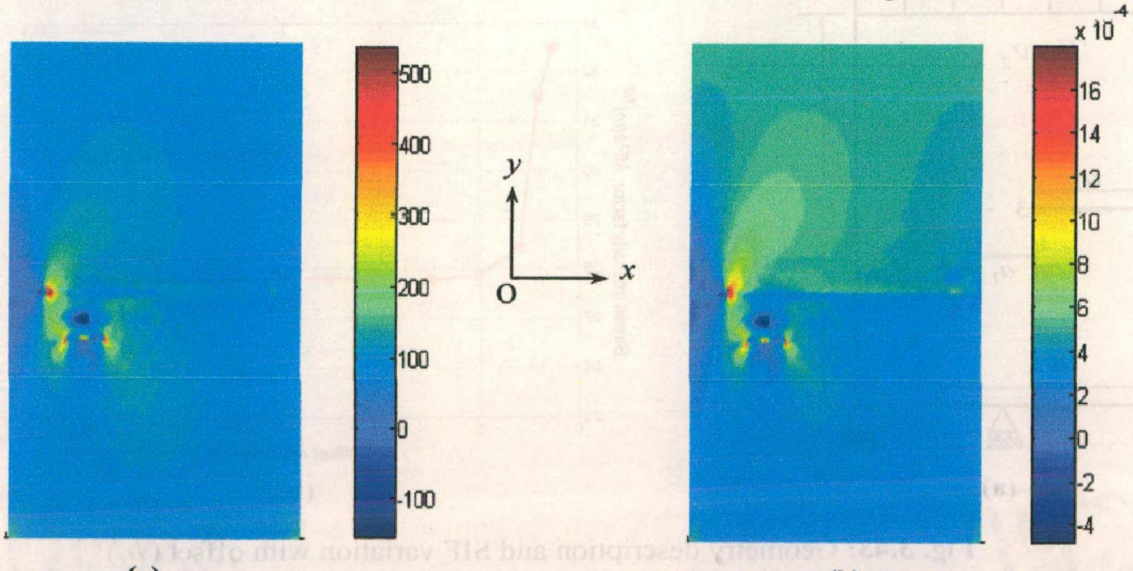

Fig. 3.46: σ_{yy} and ε_{yy} contours for bi-metallic interacting cracks

3.3.5 Sub-interface Crack at Ceramic-metal Interface

Ceramics are the centre of attraction for advanced technological applications owing to there wide range of properties and characteristics. They are used in various industrial sectors such as electronics, electro-mechanics and energetic. Most of the ceramic application requires them to be functionally or structurally interfaced with metallic structures. Joining of metal and ceramic is quite difficult because of their distinctly different properties. With the development of newer bonding techniques in recent years it has become possible upto a certain extent. In the ceramometallic assembly, the sub-interface region is highly prone to defects, which leads to crack initiation due to weakness of bond, variation of material property, etc. Moreover, a bi-material joint typically contains residual stresses that arise due to fabrication process when the assembly is cooled from a high temperature (near to the melting point of metal) to the ambient temperature. A combination of residual stresses with operating stresses can promote the failure of components. In the present problem, the variation of residual stresses near the crack tip in sub interface region of a ceramometallic assembly has been studied and highlighted.

A bi-material assembly comprising of a thin layer of copper sandwiched between alumina has been considered. Geometric dimensions along with boundary constraints are shown in Fig. 3.47. The material properties of the constituents of the bi-material assembly are presented in Table 3.4. A sub-interface crack is considered at a distance of 0.6 mm from the interface S1. The length of crack is taken as $a = 1.8$ mm. A uniform temperature change of $\Delta T = 300^{\circ}C$ is assumed to prevail throughout the problem domain. A regular arrangement of 109×15 nodes has been used for domain discretization. In each integration cell, 4×4 Gauss quadrature has been used to evaluate the stiffness matrix. The EFGM solutions are obtained using an enriched basis function

with the cubicspline weight function with $d_{\max} = 1.5$. The thermal residual stresses result from the mismatch between the thermal expansion coefficients and the stiffness of bonded materials. The distribution of normal residual stresses σ_{xx}, σ_{yy} and shear residual stresses σ_{xy} has been plotted in Figs. 3.48-3.50 along a path normal to the interface and near the crack tip. From these plots, it is observed that the temperature change ΔT, places copper in tension and alumina in compression. The level of normal and shear residual stresses are determined by the temperature of bi-material assembly. The magnitude of compressive stresses is much larger than the tensile stresses. Moreover, the tensile stresses are almost constant while the compression reaches its maximum value in the vicinity of crack tip. A comparison of results shows that the magnitude of normal residual stresses σ_{xx} is less than that of transverse residual stresses σ_{yy} as can be seen from Fig. 3.48 and Fig. 3.49. Although these transverse residual stresses have significant magnitude, they do not contribute to the crack propagation as they are directed along the length of crack. The variation of shear residual stresses σ_{xy} along the interface and near the vicinity of crack tip is shown in Fig. 3.50. From Fig. 3.50, it is observed that a significant tangential residual stress σ_{xy} is present at the crack tip whereas for the points away from crack tip, its magnitude becomes negligible. Figure 3.51 illustrates the variation of J-integral as a function of temperature gradient for different values of crack length (a). For a particular crack length, it is observed that with an increase in temperature at the time of manufacturing, there is a significant variation in J-integral. However, for a small change in temperature, the value of J-integral becomes independent of crack length. Indeed, an increase in temperature gradient causes an increase in residual stresses which leads to intensification of J-integral.

Table 3.4: Properties of bi-material assembly constituents

Material	E (GPa)	ν	$\alpha \times 10^{-6}$
Copper	113.5	0.345	16.75
Alumina	385.8	0.245	7.12

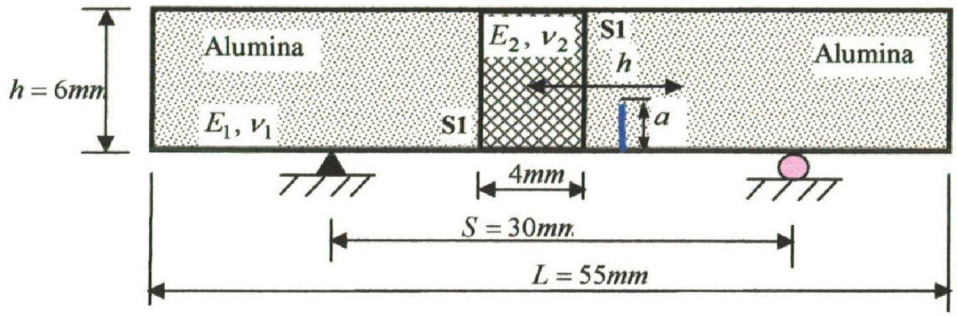

Fig. 3.47: Geometry description for ceramic-metal interface crack

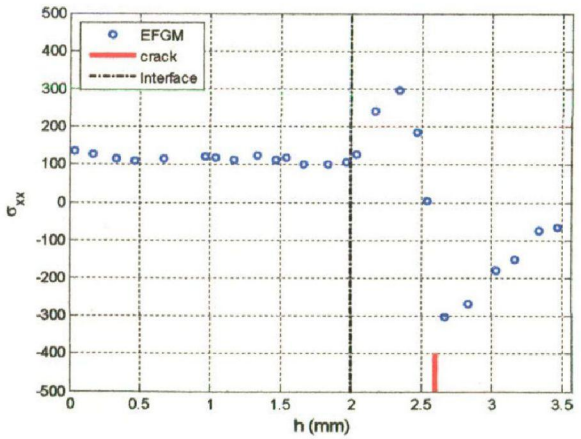

Fig. 3.48: Variation of σ_{xx} with distance (h)

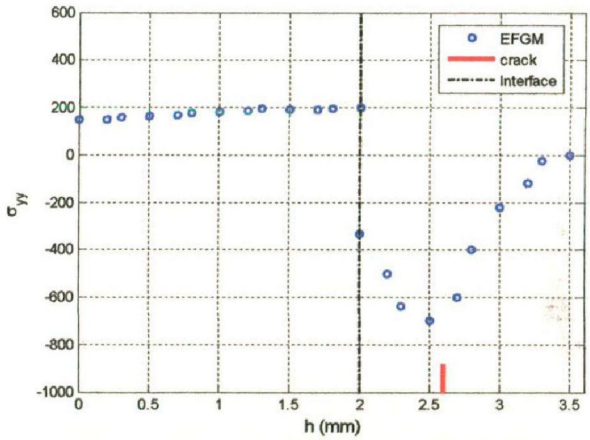

Fig. 3.49: Variation of σ_{yy} with distance (h)

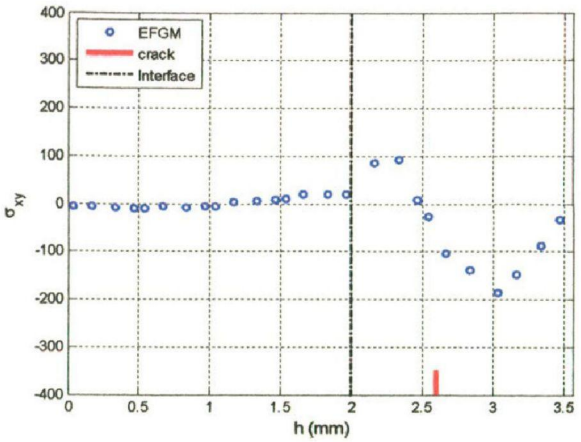

Fig. 3.50: Variation of σ_{xy} with distance (h)

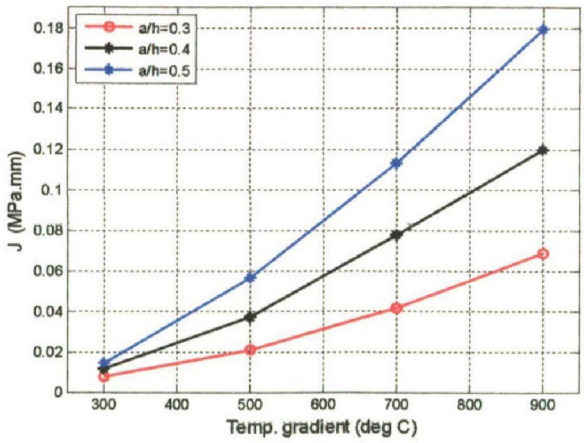

Fig. 3.51: Variation of J with temp. (ΔT)

3.4 CONCLUSION

In this chapter, the EFGM has been successfully implemented to solve the problems of weak and strong discontinuities. A comparative study of various techniques for modeling weak discontinuity revealed that the Jump function criterion is the most promising criterion. A new criterion is proposed for modeling bi-material interfacial cracks using Jump function approach. The new criterion was found quite effective in reducing the computational cost as it involves only four enrichment terms in the basis function instead of twelve enrichment terms. Further, some additional problems of bi-material interfacial cracks under mechanical/thermal loading were simulated in order to check the robustness of the proposed criterion, and it was noticed that the proposed criterion is quite successful in handling a wide range of bi-material interfacial crack problems.

Chapter 4

SIMULATION OF MULTIPLE INTERACTING CRACKS

4.1 INTRODUCTION

Cracks are inevitable in all engineering components and structures. Complex loading conditions in actual working conditions may result in either the propagation of pre-existing cracks or may initiate new cracks in the structures. The final fracture of a component is always initiated by multi site cracks. The crack tip stress fields of all such cracks interact with one another and lead to formation of one dominant crack which paves the way for final failure of a component. As such, all important failure phenomenons such as stress corrosion cracking, hydrogen embrittlement, and creep micro cracking are directly linked to the crack interactions (Muravin and Turkel, 2006a). Interaction among multiple cracks is one of the most important but less investigated phenomena in fracture mechanics. An accurate evaluation of stress intensity factor is quite essential for the prediction of failure and crack growth rate. Thus, the study of crack interactions (Muravin and Turkel, 2006a; Loehnert and Belytschko, 2007) under thermal/mechanical load is of great importance as it helps us to understand some basic phenomenon such as

- The effect of micro and macro cracks in non-uniform materials e.g. composites, concrete, piezoelectric;
- Amplification and shielding effect (Hori and Nemat, 1983) of cracks;
- Direction of crack propagation and crack branching;

Simulation of multiple interacting cracks by conventional finite element method requires an enormous mesh refinement near each crack tip along with use of singular

elements near the crack tips. Moreover, simulation of moving discontinuities requires tedious and time consuming remeshing at every time step. Even with the use of adaptive remeshing, the mapping of variables is a computationally expensive task and a source of cumulative numerical errors. Some efforts have been made in the past to study the multiple crack interactions. Horii and Nemat (1983) estimated the stress intensity factor for interacting cracks. Chen (1984) studied the general case of multiple crack problems in an infinite body. Kachanov and Laures (1989) solved some three-dimensional problems of strongly interacting arbitrarily located penny shaped cracks. Wu and Chudnovsky (1993) studied the effect of micro-crack array on stress intensity factor of the main crack. Kachanov (1985) proposed a simple technique for the stress analysis of elastic solids with cracks. Lam *et al.* (1993) simulated the interaction among micro-cracks and main crack in semi infinite medium. A most recent review of micro/macro crack interaction problems is given by Tamuzs and Petrova (2002). Budyn *et al.* (2004) devised a method for the study of multiple growing cracks, and their interactions in brittle materials without re-meshing, and Zi *et al.* (2004) further used this method for the fatigue analysis of multiple cracks. Loehnert and Belytschko (2007) investigated the amplification and shielding effect of micro crack on the macro crack. Muravin and Turkel (2006a) investigated the crack interactions by modifying the weight functions for each crack using EFGM. This criterion is not simple from the implementation points of view as each additional crack requires special treatment of weight function. In spite of a lot of analytical and numerical research, not much effort has been made to study the effect of crack interactions using meshfree methods.

In the present work, EFGM has been used to analyze crack interactions in linear elastic fracture mechanics problems under thermal/mechanical loads. Few modifications have been suggested in the intrinsic enriched basis to incorporate the interaction effect. A

comparison of the results obtained by diffraction criterion (Fleming *et al.* 1997; Organ *et al.* 1996; Belytschko and Fleming, 1999), analytical solution (Anderson, 2005) and FEM shows that the modified intrinsic enrichment is quite effective in capturing the effect of crack interactions. A new partial domain enrichment criterion has also been suggested to simulate cracks lying in non-convex domains. This proposed criterion not only eliminates the error in results due to non-convexity of the domains, but also reduces the overall computational cost of the method.

4.2 PROBLEM FORMULATION

Consider a two-dimensional domain with small displacements in the domain Ω bounded by Γ as shown in Fig. 4.1. The governing equilibrium equations are given as

$$\nabla.\boldsymbol{\sigma} + \mathbf{b} = 0 \text{ in } \Omega \tag{4.1}$$

along with the following essential and natural boundary conditions

$$\mathbf{u} = \bar{\mathbf{u}} \text{ on } \Gamma_u \tag{4.2}$$

$$\boldsymbol{\sigma}.\bar{\mathbf{n}} = \bar{\mathbf{t}} \text{ on } \Gamma_t \tag{4.3}$$

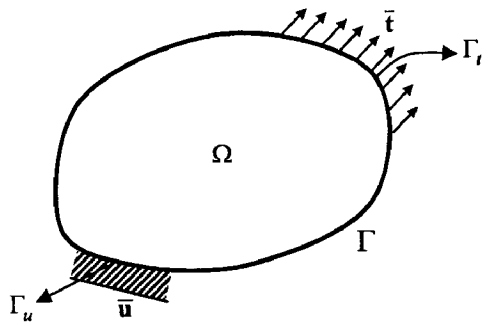

Fig. 4.1: Domain along with essential and natural boundary conditions

where, $\boldsymbol{\sigma}$ is the stress tensor which is defined as $\boldsymbol{\sigma} = D(\boldsymbol{\varepsilon} - \boldsymbol{\varepsilon}_T)$, D is the linear elastic material property matrix, ε is the strain vector, $\boldsymbol{\varepsilon}_T$ is the thermal strain vector, $\mathbf{b}$ is the body force vector, $\mathbf{u}$ is the displacement vector, $\bar{\mathbf{t}}$ is the traction force and $\bar{\mathbf{n}}$ is the unit

normal. For the case of plane stress in an isotropic material with coefficient of thermal expansion β subjected to a temperature change ΔT, the thermal strain matrix is given by

$$\varepsilon_T = \begin{Bmatrix} \beta\Delta T \\ \beta\Delta T \\ 0 \end{Bmatrix} \tag{4.4}$$

Enforcing essential boundary conditions using Lagrange multiplier approach, and applying variational principle, the following discrete equations are obtained using Eq. (2.11):

$$\begin{bmatrix} \mathbf{K} & \mathbf{G} \\ \mathbf{G}^T & 0 \end{bmatrix} \begin{Bmatrix} \mathbf{u} \\ \boldsymbol{\lambda} \end{Bmatrix} = \begin{Bmatrix} \mathbf{f} \\ \mathbf{q} \end{Bmatrix} \tag{4.5}$$

$$\text{where }, K_{IJ} = \int_{\Omega} \mathbf{B}_I^T \mathbf{D} \mathbf{B}_I \, d\Omega, \quad f_I = (f_I)_{\text{mech}} + (f_I)_{\text{thermal}} \tag{4.6}$$

$$(f_I)_{\text{mech}} = \int_{\Gamma_t} \bar{\mathbf{t}} \Phi_I \, d\Gamma_t, (f_I)_{\text{thermal}} = \int_{\Omega} \mathbf{B}_I^T \mathbf{D} \boldsymbol{\varepsilon}_T \Phi_I \, d\Omega, G_{IK} = -\int_{\Gamma_u} \Phi_I \mathbf{N}_K \, d\Gamma_u, \; q_K = -\int_{\Gamma_u} \mathbf{N}_K \bar{u} \, d\Gamma_u,$$

$$\mathbf{B}_I = \begin{bmatrix} \Phi_{I,x} & 0 \\ 0 & \Phi_{I,y} \\ \Phi_{I,y} & \Phi_{I,x} \end{bmatrix}, \; \mathbf{N}_K = \begin{bmatrix} N_K & 0 \\ 0 & N_K \end{bmatrix}, \; \mathbf{D} = \frac{E}{1-\nu^2} \begin{bmatrix} 1 & \nu & 0 \\ \nu & 1 & 0 \\ 0 & 0 & (1-\nu)/2 \end{bmatrix} \text{ for plane stress}$$

4.3 INTRINSIC ENRICHMENT FOR SINGLE CRACK

In enrichment based criterion (Fleming *et al.*, 1997), the presence of a crack is ensured by enrichment terms i.e. by adding extra terms either in the basis function or in the approximation function. In this criterion, the presence of crack is modeled by use of enrichment functions. In the intrinsic enrichment criterion, the meshfree standard basis functions are intrinsically enriched by including the near-tip asymptotic field to solve problems with strong discontinuities such as cracks. The choice of enrichment functions depends on the coarse mesh accuracy desired. For higher accuracy, one can include the full asymptotic field, while for higher speed at some cost of accuracy; only $\sqrt{r}$ can be

included in the basis. A regular/standard enriched basis function can be given as

$$\mathbf{P}^T(\mathbf{x}) = \left[\underbrace{1,\ x,\ y}_{\substack{\text{standard} \\ \text{basis}}}, \underbrace{\sqrt{r}\cos\frac{\theta}{2}, \sqrt{r}\sin\frac{\theta}{2}, \sqrt{r}\sin\frac{\theta}{2}\sin\theta, \sqrt{r}\cos\frac{\theta}{2}\sin\theta}_{\text{enrichment terms}} \right] \tag{4.7}$$

where, $\mathbf{P(x)}$ is the enriched basis function, r and θ are the local crack tip parameters. First three terms of Eq. (4.7) represents the standard basis function $(1, x, y)$ and remaining four terms obtained from the crack tip solution makes up the enrichment part.

A single edge crack along with an evaluation point and local crack tip parameters (r, θ) is shown in Fig. 4.2. In the single crack configuration, the enrichment terms are to be added with reference to the only crack tip present in the domain at the evaluation/Gauss point during numerical integration, which can be easily done either for a part of the region near crack tip or over the entire solution domain.

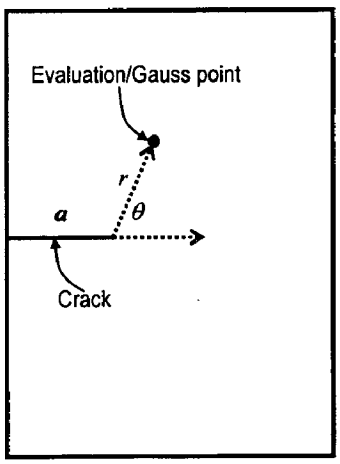

Fig. 4.2: Single edge crack along with crack tip parameters

The above intrinsic enrichment criterion works well only for single crack, but can not be used for multiple crack tip configurations.

4.4 INTRINSIC ENRICHMENT FOR MULTIPLE CRACKS

The intrinsic enrichment criterion is based on the addition of extra terms in the standard basis function. These additional terms are generally obtained from the theoretical background of the problem. The simulation of a crack using intrinsic enrichment requires four additional functions in the basis corresponding to each crack tip, whereas the simulation of multiple cracks using intrinsic enrichment criterion will require many enrichment terms depending upon the number of crack tips present in the domain (Muravin, 2003). Hence, the simulation of multiple cracks using this approach will be very expensive from the computational time point of view. Therefore, a simple and efficient method has been proposed to simulate the multiple cracks.

4.4.1 Modified Intrinsic Enrichment Criterion

In case of a single crack, the enrichment is done for the each evaluation/Gauss point of the domain, which consists of four additional terms related with the only crack present in the domain. Therefore, in the present work, regular intrinsic enrichment criterion has been modified for handling multiple cracks. According to the proposed criterion, the enrichment decision with reference to a particular crack tip has to be made i.e. it is to be ensured that the additional terms need to be added with respect to a particular crack tip from the all the available crack tips in the domain. This decision is made on the basis of normalized distances between the evaluation/Gauss points and the crack tips. According to this criterion, the distances of an evaluation point from all the crack tips are evaluated and normalized by their corresponding crack lengths, and then the enrichment is decided on the basis of minimum normalized distance. For example, three cracks of length a_1, a_2 and a_3 are taken as shown in Fig. 4.3, and the location of a particular evaluation/Gauss point with respect to different crack tips are (r_1, θ_1), (r_2, θ_2) and (r_3, θ_3) respectively.

Now at particular evaluation point during numerical integration over the domain, the enrichment terms are to be added with respect to the only one crack tip from all available crack tips. This decision of enrichment with respect to a particular crack tip is based on the normalized distances of each crack tip i.e. r_i / a_i with $i = 1, 2, 3$. The enrichment of the basis function with respect to a particular crack tip is decided on the basis of minimum normalized distance. This criterion works well while studying and analyzing the interaction effect of similar size cracks, but can not handle significantly unequal size cracks properly. Hence, the existing intrinsic enriched criterion required further improvement for the study of both nearly equal and significantly unequal size multiple cracks. Therefore, a new weighted criterion was established, which can be used to study the interaction effect of both nearly equal and significantly unequal size multiple cracks.

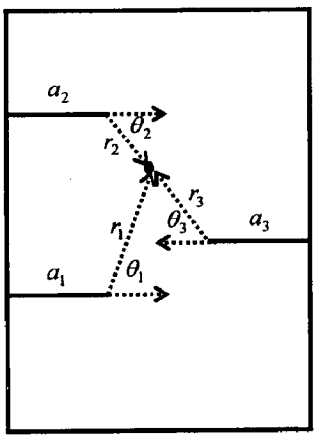

Fig. 4.3: Three edge cracks along with crack tip parameters

4.4.2 Weighted Intrinsic Enrichment Criterion

In the intrinsic enrichment criterion proposed in the previous section, it becomes difficult to handle significantly unequal size multiple cracks. Therefore, this enrichment criterion is further modified to handle multiple cracks of equal/unequal sizes. In the proposed criterion, all cracks contributes to the stiffness matrix (K_{IJ} in Eq. 4.6) at each evaluation point in contrast to the existing criterion where only one crack contributes to K_{IJ} at each

evaluation point. For example, three cracks of length a_1, a_2 and a_3 are taken as shown in Fig. 4.3, and the location of a particular evaluation/Gauss point with respect to various crack tips are (r_1,θ_1), (r_2,θ_2) and (r_3,θ_3) respectively. Now, during numerical integration at a particular evaluation/Gauss point, enriched basis and shape functions are constructed separately for each crack tip. Once the shape functions are obtained using enriched basis for each crack tip at an evaluation point, then the contribution of each crack tip to the stiffness matrix is decided on the basis of the normalized distances i.e. $d_i = r_i / a_i$ with $i = 1, 2, 3$. Mathematically, total K_{IJ} at an evaluation/Gauss point (in Eq. 4.6) is evaluated as

$$[K_{IJ}]_{total} = [K_{IJ}]_1 \times R_1 + [K_{IJ}]_2 \times R_2 + \ldots\ldots\ldots\ldots [K_{IJ}]_N \times R_N = \sum_{i=1}^{N} [K_{IJ}]_i \times R_i \qquad (4.8)$$

where, N denotes the number of cracks present in the domain, R_i is a parameter which decides the contribution of a particular crack, and $[K_{IJ}]_i$ is evaluated by Eq. 4.6 as $[K_{IJ}]_i = \int_{\Omega} \mathbf{B}_I^T \mathbf{D} \mathbf{B}_J \, d\Omega$ with a different $\mathbf{B}_I$ for each crack. The value of R_i in Eq. 4.8 is numerically evaluated as

$$R_i = \frac{S_i}{\sum_{j=1}^{N} S_j} \quad \text{with} \quad \sum_{i=1}^{N} R_i = 1 \qquad (4.9)$$

where, $S_i = d_i^{\tilde{C}}$ and d_i represents normalized crack tip distance ($d_i = r_i / a_i$) for a particular crack and $\tilde{C}$ is a predefined constant, which is calculated by performing the sensitivity analysis of $\tilde{C}$, and its acceptable range is found to be $-50 < \tilde{C} < -100$.

As the proposed criterion considers the effect of all cracks at each evaluation point, it can be used to simulate both equal and unequal size multiple cracks. The existing intrinsic enrichment criterion can be seen as a particular case of the proposed criterion

where at each evaluation point, the contribution of one crack is taken as 100%, while the contribution of other cracks is taken as zero.

4.5 RESULTS AND DISCUSSIONS

4.5.1 Crack Interactions under Mechanical Loading

The dimensions of the cracked body used in the present study are taken as $H = 200$ mm, $W = 100$ mm as shown in Fig. 4.4. The material selected for present study is ASTM 36 steel (Beer *et al.*, 2002) with modulus of elasticity (E) = 200 GPa, Poisson's ratio (ν) = 0.3. A far field stress, (σ_o) = 100 MPa is applied at the top edge.

Few cases of edge crack problems have been solved to study the effect of crack interactions. The first crack has been taken at a distance of $H/2$ i.e. 100 mm from the bottom with an orientation of $\alpha = 0°$ ($\alpha = 0°$ implies that the crack is parallel to the x - axis, Fig. 4.4), whereas, the second and third crack (if present) has been placed at different locations and orientation to study and analyze the effect of crack interactions. To validate the EFGM results, single edge crack problem has been solved under mode-I loading by both intrinsic enrichment and diffraction criterion using multiple crack weight approach (Muravin and Turkel, 2006a).

Single edge crack along with its geometry and boundary conditions is shown in Fig. 4.4. The bottom edge has been constrained along y-direction, and an external far field stress is applied at the top edge as shown in Fig. 4.4. The problem domain has been discretized using 800 uniformly distributed nodes for intrinsic enrichment while for diffraction criterion, additional nodes has been defined at the crack surface and crack tip. Six point Gauss quadrature (Dolbow and Belytschko, 1999) has been used for the numerical integration (Dolbow and Belytschko, 1998) of the Galerkin weak form. A plane stress condition has been assumed. The values of mode-I and mode-II stress

intensity factors i.e. K_I and K_{II} have been calculated using domain based interaction integral (Dolbow and Belytschko, 1999; Dag, 2006) approach.

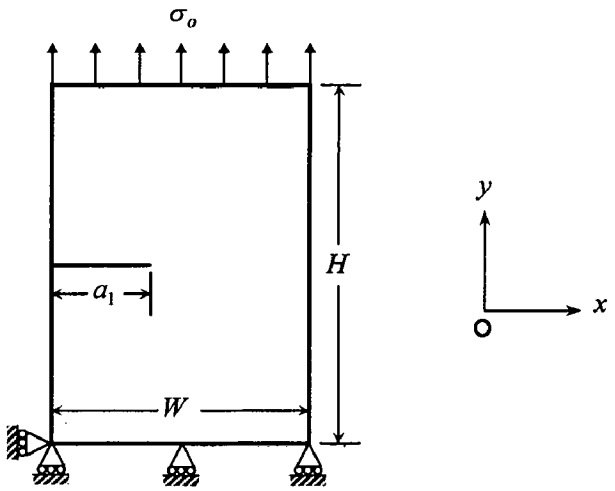

Fig. 4.4: Problem geometry along with boundary conditions

The results have been obtained by EFGM for various crack configurations. Figure 4.5a shows a single edge crack configuration subjected to external far field stress. Both mode-I and mode-II stress intensity factors have been calculated at the crack tip for different values of crack length a_1 as presented in Fig. 4.5b. A comparison of results obtained by both diffraction criterion and intrinsic enrichment shows a similar trend of K_I and K_{II} but the values of K_I obtained by intrinsic enrichment are closer to the analytical solution (Anderson, 2005) as compared to diffraction criterion as can be clearly seen from Fig. 4.5b.

Figure 4.6a shows two cracks of equal length $(a_1 = a_2 = 40\,\text{mm})$ on the same edge of cracked specimen. The first crack has fixed orientation along the width while the orientation of the second crack is varied. Both K_I and K_{II} are calculated at the tip of the first crack. Figure 4.6b presents the variation of the stress intensity factors of the first crack with the orientation of the second crack. It can be seen that K_I shows an

increasing trend with the increase of α with a minimum value of 59.92 MPa$\sqrt{m}$ (Intrinsic enrichment) while K_{II} has a maximum value of 11.85 MPa$\sqrt{m}$ (Intrinsic enrichment) for α=0°, which tends to zero with the increase of α. At higher values of α, the tip of the first crack is far away from the second crack tip, thereby K_I of the first crack remains almost unaffected. However, when α is small, K_I of the first crack is reduced due to the presence of lower stress region below second crack. Figure 4.6b also shows that the values obtained by modified intrinsic enrichment are in good agreement with those obtained by diffraction criterion.

The effect of offset i.e. d (as shown in Fig. 4.7a) between two parallel cracks of equal length $(a_1 = a_2 = 40\,\text{mm})$ lying on the same edge has been analyzed next. Figure 4.7b shows the effect of offset on the stress intensity factors of first crack (lower crack). From the results presented in Fig. 4.7b, it can be seen that the presence of equal length second crack lowers the value of K_I of the first crack while K_{II} becomes non-zero. With the increase of offset, K_I increases continuously, and approaches a value corresponding to a single crack only. The value of K_{II} is found to be maximum at $d = 20$ mm and thereafter decreases with the increase in offset. The results obtained by both diffraction and modified intrinsic enrichment approaches are quite close to each other, and have a maximum 2.4% difference in values of K_I.

Figure 4.8a shows two parallel cracks configuration both lying on the same edge. The length of the first crack (a_1) i.e. lower crack is taken as 40 mm, while the length of second parallel crack (a_2) i.e. upper crack is varied. The distance between two parallel cracks is taken to be equal to length of lower crack i.e. $d = a_1$. The stress intensity factors have been evaluated at the tip of first crack. For $a_2 < a_1/2$, K_I of first crack has been found nearly same as that of a same length single edge crack (Fig. 4.8b). The value of

K_I keeps on decreasing and K_{II} shows an increasing trend with the increase in the length of second crack. The decreasing trend in value of K_I of lower crack is due to the fact that with the increase in length of upper crack it tends to become the major crack there by reducing the stress concentration at the tip of lower crack.

A specimen with two cracks on the opposite edges has been considered as shown in Fig. 4.9a. The crack on left edge is kept at $\alpha = 0°$ with the horizontal, while the crack on right edge has a variable orientation (α). Both cracks have equal length i.e. $a_1 = a_2 = 40\,\text{mm}$. The values of stress intensity factors have been calculated at the tip of first crack (tip of the left edge crack). K_I shows an increasing trend with the increase in α, while K_{II} reaches its peak value around $\alpha = 20°$, and thereafter nearly approaches zero at $\alpha = 60°$ as shown in Fig. 4.9b. At $\alpha = 0°$ the value of K_I calculated by diffraction criterion is $53.10\,\text{MPa}\sqrt{\text{m}}$ while the proposed intrinsic enrichment criterion predicts nearly a same value i.e. $52.92\ \text{MPa}\sqrt{\text{m}}$. For $\alpha > 50°$, intrinsic enrichment criterion predicts SIF values on higher side as compared to diffraction criterion, and a maximum difference of 5% is noticed between them.

The effect of offset (d) between two parallel cracks of same length i.e. $a_1 = a_2 = 40\,\text{mm}$ lying on opposite edges (Fig. 4.10a) has been analyzed next. K_I and K_{II} have been evaluated at the tip of left edge crack. For an offset of $d = 0$, the geometry behaves as two collinear cracks of equal length, and both diffraction and intrinsic enrichment criterions predicts an equal K_I values i.e. $53.10\ \text{MPa}\sqrt{\text{m}}$ which are quite close to the analytical value (Anderson, 2005) i.e. $53.43\ \text{MPa}\sqrt{\text{m}}$. For offset less than 30 mm, the values predicted by both criteria are close to each other but for offset greater than 30 mm, the value predicted by intrinsic enrichment is more as compared to

diffraction. Figure 4.10b shows that the variation of K_I and K_{II} predicted by diffraction criterion and intrinsic enrichment are same.

Three different cases of collinear edge cracks have been considered. Figure 4.11a shows the configuration where length of both cracks is incremented by equal magnitude. The values of K_I and K_{II} have been evaluated at the tip of left edge crack. A comparison of results obtained by diffraction criterion and intrinsic enrichment with that of analytical solution suggests that intrinsic enrichment predicted values are close to the analytical solution as can be clearly seen from Fig. 4.11b. The values of K_{II} remain nearly zero for all values of crack length.

For the second case of collinear cracks, the length of left edge crack is kept constant i.e. 40 mm, while the length of right edge crack is varied continuously as shown in Fig. 4.12a. The values of K_I and K_{II} are evaluated at the tip of left edge crack. For smaller values of a_1, the value of K_I for left edge crack is higher but as a_1 increases, the value of K_I goes on decreasing as can be seen in Fig. 4.12b. Both diffraction and intrinsic enrichment criteria predict a similar trend of K_I; although for smaller values of crack length a_1, intrinsic enrichment predicts SIF values are on higher side as compared to diffraction criterion.

In third case of two collinear cracks, the length of right edge crack is kept constant i.e. 40 mm, while the length of left crack i.e. a_1 is changed as shown in Fig. 4.13a. The values of K_I and K_{II} have been evaluated at the tip of left edge crack. Both diffraction and intrinsic enrichment predict nearly equal values of SIF as can be clearly seen from Fig. 4.13b. The negative values of K_I shows the dominance of right edge crack for smaller values of crack length a_1. The results obtained for different crack configurations

show that proposed intrinsic enrichment criterion works well, and produces better results as compared to the diffraction criterion.

Next, the intrinsic enrichment is used to solve three edge crack problems subjected to plane stress condition. Different crack orientations have been chosen for this study and the results obtained by modified intrinsic enrichment criterion are compared with those obtained by FEM. Figure 4.14a shows three edge crack configuration with one crack on left edge and two cracks on right edge. Two right edge cracks were placed at an offset of $d = 40\,\text{mm}$. The values of K_I and K_{II} have been evaluated at the tip of left edge crack. The values of crack length are kept same for all three cracks, and then same increment in the crack length is made in all three cracks for this study. A finite value of K_I is obtained at the crack tip, while the value of K_{II} nearly remains nearly zero. The SIF values and their trend show a close proximity with FEM solution as shown in Fig. 4.14b.

The effect of offset distance between two right edge cracks on K_I and K_{II} of the left edge crack has been considered in Fig. 4.15a. The length of all three cracks chosen for this analysis is taken as 40 mm. The values of K_I and K_{II} have been evaluated at the tip of left edge crack. For smaller offset, the results obtained by intrinsic enrichment estimates K_I on lower side in comparison to FEM but with the increase in offset, the results comes closer to each other as can be seen in Fig. 4.15b.

A similar geometry having three cracks as above is considered again. The lengths of all three cracks are equal i.e. 40 mm. The effect of inclination of the two right edge cracks on left edge crack is shown in Fig. 4.16a. The inclination (α) has been changed in such a way that tip of two right edge cracks move away from each other. The values of K_I and K_{II} are evaluated at the tip of left edge crack. The results show that with the increase in α, the values of K_I keep on increasing, while K_{II} remains nearly zero for

all values of α. The results obtained by both intrinsic enrichment and FEM are almost similar for all values of α as shown in Fig. 4.16b.

Another three cracks configuration is considered as shown in Fig. 4.17a, where the inclination of right edge cracks has been taken in such a way that the crack tip approaches to each other. The values of K_I and K_{II} have been evaluated at the tip of left edge crack. K_I values initially have a decreasing trend up to 30° crack inclination, then an increasing trend up to 70° inclination and become constant after that as shown in Fig. 4.17b. The results obtained by intrinsic enrichment are quite close to the FEM solution.

In order to have a clear visualization of crack tip stress field and interaction effect of second crack, the contours of stress component σ_{yy} have been plotted over the specimen geometry. For inclined cracks, three different cases with the inclination of 10°, 30° and 50° have been considered as shown in Fig. 4.18 & 4.19. The interaction effect has been found to be more prominent with lower angle of inclination. For specimen geometry with two parallel cracks, the contours have been plotted for 30 mm, 50 mm and 70 mm offset as shown in Fig. 4.20. Figure 4.21 shows the effect of crack interaction for two parallel cracks lying on the opposite faces. In this case, the length of two cracks has been kept constant i.e. 40 mm each while the offset has been changed from 0 to 70 mm. The contours have been plotted for three different values of offset i.e. 30, 50 and 70 mm. Figure 4.22 shows contour plots over the domain for two collinear cracks. Three different models have been considered with crack tip distance equal to 40, 30 and 20 mm respectively. Plot shows that the interaction effect tends to fade away when the distance between crack tips is increased. It can be clearly observed from these contours that both angular and spatial location of crack have a prominent effect over the degree of interaction which leads to distortion of the contour lines over the problem domain.

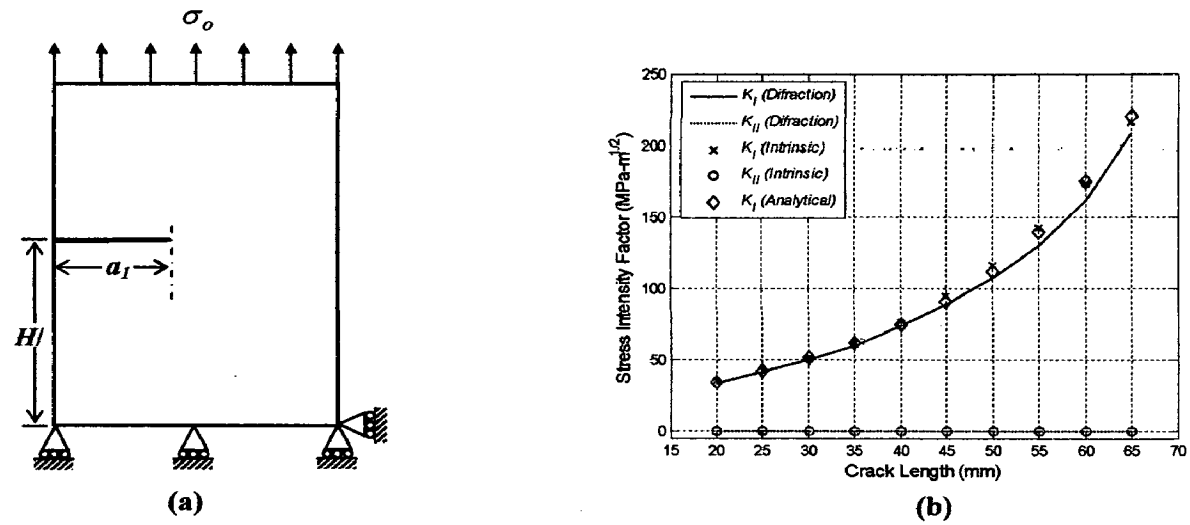

Fig. 4.5: Problem geometry and variation of SIF with crack length

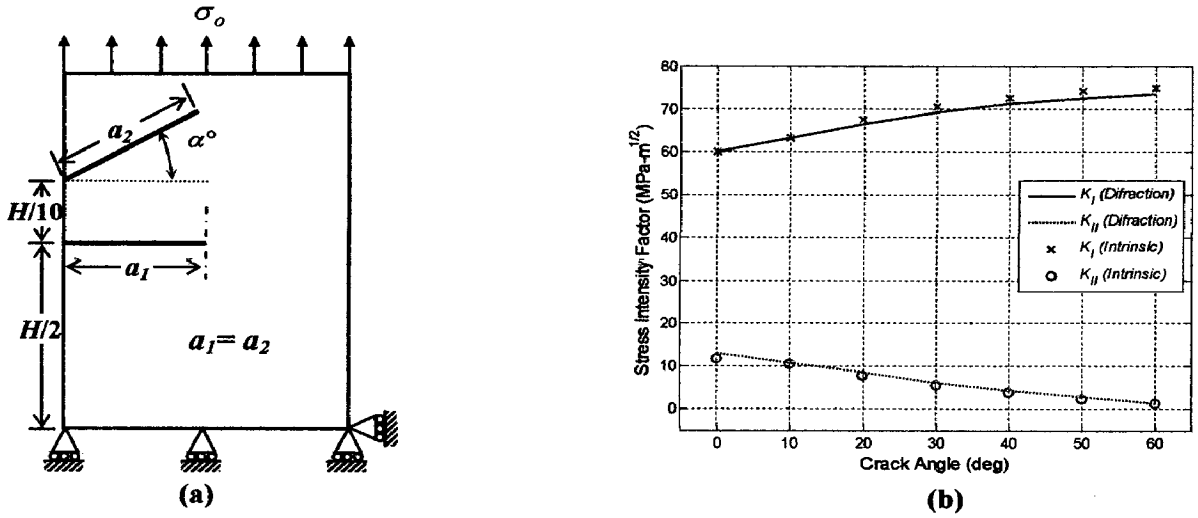

Fig. 4.6: Problem geometry and variation of SIF with crack inclination

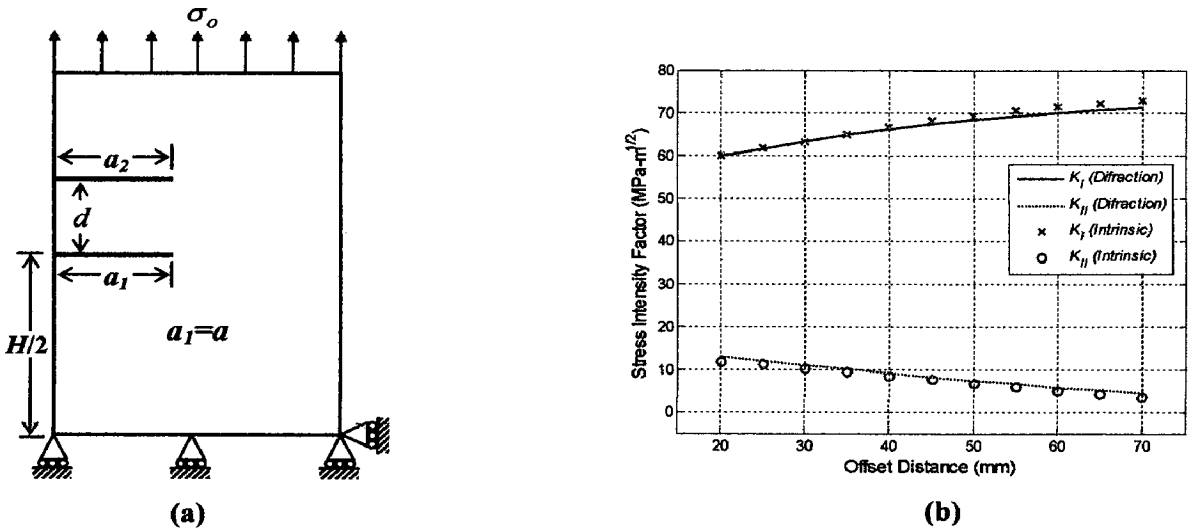

Fig. 4.7: Problem geometry and variation of SIF with offset

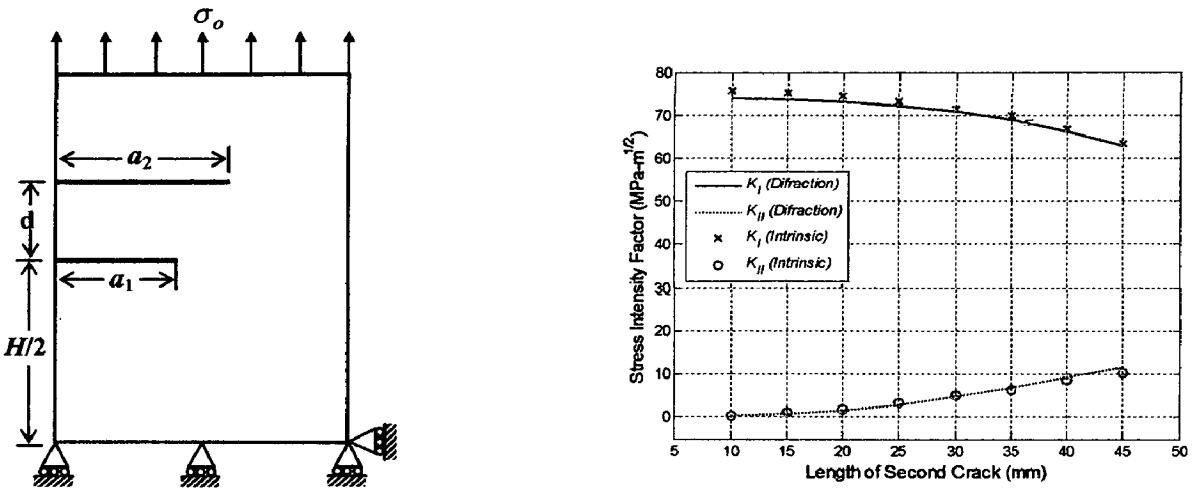

(a) (b)

Fig. 4.8: Problem geometry and variation of SIF with crack length

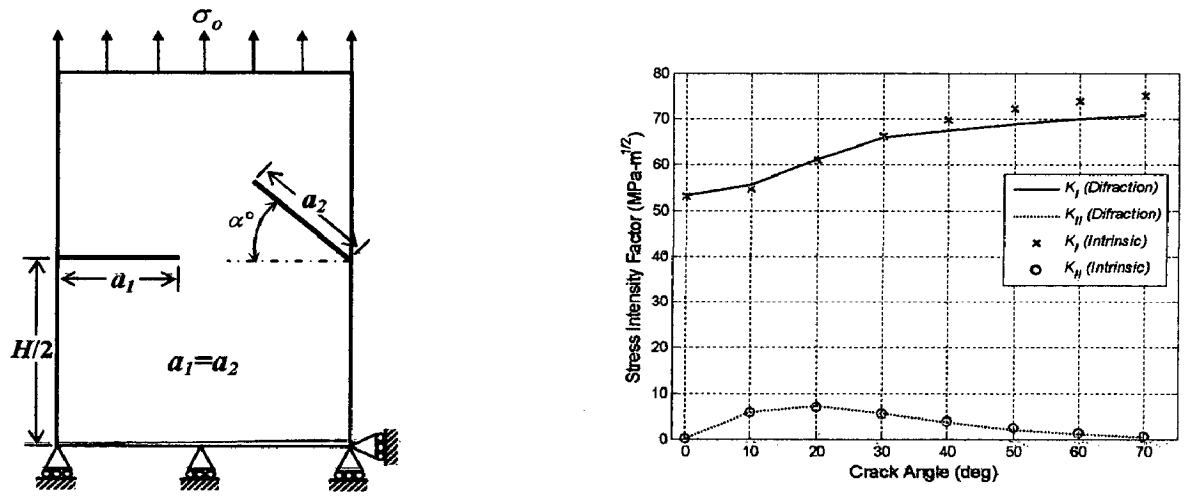

(a) (b)

Fig. 4.9: Problem geometry and variation of SIF with crack inclination

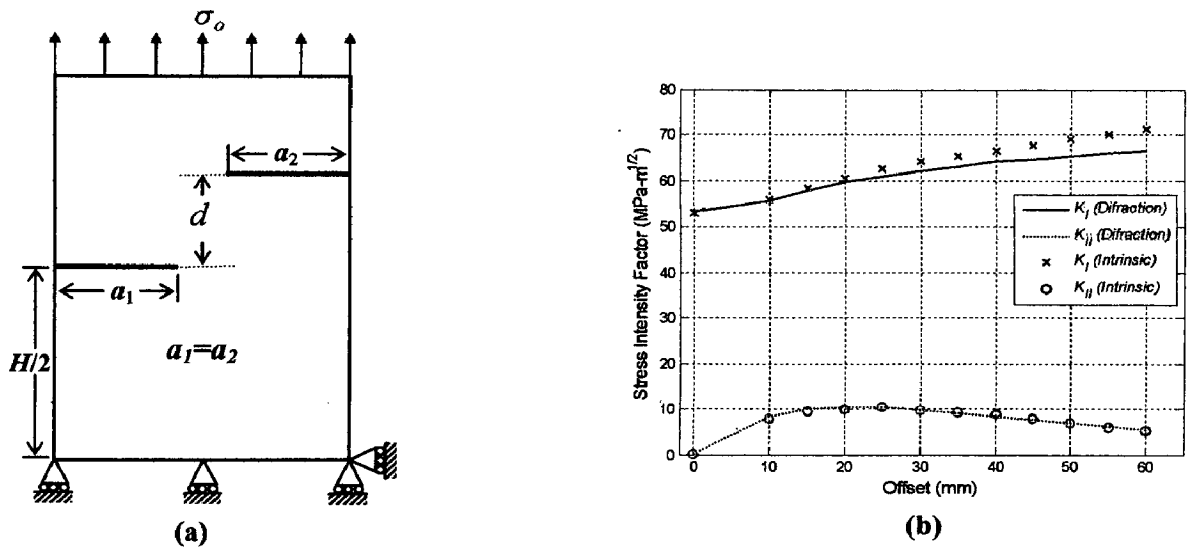

(a) (b)

Fig. 4.10: Problem geometry and variation of SIF with offset

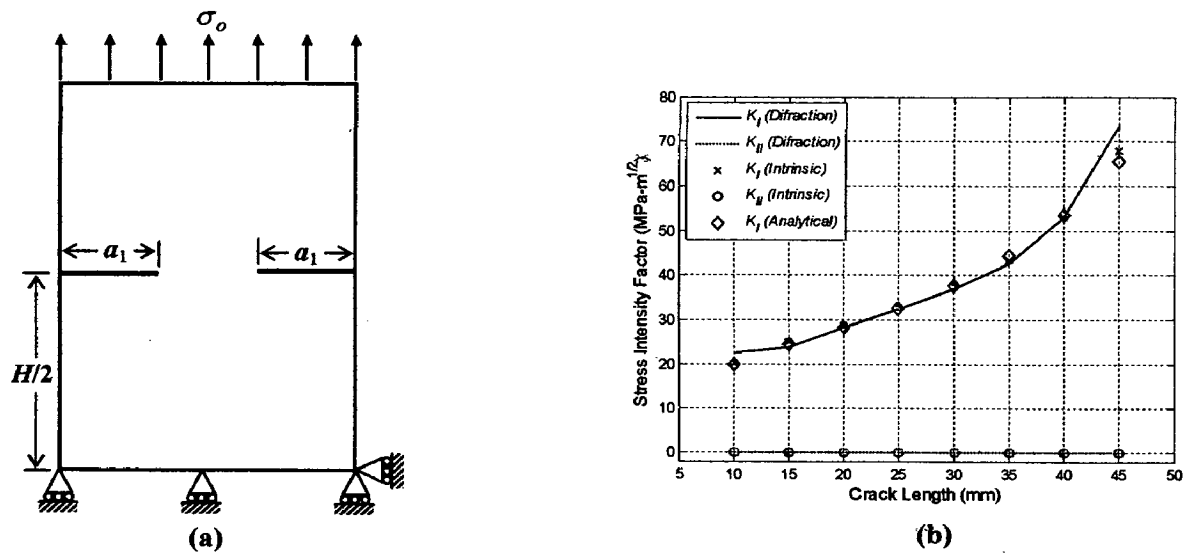

Fig. 4.11: Problem geometry and variation of SIF with crack length

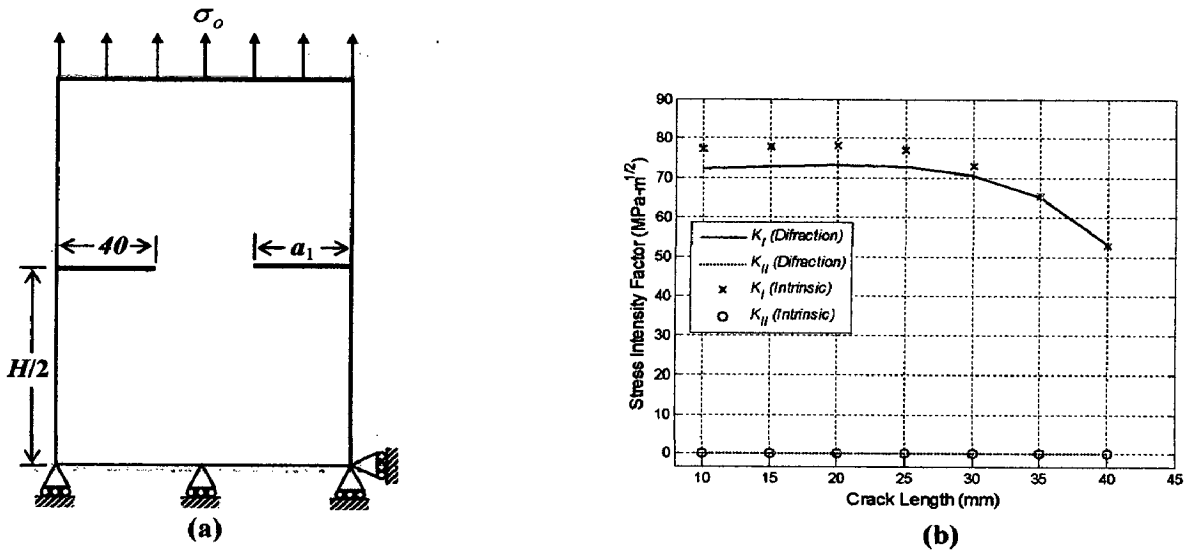

Fig. 4.12: Problem geometry and variation of SIF with crack length

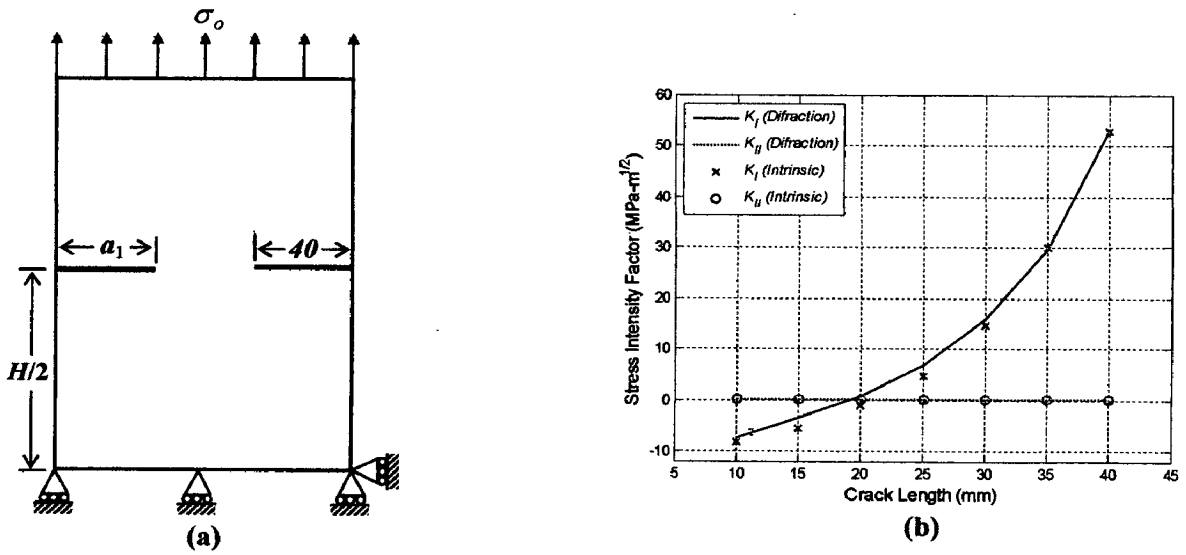

Fig. 4.13: Problem geometry and variation of SIF with crack length

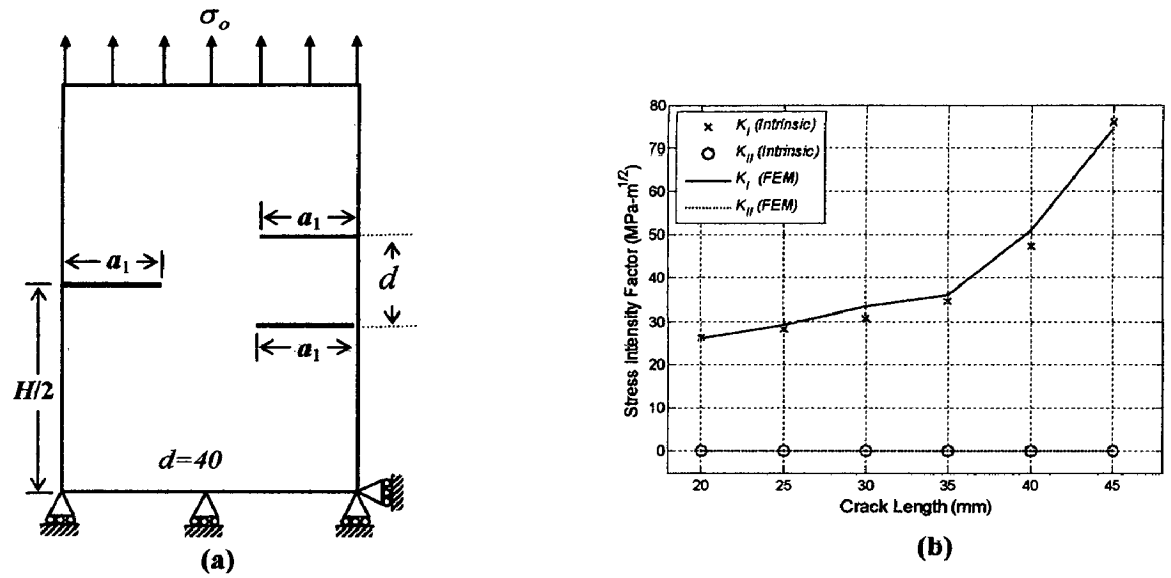

Fig. 4.14: Problem geometry and variation of SIF with crack length

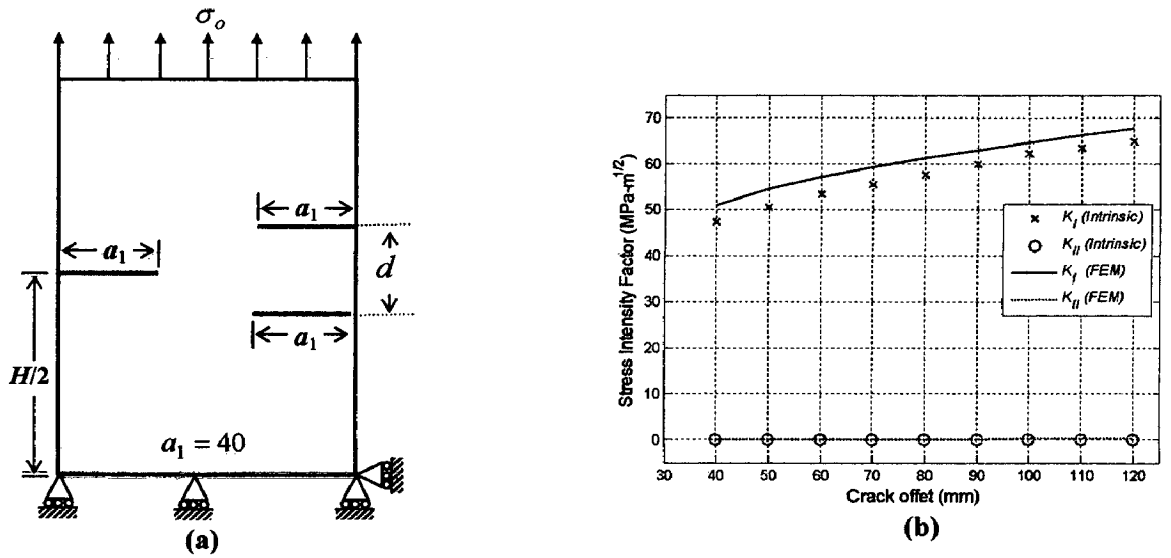

Fig. 4.15: Problem geometry and variation of SIF with offset

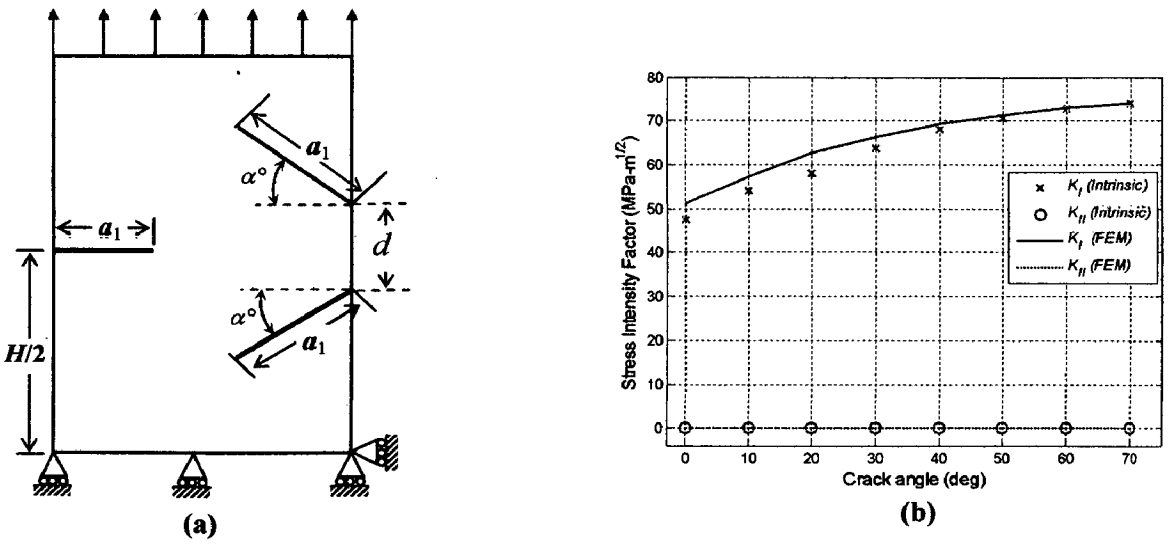

Fig. 4.16: Problem geometry and variation of SIF with crack inclination

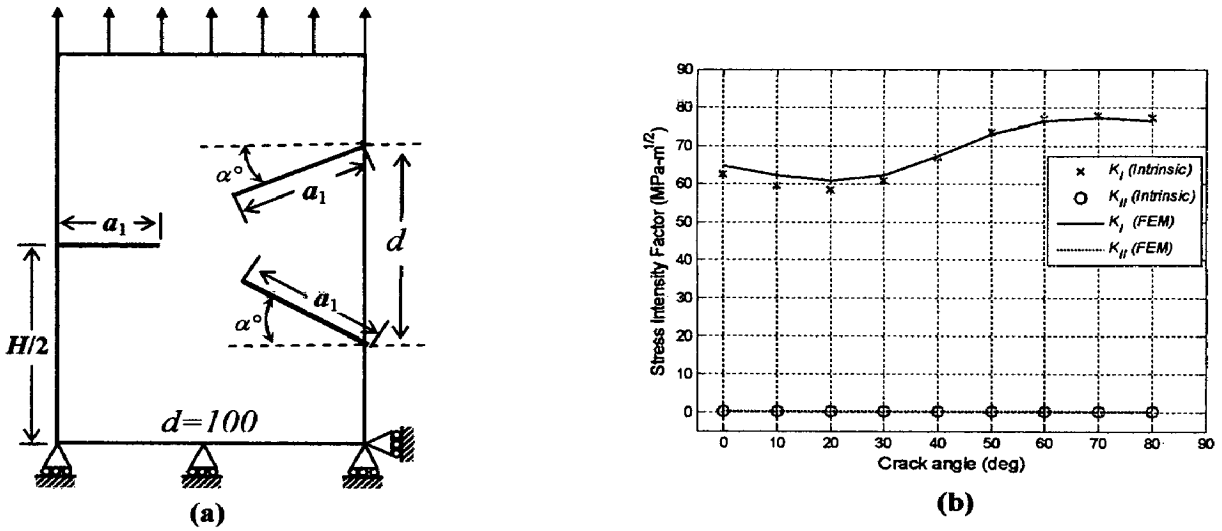

Fig. 4.17: Problem geometry and variation of SIF with crack inclination

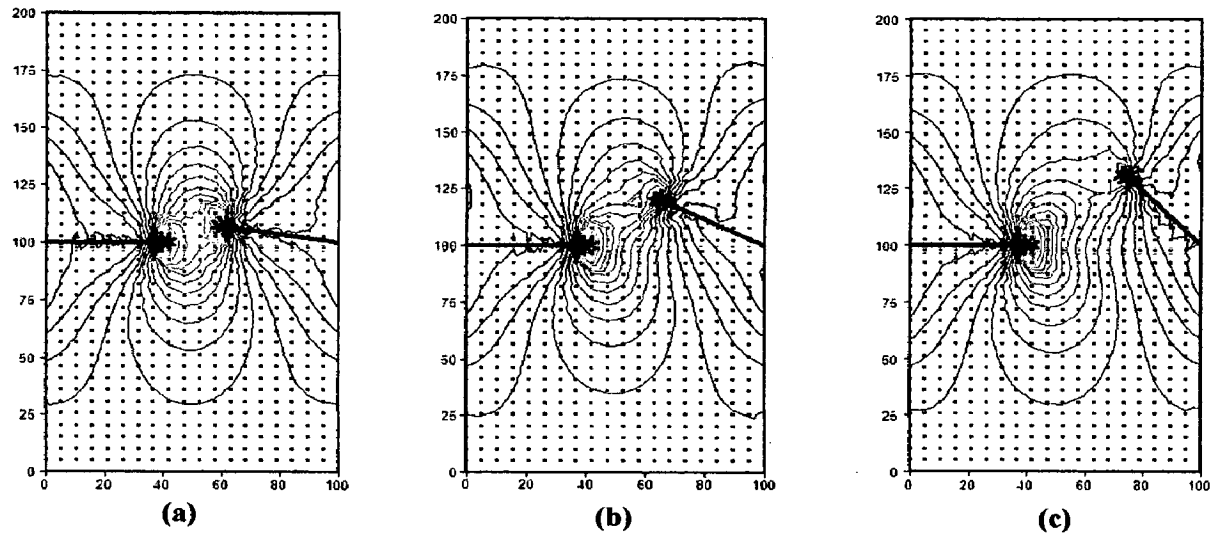

Fig. 4.18: Stress contours of σ_{yy} for different crack configurations

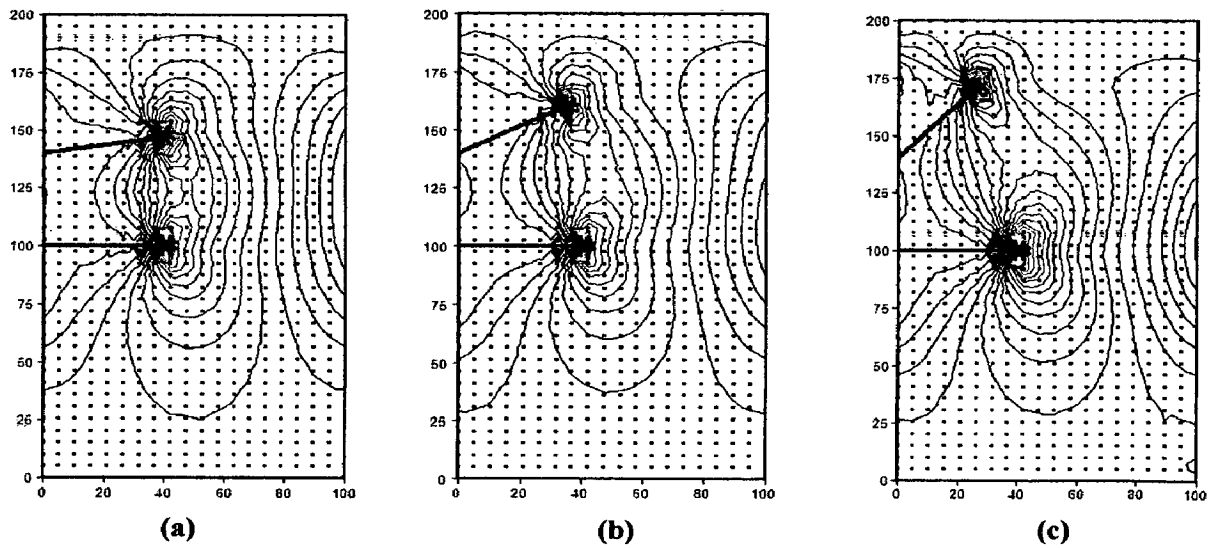

Fig. 4.19: Stress contours of σ_{yy} for different crack configurations

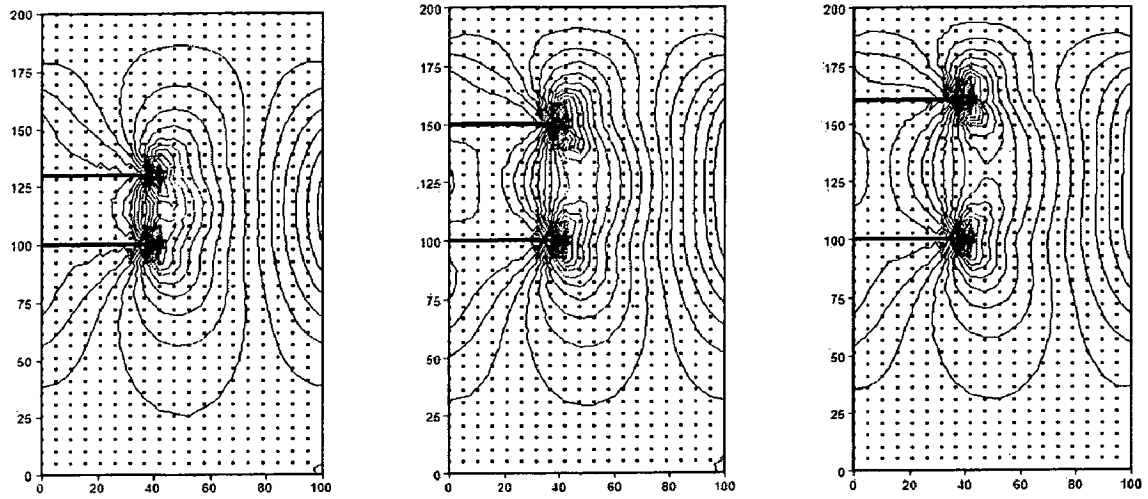

Fig. 4.20: Stress contours of σ_{yy} for different crack configurations

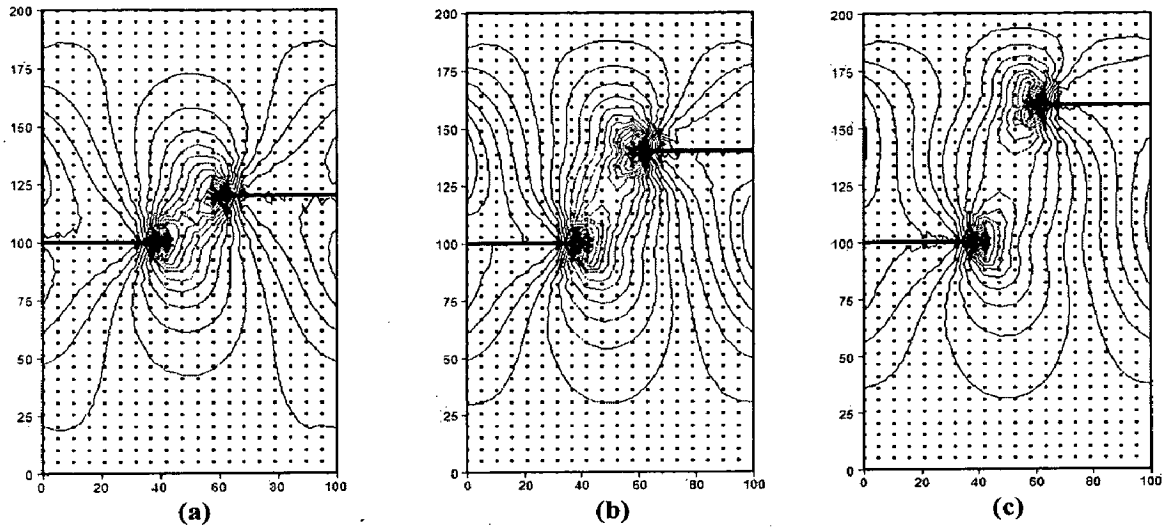

Fig. 4.21: Stress contours of σ_{yy} for different crack configurations

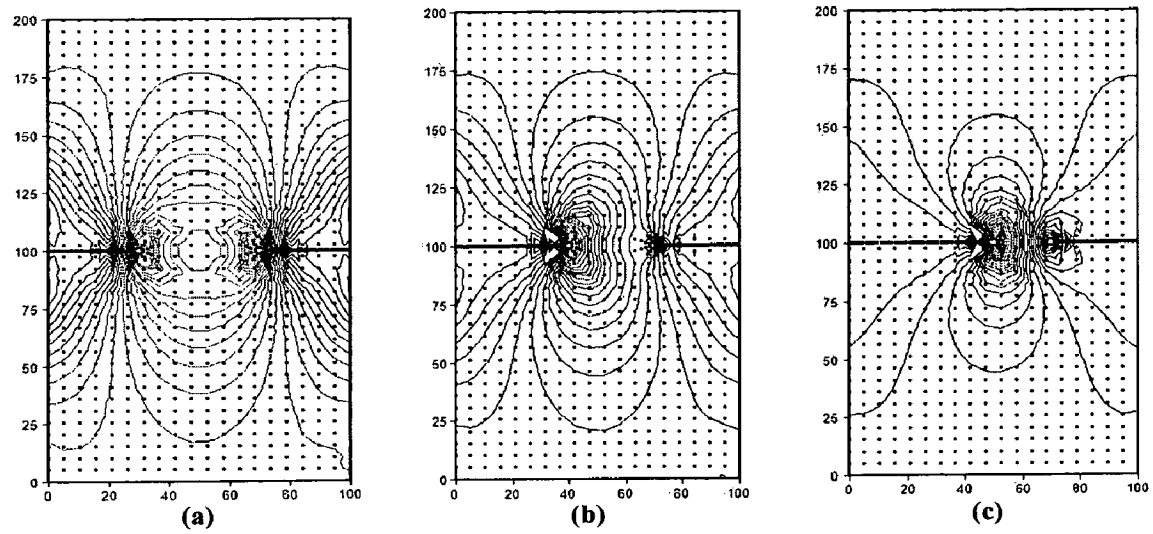

Fig. 4.22: Stress contours of σ_{yy} for different crack configurations

4.5.2 Crack Interactions under Thermal Loading

The dimensions of the cracked plate used for investigating thermal loading are taken as $H = 200$ mm, $W = 100$ mm as shown in Fig. 4.23a. The material used in study is ASTM 36 steel (Beer et al., 2002) with modulus of elasticity $E = 200\,\text{GPa}$, Poisson's ratio $\nu = 0.3$ and coefficient of thermal expansion $\beta = 11.7 \times 10^{-6}$. For the case of thermal loading, both top and bottom edges are constrained along y-direction and thermal stresses are developed due to the change in temperature. A uniform temperature change $\Delta T = -43.7\,^{o}C$ has been assumed such that it produces an equivalent mechanical stress $E\,\beta\,\Delta T = 200 \times 10^{3} \times 11.7 \times 10^{-6} \times 43.7 = 99.9 \approx 100\,\text{MPa}$. Different crack configurations under thermal loading have been analyzed in this section.

Figure 4.23a shows two cracks lying on the same edge in a specimen. The first crack lying on the left edge has a fixed orientation along the width, while the orientation of second crack is varied. The length of both cracks is taken as 40 mm. Both K_I and K_{II} are calculated at the tip of first crack. Figure 4.23b presents the variation of the stress intensity factors of the first crack with the angular orientation (α) of the second crack. From the results presented in Fig. 4.23b, it is noticed that the values of K_I increases with the increase of α, whereas K_{II} decreases with the increase of α. At $\alpha = 0°$, K_I and K_{II} are found to be minimum and maximum respectively. A good agreement between the results obtained by diffraction criteria and intrinsic enrichment can be clearly seen from Fig. 4.23b.

The effect of offset distance i.e. d (as shown in Fig. 4.24a) between two parallel cracks of equal length (40 mm) lying on the same edge has been analyzed in this sub-section. Figure 4.24b shows that effect of d on the stress intensity factors of lower crack/first crack. From the resulted presented in Fig. 4.24b, it is seen that the presence of

equal length upper crack lowers the value of K_I to $23.25\,\text{MPa}\sqrt{\text{m}}$ whereas K_{II} becomes non-zero due to change in applied stress field for the lower crack. With the increase in offset distance, K_I increases continuously, while K_{II} shows a decreasing trend. From Fig. 4.24b it is clear that the results obtained by the intrinsic enrichment and diffraction criterion are in good agreement with each other.

Figure 4.25a shows two parallel cracks configuration both lying on the same edge. The length (a_1) of the first crack i.e. lower crack is taken as 40 mm, while the length (a_2) of second crack i.e. upper crack is varied. The distance between two parallel cracks (d) is taken as 40 mm. The stress intensity factors have been evaluated at the tip of first crack. From the results presented in Fig. 4.25b, it is found that with the increase in the length of the second crack, K_I decreases, and K_{II} increases. The decrease in value of K_I for the first crack with the increase in the length of upper crack is due to the tendency of upper crack to become the major crack. Moreover, the results presented by diffraction criterion and intrinsic enrichment are quite close to each other.

A specimen with two cracks of equal length (40 mm) lying on the opposite edges is considered as shown in Fig. 4.26a. The crack on left edge is kept at $\alpha = 0$ with the horizontal, while the orientation (α) of the crack on the right edge has been varied from 0° to 60°. The values of stress intensity factors have been calculated at the tip of the left edge crack. From the results presented in Fig. 4.26b, it is observed that with the increase in α, K_I keeps on increasing, whereas K_{II} initially increases upto $\alpha = 20°$, and decreases after that. The variation in value of K_I for a 60° change in inclination is less as compared to the same in mechanical loading. From the results presented in Fig. 4.26b, it is seen that the results obtained by diffraction criterion are slightly on the higher side as compared to the intrinsic enrichment. However, the trend is similar in both techniques.

Two parallel cracks of same length i.e. $a_1 = a_2 = 40\,\text{mm}$ lying on opposite edges (Fig. 4.27a) have been analyzed by varying the offset (d) between them. K_I and K_{II} have been evaluated at the tip of left edge crack for various values of d. The effect of d on K_I and K_{II} is presented in Fig. 4.27b evaluated by diffraction criterion and intrinsic enrichment. The minimum value of K_I is obtained at $d = 0$, then K_I increases continuously with the increase of d. The maximum value of K_{II} is found at $d = 20\,mm$.

Next, a case of collinear edge cracks have been considered. Figure 4.28a shows the configuration where length of both collinear cracks is increased by equal amount. The values of K_I and K_{II} are evaluated at the tip of left edge crack. A comparison of the results obtained by diffraction criterion and intrinsic enrichment suggests that the values are quite close for crack length $a_1 > 25\,\text{mm}$ as can be seen from Fig. 4.28b. For all values of crack length, K_I values obtained by diffraction criterion are smaller in comparison to intrinsic enrichment, whereas K_{II} nearly remains zero for all values of crack length.

Again stress (σ_{yy}) contour plots for different spatial and angular orientation have been generated for the case of thermal loading as shown in Figs. 4.29- 4.33. It is observed that the contour patterns for thermal loading are different from those of mechanical loading.

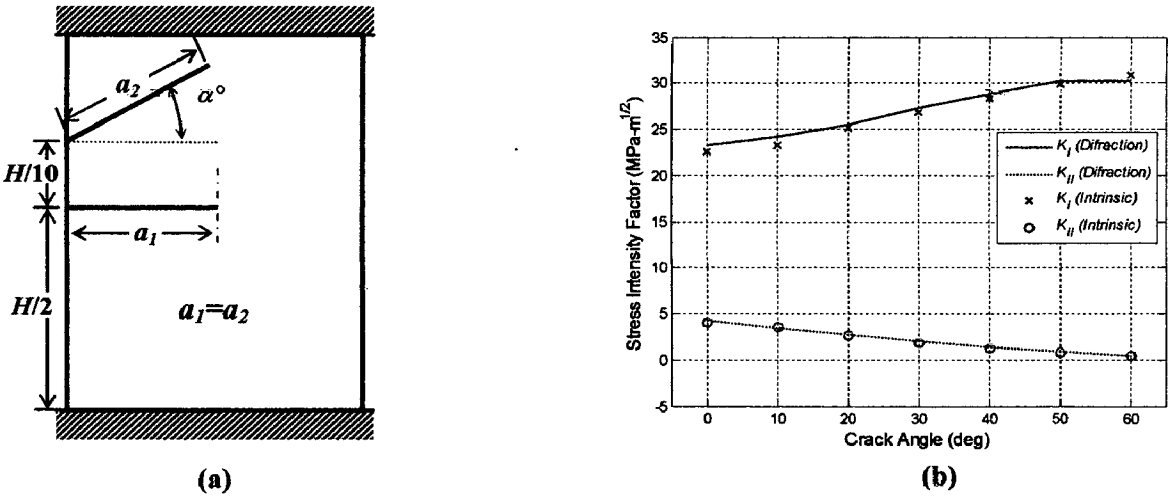

Fig. 4.23: Problem geometry and variation of SIF with crack inclination

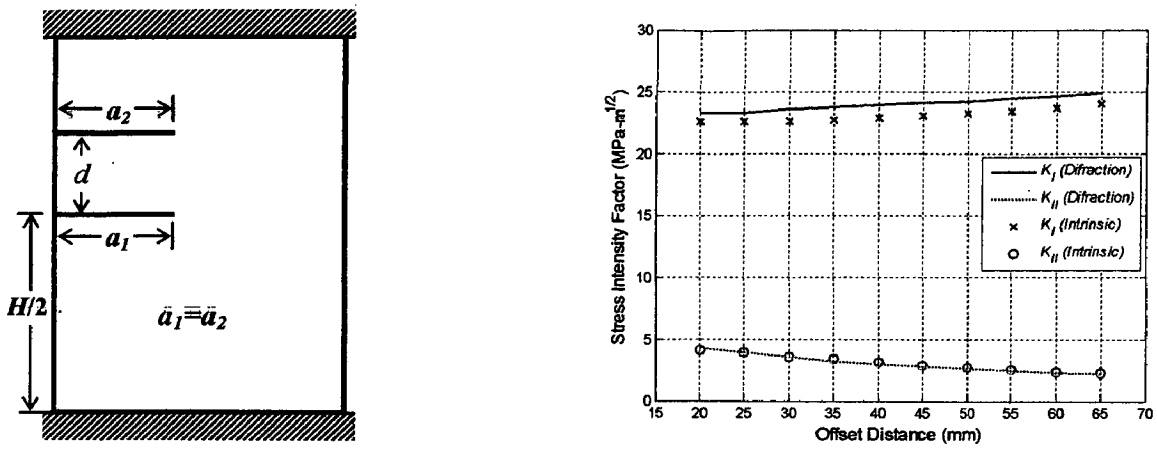

(a) (b)

Fig. 4.24: Problem geometry and variation of SIF with crack offset

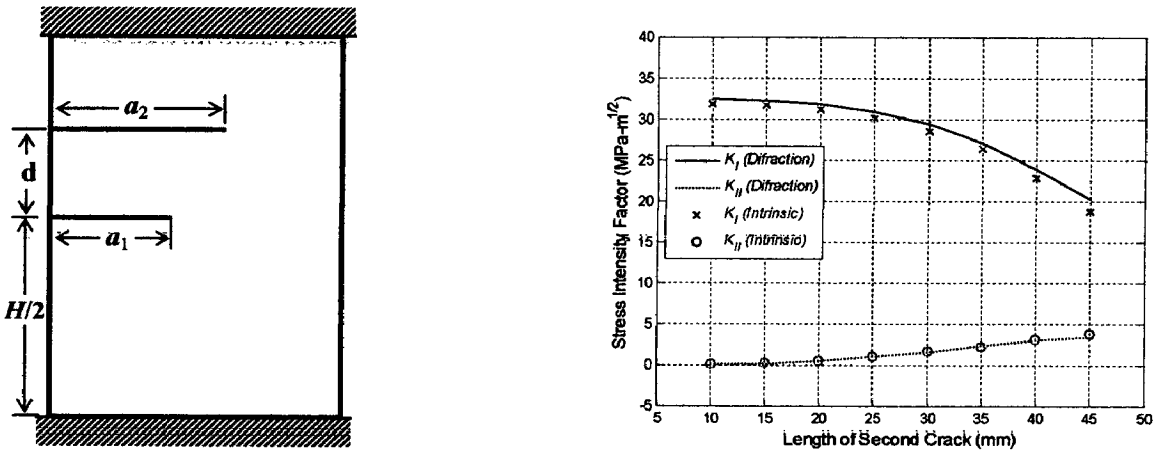

(a) (b)

Fig. 4.25: Problem geometry and variation of SIF with crack length

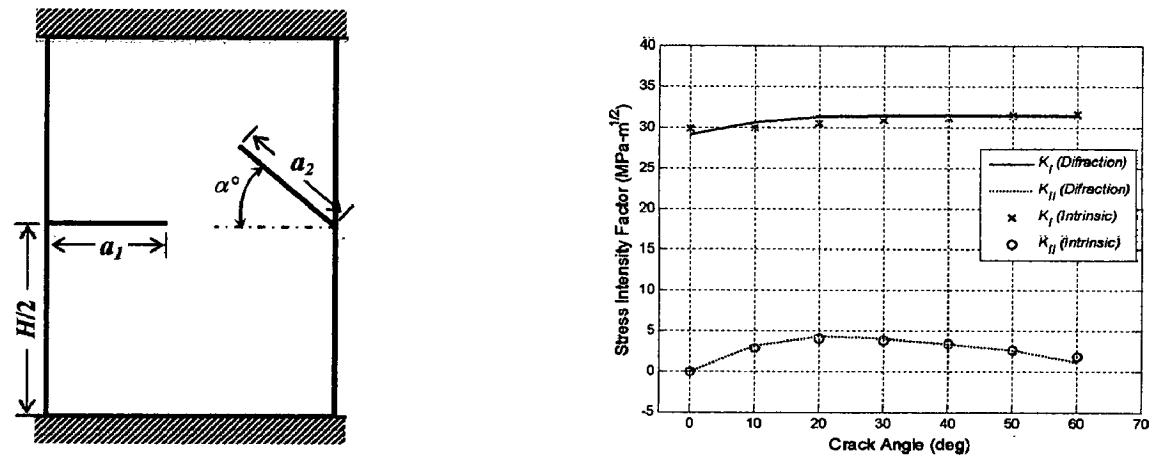

(a) (b)

Fig. 4.26: Problem geometry and variation of SIF with crack inclination

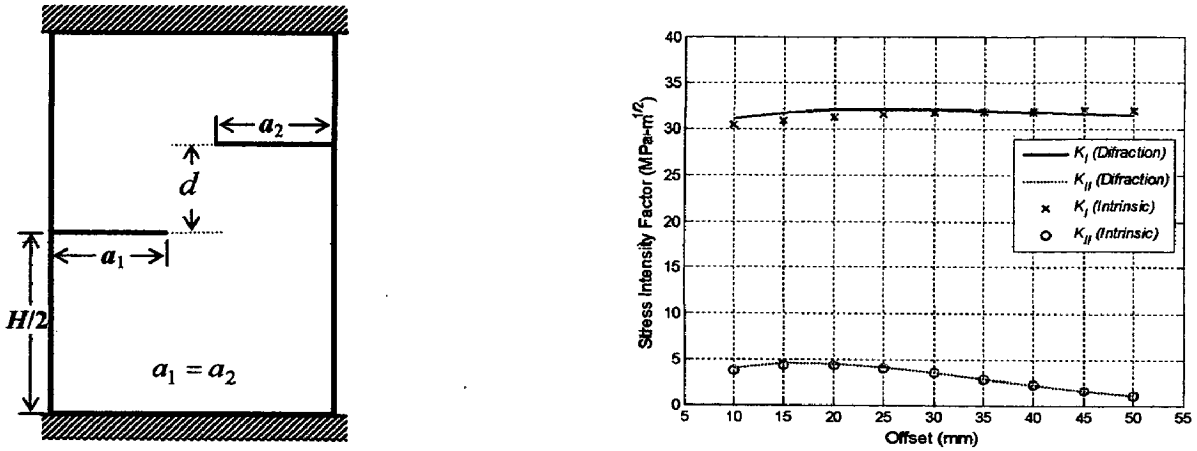

(a) (b)

Fig. 4.27: Problem geometry and variation of SIF with crack offset

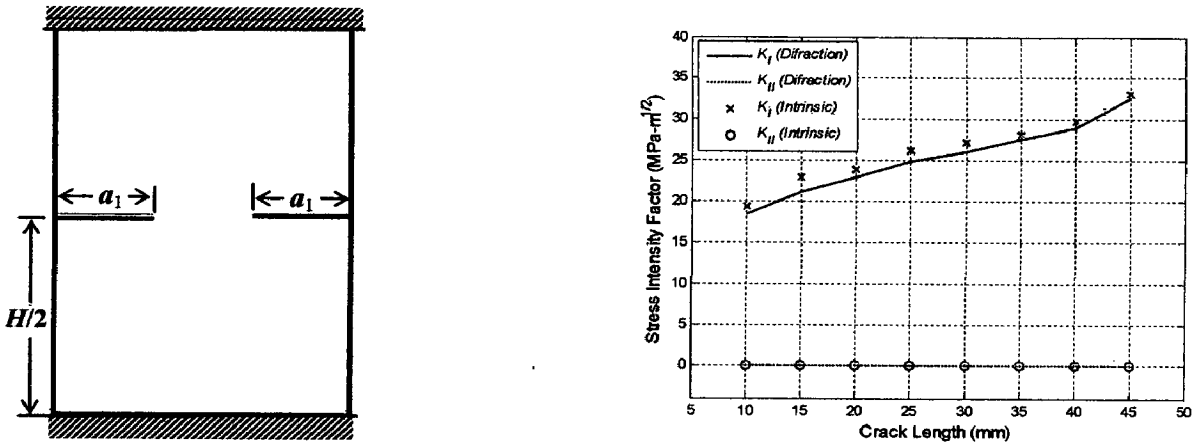

(a) (b)

Fig. 4.28: Problem geometry and variation of SIF with crack length

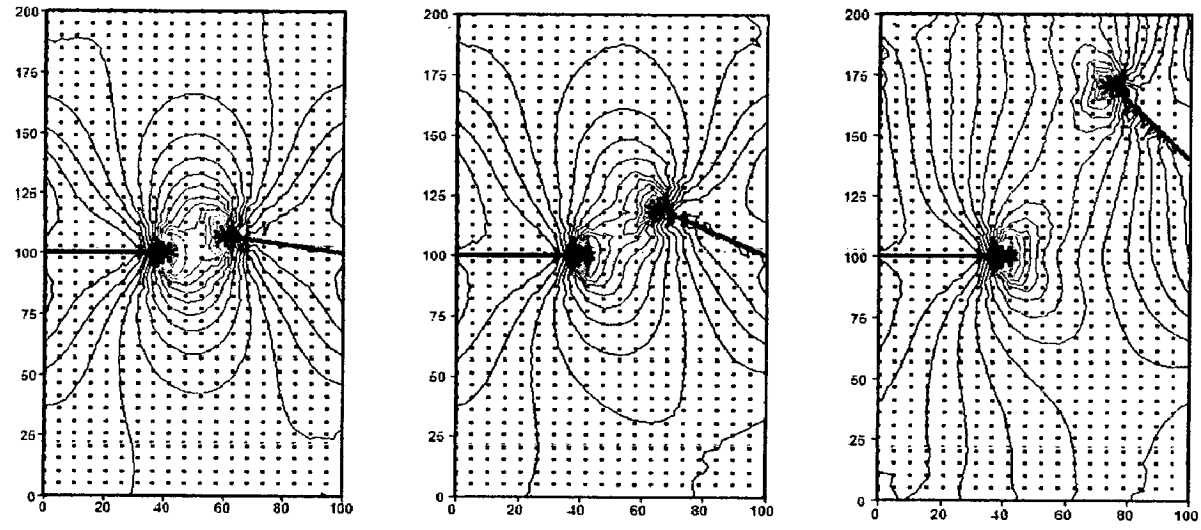

(a) (b) (c)

Fig. 4.29: Stress contours of σ_{yy} for different crack configurations

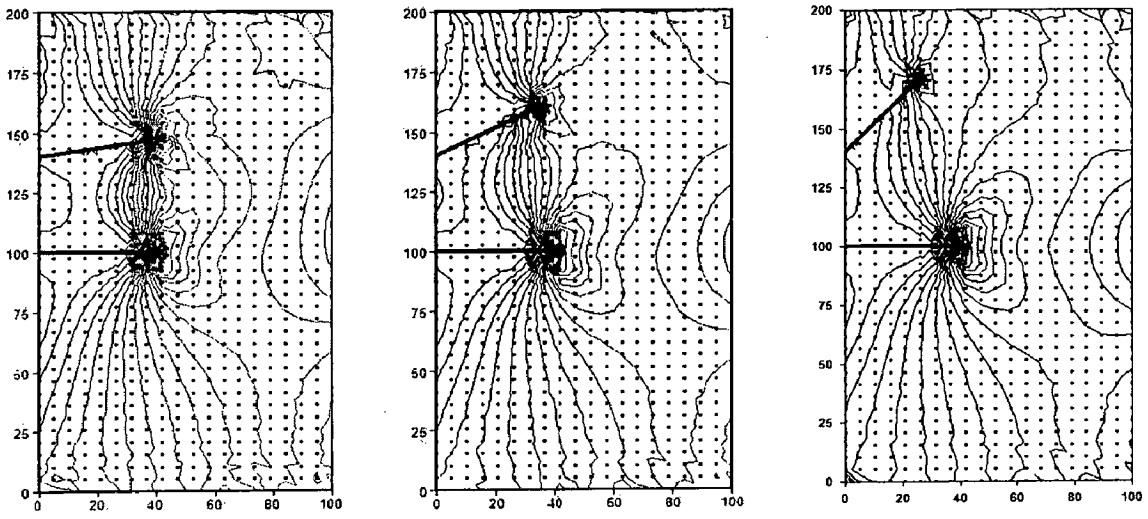

(a) (b) (c)

Fig. 4.30: Stress contours of σ_{yy} for different crack configurations

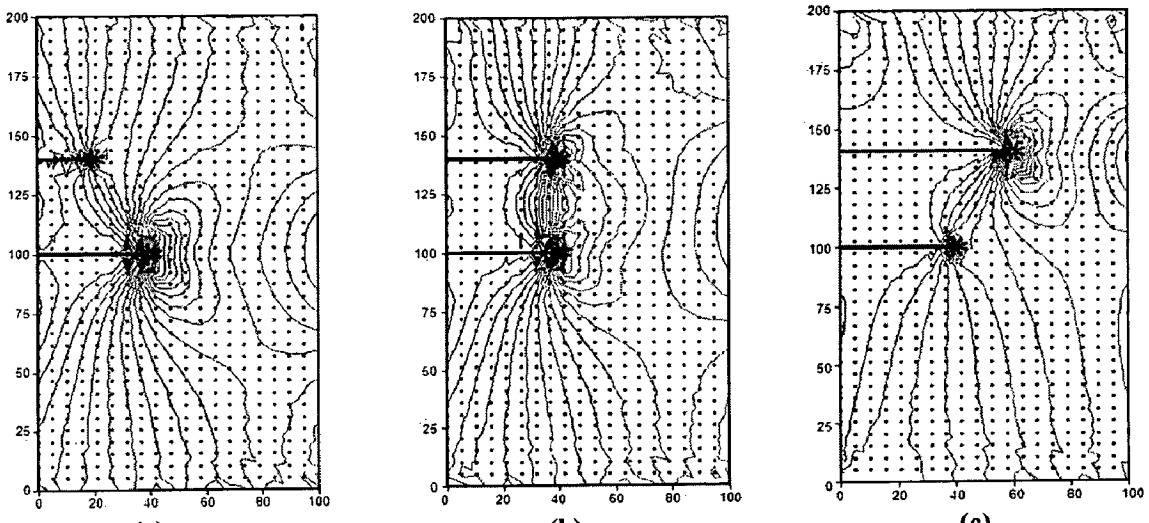

(a) (b) (c)

Fig. 4.31: Stress contours of σ_{yy} for different crack configurations

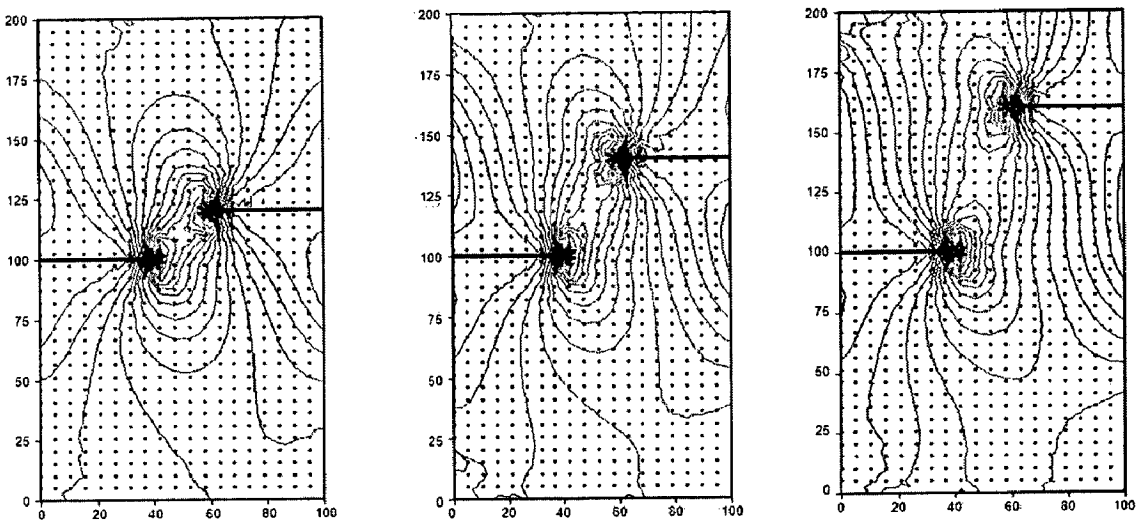

(a) (b) (c)

Fig. 4.32: Stress contours of σ_{yy} for different crack configurations

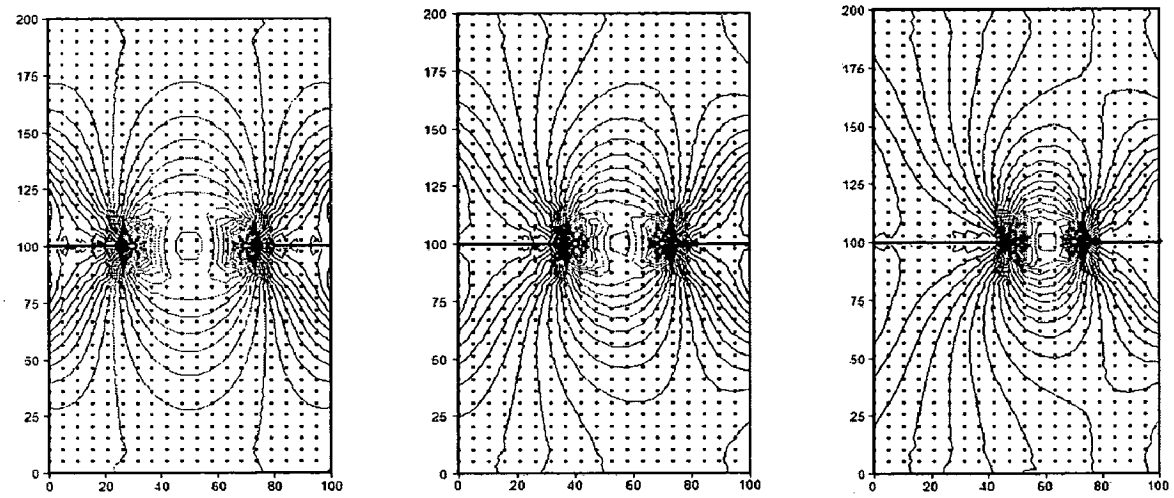

Fig. 4.33: Stress contours of σ_{yy} for different crack configurations

4.6 CRACKS IN NON-CONVEX DOMAINS

A domain is said to be non-convex if a line joining any two points of the domain intersect the domain boundary. Figure 4.34 represents a non-convex domain as a line joining points A and B intersect the domain boundary at two points. It has been found in the present simulation that the full domain intrinsic enriched criterion gives misleading results for cracks lying in non-convex domains. This happens due to the enrichment of the evaluation points lying in the non-convex domain. It has been found that the use of enriched basis for the entire domain not only increases the computational cost of the method but also gives misleading results for the cracks lying in non-convex domains. Therefore, a new partial domain enrichment based criterion has been proposed in this section.

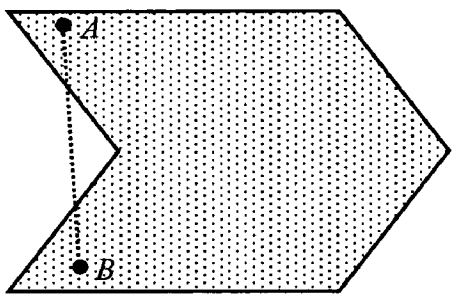

Fig. 4.34: A non-convex domain

4.6.1 Full Intrinsic Enrichment Criterion

In full intrinsic enrichment based criterion (Fleming et al., 1997), the presence of a crack is ensured by enrichment terms i.e. by adding extra terms in the basis function. In intrinsic enrichment criterion, the meshfree standard basis functions are intrinsically enriched by few functions obtained from near crack tip displacement field to solve the problems with strong discontinuities such as cracks. A regular/standard enriched basis function can be given as

$$\mathbf{P}^T(\mathbf{x}) = \left[\underbrace{1,\ x,\ y}_{\substack{\text{standard} \\ \text{basis}}},\ \underbrace{\sqrt{r}\cos\frac{\theta}{2}, \sqrt{r}\sin\frac{\theta}{2}, \sqrt{r}\sin\frac{\theta}{2}\sin\theta, \sqrt{r}\cos\frac{\theta}{2}\sin\theta}_{\text{enrichment terms}} \right] \tag{4.10}$$

where, $\mathbf{P}(\mathbf{x})$ is the enriched basis function, r and θ are the local crack tip parameters. The first three terms of Eq. 4.10 represent the standard basis function $(1, x, y)$ while remaining four terms obtained from the near crack tip solution makes up the enrichment part.

A single edge crack along with an evaluation point and local crack tip parameters (r, θ) is shown in Fig. 4.35. According to full domain enrichment (FDE) criterion, the entire problem domain has to be enriched, which is unnecessary from the computational time point of view. The other drawback of full domain enrichment criterion lies in its inability to solve problems involving cracks lying in non-convex domains.

It has been found during the present simulation that the full domain intrinsic enriched criterion gives misleading results for cracks lying in non-convex domains. This happens due to the improper enrichment of the evaluation points lying in the non-convex domain. However, the proposed partial domain enrichment criterion eliminates this problem as the enrichment is made locally in the region around the crack tip. This ability of partial

domain enrichment (PDE) criterion to deal with the cracks present in non-convex domains makes it a very useful, computationally efficient and versatile technique for handling crack problems.

4.6.2 Partial Domain Intrinsic Enrichment Criterion

In the partial domain enrichment (PDE) criterion, two concentric circular regions are defined around a crack tip as shown in Fig. 4.36. The location of an evaluation point within these regions decides the degree of enrichment. Figure 4.36 represents the problem domain with an edge crack of length a. Two concentric circular regions are defined. The radius of the inner circle is equal to the crack length a, and the radius of outer circle is $\bar{c} \times a$ $(\bar{c} > 1)$. In the present study an optimum value of $\bar{c} = 2$ has been considered after performing a parameter sensitivity analysis as discussed later. In doing so, three different regions namely A, B and C are obtained. During implementation of this criterion, the distance of each evaluation point from the crack tip is calculated in order to decide its location. If the point lies within the inner most region A, then the full intrinsic enrichment basis is used. No enrichment is done for those evaluation points which lie in region C i.e. in region C, only standard linear basis is used.

If the evaluation point lies in region B, then the approximation functions are constructed using both linear basis and enriched basis, and their contributions to the stiffness matrix are decided as:

$$[\mathbf{K}]_{Total} = [\mathbf{K}]_{Enriched\ basis} \times R + [\mathbf{K}]_{Linear\ basis} \times (1 - R) \tag{4.11}$$

where, $[\mathbf{K}]_{Enriched\ basis}$ is the stiffness matrix obtained using enriched basis as given by Eq. (4.10), $[\mathbf{K}]_{Linear\ basis}$ is the stiffness matrix evaluated using linear basis only, R is a parameter which decides the contribution of each component to the stiffness matrix. The value of R can be numerically evaluated from the Eq. 4.12 given below:

$$R = \frac{(\bar{c} \times a - r_g)}{(\bar{c} - 1) \times a} \tag{4.12}$$

where, $\bar{c}$ is a constant which decides the size of region B, a is the crack length and r_g is the distance of an evaluation point from the crack tip. At any point in the region B near the boundary of region A, the contribution of enriched basis part to the total stiffness matrix will be maximum while that of the linear basis part will be minimum. Moving from region A to region B the value of R follows a linear variation and approaches zero on outer part of region B. Thus, the contribution of enrichment part keeps on decreasing as the location of evaluation point shifts from region A to region B. At the outer periphery of region B, the contribution of linear basis to the total stiffness matrix becomes maximum. This proposed criterion not only accurately simulates the cracks in non-convex region but also reduces the computational time.

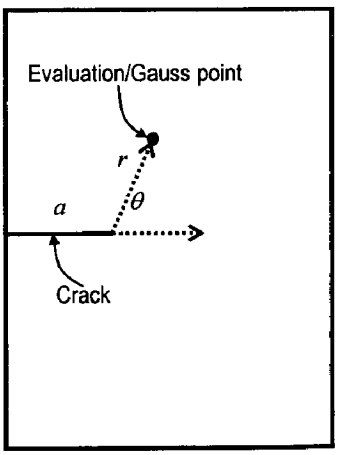

Fig. 4.35: Full domain enrichment

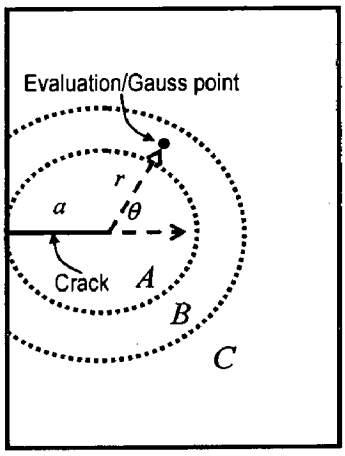

Fig. 4.36: Partial domain enrichment criterion

4.7 RESULTS AND DISCUSSIONS

4.7.1 Cracks lying in Convex Domain

Two test problems of cracks lying in a convex domain have been solved by both FDE and PDE criteria under plane stress condition. The dimensions of the cracked body used

in the present study are taken as $H = 200$ mm, $W = 100$ mm, modulus of elasticity (E) = 200 GPa, Poisson's ratio (ν) = 0.3. A far field stress, (σ_o) = 100 MPa is applied to the problem. A uniform nodal density of 800 nodes along with six point Gauss quadrature for numerical integration is utilized for this simulation.

In first case, two collinear edge cracks lying on two opposite edges are solved by both PDE and FDE criteria as shown in Fig. 4.37a. The first crack has been taken at a distance of $H/2$ i.e. 100 mm from the bottom on left edge with crack inclination $\alpha = 0°$ ($\alpha = 0°$ means that the crack is parallel to the x–axis), while the second crack is placed on right edge with crack inclination $\alpha = 0°$. The lengths of both cracks are incremented by equal amount. The results obtained by both PDE and FDE are presented in Fig. 4.37b. The values of K_I and K_{II} have been evaluated at the tip of left edge crack. The results predicted by PDE are compared with those obtained by FDE, and it is noticed that the results obtained by both the criteria are quite close to each other. The maximum difference in K_I values is found to be less than 4%. The values of K_{II} nearly remain zero for all values of crack length as can be seen in Fig. 4.37b.

In the second case, the proposed PDE criterion is used to solve three edge crack problems subjected to mode-I loading under plane stress condition as shown in Fig. 4.38a. The lengths of all three cracks are kept equal i.e. $a_1 = 40$ mm. The effect of two right edge cracks inclination on the left edge crack is analyzed as shown in Fig. 4.38a. The inclination angle α has been changed in such a way that the tips of the two right edge cracks move away from each other. The values of K_I and K_{II} are evaluated at the tip of left edge crack. The results show that with increase in α, the values of K_I keeps on increasing, while K_{II} remains nearly zero for all values of α. The results obtained by PDE and FDE are almost identical for all values of α as shown in Fig. 4.38b.

On the basis of above simulations, it is clearly seen that the results obtained by both partial domain enriched and full domain enriched criteria are in good agreement with each other for the cracks lying in convex domain. Therefore, a crack lying in a non-convex domain has been analyzed next to show the superiority of the proposed partial domain enriched criterion.

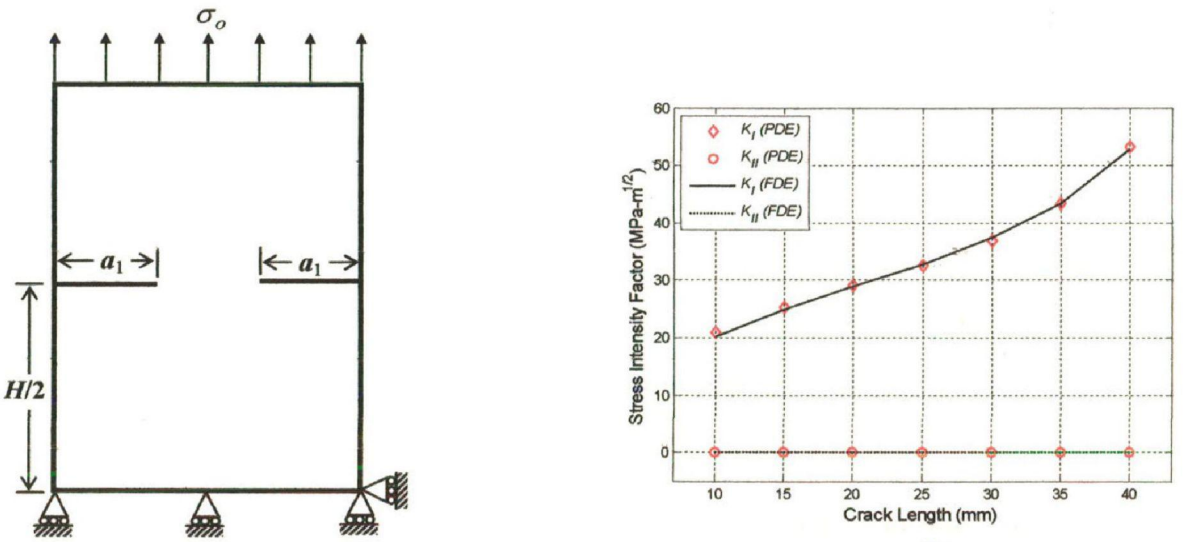

Fig. 4.37: Problem geometry and variation of SIF with crack length

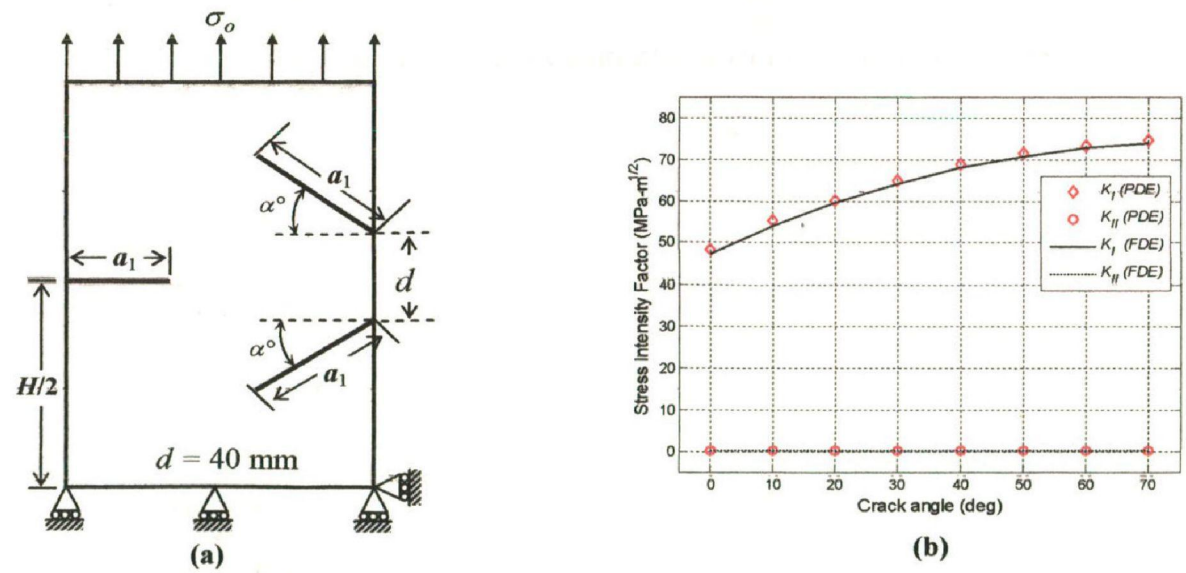

Fig. 4.38: Problem geometry and variation of SIF with crack inclination

4.7.2 Computational Cost Analysis

As in PDE criterion, the enriched basis has been used over a small region around the crack tip, it is expected that there will be some reduction in computational cost as compared to FDE, hence the computational cost comparison of the proposed and existing criteria are also performed. In order to estimate the computational cost of the proposed criterion, the simulations are performed for an edge crack configuration as shown in Fig. 4.37a with a crack length $a_1 = 40$ mm. The total time required in the computation of stiffness matrix has been calculated for both partial domain enrichment and full domain enrichment criteria. The computational time has been calculated for a set of nodal data. Figure 4.39 shows the plot of computational time with nodal density for both partial domain enrichment and full domain enrichment criteria. From this plot, it is clearly seen that for lower nodal density of nodes there is not much difference in computational time, but as the number of nodes in the domain increases, a significant difference in computational time is observed, which can be clearly seen from Fig. 4.39. Figure 4.40 shows the plot of computational time difference between two criteria with increasing nodal density, which shows a steep rise in the slope of curve beyond a nodal density of 1000 nodes. This suggests that with the increase in nodal density, the computational time difference between two criteria keeps on increasing. This proves the worth of proposed partial domain enrichment criterion from computational time point of view.

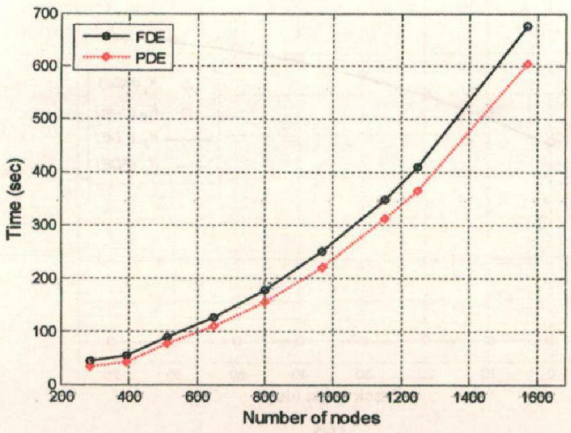

(a)

Fig. 4.39: Variation of computational time with nodal density

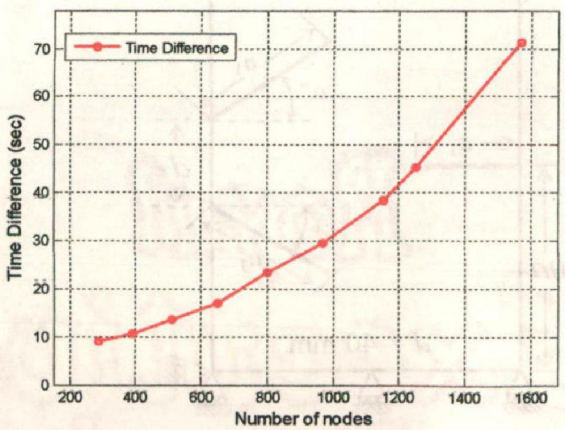

(b)

Fig. 4.40: Variation of computational time difference with nodal density

4.7.3 Cracks lying in Non-Convex Domain

Two model problems of cracks lying in non-convex domain have been taken to show the strength of the proposed PDE criterion over the FDE criterion. A nodal density of 657 nodes along with 4 point Gauss quadrature has been employed to simulate the problems.

Figure 4.41 shows an annular metallic disc (r_i= 100 mm and r_o = 300 mm) having an edge crack of length a with material properties same as that of the plate considered earlier. This problem has been solved by both full domain intrinsic enrichment and partial domain enrichment criteria under plane stress condition. The values of stress intensity factor K_I are evaluated for different crack lengths using both PDE and FDE criteria. Figure 4.42 shows a comparison of results obtained by PDE and FDE criteria with FEM solution. It is clearly seen that for all values of crack length, the results obtained by PDE criterion are in good agreement with those obtained by FEM, whereas the results obtained by FDE are not matching with FEM solution.

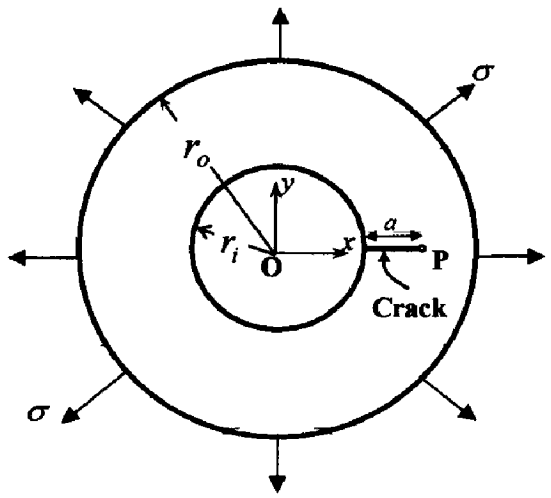

Fig. 4.41: Annular disc with an interior edge crack configuration

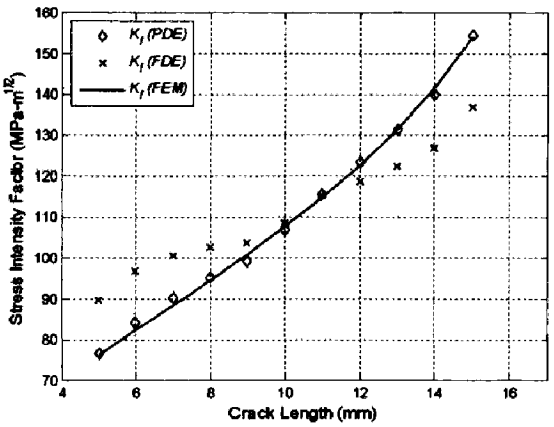

Fig. 4.42: Variation of stress intensity factor K_I with crack length

For a better understanding of the results obtained by both FDE and PDE criteria, the contours of stress and displacement field components are plotted as shown in Figs. 4.43-4.46. Figure 4.43a shows the displacement contour of U_x obtained by partial domain enrichment criterion, whereas Figure 4.43b shows the displacement contour obtained by full domain enrichment criterion. From Fig. 4.43, it can be seen that U_x is symmetric about x-axis. The displacement contours of U_y obtained by PDE and FDE criteria are shown in Fig. 4.44a and Fig. 4.44b. Although, the results obtained by both criteria look symmetric about crack line but in FDE, it seems that a non-existent discontinuity is inadvertently modeled in the domain at another location as can be seen in Fig. 4.44b.

Figure 4.45a shows the contour of stress component σ_{xx} over the problem domain using the proposed PDE criterion. This contour shows that the crack surfaces are almost traction free in x-direction as expected. The stress contour of σ_{xx} generated using FDE criterion shows a nearly zero stress level throughout the domain along with some compressive stress region opposite side of the crack as shown in Fig. 4.45b. Thus, σ_{xx} values obtained by FDE criterion are misleading and incorrect. The stress contours of σ_{yy} are plotted and analyzed using both the criteria. Figure 4.46a presents the contour of σ_{yy} using PDE criterion. The crack surfaces are almost traction free in y-direction as per expectation. The stress level at the crack tip is high in comparison to the rest of the domain, which represents stress singularity at the crack tip. Figure 4.46b shows contour of σ_{yy} obtained by FDE criterion. In this contour, the high stress zone at crack tip is completely missing. Moreover, a uniform stress field has been observed throughout the domain, which is incorrect.

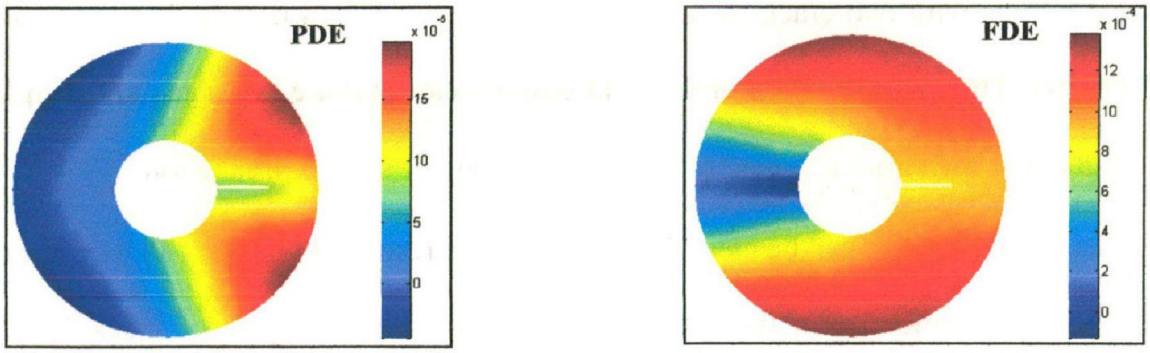

(a) (b)

Fig. 4.43: Contours of displacement component U_x

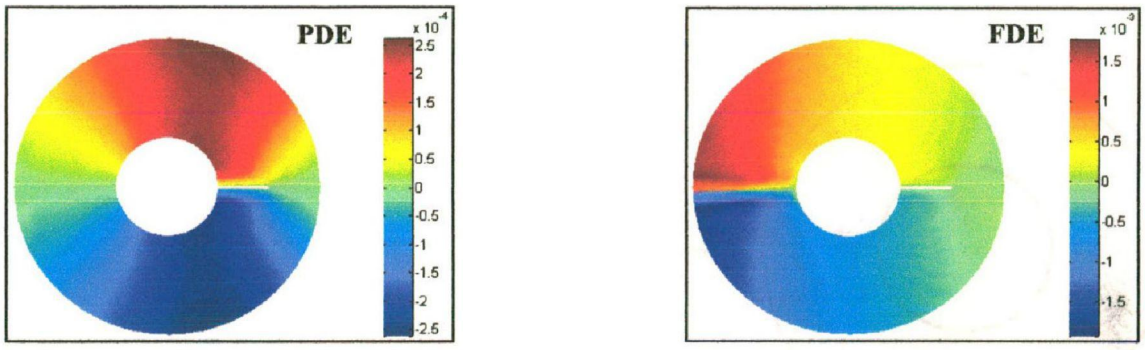

(a) (b)

Fig. 4.44: Contours of displacement component U_y

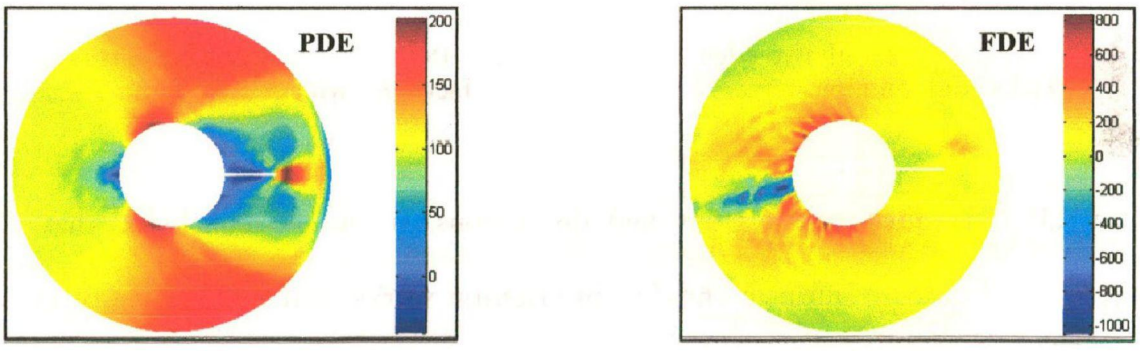

(a) (b)

Fig. 4.45: Contours of stress component σ_{xx}

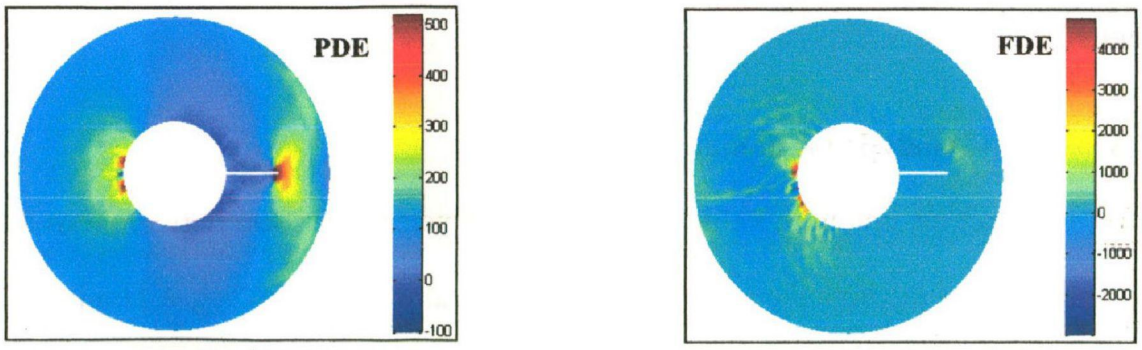

(a) (b)

Fig. 4.46: Contours of stress component σ_{yy}

Next, a disc with two cracks as shown in Fig. 4.47 is solved next by both FDE and PDE criteria. The values of mode-I stress intensity factor (K_I) are evaluated at the tip of left edge crack for various values of a_1, and are plotted in Fig. 4.48. From the results presented in Fig. 4.48, it can be clearly noticed that the results obtained by PDE criterion are in good agreement with those obtained by FEM for all values of crack length, whereas the results obtained by FDE are not reliable.

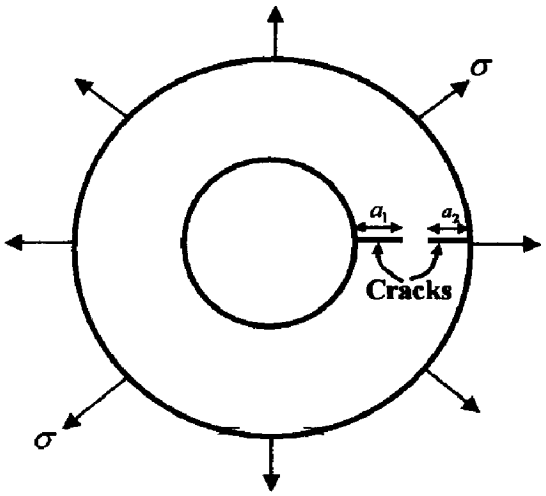

Fig. 4.47: Annular disc with two edge cracks configuration

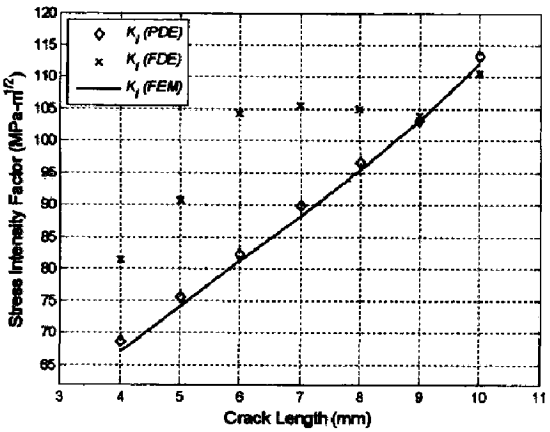

Fig. 4.48: Variation of stress intensity factor K_I with crack length

From all the above comparisons and discussions, it can be concluded that the proposed partial domain intrinsic enrichment criterion works well for all type of crack problems including cracks in non-convex domain, whereas the full domain intrinsic enrichment criterion gives misleading and wrong results for cracks lying in non-convex domains.

4.7.4 Sensitivity Analysis for domain parameter ($\bar{c}$)

In order to select an optimum value of domain parameter $\bar{c}$, a sensitivity analysis has been carried out for the both the annular crack configuration shown in Fig. 4.41 and 4.47. The same material property and boundary conditions were used for this simulation.

Figure 4.49 shows the variation of stress intensity factor for different values of domain parameter $\bar{c}$. At first an annular disc with a single edge crack of length $a = 15\,\text{mm}$ was analyzed by varying the value of domain parameter and the results were plotted as shown in Fig. 4.49a. The value of stress intensity factor obtained by PDE are quite close to the FEM solution for $\bar{c} = (1.75 - 2.5)$, with a maximum error of 0.08 %. The next study was done for double crack annular disc as shown in Fig.4.47. The crack lengths were taken as $a_1 = 6\,\text{mm}$ and $a_2 = 5\,\text{mm}$. The value of stress intensity was calculated at the tip of crack having length a_1. The variation of stress intensity factor for different values of domain parameter is shown in Fig. 4.49b. Again, the SIF values obtained by PDE criterion are close to the FEM results for $\bar{c} = (2 - 2.5)$ with a maximum error of 0.03%. Taking in consideration the above two simulation for sensitivity analysis of domain parameter we chose an optimum value of $\bar{c} = 2$ for all the previously simulated problems.

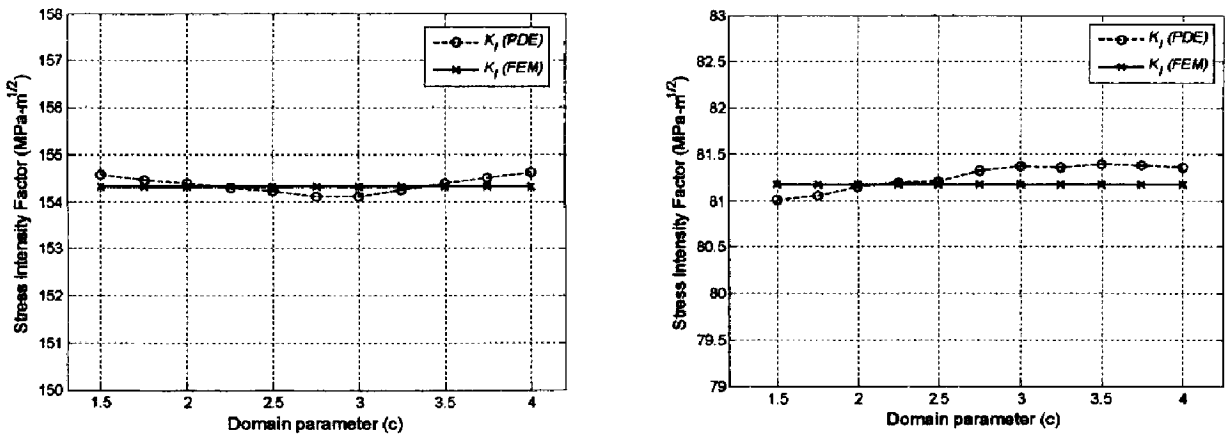

Fig. 4.49: Variation of stress intensity factor with domain parameter ($\bar{c}$)

4.8 CONCLUSION

In this Chapter, EFGM have been successfully employed for the simulation of multiple interacting cracks in both convex and non-convex domains. Two new criteria have been

proposed for simulating multiple interacting cracks. The first criterion is based on discrete contribution scheme in which the whole contribution of an evaluation point is imparted to only one crack while the second criterion is based on weighted contribution methodology in which the contribution of an evaluation point is shared among all the cracks present in the domain. In order to prove the worth of the proposed criteria, results were compared with those obtained by diffraction based multiple crack weight approach and FEM solution. A good agreement in results was obtained for both mechanical and thermal loading. The modeling capabilities and accuracy of the proposed criteria are amply demonstrated. Further, a partial domain intrinsic enrichment criterion was proposed in order to accurately simulate the cracks lying in non-convex domains. Numerical simulations were performed for few edge cracks lying in convex and non-convex domains under plane stress conditions. The proposed criterion not only simulates the problems of non-convex domains but also reduces the computational cost of the EFGM. The capability of the proposed partial domain intrinsic enrichment criterion to handle the cracks in both convex and non-convex domain along with less computation time in comparison to the full domain enrichment criterion establishes its potential for simulating real life crack problems.

Chapter 5

CRACKS UNDER THERMOELASTIC LOADING

5.1 INTRODUCTION

The determination of stress intensity factor for cracks subjected to thermal boundary condition is a topic of keen interest in fracture mechanics. The study of thermo-elastic fracture mechanics (Prasad and Aliabadi, 1994), which deals with the catastrophic propagation of existing cracks under thermal loading, is considered to be of great importance in the design of structures such as aerospace components, combustion chambers, turbines and nuclear pressure vessels. Whenever a steady heat flow is disturbed by the presence of a crack, there is a local intensification of thermal gradients accompanied by large thermal stresses in the neighborhood of crack tip (Sih, 1962). This may finally lead to sudden failure of the components resulting in loss of property and lives. Thus, the computation of stress intensity factor plays an important role in the safety assessment of components.

A lot of analytical research work has been carried out on some common configurations such as a crack in infinite and finite domains. Sih (1962) considered the singularities of two dimensional thermal stresses at the crack tips in an infinite medium, and showed that the $1/\sqrt{r}$ stress singularity is preserved in the thermal stress problems. Sekine (1974) obtained the numerical solution for thermal stress intensity factors for a Griffith crack in two dimensional semi-infinite body under uniform heat flow by using thermal dislocation concept and complex variable method. Sumi (1980) utilized the modified mapping collocation method to obtain the numerical solution for thermal stress intensity factor for Griffith crack in finite rectangular plates subjected to uniform heat

$$\begin{bmatrix} \mathbf{K} & \mathbf{G} \\ \mathbf{G}^T & 0 \end{bmatrix} \begin{Bmatrix} \mathbf{u} \\ \boldsymbol{\lambda} \end{Bmatrix} = \begin{Bmatrix} \mathbf{f} \\ \mathbf{q} \end{Bmatrix} \tag{5.4}$$

where , $K_{IJ} = \int_{\Omega} \mathbf{B}_I^T \mathbf{D} \mathbf{B}_J \, d\Omega$, $f_I = \int_{\Gamma_t} \bar{\mathbf{t}} \Phi_I \, d\Gamma$, $q_K = -\int_{\Gamma_u} \mathbf{N}_K \bar{u} \, d\Gamma$,

$$\mathbf{B}_I = \begin{bmatrix} \Phi_{I,x} & 0 \\ 0 & \Phi_{I,y} \\ \Phi_{I,y} & \Phi_{I,x} \end{bmatrix}, \ \mathbf{N}_K = \begin{bmatrix} N_K & 0 \\ 0 & N_K \end{bmatrix}, \ \mathbf{D} = \frac{E}{1-\nu^2} \begin{bmatrix} 1 & \nu & 0 \\ \nu & 1 & 0 \\ 0 & 0 & (1-\nu)/2 \end{bmatrix} \text{ (for plane stress)}$$

5.2.1 Governing Equations of Thermo-elasticity

The equations for static linear isotropic thermo-elasticity problem with small displacements on the domain Ω bounded by Γ is given as

$$\mathbf{q} = -k \nabla T \tag{5.5}$$

$$-\nabla \mathbf{q} + \bar{Q} = 0 \tag{5.6}$$

$$\boldsymbol{\varepsilon} = \nabla_s \mathbf{u} \tag{5.7}$$

$$\boldsymbol{\varepsilon}_T = \beta (T - T_0) \bar{\mathbf{I}} \tag{5.8}$$

$$\boldsymbol{\sigma} = \mathbf{C} : (\boldsymbol{\varepsilon} - \boldsymbol{\varepsilon}_T) \tag{5.9}$$

$$\nabla \cdot \boldsymbol{\sigma} + \mathbf{b} = 0 \tag{5.10}$$

In the above equations , T is temperature, $\mathbf{q}$ is heat flux vector, $\mathbf{u}$ is displacement vector, $\boldsymbol{\varepsilon}$ is strain tensor, $\boldsymbol{\sigma}$ is stress tensor, and $\boldsymbol{\varepsilon}_T$ thermal strain vector defined with respect to a reference temperature T_0 , β is thermal expansion coefficient, k is thermal conductivity, $\mathbf{C}$ is isotropic fourth order Hooks tensor, $\mathbf{b}$ is prescribed body force and $\bar{Q}$ is the prescribed heat source. $\bar{\mathbf{I}}$ represents the second order identity tensor and ∇_s is the symmetric gradient operator on vector field. The essential and natural boundary conditions are given as

$$\mathbf{u} = \bar{\mathbf{u}} \text{ on } \Gamma_u \tag{5.11}$$

$$\boldsymbol{\sigma}.\bar{\mathbf{n}}=\bar{\mathbf{t}} \text{ on } \Gamma_t \tag{5.12}$$

$$\mathbf{T}=\bar{\mathbf{T}} \text{ on } \Gamma_T \tag{5.13}$$

$$\mathbf{q}\cdot\mathbf{n}=\bar{q} \text{ on } \Gamma_q \tag{5.14}$$

where, $\bar{\mathbf{t}}$ is the traction force, $\bar{\mathbf{n}}$ is the unit normal with $\Gamma_T \cup \Gamma_q = \Gamma_u \cup \Gamma_t = \Gamma$ and $\Gamma_T \cap \Gamma_q = \Gamma_u \cap \Gamma_t = \phi$. The crack surface within the domain is represented by Γ_c and is considered traction free.

To obtain the solution of a thermo-elastic problem, initially Eq. (5.5) and Eq. (5.6) are solved for thermal solution. This solution is then used in Eq. (5.7) to Eq. (5.10) to obtain the solution of thermo-elastic problem. Two different cases are chosen by assuming crack surfaces as either adiabatic or isothermal.

5.2.2 Modeling of Adiabatic Crack

For an adiabatic crack, both displacement and temperature fields become discontinuous across the crack surface and heat flux is found singular at the crack tip (Sih, 1962). The boundary condition for an adiabatic crack can be stated as

- $\mathbf{q}.\bar{\mathbf{n}}=0$ on Γ_c, hence $\mathbf{T}$ is discontinuous across Γ_c
- $\boldsymbol{\sigma}.\bar{\mathbf{n}}=0$ on Γ_c, hence $\mathbf{u}$ discontinuous across Γ_c

Thus, the case of adiabatic crack is a simple extension of EFGM in elasticity. Here both temperature and displacement fields are to be enriched intrinsically. Once the temperature distribution is obtained, it can be employed as input for determining the stress and displacement fields. According to intrinsic enrichment criterion, the presence of a crack is ensured by enrichment terms i.e. by adding extra terms in the basis function. The choice of enrichment functions depends on the accuracy desired. For higher accuracy, one can include the full asymptotic field, while for higher speed at the cost of

accuracy; only $\sqrt{r}$ can be included in the basis. A full intrinsic enriched basis function used in the present analysis for adiabatic crack is given as

$$\mathbf{P}^T(\mathbf{x}) = \left[\underbrace{1,\ x,\ y}_{\substack{\text{standard} \\ \text{basis}}},\ \underbrace{\sqrt{r}\cos\frac{\theta}{2}, \sqrt{r}\sin\frac{\theta}{2}, \sqrt{r}\sin\frac{\theta}{2}\sin\theta, \sqrt{r}\cos\frac{\theta}{2}\sin\theta}_{\text{enrichment terms}} \right] \tag{5.15}$$

where, $\mathbf{P}(\mathbf{x})$ is the enriched basis function, r and θ are the local crack tip parameters. The first three terms of Eq. (5.15) represent the standard basis function $(1,\ x,\ y)$ while the remaining four terms obtained from the crack tip solution makes up the enrichment part. For modelling an adiabatic crack, the above equation is used as basis function for the modelling of the thermal and mechanical parts.

5.2.3 Modelling of an Isothermal Crack

In case of an isothermal crack, the temperature is prescribed at the crack surface. The basic features of an isothermal crack formulation (Duflot, 2008) are described below

- Temperature is specified on crack surface (Γ_c) and hence, the heat flux becomes discontinuous across the crack.
- The crack surface (Γ_c) is considered as a part of essential boundary (Γ_T), hence the variational formulation changes accordingly.
- Angular variation of singularity at the crack tip is different from a crack under mechanical load.

The thermal boundary condition for an isothermal crack can be stated as $\mathrm{T} = \overline{\mathrm{T}}$ on Γ_c. The imposition of essential boundary condition over the crack surface is carried out by Lagrange Multiplier scheme (Yagawa and Furukawa, 2000; Phu *et al.*, 2008). For this

purpose, extra nodes are defined over the crack surface Γ_c, which is a part of the essential boundary. The leading terms of the asymptotic expansion of temperature and flux near an isothermal crack are as follows (Duflot, 2008)

$$T = \frac{K_T}{k}\sqrt{\frac{2r}{\pi}}\cos\left(\frac{\theta}{2}\right) \tag{5.16}$$

$$\mathbf{q} = \frac{K_T}{2\pi r}\begin{pmatrix}\cos\left(\frac{\theta}{2}\right)\\ \sin\left(\frac{\theta}{2}\right)\end{pmatrix} \tag{5.17}$$

The crack tip enrichment is carried out using first term of enrichment function used previously, hence the basis for isothermal crack in the present analysis becomes

$$\mathbf{P}^T(\mathbf{x}) = \left[\underbrace{1,\ x,\ y}_{\substack{\text{standard}\\ \text{basis}}},\ \underbrace{\sqrt{r}\cos\frac{\theta}{2}}_{\text{enrichment terms}}\right] \tag{5.18}$$

The above Eq. (5.18) is used as enrichment function for the thermal solution only while Eq. (5.15) is used as basis for the mechanical solution.

5.3 EVALUATION OF STRESS INTENSITY FACTORS

For thermo-elastic problems (Khandelwal and Kishen, 2007), the detailed procedure of evaluating the stress intensity factors is described below for the sake of completeness.

5.3.1 Conservative M-Integral for Thermo-Elastic Loading

Consider a homogeneous cracked body subjected to a two-dimensional deformation fields (plane strain, generalized plane stress, anti-plane strain). Suppose the body contains a crack of the type shown in Fig. 5.2 having flat surfaces parallel to x_1-axis. Let Γ be a path surrounding the crack with an enclosed area A_o.

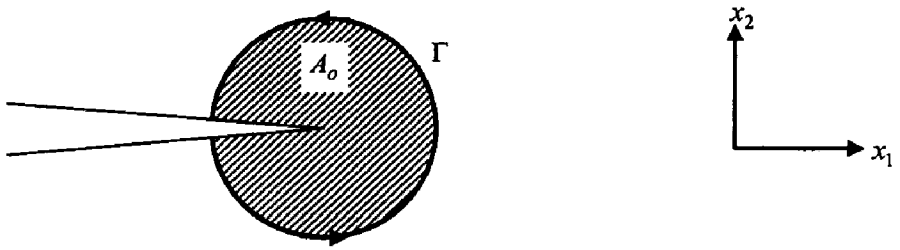

Fig. 5.2: Path Γ surrounding a crack with an enclosed area A_o

For an isothermal problem, the path independent J - integral near a crack tip is given by (Wilson and Yu, 1979).

$$J = \int_{\Gamma}\left(\tilde{W}\delta_{1j} - \sigma_{ij}\frac{\partial u_i}{\partial x_1}\right)n_j\, d\Gamma \tag{5.19}$$

where, $\tilde{W}$ is the strain energy density and n_j is the j_{th} component of outward unit normal to an arbitrary contour Γ enclosing the crack tip. For linear elastic models, it can be shown that $\tilde{W} = \varepsilon_{ij}\sigma_{ij}/2$. J-integral defined in Eq. (5.19) is not path independent for a thermo-elastic problem. Suppose the integral in Eq. (5.19) is taken on a closed path Γ_0 then the contour integral can be converted into an equivalent area integral

$$J_1 = \oint_{\Gamma_0}\left(\tilde{W}\delta_{ij} - \sigma_{ij}\frac{\partial u_i}{\partial x_1}\right)n_j d\Gamma = \int_{A_o}\left(\frac{d\tilde{W}}{dx_1} - \sigma_{ij}\frac{\partial \varepsilon_{ij}}{\partial x_1}\right)dA \tag{5.20}$$

where, A_o is the area enclosed by the path Γ_0 and $\tilde{W}$ is the strain energy density given by

$$\tilde{W} = \frac{1}{2}\left(\sigma_{11}\varepsilon_{11} + \sigma_{12}\varepsilon_{12} + \sigma_{21}\varepsilon_{21} + \sigma_{22}\varepsilon_{22}\right) \tag{5.21}$$

$$\frac{d\tilde{W}}{dx_1} = \frac{1}{2}\left(\sigma_{11}\frac{\partial \varepsilon_{11}}{\partial x_1} + \sigma_{12}\frac{\partial \varepsilon_{12}}{\partial x_1} + \sigma_{21}\frac{\partial \varepsilon_{21}}{\partial x_1} + \sigma_{22}\frac{\partial \varepsilon_{22}}{\partial x_1}\right) +$$

$$\frac{1}{2}\left(\frac{\partial \sigma_{11}}{\partial x_1}\varepsilon_{11} + \frac{\partial \sigma_{12}}{\partial x_1}\varepsilon_{12} + \frac{\partial \sigma_{21}}{\partial x_1}\varepsilon_{21} + \frac{\partial \sigma_{22}}{\partial x_1}\varepsilon_{22}\right) \tag{5.22}$$

$$\frac{d\widetilde{W}}{dx_1} = \frac{1}{2}\sigma_{ij}\frac{\partial \varepsilon_{ij}}{\partial x_1} + \mathrm{X}/2 \tag{5.23}$$

$$\text{where, } \mathrm{X} = \left(\frac{\partial \sigma_{11}}{\partial x_1}\varepsilon_{11} + \frac{\partial \sigma_{12}}{\partial x_1}\varepsilon_{12} + \frac{\partial \sigma_{21}}{\partial x_1}\varepsilon_{21} + \frac{\partial \sigma_{22}}{\partial x_1}\varepsilon_{22}\right) \tag{5.24}$$

The constitutive relations for thermal loading are

$$\varepsilon_{11} = \frac{1}{E}(\sigma_{11} - \nu\sigma_{22}) + \beta T \quad , \quad \sigma_{11} = \frac{E}{1-\nu^2}[\varepsilon_{11} + \nu\varepsilon_{22} - (1+\nu)\beta T]$$

$$\varepsilon_{22} = \frac{1}{E}(\sigma_{22} - \nu\sigma_{11}) + \beta T \quad , \quad \sigma_{22} = \frac{E}{1-\nu^2}[\varepsilon_{22} + \nu\varepsilon_{11} - (1+\nu)\beta T]$$

$$\varepsilon_{12} = \varepsilon_{21} = \frac{1}{2G}\sigma_{12} = \frac{1+\nu}{E}\sigma_{12} \quad , \quad \sigma_{12} = \sigma_{21} = \frac{E}{1+\nu}\varepsilon_{12} = \frac{E}{1+\nu}\varepsilon_{21}$$

Substituting above constitutive relations in Eq. (5.24), we get

$$\mathrm{X} = \frac{E}{1-\nu^2}\left[\frac{\partial \varepsilon_{11}}{\partial x_1} + \nu\frac{\varepsilon_{22}}{\partial x_1} - (1+\nu)\beta\frac{\partial T}{\partial x_1}\right]\varepsilon_{11} + \sigma_{12}\frac{\partial \varepsilon_{12}}{\partial x_1} +$$

$$\sigma_{21}\frac{\partial \varepsilon_{21}}{\partial x_1} + \frac{E}{1-\nu^2}\left[\frac{\partial \varepsilon_{22}}{\partial x_1} + \nu\frac{\varepsilon_{11}}{\partial x_1} - (1+\nu)\beta\frac{\partial T}{\partial x_1}\right]\varepsilon_{22}$$

$$= \frac{E}{1-\nu^2}(\varepsilon_{11} + \nu\varepsilon_{22})\frac{\partial \varepsilon_{11}}{\partial x_1} + \frac{E}{1-\nu^2}(\varepsilon_{22} + \nu\varepsilon_{11})\frac{\partial \varepsilon_{22}}{\partial x_1} - \frac{E\beta}{1-\nu}\left(\frac{\partial T}{\partial x_1}\right)\varepsilon_{kk} + \sigma_{12}\frac{\partial \varepsilon_{12}}{\partial x_1} + \sigma_{21}\frac{\partial \varepsilon_{21}}{\partial x_1}$$

$$= \left(\sigma_{11} + \frac{E\beta T}{1-\nu}\right)\frac{\partial \varepsilon_{11}}{\partial x_1} + \left(\sigma_{22} + \frac{E\beta T}{1-\nu}\right)\frac{\partial \varepsilon_{22}}{\partial x_1} - \frac{E\beta}{1-\nu}\left(\frac{\partial T}{\partial x_1}\right)\varepsilon_{kk} + \sigma_{12}\frac{\partial \varepsilon_{12}}{\partial x_1} + \sigma_{21}\frac{\partial \varepsilon_{21}}{\partial x_1}$$

$$\mathrm{X} = \sigma_{ij}\frac{\partial \varepsilon_{ij}}{\partial x_1} + \left(\frac{E\beta}{1-\nu}\right)T\frac{\partial \varepsilon_{kk}}{\partial x_1} - \left(\frac{E\beta}{1-\nu}\right)\frac{\partial T}{\partial x_1}\varepsilon_{kk} \tag{5.25}$$

Substituting the value of X from Eq. (5.25) into Eq. (5.23), we get

$$\frac{d\widetilde{W}}{dx_1} = \sigma_{ij}\frac{\partial \varepsilon_{ij}}{\partial x_1} + \frac{1}{2}\left(\widetilde{\beta}T\frac{\partial \varepsilon_{kk}}{\partial x_1} - \widetilde{\beta}\frac{\partial T}{\partial x_1}\varepsilon_{kk}\right), \quad \text{where} \quad \widetilde{\beta} = \frac{E\beta}{1-\nu}$$

Hence, from Eq. (5.20) domain form of J-integral for thermal loading becomes

$$J_1 = \frac{1}{2}\int_{A_o}\left(\widetilde{\beta}T\frac{\partial \varepsilon_{kk}}{\partial x_1} - \widetilde{\beta}\frac{\partial T}{\partial x_1}\varepsilon_{kk}\right)dA \tag{5.26}$$

$$J_1 - \frac{1}{2}\int_{A_o}\left(\widetilde{\beta}T\frac{\partial \varepsilon_{kk}}{\partial x_1} - \widetilde{\beta}\frac{\partial T}{\partial x_1}\varepsilon_{kk}\right)dA = 0 \tag{5.27}$$

$$J_1 - \int_{A_o}\frac{\widetilde{\beta}}{2}\left(\frac{\partial}{\partial x_1}(T\varepsilon_{kk}) - 2\frac{\partial T}{\partial x_1}\varepsilon_{kk}\right)dA = 0 \tag{5.28}$$

$$J_1 - \int_{\Gamma}\frac{\widetilde{\beta}}{2}T\,\varepsilon_{kk}\,\delta_{1j}n_j d\Gamma + \widetilde{\beta}\int_{A_o}\frac{\partial T}{\partial x_1}\varepsilon_{kk}\,dA = 0 \tag{5.29}$$

Substituting the expression of J_1 from Eq. (5.19), the integral on a closed path Γ_0

$$\oint_{\Gamma_0}\left[\left(W - \frac{\widetilde{\beta}}{2}T\,\varepsilon_{kk}\right)\delta_{1j} - \sigma_{ij}\frac{\partial u_i}{\partial x_1}\right]n_j\,d\Gamma_0 + \widetilde{\beta}\int_{A_o}\frac{\partial T}{\partial x_1}\varepsilon_{kk}\,dA_o = 0 \tag{5.30}$$

and hence, $\int_{\Gamma}\left[\left(W - \frac{\widetilde{\beta}}{2}T\,\varepsilon_{kk}\right)\delta_{1j} - \sigma_{ij}\frac{\partial u_i}{\partial x_1}\right]n_j\,d\Gamma + \widetilde{\beta}\int_{A_o}\frac{\partial T}{\partial x_1}\varepsilon_{kk}\,dA_o$ is path independent for the case of thermal loading.

5.3.1.1 Thermal Interaction Integral for Homogeneous Materials

For calculating the thermal interaction integral for a homogeneous body, we consider two equilibrium states of a cracked body. State 1 is the actual state with given boundary conditions while state 2 is an auxiliary state. Superscript a represents the parameters for auxiliary state problem. Temperature for auxiliary state is considered zero.

Actual state: σ_{ij} ε_{ij} u_i T J^1

Auxiliary state: σ^a_{ij} ε^a_{ij} u^a_i 0 J^a

Defining thermal J - integral for both states

$$J^1 = \int_{\Gamma}\left[\left(\widetilde{W}_1 - \frac{\widetilde{\beta}}{2}T\,\varepsilon_{kk}\right)\delta_{1j} - \sigma_{ij}\frac{\partial u_i}{\partial x_1}\right]n_j\,d\Gamma + \widetilde{\beta}\int_{A_o}\frac{\partial T}{\partial x_1}\varepsilon_{kk}\,dA_o \tag{5.31}$$

$$J^2 = \int_{\Gamma}\left[\left(\widetilde{W}_a\,\delta_{1j}\right) - \sigma^a_{ij}\frac{\partial u^a_i}{\partial x_1}\right]n_j\,d\Gamma \tag{5.32}$$

The J-integral for the two superimposed state will be given as

$$J_{Total} = \int_{\Gamma}\left[\left\{\left(\tilde{W}_1 + \tilde{W}_2 + \tilde{W}_{12}\right) - \frac{\tilde{\beta}}{2}T\left(\varepsilon_{kk} + \varepsilon^a_{kk}\right)\right\}\delta_{1j} - \left(\sigma_{ij} + \sigma^a_{ij}\right)\left(\frac{\partial u_i}{\partial x_1} + \frac{\partial u^a_i}{\partial x_1}\right)\right] n_j \, d\Gamma$$

$$+ \tilde{\beta}\int_{A_o}\frac{\partial T}{\partial x_1}\left(\varepsilon_{kk} + \varepsilon^a_{kk}\right) dA_o \tag{5.33}$$

$$J_{Total} = J^1 + J^2 + M_{12} \tag{5.34}$$

where,

$$M_{12} = \int_{\Gamma}\left[\left\{\tilde{W}_{12} - \frac{\tilde{\beta}}{2}T\,\varepsilon^a_{kk}\right\}\delta_{1j} - \sigma_{ij}\frac{\partial u^a_i}{\partial x_1} - \sigma^a_{ij}\frac{\partial u_i}{\partial x_1}\right] n_j d\Gamma + \tilde{\beta}\int_{A_o}\frac{\partial T}{\partial x_1}\varepsilon^a_{kk}\, dA_o \tag{5.35}$$

In order to enhance the usefulness and convenience, the contour form of M integral in Eq. (5.35) can be converted to equivalent domain integral form. Figure 5.2 is modified by defining an another path Γ_1 around the crack tip such that the area enclosed within the closed domain is A . The two paths Γ and Γ_1 are connected by two different paths C_+ and C_- defined parallel to X - axis as shown in Fig. 5.3.

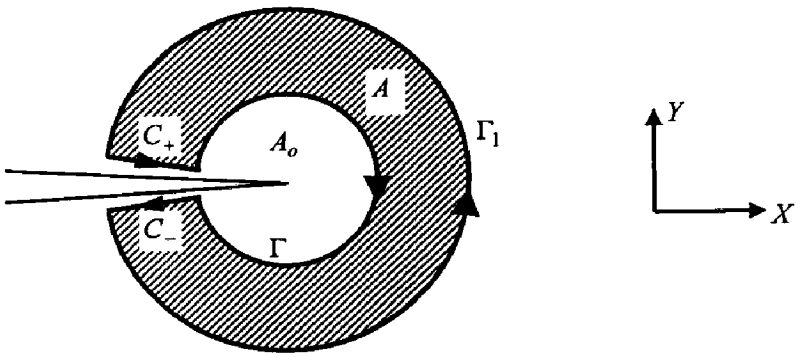

Fig. 5.3: Path independent closed contour around the crack tip

Hence, Eq. (5.35) can be converted to a path integral on a closed path consisting of Γ, C_-, Γ_1 and C_+.

$$M_{12} = -\oint\left[\left\{\tilde{W}_{12} - \frac{\tilde{\beta}}{2}T\,\varepsilon^a_{kk}\right\}\delta_{1j} - \sigma_{ij}\frac{\partial u^a_i}{\partial x_1} - \sigma^a_{ij}\frac{\partial u_i}{\partial x_1}\right] n_j \bar{q}\, ds + \tilde{\beta}\int_{A_o}\frac{\partial T}{\partial x_1}\varepsilon^a_{kk}\, dA_o \tag{5.36}$$

where, $\bar{q}$ is a weight function chosen such that it has a value of *unity* at the inner path Γ, *zero* along the outer path Γ_1, and arbitrary elsewhere. The (-) sign in Eq. (5.36) appears because the path Γ is being traversed in clockwise sense as opposed to the counter clockwise sense in Fig. 5.2,

Converting the line integral into area integral using Gauss divergence theorem, we get

$$M_{12} = \int_A \left[\sigma_{ij} \frac{\partial u_i^a}{\partial x_1} + \sigma_{ij}^a \frac{\partial u_i}{\partial x_1} - \left(\tilde{W}_{12} - \frac{\tilde{\beta}}{2} T \varepsilon_{kk}^a \right) \delta_{1j} \right] \frac{\partial \bar{q}}{\partial x_j} dA + + \tilde{\beta} \int_{A_o} \frac{\partial T}{\partial x_1} \varepsilon_{kk}^a \, dA$$

$$+ \int_A \frac{\partial}{\partial x_j} \left[\sigma_{ij} \frac{\partial u_i^a}{\partial x_1} + \sigma_{ij}^a \frac{\partial u_i}{\partial x_1} - \left(\tilde{W}_{12} - \frac{\tilde{\beta}}{2} T \varepsilon_{kk}^a \right) \delta_{1j} \right] \bar{q} \, dA \tag{5.37}$$

$\tilde{W}_{12}$ may be expressed as

$$\tilde{W}_{12} = \frac{1}{2} \left[\sigma_{ij} \varepsilon_{ij}^a + \sigma_{ij}^a \varepsilon_{ij} \right]$$

$$= \frac{1}{2} \left[\sigma_{ij} \varepsilon_{ij}^a + \frac{E}{1-\nu^2} \left(\varepsilon_{11}^a + \nu \varepsilon_{22}^a \right) \varepsilon_{11} + \frac{E}{1+\nu} \left(\varepsilon_{12}^a \varepsilon_{12} + \varepsilon_{21}^a \varepsilon_{21} \right) + \frac{E}{1-\nu^2} \left(\varepsilon_{22}^a + \nu \varepsilon_{11}^a \right) \varepsilon_{22} \right]$$

$$= \frac{1}{2} \left[\sigma_{ij} \varepsilon_{ij}^a + \frac{E}{1-\nu^2} \left(\varepsilon_{11} + \nu \varepsilon_{22} \right) \varepsilon_{11}^a + \varepsilon_{12}^a \sigma_{12} + \varepsilon_{21}^a \sigma_{21} + \frac{E}{1-\nu^2} \left(\nu \varepsilon_{11} + \varepsilon_{22} \right) \varepsilon_{22}^a \right]$$

$$= \frac{1}{2} \left[\sigma_{ij} \varepsilon_{ij}^a + \left(\sigma_{11} + \frac{E}{1-\nu} \beta T \right) \varepsilon_{11}^a + \varepsilon_{12}^a \sigma_{12} + \varepsilon_{21}^a \sigma_{21} + \left(\sigma_{22} + \frac{E}{1-\nu} \beta T \right) \varepsilon_{22}^a \right]$$

$$= \frac{1}{2} \left[\sigma_{ij} \varepsilon_{ij}^a + \sigma_{ij} \varepsilon_{ij}^a + \frac{E}{1-\nu} \beta T \varepsilon_{kk}^a \right]$$

$$= \frac{1}{2} \left[\sigma_{ij} \varepsilon_{ij}^a + \sigma_{ij} \varepsilon_{ij}^a + \tilde{\beta} T \varepsilon_{kk}^a \right]$$

$$= \sigma_{ij} \varepsilon_{ij}^a + \frac{\tilde{\beta}}{2} T \varepsilon_{kk}^a \tag{5.38}$$

Substituting the value of $\tilde{W}_{12}$ in Eq. (5.37), we get the following expression of interaction integral

$$M_{12} = \int_A \left(\sigma_{ij} \frac{\partial u_i^a}{\partial x_1} + \sigma_{ij}^a \frac{\partial u_i}{\partial x_1} - \sigma_{ik}\, \varepsilon_{ik}^a \delta_{1j} \right) \frac{\partial \overline{q}}{\partial x_j} dA + \tilde{\beta} \int_{A_o} \frac{\partial T}{\partial x_1} \varepsilon_{kk}^a \, dA$$

$$+ \int_A \frac{\partial}{\partial x_j} \left[\sigma_{ij} \frac{\partial u_i^a}{\partial x_1} + \sigma_{ij}^a \frac{\partial u_i}{\partial x_1} - \sigma_{ik} \varepsilon_{ik}^a \delta_{ij} \right] \overline{q} \, dA \tag{5.39}$$

$$M_{12} = \int_A \left(\sigma_{ij} \frac{\partial u_i^a}{\partial x_1} + \sigma_{ij}^a \frac{\partial u_i}{\partial x_1} - \sigma_{ik}\, \varepsilon_{ik}^a \delta_{1j} \right) \frac{\partial \overline{q}}{\partial x_j} dA + \tilde{\beta} \int_{A_o} \frac{\partial T}{\partial x_1} \varepsilon_{kk}^a \, dA + \int_A Z\, \overline{q} \tag{5.40}$$

where, $Z = \dfrac{\partial}{\partial x_j} \left[\sigma_{ij} \dfrac{\partial u_i^a}{\partial x_1} + \sigma_{ij}^a \dfrac{\partial u_i}{\partial x_1} - \sigma_{ik} \varepsilon_{ik}^a \delta_{1j} \right]$ (5.41)

$$= \frac{\partial \sigma_{ij}}{\partial x_j} \frac{\partial u_i^a}{\partial x_1} + \sigma_{ij} \frac{\partial}{\partial x_1} \left(\frac{\partial u_i^a}{\partial x_j} \right) + \frac{\partial \sigma_{ij}^a}{\partial x_j} \frac{\partial u_i}{\partial x_1} + \sigma_{ij}^a \frac{\partial}{\partial x_1} \left(\frac{\partial u_i}{\partial x_j} \right) - \frac{\partial}{\partial x_1} \left(\sigma_{ij}\, \varepsilon_{ij}^a \right)$$

$$= \sigma_{ij} \frac{\partial \varepsilon_{ij}^a}{\partial x_1} + \sigma_{ij}^a \frac{\partial \varepsilon_{ij}}{\partial x_1} - \sigma_{ij} \frac{\partial \varepsilon_{ij}^a}{\partial x_1} - \frac{\partial \sigma_{ij}}{\partial x_1} \varepsilon_{ij}^a$$

$$= \sigma_{ij}^a \frac{\partial \varepsilon_{ij}}{\partial x_1} - \frac{\partial \sigma_{ij}}{\partial x_1} \varepsilon_{ij}^a \tag{5.42}$$

Also,

$$\frac{\partial \sigma_{ij}}{\partial x_1} \varepsilon_{ij}^a = \frac{\partial}{\partial x_1} \left[\frac{E}{1-\nu^2} \{ \varepsilon_{11} + \nu \varepsilon_{22} - (1+\nu) \beta T \} \right] \varepsilon_{11}^a + \frac{\partial}{\partial x_1} \left[\frac{E}{1-\nu^2} \{ \varepsilon_{22} + \nu \varepsilon_{11} - (1+\nu) \beta T \} \right] \varepsilon_{22}^a$$

$$+ \frac{E}{1+\nu} \left(\frac{\partial \varepsilon_{12}}{\partial x_1} \right) \varepsilon_{12}^a + \frac{E}{1+\nu} \left(\frac{\partial \varepsilon_{21}}{\partial x_1} \right) \varepsilon_{21}^a$$

$$= \frac{\partial \varepsilon_{11}}{\partial x_1} \left[\frac{E}{1-\nu^2} \{ \varepsilon_{11}^a + \nu \varepsilon_{22}^a \} \right] + \frac{\partial \varepsilon_{12}}{\partial x_1} \sigma_{12}^a + \frac{\partial \varepsilon_{21}}{\partial x_1} \sigma_{22}^a + \frac{\partial \varepsilon_{22}}{\partial x_1} \left[\frac{E}{1-\nu^2} \{ \varepsilon_{22}^a + \nu \varepsilon_{11}^a \} \right] - (1+\nu) \beta \frac{\partial T}{\partial x_1} \varepsilon_{kk}^a$$

$$= \sigma_{ij}^a \frac{\partial \varepsilon_{ij}}{\partial x_1} - \tilde{\beta} \frac{\partial T}{\partial x_1} \varepsilon_{kk}^a \tag{5.43}$$

Hence, $Z = \tilde{\beta}\frac{\partial T}{\partial x_1}\varepsilon^a_{kk}$ (5.44)

Substituting the value of Z in Eq. (5.40), we get

$$M_{12} = \int_A \left(\sigma_{ij}\frac{\partial u_i^a}{\partial x_1} + \sigma_{ij}^a\frac{\partial u_i}{\partial x_1} - \sigma_{ik}\,\varepsilon_{ik}^a\delta_{1j} \right)\frac{\partial \overline{q}}{\partial x_j}dA + \tilde{\beta}\int_{A_o}\frac{\partial T}{\partial x_1}\varepsilon_{kk}^a\,dA + \tilde{\beta}\int_A \frac{\partial T}{\partial x_1}\varepsilon_{kk}^a\,\overline{q}\,dA \quad (5.45)$$

In its limiting case, the inner path Γ is taken so small that it nearly shrinks to the crack tip, and the enclosed area can be considered as zero i.e. $A_o \approx 0$. Hence, expression of interaction integral becomes

$$M_{12} = \int_A \left(\sigma_{ij}\frac{\partial u_i^a}{\partial x_1} + \sigma_{ij}^a\frac{\partial u_i}{\partial x_1} - \sigma_{ik}\,\varepsilon_{ik}^a\delta_{1j} \right)\frac{\partial \overline{q}}{\partial x_j}dA + \tilde{\beta}\int_A \frac{\partial T}{\partial x_1}\varepsilon_{kk}^a\,\overline{q}\,dA \quad (5.46)$$

$\because \varepsilon_{kk} = \frac{1-\nu}{E}\sigma_{kk}$

$\therefore \tilde{\beta}\varepsilon_{kk}^a = \beta\sigma_{kk}^a$

$$M_{12} = \int_A \left(\sigma_{ij}\frac{\partial u_i^a}{\partial x_1} + \sigma_{ij}^a\frac{\partial u_i}{\partial x_1} - \sigma_{ik}\,\varepsilon_{ik}^a\delta_{1j} \right)\frac{\partial \overline{q}}{\partial x_j}dA + \beta\int_A \frac{\partial T}{\partial x_1}\sigma_{kk}^a\,\overline{q}\,dA \quad (5.47)$$

For a bi-material interface crack having the crack as well as the interface in x_1 direction the above expression of interaction integral gets modified in a very simple way. It may be expressed as

$$M_{12} = \sum_{\tilde{k}=1}^{2}\int_{A_{\tilde{k}}} \left(\sigma_{ij}\frac{\partial u_i^a}{\partial x_1} + \sigma_{ij}^a\frac{\partial u_i}{\partial x_1} - \sigma_{ik}\,\varepsilon_{ik}^a\delta_{1j} \right)\frac{\partial \overline{q}}{\partial x_j}dA + \sum_{\tilde{k}=1}^{2}\beta\int_{A_{\tilde{k}}}\frac{\partial T}{\partial x_1}\sigma_{kk}^a\,\overline{q}\,dA \quad (5.48)$$

where, $\tilde{k} = 1,2$ represents the two materials of the bi-material domain

For linear-elastic solids under mixed mode loading conditions, the J-integral is also equal to the energy release rate and hence, it can be written as

$$J = \frac{1}{\overline{H}}\left(K_I^2 + K_{II}^2\right) \tag{5.49}$$

where, $\overline{H} = E^*$ for isotropic material and $\frac{1}{\overline{H}} = \frac{1/E_1^* + 1/E_2^*}{2\cosh^2 \pi\tilde{\varepsilon}}$ for bi-material.

$$E^* = \begin{cases} \dfrac{E}{1-\nu^2} & Plane\ strain \\ E & Plane\ stress \end{cases} \tag{5.50}$$

Applying Eq. (5.49) to both main and auxiliary state, we get

$$J^1 = \frac{1}{\overline{H}}\left(K_I^{(1)^2} + K_{II}^{(1)^2}\right) \tag{5.51}$$

$$J^2 = \frac{1}{\overline{H}}\left(K_I^{(2)^2} + K_{II}^{(2)^2}\right) \tag{5.52}$$

The superimposed state can be written as

$$J^s = \frac{1}{\overline{H}}\left[\left(K_I^{(1)} + K_I^{(2)}\right)^2 + \left(K_{II}^{(1)} + K_{II}^{(2)}\right)^2\right] \tag{5.53}$$

$$= \frac{1}{\overline{H}}\left[\left(K_I^{(1)^2} + K_{II}^{(1)^2}\right) + \left(K_I^{(2)^2} + K_{II}^{(2)^2}\right) + 2\left(K_I^{(1)}K_I^{(2)} + K_{II}^{(1)}K_{II}^{(2)}\right)\right]$$

$$= J^1 + J^2 + \frac{2}{\overline{H}}\left(K_I^{(1)}K_I^{(2)} + K_{II}^{(1)}K_{II}^{(2)}\right) \tag{5.54}$$

Comparing Eq. (5.54) with Eq. (5.34), we get

$$M_{12} = \frac{2}{\overline{H}}\left(K_I^{(1)}K_I^{(2)} + K_{II}^{(1)}K_{II}^{(2)}\right) \tag{5.55}$$

The individual SIFs for the actual state can be obtained by judiciously choosing the auxiliary state (state 2). For example, if state 2 is chosen to correspond to a mode I state, then $K_I^{(2)} = 1$ and $K_{II}^{(2)} = 0$. Hence Eq. (5.55) is reduced to

$$M_{1I} = \frac{2K_I^{(1)}}{\overline{H}} \tag{5.56}$$

$$\text{or } K_I^{(1)} = \frac{\overline{H} M_{1I}}{2} \tag{5.57}$$

Similarly, if state 2 is chosen to correspond to a mode II state, then $K_I^{(2)} = 0$ and $K_{II}^{(2)} = 1$, then following the same considerations, we get

$$K_{II}^{(1)} = \frac{\overline{H} M_{1II}}{2} \tag{5.58}$$

The interaction integral evaluated from Eq. (5.47) and Eq. (5.48) can be used further for calculating the SIFs under various mixed mode loading conditions.

5.4 RESULTS AND DISCUSSIONS

Numerical results are presented for different problems in order to validate the applicability of EFGM in thermo-elastic problems. Plane strain condition is assumed in all examples due to availability of reference solutions. The boundary conditions are given with respect to the reference temperature $\Theta = T - T_0$, where, T is the applied temperature and T_0 is the reference temperature. The value of Poisson's ratio is taken as 0.3. The problem domain has been divided into background cells, and in each background cell, six points Gauss quadrature (Krongauz and Belytschko, 1996) i.e. 36 Guass points have been used for the numerical integration (Phu *et al.*, 2008) of the Galerkin weak form. During numerical integration, the number of nodes in the domain of influence varies for each evaluation point but an average number of nodes in the domain of influence are prescribed for each solved example.

5.4.1 Edge Crack under Constant Heat Flux

The first example considered is an edge cracked rectangular strip as shown in Fig. 5.4a having the dimensions $H = 1$, $W = 0.5$ and $a = 0.25$. The problem domain has been discretized by taking 20 uniformly distributed nodes along x-direction and 40 nodes along y-direction i.e. total 800 (20x40) nodes.

The crack is modelled as an adiabatic crack. Known temperature is applied on right and left sides such that the crack is subjected to a constant heat flux (parallel to crack surface). In this case, heat flux and temperature remain unaffected by the presence of crack as can be clearly seen in Fig. 5.4b. Displacement boundary conditions are prescribed in such a way that the vertical displacement of top and bottom sides is restrained. The body is free from any external traction. A pure mode-I loading is generated under the prescribed thermal and mechanical boundary conditions.

Numerical values of stress intensity factor have been evaluated by modified *M*-integral, and are normalized according to the relation

$$\widetilde{F}_I = \frac{K_I}{\dfrac{E}{1-\nu}\beta\Theta\sqrt{\pi a}} \tag{5.59}$$

where, E is the Young's modulus, ν is the Poisson's ratio, β is the coefficient of linear expansion, a is the crack length and $\Theta = T - T_0$ with T is the applied temperature and T_0 is the reference temperature. In order to validate the domain independence of the modified *M*- integral, the value of $\widetilde{F}_I$ has been evaluated for different domains surrounding the crack tip. The results show a good agreement with the results available in literature (Duflot, 2008) with the maximum error of 0.08 percent.

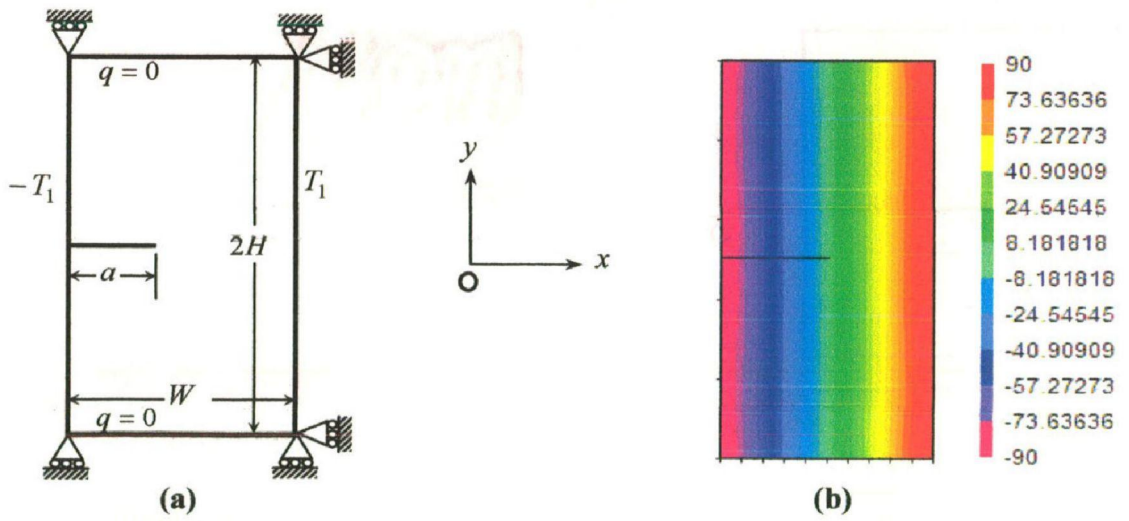

Fig. 5.4: Edge crack under constant flux: (**a**) Problem geometry (**b**) Temperature Profile

5.4.2 Square Plate with Centre Crack

Next we consider a centre crack in a square plate subjected to two different set of boundary conditions:

- ❖ An adiabatic crack subjected to a heat flux perpendicular to the crack surface.
- ❖ An isothermal crack at a temperature different from the temperatures at the boundary.

Figure 5.5a shows the geometry of a square plate along with mechanical and thermal boundary conditions. The length parameter $W = 1$ unit while a varies from 0.1 to 0.6 with a step increment of 0.1. Temperatures are prescribed at the top and bottom edges of the plate. The applied temperatures are equal but opposite in magnitude so that a constant heat flux is obtained which is normal to the crack surface.

The right and left edges are considered to be insulated so that there in no heat flow through them. The crack surfaces are considered adiabatic, and hence a temperature discontinuity is expected across them. Figure 5.5b shows the temperature profile over the cracked rectangular plate having an adiabatic crack at the centre. The presence of a crack generates a discontinuity in temperature as can be clearly seen from the figure. Moreover, the temperature profile has a symmetric pattern about the crack line.

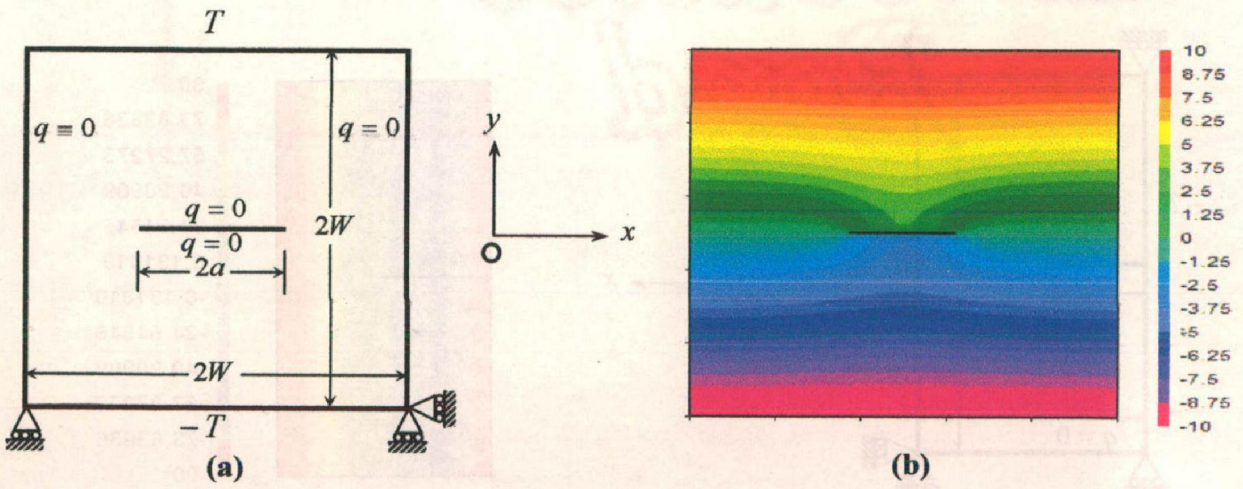

Fig. 5.5: Adiabatic Centre crack: (a) Problem geometry (b) Temperature profile

In the next case, a similar geometric configuration has been considered but with a different set of thermal boundary conditions. Figure 5.6a shows a square plate with a centre crack subjected to equal temperature at all four edges. Here, the crack surface is considered a part of essential boundary, which is also subjected to a different prescribed temperature. Thus, unlike the previous case, a continuous temperature profile is obtained across the crack surface as can be seen from Fig. 5.6b. In case of isothermal crack, the angular variation of singularity in temperature at the crack tip differs from the adiabatic case. This difference of angular variation is accounted during the selection of enrichment function for generating temperature profile over the domain.

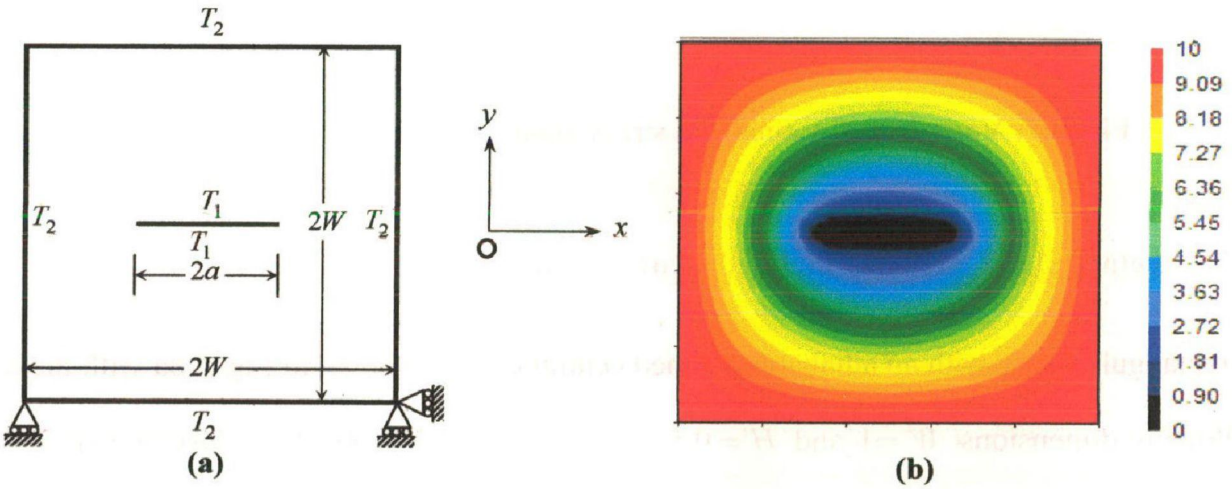

Fig. 5.6: Isothermal Centre Crack: (a) Problem geometry (b) Temperature profile

The first set of boundary condition induces a pure sliding mode (mode-II) while the second produces a pure opening mode (mode-I). The value of stress intensity factor (K_{II}) have been evaluated for different ratio of $\left(\frac{a}{W}\right)$ with a nodal density of 1152 nodes. The value of SIF's are normalized by $\beta(\Theta_2 - \Theta_1)E\sqrt{W}$. Figure 5.7a shows the variation of normalized mode-II stress intensity factor for an adiabatic crack while Fig. 5.7b shows the variation of normalized mode-I stress intensity factor for an isothermal crack with

different $\left(\frac{a}{W}\right)$ ratio. The numerical values evaluated by EFGM in the present work are found to be in good agreement with the reference values (Prasad *et al.*, 1994; Duflot, 2008).

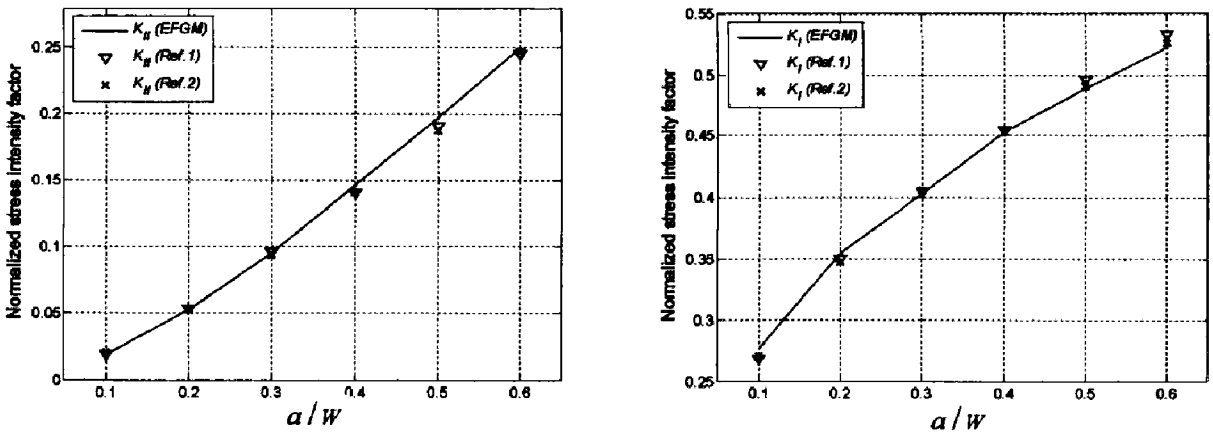

(a) Adiabatic crack **(b)** Isothermal crack

Fig. 5.7: Variation of normalized stress intensity factor with crack length

5.4.3 Rectangular Plate with Inclined Centre Crack

A rectangular plate with an adiabatic inclined central crack is shown in Fig. 5.8a with the following dimensions, $W = 1$ and $H = 0.5$. The plate geometry has been discretized by taking 24 and 48 uniformly distributed nodes in x and y-directions respectively. The crack surface is considered adiabatic. The equal and opposite temperature values are imposed at the top and bottom edges of plate, whereas the right and left edges are considered insulated with no heat flow through them. The presence of the crack at the centre of the plate generates a discontinuity in the temperature field which is clearly visible in Fig. 5.8b.

Further, a rectangular plate having an isothermal central crack is analyzed. The plate has been discretized using 32 uniformly distributed nodes in x-direction and 64 uniformly distributed nodes in y-direction. Figure 5.9a shows the geometry of plate with

following dimensions $W=1$ and $H=2$. All four edges of the plate are subjected to the same temperature T_2, while the crack surface is prescribed a different value of temperature T_1 such that $T_1 < T_2$. Since the crack surface is considered a part of essential boundary with a prescribed temperature value, the temperature profile across it remains continuous as can be seen from Fig. 5.9b.

Crack inclination and presence of finite temperature gradient at the crack tip results in mix mode loading for the crack tips. The value of stress intensity factor K_I and K_{II} have been evaluated for different values of crack inclination α (varying from 0 to 90 degree) with a constant (a/W) ratio of 0.3. The value of stress intensity factors are normalized by $\beta\Theta(W/H)E\sqrt{2W}$ for the adiabatic crack and $\beta(T_2-T_1)E\sqrt{2W}$ for the isothermal crack.

Figure 5.10a shows the variation of normalised stress intensity factor for an adiabatic crack with different inclination angle. The value of mode-II stress intensity factor i.e. K_{II} is found maximum for $\alpha=0^\circ$ which finally decreases to zero for $\alpha=90^\circ$. The value of mode-I stress intensity factor is found maximum at $\alpha=45^\circ$ but approaches to zero for $\alpha=0^\circ$ and 90° as can be seen from Fig. 5.10a. Moreover, the values of K_I and K_{II} are found in good agreement with the results available in literature (Prasad *et al.*, 1994; Duflot, 2008).

The variation of normalized stress intensity factor for an isothermal crack with different angular orientation is shown in Fig. 5.10b. Both mode-I and mode-II stress intensity factors are obtained. The value of K_{II} becomes maximum for $\alpha=45^\circ$ and approaches to zero for $\alpha=0^\circ$ and 90°. The value of mode-I stress intensity factor K_I exhibits a decreasing trend with a maximum value at $\alpha=0^\circ$ to a minimum value at

$\alpha = 90^{\circ}$. The values of K_I and K_{II} are quite close to the results available in literature (Prasad *et al.*, 1994; Duflot, 2008).

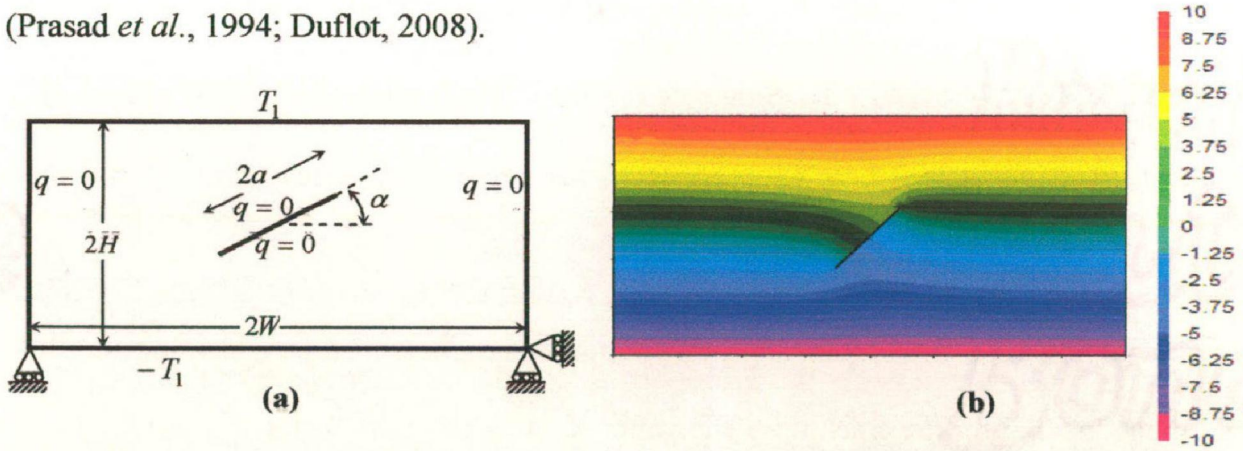

Fig. 5.8: Adiabatic Inclines crack: (a) Problem geometry (b) Temperature profile

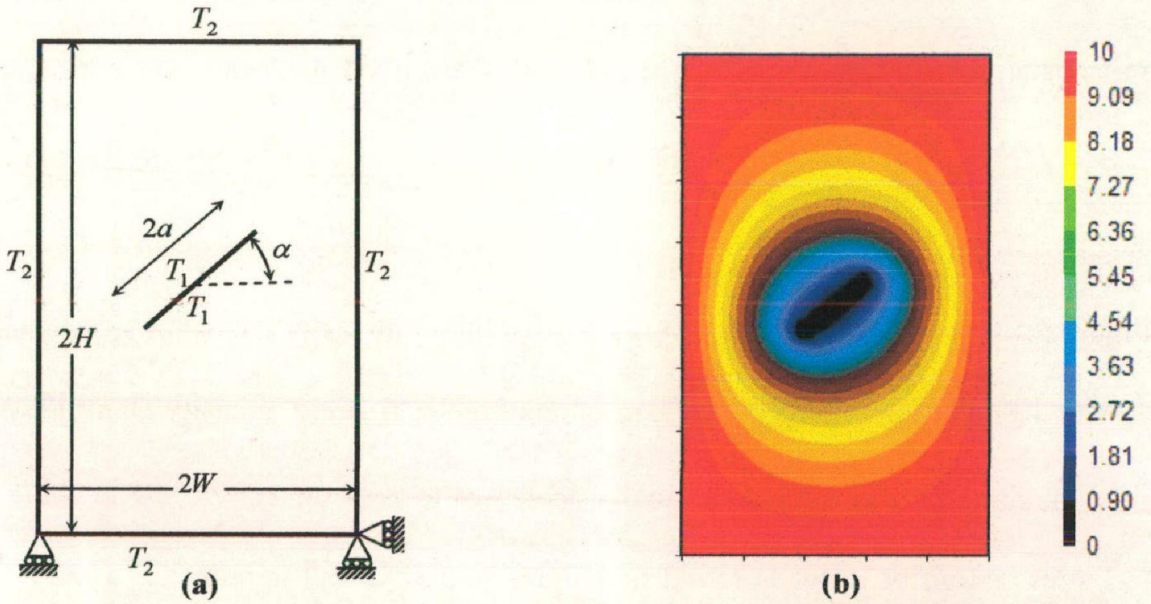

Fig. 5.9: Isothermal Inclines crack: (a) Problem geometry (b) Temperature profile

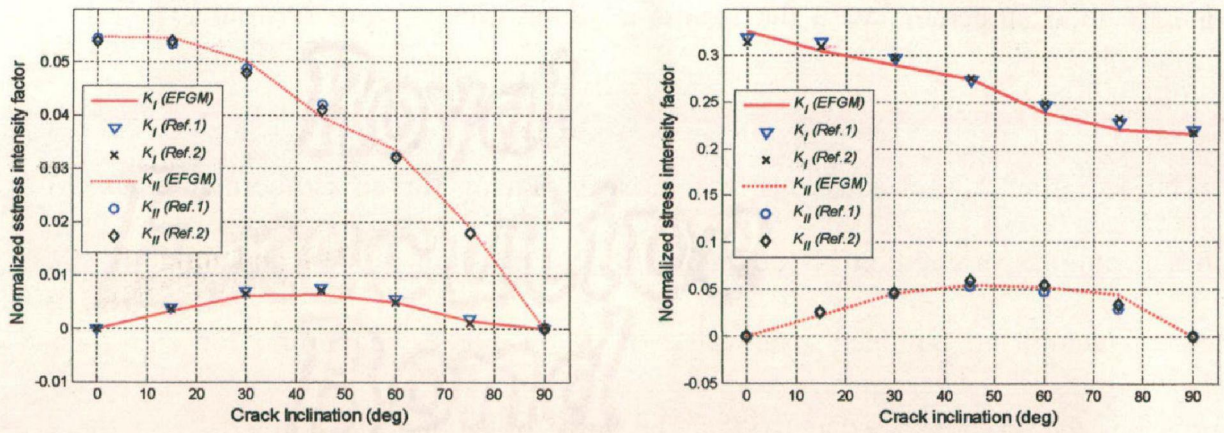

(a) Adiabatic crack **(b)** Isothermal crack

Fig. 5.10 Variation of Normalized stress intensity factor with crack inclination

5.4.4 Bi-Metallic Interface Cracks under Thermoelastic Loading

The increasing demand of multifunctional materials (having good resistance to corrosion, wear, stiffness, thermal and chemical resistance) in mechanical, aerospace and biomedical applications has imparted the layered materials, a coveted place in the world of engineering materials. Layered materials are found in a variety of important structures such as adhesive joints, composite laminates, and various electronics and optic components. The overall mechanical behavior and response of layered systems depends on the mechanical properties and the fracture behavior at the interface. The abrupt change in properties along with weakness of interface bond is an additional source of failure of layered materials. Thermoelastic loading of bi-material results in the development of residual stresses at the interface due to mismatch in material properties. These residual stresses may initiate a new crack or may result in the propagation of a pre-existing crack leading to final failure of the component. Hence, the study of bi-metallic interfacial crack under thermoelastic loading is of great importance. Motivated by this thought, and to extend the applicability of EFGM for bi-metallic interfacial cracks under thermoelastic loading, few problems have been tackled in this subsection.

5.4.1.1 Bi-material Body with Edge Interface Cracks

A bi-material body containing interface cracks is shown in Fig. 5.11. The two materials are assumed to be linear elastic, homogeneous and isotropic. This problem has been solved analytically by Brown and Erdogan, (1968) and numerically by Ikeda and Sun, (2001). Plane strain conditions were assumed. The same material properties as used by Ikeda and Sun (2001) are employed in this work (Table 5.1). To produce a 'semi infinite' body, the dimensions are taken such that $W = 200b$ and $H = 400b$ with $b = 10\,mm$.

Thermal conductivity for both materials are $k_1 = k_2 = 100\,\mathrm{W/m\,^{\circ}C}$. In this problem, a constant heat flux, $q = 10^5\ \mathrm{W/m^2}$ is applied in the negative X_2-direction. The crack faces are considered to be non-insulated which causes a linear temperature distribution. A uniform nodal density of 1250 nodes has been used to discretize the problem domain. The numerical results obtained using thermal interaction integral for bi-material problems are normalized as $\widetilde{F} = KW/(\sigma\sqrt{\pi b})$, where, W and b are length parameter, σ is the value of stress which can be evaluated as $\sigma = \dfrac{q\sigma_0 b(\beta_2\eta_2 k_1 - \beta_1\eta_1 k_2)}{k_1 k_2}$ where, $\sigma_0 = \dfrac{4\mu_1\mu_2 \cosh \pi\tilde{\varepsilon}}{\mu_1 + \mu_2 k_1 + \mu_2 + \mu_1 k_2}$ and $\eta = 1 + \nu$

μ represents the shear modulus of the respective material.

The values of stress intensity factors obtained by analytical (Sills and Dolev, 2004) approach are $\widetilde{F}_I = 0.4885$ and $\widetilde{F}_{II} = 0.1516$ whereas the values obtained from the present study are found to be $\widetilde{F}_I = 0.4852$ and $\widetilde{F}_{II} = 0.1412$.

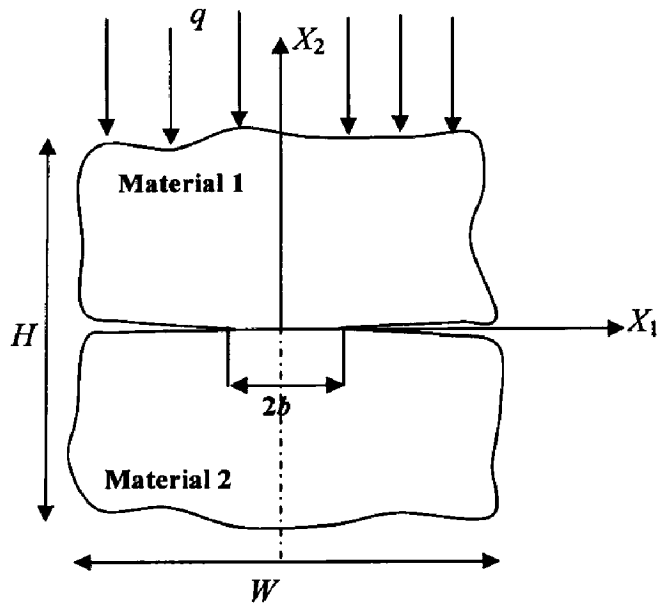

Fig. 5.11: Bi-material body with interface crack

Table 5.1: Material properties

Material	E (GPa)	ν	$\beta \times 10^{-6}$
1	100	0.3	0.1
2	1000	0.3	1.0

5.4.1.2 Bi-material Body with Central Interface Cracks

Next, a central crack is taken along the interface of an infinite body composed of two linear isotropic materials as shown in Fig. 5.12. The body is subjected to a constant heat flux $q = 10^5\ \mathrm{W/m^2}$ in the negative X_2-direction. The values of thermal conductivity are chosen to be same i.e. $k_1 = k_2 = 100\ \mathrm{W/m\,°C}$. In this case, the crack surfaces are assumed to be insulated. The material properties are taken same as given in Table 5.1. So as to approach infinite dimensions, the height and width of the body are taken to be $H = W = 40a$ with $a = 1mm$. Plane strain condition is assumed to prevail over the body. The insulation of crack causes a temperature gradient in the neighborhood of the crack tip. Again a uniform nodal density of 1250 nodes is employed to discretize the domain. The numerical results obtained by thermal interaction integral for bi-material problems are normalized as

$$\widetilde{F} = KW / \sigma\sqrt{\pi a},$$

where, W and a are length parameter, and

$$\sigma = \frac{2\mu_1\mu_2\widetilde{P}qa}{k_1k_2\cosh\pi\widetilde{\varepsilon}}$$

where, $\widetilde{P} = \dfrac{\beta_1\eta_1k_2(\mu_1\kappa_2+\mu_2)+\beta_2\eta_2k_1(\mu_2\kappa_1+\mu_1)}{(\mu_1\kappa_2+\mu_2)(\mu_2\kappa_1+\mu_1)}$; μ denotes the shear modulus, κ is the Kolosov constant, q is the heat flux, k is the thermal conductivity of the material, $\widetilde{\varepsilon}$ is the oscillatory parameter for bi-material. In the present study, the values of normalized stress intensity factors are found to be $\widetilde{F}_I = -4.130$ and $\widetilde{F}_{II} = -0.232$, which are in good agreement with the reference solution (Sills and Dolev, 2004) i.e. $\widetilde{F}_I = -4.132$ and $\widetilde{F}_{II} = -0.227$.

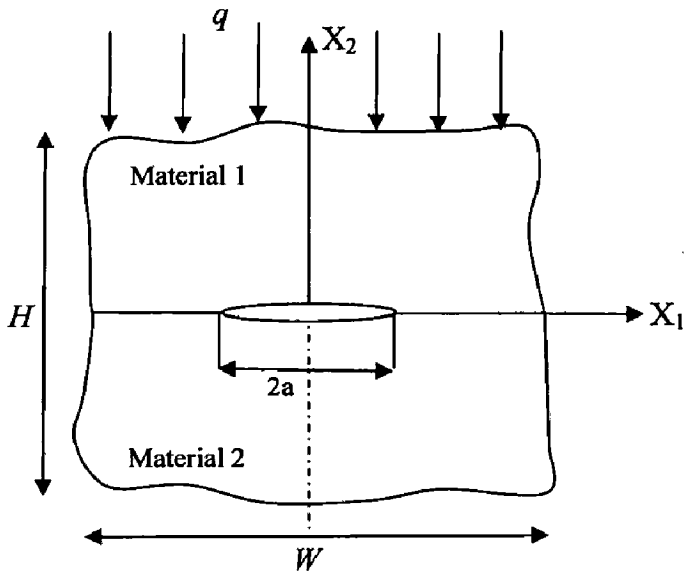

Fig. 5.12: Bi-material body with a finite crack along the interface

5.4.1.3 Bi-material Brazilian Disc with Central Interface Cracks

A bi-material Brazilian disc specimen composed of epoxy and glass is taken as illustrated in Fig. 5.13. This problem is solved by Ashkenazi (1999) employing weight functions under plane strain condition. The geometric parameters chosen for this study are taken as $a/R = 0.5$ with radius of disc $R = 20$ mm. The material properties are presented in Table 5.2. The disc is subjected to a constant temperature change of $-5\,^{\circ}\mathrm{C}$. The stress intensity factors are evaluated using the expression of thermal interaction integral for bi-material. The numerical values of stress intensity factor are normalized as $\widetilde{F} = KL/\sigma\sqrt{\pi a}$, with $L = a$ and $\sigma = \dfrac{(1-\nu_1)\beta_1 - (1-\nu_2)\beta_2}{(1/\overline{E}_2 - 1/\overline{E}_1)} \times \Delta T$, where ν is the Poisson's ratio, α is the coefficient of linear expansion, ΔT denotes the change in temperature and $\overline{E} = E/(1-\nu^2)$ for plane strain condition. A comparison of results obtained by EFGM as presented in Table 5.3 shows a good agreement with the previous studies.

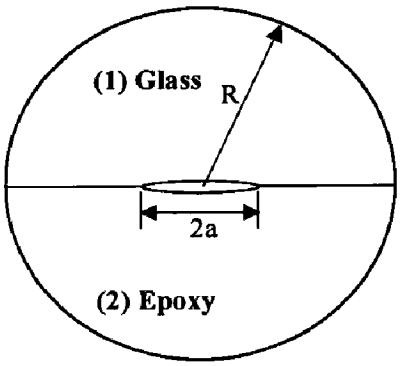

Table 5.2: Brazilian disc Properties

Material	E **(GPa)**	ν	$\beta \times 10^{-6}$
Glass	73	0.22	8
Epoxy	2.9	0.29	73

Table 5.3: Normalized SIF's for Brazilian disc

Method	$\widetilde{F}_1$	$\widetilde{F}_2$
EFGM (Present)	**-0.3523**	**0.2342**
Weight Function	-0.3654	0.2455
FEM	-0.3466	0.2389

5.5 CONCLUSION

In this Chapter, element free Galerkin method has been extended to solve thermo-elastic fracture problems in homogeneous and non-homogeneous materials (bi-materials). A thermo-elastic fracture problem is decoupled into two separate problems. At first, the temperature distribution is obtained by solving the heat conduction problem. The temperature field obtained from the solution of the thermal problem is then employed as input for the mechanical problem to determine the displacement and stress fields. The disturbances due to the presence of the crack results in a non-smooth temperature distribution, and induces a singularity in the heat flux at the crack tip. Thermal as well as mechanical problems are enriched intrinsically in order to represent the discontinuous

temperature, heat flux, displacement and traction across the crack surfaces. Both isothermal and adiabatic conditions are assumed at the crack surfaces. The conservative M -integral technique has been modified in order to extract the mixed mode stress intensity factor for thermo-elastic fracture mechanics problems. The present analysis establishes the EFGM as a robust tool for the analysis of fracture problems subjected to thermoelastic loading.

Chapter 6

CRACKS IN FUNCTIONALLY GRADED MATERIALS

6.1 INTRODUCTION

Many structures and components are subjected to adverse thermo-mechanical environments. Quite often these components are required to fulfill widely different requirements at different locations in the same component. This has fuelled the development of a new class of composite materials called functionally graded materials (FGMs). The FGM concept originated in 1984 in Japan during a space-plane project, in the form of a proposed thermal barrier material capable of withstanding a surface temperature of 2000 K and a temperature gradient of 1000 K across a cross section <10 mm. FGMs were initially designed as thermal barrier materials for aerospace structural components. They are now being developed for general use as structural components in extremely high temperature environments. FGMs are characterized by gradual spatial variation in composition, microstructure and material properties of each component. The goal of producing such engineered material systems is to utilize the strength of each material at specific locations. The significant proportions of an FGM contain the pure form of each component, and the need for compromise is eliminated by properly utilizing the properties of each component. For example, the toughness of a metal can be mated with the refractoriness of a ceramic, without any compromise in the toughness of the metal side or the refractoriness of the ceramic side. Ideally, functionally graded materials are continuously graded leading to the reduction of residual stresses developed at the interface of bi-material systems developed for the same purpose. However, in practice FGMs are often composed of a number of layers in which the volume fraction of second

phase increases with addition of each layer. As a result the interface stresses gets redistributed across multiple layers. These advantages have led to application of FGMs in many areas including civil and mechanical engineering, biomechanics and optics etc. FGMs offer great promise in applications where the operating conditions are quite severe, e.g. wear-resistant linings for handling large heavy abrasive ore particles, rocket heat shields, heat exchanger tubes, thermoelectric generators, heat-engine components, plasma facings for fusion reactors, piezoelectric devices, graded refractive index materials, thermionic converters, dental and other implants, fire retardant doors, solid oxide fuel cell and electrically insulating metal/ceramic joints. FGMs are also ideal for minimizing the thermo-mechanical mismatch in metal-ceramic bonds.

6.2 FRACTURE IN FUNCTIONALLY GRADED MATERIALS

The microstructure of functionally graded materials is generally heterogeneous in nature and the dominant type of failure is crack initiation and growth from inclusions. The extent to which constituent material properties and microstructure of FGMs can be altered remains an area of keen interest. This situation has lead to a lot of analytical and computational research in the area of fracture behavior of FGMs. Analytical work on FGMs goes back to 1960s with modeling of soil as a non-homogeneous material by Gibson (1967). Crack problems for non-homogeneous materials subjected to mechanical loading were solved by Atkinson and List (1978), Dhaliwal and Singh (1978) and Delale and Erdogan (1983). The asymptotic crack tip stress field in FGMs is found to possess the square root singularity as that of homogeneous material (Delale and Erdogan, 1983). The thermal stress intensity factors for non-homogeneous solids were computed by Jim and Noda (1993) assuming an exponential variation of thermal properties. Gu and Asaro (1997) analyzed a semi-infinite crack in a strip of FGM. They obtained the SIFs for commonly used fracture specimens. An equivalent domain integral technique was

presented by Gu *et al.* (1999) for calculating the crack tip fields of functionally graded materials. Anlas *et al.* (2000) evaluated the stress intensity factors in FGMs using finite element method, where the material property variation is achieved by assigning different homogeneous elastic properties to each element. Both experimental and FEM analyses were carried out by Marur and Tippur (2000) for a crack lying normal to elastic gradient. Kim and Paulino (2002) evaluated the mixed-mode fracture parameters in FGMs using FEM.

From above literature review, it is observed that most of the numerical work in FGMs is performed using FEM. However, due to inherent structure of FEM and other mesh based methods, the analysis of crack growth problems becomes cumbersome. The only way to cope with this problem is to remesh the domain again and again so as to ensure the coincidence of crack geometry with the FEM mesh. This is quite a tedious and time consuming job and often leads to numerical complexities and degradation in solution accuracy. Thereby, in recent years, Rao and Rahman (2003) used the EFGM to solve the problems involving cracks in isotropic functionally graded materials. They proposed two new interaction integrals formulations for the analysis of fracture in FGMs. Thermo-mechanical analysis of functionally graded plates using EFGM was performed by Dai *et al.* (2005). So far, very little work has been performed in FGMs using EFGM. Thus, motivated by the wide applicability and advantages of FGMs over conventional materials, the present Chapter extends the application of EFGM in functionally graded materials under mechanical/thermal loads.

6.3 EFGM FORMULATION FOR FUNCTIONALLY GRADED MATERIALS

In EFGM, the field variable u is approximated by moving least square approximation function $u^h(\mathbf{x})$, which is given as

$$u^h(\mathbf{x}) = \sum_{I=1}^{n} \Phi_I(\mathbf{x}) u_I \tag{6.1}$$

Consider a two-dimensional domain with small displacements on the domain Ω bounded by Γ (Fig. 6.1). It is assumed that the material properties such as modulus of elasticity E, Poisson's ratio ν, thermal conductivity, k and coefficient of thermal expansion, β vary as follows:

$$E = E(x_1, x_2) = E(x) \tag{6.2}$$

$$\nu = \nu(x_1, x_2) = \nu(x) \tag{6.3}$$

$$k = k(x_1, x_2) = k(x) \tag{6.4}$$

$$\beta = \beta(x_1, x_2) = \beta(x) \tag{6.5}$$

The governing equilibrium equations are given as

$$\nabla.\boldsymbol{\sigma} + \mathbf{b} = 0 \text{ in } \Omega \tag{6.6}$$

with the following essential and natural boundary conditions:

$$\mathbf{u} = \bar{\mathbf{u}} \text{ on } \Gamma_u \tag{6.7}$$

$$\boldsymbol{\sigma}.\bar{\mathbf{n}} = \bar{\mathbf{t}} \text{ on } \Gamma_t \tag{6.8}$$

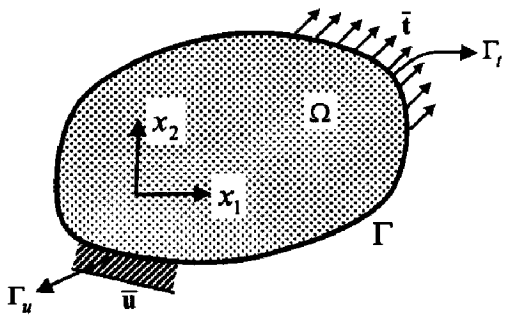

Fig. 6.1: Domain along with essential and natural boundary conditions

where, $\boldsymbol{\sigma}$ is the stress tensor which is defined as $\boldsymbol{\sigma} = \mathbf{D}(\mathbf{x})[\boldsymbol{\varepsilon} - \boldsymbol{\varepsilon}_T]$, $\mathbf{D}(\mathbf{x})$ is the material property matrix, $\boldsymbol{\varepsilon}$ is the strain vector, $\boldsymbol{\varepsilon}_T = \beta \Delta T \bar{\mathbf{I}}$ is the thermal strain vector, $\mathbf{b}$ is the

body force vector, $\mathbf{u}$ is the displacement vector, $\bar{\mathbf{t}}$ is the traction force and $\bar{\mathbf{n}}$ is the unit normal.

By enforcing essential boundary conditions using Lagrange multiplier approach, and applying variational principle, the following discrete equations are obtained from Eq. (6.1):

$$\begin{bmatrix} \mathbf{K} & \mathbf{G} \\ \mathbf{G}^T & 0 \end{bmatrix} \begin{Bmatrix} \mathbf{u} \\ \boldsymbol{\lambda} \end{Bmatrix} = \begin{Bmatrix} \mathbf{f} \\ \mathbf{q} \end{Bmatrix} \tag{6.9}$$

$$\text{where, } K_{IJ} = \int_{\Omega} \mathbf{B}_I^T \mathbf{D} \mathbf{B}_J \, d\Omega \tag{6.10}$$

$$f_I = \int_{\Gamma_t} \bar{\mathbf{t}} \Phi_I \, d\Gamma_t \;,\; q_K = -\int_{\Gamma_u} \mathbf{N}_K \bar{u} \, d\Gamma_u \;, \tag{6.11}$$

$$\mathbf{B}_I = \begin{bmatrix} \Phi_{I,x} & 0 \\ 0 & \Phi_{I,y} \\ \Phi_{I,y} & \Phi_{I,x} \end{bmatrix}, \quad \mathbf{N}_K = \begin{bmatrix} N_K & 0 \\ 0 & N_K \end{bmatrix}, \tag{6.12}$$

$$\mathbf{D}(x) = \frac{E(x)}{1-\nu(x)^2} \begin{bmatrix} 1 & \nu(x) & 0 \\ \nu(x) & 1 & 0 \\ 0 & 0 & (1-\nu(x))/2 \end{bmatrix} \quad \text{(for plane stress)}$$

$$= \frac{E(x)}{[1+\nu(x)][(1-2\nu(x))]} \begin{bmatrix} 1-\nu(x) & \nu(x) & 0 \\ \nu(x) & 1-\nu(x) & 0 \\ 0 & 0 & (1-2\nu(x))/2 \end{bmatrix} \quad \text{(for plane strain)} \tag{6.13}$$

In functionally graded materials, the elasticity matrix $\mathbf{D}(x)$ is spatially dependent because of functionally graded material properties. The effect of material gradation on stiffness matrix $\mathbf{K}$ can be incorporated directly by calculating the material properties at Gauss points lying over the domain

6.4 THERMAL INTERACTION INTEGRAL FOR FGMs

Similar to monolithic materials, the *J*-integral approach can also be used to compute the stress intensities for FGMs; however, it must account for material gradients. Generally, during formulation of interaction integral, terms such as derivatives of the elastic constants are discarded. For a monolithic material, the derivatives of elastic constants are

zero, and have no contribution in calculation of stress intensities. However, for the case of a continuously graded material, these terms are non-zero and must be retained in order to maintain the path independence of the *J*-integral. Several formulation of interaction integral for non-homogeneous materials have been developed (Sladek and Sladek, 1997; Rao, 2003; Paulino and Kim, 2004). In the present work, thermal interaction integral will be used to account for both mechanical/thermal loading. For a homogenous cracked body, the path independent *J*-integral (Wilson and Yu, 1979) is given as

$$J = \int_{\Gamma}\left(\tilde{W}\delta_{1j} - \sigma_{ij}\frac{\partial u_i}{\partial x_1}\right)n_j d\Gamma \tag{6.14}$$

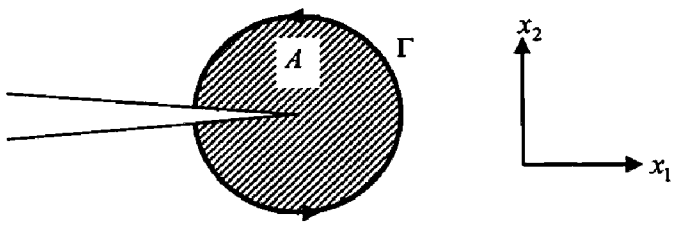

Fig. 6.2: Path Γ surrounding a crack with an enclosed area A

where, W is the strain energy density and n_j is the j-th component of the outward unit vector normal to an arbitrary contour Γ enclosing the crack tip (Fig. 6.2). For linear elastic materials subjected to thermal loads

$$\tilde{W} = \frac{\sigma_{ij}\varepsilon_{ij}^{m}}{2} = \frac{1}{2}\sigma_{ij}\left(\varepsilon_{ij}^{t} - \beta\Delta T\delta_{ij}\right) \tag{6.15}$$

where ε_{ij}^{m} denotes the mechanical part of strain, ε_{ij}^{t} the total strain, $\beta = \beta(x)$ the coefficient of thermal expansion that varies with spatial coordinates, $\Delta T = T - T_0$ with T_0 is the reference temperature and δ_{ij} is the Kronecker delta.

In order to enhance its usefulness, the contour integral in Eq. (6.14) can be converted into an equivalent domain form using divergence theorem (Rice, 1968).

$$J = \int_A \left(\sigma_{ij} \frac{\partial u_i}{\partial x_1} - \tilde{W}\delta_{1j} \right) \frac{\partial \bar{q}}{\partial x_j} dA + \int_A \frac{\partial}{\partial x_j} \left(\sigma_{ij} \frac{\partial u_i}{\partial x_1} - \tilde{W}\delta_{1j} \right) \bar{q} dA \tag{6.16}$$

where, A is the area inside the contour and $\bar{q}$ is a weight function chosen such that it has a value *unity* at the crack tip, *zero* along the boundary of the domain, and arbitrary elsewhere.

For calculating the interaction integral, two equilibrium states of a cracked body are considered. State 1 corresponds to be the actual state with the given boundary conditions while state 2 is defined to be an auxiliary state. The superposition of two states leads to another equilibrium state S for which the domain form of the J-integral (Amit and Kim, 2008) is given as

$$J^s = \int_A \left\{ \left(\sigma_{ij} + \sigma_{ij}^{aux}\right)\left(u_{i,1} + u_{i,1}^{aux}\right) - \frac{1}{2}\left(\sigma_{ik} + \sigma_{ik}^{aux}\right)\left(\varepsilon_{ik}^{m} + \varepsilon_{ik}^{aux}\right)\delta_{ij} \right\} \bar{q}_{,j}\, dA +$$

$$\int_A \left\{ \left(\sigma_{ij} + \sigma_{ij}^{aux}\right)\left(u_{i,1} + u_{i,1}^{aux}\right) - \frac{1}{2}\left(\sigma_{ik} + \sigma_{ik}^{aux}\right)\left(\varepsilon_{ik}^{m} + \varepsilon_{ik}^{aux}\right)\delta_{ij} \right\}_{,j} \bar{q}\, dA \tag{6.17}$$

The Eq. (6.17) can be decomposed into

$$J^s = J^1 + J^{aux} + M \tag{6.18}$$

where, the interaction integral M is given by

$$M = \int_A \left\{ \sigma_{ij} u_{i,1}^{aux} + \sigma_{ij}^{aux} u_{i,1} - \frac{1}{2}\left(\sigma_{ik}\varepsilon_{ik}^{aux} + \sigma_{ik}^{aux}\varepsilon_{ik}^{m}\right)\delta_{1j} \right\} \bar{q}_{,j}\, dA +$$

$$\int_A \left\{ \sigma_{ij} u_{i,1}^{aux} + \sigma_{ij}^{aux} u_{i,1} - \frac{1}{2}\left(\sigma_{ik}\varepsilon_{ik}^{aux} + \sigma_{ik}^{aux}\varepsilon_{ik}^{m}\right)\delta_{1j} \right\}_{,j} \bar{q}\, dA \tag{6.19}$$

Based on non-equilibrium formulation for FGMs, we have

$$\sigma_{ij}\varepsilon_{ij}^{aux} = C_{ijkl}(x)\varepsilon_{kl}^{m}\varepsilon_{ij}^{aux} = \sigma_{kl}^{aux}\varepsilon_{kl}^{m} = \sigma_{ij}^{aux}\varepsilon_{ij}^{m}$$

Again rewriting Eq. (6.19) as $M = M_1 + M_2$

$$= \int_A \left\{ \sigma_{ij} u_{i,1}^{aux} + \sigma_{ij}^{aux} u_{i,1} - \sigma_{ik}\varepsilon_{ik}^{aux}\delta_{1j} \right\} \bar{q}_{,j}\, dA + \int_A \left\{ \sigma_{ij} u_{i,1}^{aux} + \sigma_{ij}^{aux} u_{i,1} - \sigma_{ik}\varepsilon_{ik}^{aux}\delta_{1j} \right\}_{,j} \bar{q}\, dA \tag{6.20}$$

The last term of integral M_2 in Eq. (6.20) is expressed as

$$\left(\sigma_{ik}\varepsilon_{ik}^{aux}\delta_{1j}\right)_{,j} = \left(\sigma_{ij}\varepsilon_{ij}^{aux}\right)_{,1} = \left(C_{ijkl}\varepsilon_{kl}^{m}\varepsilon_{ij}^{aux}\right)_{,1} = C_{ijkl,1}\varepsilon_{kl}^{m}\varepsilon_{ij}^{aux} + C_{ijkl}\varepsilon_{kl,1}^{m}\varepsilon_{ij}^{aux} + C_{ijkl}\varepsilon_{kl}^{m}\varepsilon_{ij,1}^{aux}$$

$$= C_{ijkl,1}\varepsilon_{kl}^{m}\varepsilon_{ij}^{aux} + \sigma_{ij}^{aux}\varepsilon_{ij,1}^{m} + \sigma_{ij}\varepsilon_{ij,1}^{aux} \tag{6.21}$$

Substituting Eq. (6.21) into M_2 of Eq. (6.20) leads to

$$M_2 = \int_A \left(\sigma_{ij,j}u_{i,1}^{aux} + \sigma_{ij}u_{i,1j}^{aux} + \sigma_{ij,j}^{aux}u_{i,1} + \sigma_{ij}^{aux}u_{i,1j}\right)\overline{q}\,dA -$$

$$\int_A \left(C_{ijkl,1}\varepsilon_{kl}^{m}\varepsilon_{ij}^{aux} + \sigma_{ij}^{aux}\varepsilon_{ij,1}^{m} + \sigma_{ij}\varepsilon_{ij,1}^{aux}\right)\overline{q}\,dA \tag{6.22}$$

Using compatibility conditions (actual and auxiliary) and equilibrium condition (actual) i.e. $\sigma_{ij,j} = 0$, Eq. (6.22) can be simplified as

$$M_2 = \int_A \left\{\sigma_{ij,j}^{aux}u_{i,1} - C_{ijkl,1}\varepsilon_{kl}^{m}\varepsilon_{ij}^{aux} + \sigma_{ij}^{aux}(u_{i,1j} - \varepsilon_{ij,1}^{m})\right\}\overline{q}\,dA \tag{6.23}$$

$$= \int_A \left\{\sigma_{ij,j}^{aux}u_{i,1} - C_{ijkl,1}\varepsilon_{kl}^{m}\varepsilon_{ij}^{aux} + \sigma_{ij}^{aux}\left(\beta_{,1}\Delta T + \beta(\Delta T)_{,1}\right)\delta_{ij}\right\}\overline{q}\,dA \tag{6.24}$$

Therefore, the resulting interaction integral (M) becomes

$$M = \int_A \left\{\sigma_{ij,j}^{aux}u_{i,1} - C_{ijkl,1}\varepsilon_{kl}^{m}\varepsilon_{ij}^{aux} + \sigma_{ij}^{aux}\left(\beta_{,1}\Delta T + \beta(\Delta T)_{,1}\right)\delta_{ij}\right\}\overline{q}\,dA +$$

$$\int_A \left\{\sigma_{ij}u_{i,1}^{aux} + \sigma_{ij}^{aux}u_{i,1} - \sigma_{ik}\varepsilon_{ik}^{aux}\delta_{1j}\right\}\overline{q}_{,j}\,dA \tag{6.25}$$

where, the term $\sigma_{ij}u_{i,1}^{aux}$ appears due to non-equilibrium of auxiliary stress fields.

6.4.1 Evaluation of Stress Intensity Factors

For linear elastic solid under mixed-mode loading conditions, J-integral is also equal to the energy release rate and hence, J-integral can be written as

$$J = \frac{1}{E^*}\left(K_I^2 + K_{II}^2\right) \tag{6.26}$$

where, $E^* = \begin{Bmatrix} \dfrac{E}{1-\nu^2} & \text{Plane strain} \\ E & \text{Plane stress} \end{Bmatrix}$

Applying Eq. (6.26) to states 1(actual), state 2(auxiliary), and the superimposed state S gives

$$J^{(1)} = \frac{1}{E^*}\left(K_I^{(1)^2} + K_{II}^{(1)^2}\right) \tag{6.27}$$

$$J^{(aux)} = \frac{1}{E^*}\left(K_I^{(aux)^2} + K_{II}^{(aux)^2}\right) \tag{6.28}$$

and

$$\begin{aligned} J^{(S)} &= \frac{1}{E^*}\left[\left(K_I^{(1)} + K_I^{(aux)}\right)^2 + \left(K_{II}^{(1)} + K_{II}^{(aux)}\right)^2\right] \\ &= \frac{1}{E^*}\left[\left(K_I^{(1)^2} + K_{II}^{(1)^2}\right) + \left(K_I^{(1)^2} + K_{II}^{(aux)^2}\right) + 2\left(K_I^{(1)}K_I^{(aux)} + K_{II}^{(1)}K_{II}^{(aux)}\right)\right] \\ &= J^{(1)} + J^{(aux)} + \frac{2}{E^*}\left(K_I^{(1)}K_I^{(aux)} + K_{II}^{(1)}K_{II}^{(aux)}\right) \end{aligned} \tag{6.29}$$

By comparing Eq. (6.18) with Eq. (6.29),

$$M = \frac{2}{E^*}\left[\left(K_I^{(1)}K_I^{(aux)} + K_{II}^{(1)}K_{II}^{(aux)}\right)\right] \tag{6.30}$$

The individual SIFs for the actual state can be obtained by judiciously choosing the auxiliary state (state 2). For example, if state 2 (auxiliary state) is chosen in mode-I i.e. mode-I near tip displacement and stress field is chosen as the auxiliary state, then $K_I^{(2)} = 1$ and $K_{II}^{(2)} = 0$. Hence, Eq. (6.30) can be reduced to

$$M^{(1,I)} = \frac{2K_I^{(1)}}{E^*_{tip}} \tag{6.31}$$

or

$$K_I^{(1)} = \frac{M^{(1,I)}E^*_{tip}}{2} \tag{6.32}$$

Similarly, if state 2 is chosen to be in mode-II, i.e. the mode-II near tip displacement and stress field is chosen as the auxiliary state, then $K_I^{(2)} = 0$ and $K_{II}^{(2)} = 1$. Following the similar considerations, where E_{tip}^{*} is calculated using Eq.6.2.

$$K_{II}^{(1)} = \frac{M^{(1,II)} E_{tip}^{*}}{2} \tag{6.33}$$

Thus, numerical evaluation of interaction integral from Eq. (6.25) allows us to calculate the mixed mode stress intensity factors.

6.5 RESULTS AND DISCUSSIONS

Some example problems have been solved to show the capability of EFGM by modeling the fracture mechanics problems in FGMs.

6.5.1 Edge Crack Plate Subjected to Mode-I Mechanical Loading

An edge crack plate of dimensions, $H = 8$ units, $W = 1$ unit and a crack of length of a is considered as shown in Fig. 6.3. The elastic modulus of the FGM plate is assumed to follow an exponential gradation as given by the function $E(x_1) = E_1 \exp(\eta x_1 / W)$, $0 \le x_1 \le W$ with $E_1 = E(0)$, $E_2 = E(W)$ and $\eta = \ln(E_2/E_1)$. A uniform nodal distribution is used for the simulation, and six point Gauss quadrature is used in each cell. The results are obtained under plane strain condition with $E_1 = 1$ unit, $\nu = 0.3$, $E_2/E_1 = \exp(\eta) = 0.1, 0.2, 5, 10$ with a varying ratio of $a/W = 0.2, 0.3, 0.4, 0.5, 0.6$. The values of mode-I stress intensity factor are normalized according to the relation $\tilde{F}_I = \frac{K_I}{\sigma_o \sqrt{\pi a}}$. Figure 6.4a shows the variation of normalized stress intensity factor (K_I) with varying (a/W) ratio for $E_2/E_1 = 0.1$. Figure 6.4b shows the variation of modulus of elasticity (E). The results obtained by EFGM exhibit a good agreement with available solutions in Ref.1 (Erdogen & Wu, 1997) and in Ref.2 (Chen et al., 2000). Similar results

are obtained by varying the E_2/E_1 ratio as shown in Fig. 6.5a—6.7a along with the corresponding spatial variation of modulus of elasticity (E) as shown in Fig. 6.5b—6.7b.

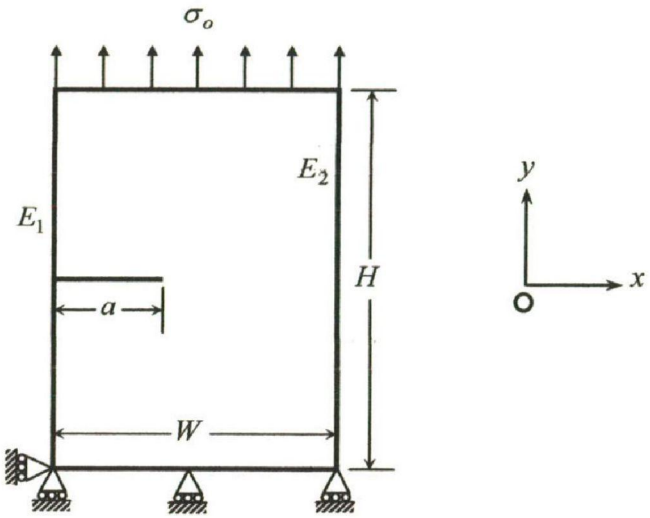

Fig. 6.3: Problem geometry along with dimensions and boundary conditions

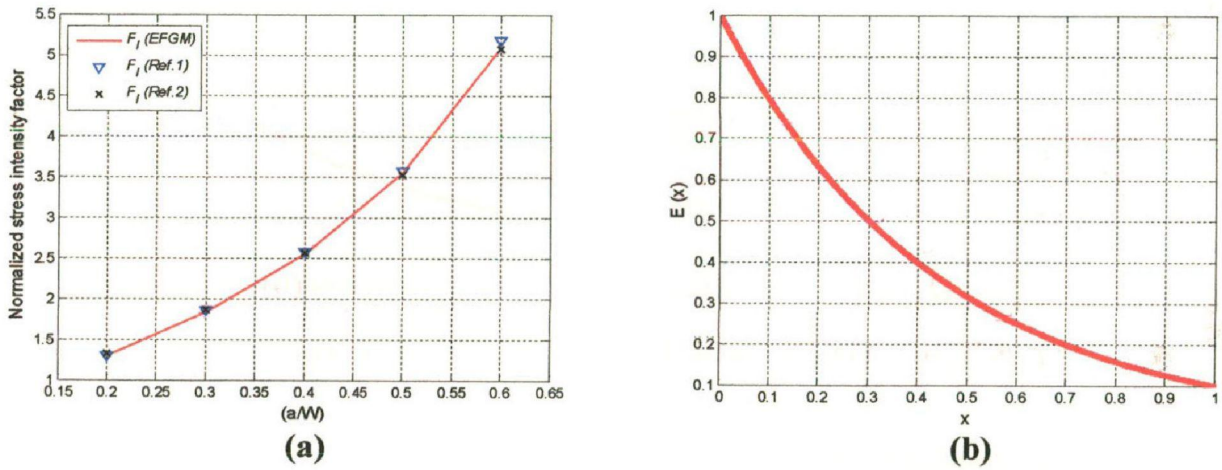

(a) (b)

Fig. 6.4: SIF variation and modulus of elasticity gradation for $E_2/E_1 = 0.1$

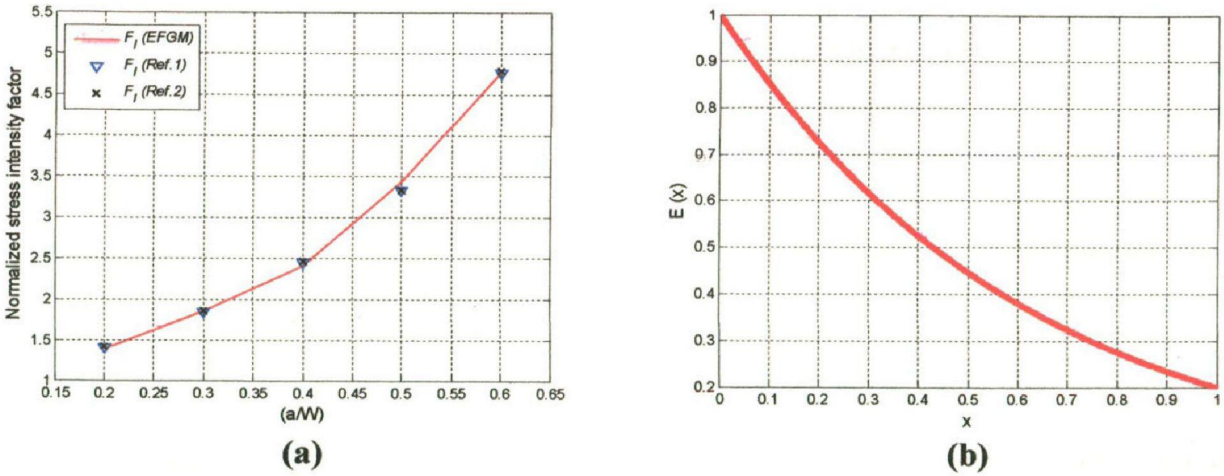

(a) (b)

Fig. 6.5: SIF variation and modulus of elasticity gradation for $E_2/E_1 = 0.2$

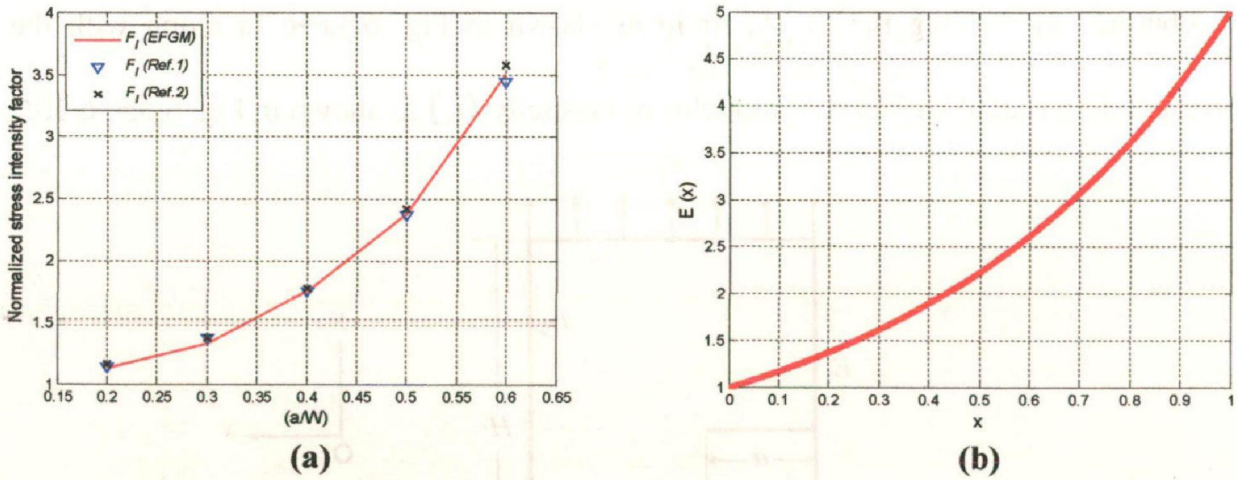

(a) (b)

Fig. 6.6: SIF variation and modulus of elasticity gradation for $E_2/E_1 = 5$

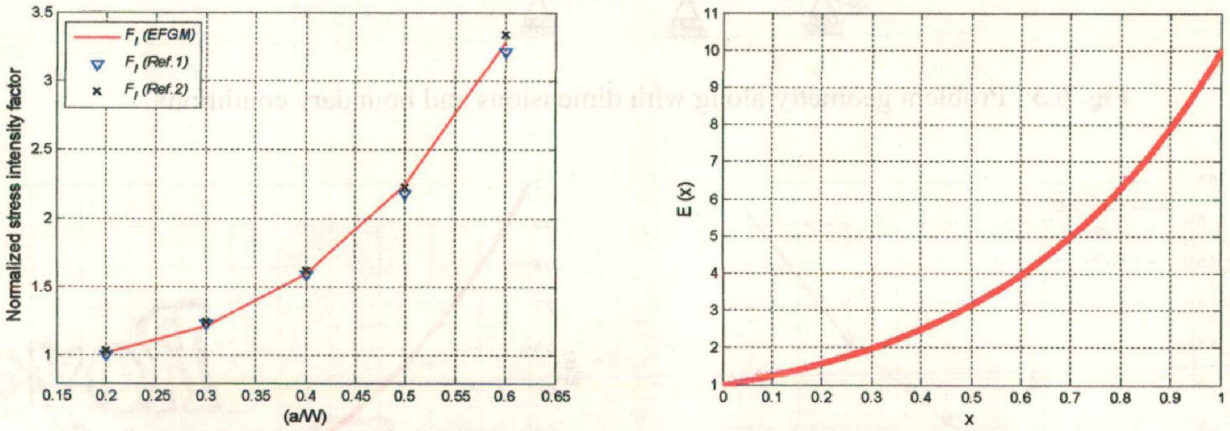

(a) (b)

Fig. 6.7: SIF variation and modulus of elasticity gradation for $E_2/E_1 = 10$

6.5.2 Edge Crack Plate Subjected to Thermal Loading

6.5.2.1 FGM with linear gradation of material properties

Next, an edge crack plate ($W = 1$ unit and $H = 4$ units) subjected to thermal load is considered. The material properties of plate follow a linear variation from left edge to right edge. The geometrical dimensions of plate along with boundary conditions are shown in Fig. 6.8a along with its boundary conditions. Temperature is prescribed on left and right edges, while the top and bottom edges are considered to be insulated. A

uniform nodal distribution of 784 nodes along with six point Gauss quadrature in each cell is used to simulate the problem. A plane strain condition is assumed over the problem domain. The values of mode-I stress intensity factors i.e. K_I are calculated using domain based interaction integral approach. The following numerical data is used in the present analysis: $E_1 = 1\times10^5$ units, $E_2 = 0.5\times10^5$ units, $\nu_1 = 0.3$, $\nu_2 = 0.35$, $\beta_1 = 1.67\times10^{-5}/^oC$ units, $\beta_2 = 1\times10^{-5}/^oC$ units, $T_1 = 0^oC$, $T_2 = 1^oC$.

A plot of steady state temperature distribution is shown in Fig. 6.8b. This plot shows that the temperature distribution remains unaffected by the presence of the crack as the heat flux is parallel to the crack surface. The prescribed boundary conditions generate a pure mode-I loading as can be clearly seen from displaced nodal positions in Fig. 6.9a. The values of mode-I stress intensity factor i.e. K_I have been calculated for different $\left(\frac{a}{W}\right)$ ratio as shown in Fig. 6.9b. The results obtained by EFGM are found to be in good agreement with those obtained by FEM (Amit and Kim, 2008).

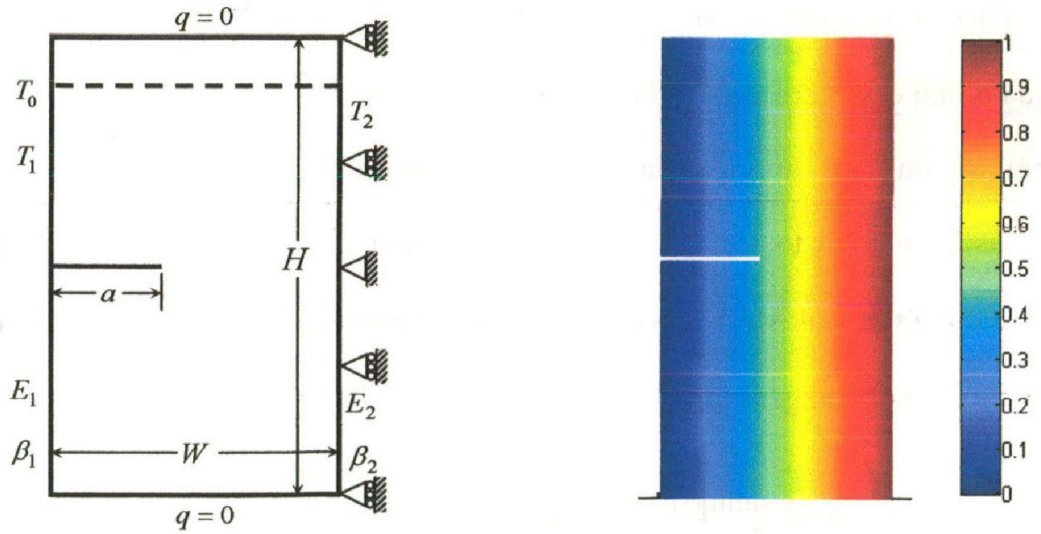

(a) (b)

Fig. 6.8: Problem geometry and temperature distribution over the domain

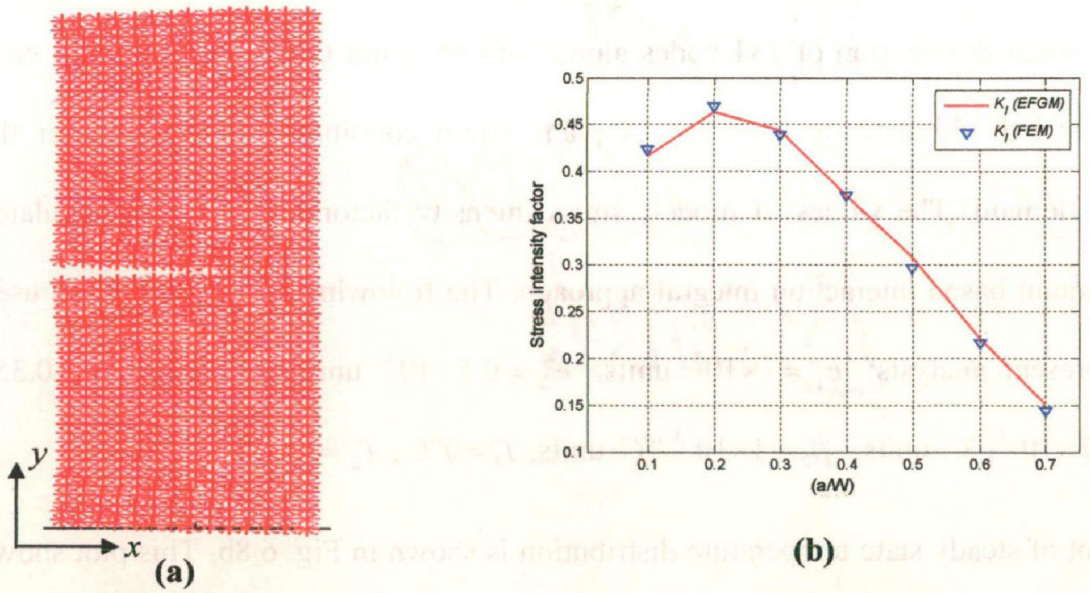

Fig. 6.9: Displaced nodal positions and variation of stress intensity factor

6.5.2.2 FGM with hyperbolic-tangent gradation of material properties

An edge cracked functionally graded plate with material properties variation defined by hyperbolic tangent function is analyzed in this sub-section. Figure 6.10a shows the dimensions ($W = 2$ units and $H = 4$ units) of FGM plate along with an edge crack of length a. The top and bottom edges are constraint in the y-direction. The problem domain is subjected to a steady state thermal loading having $T_1 = -10^{o}C$ and $T_2 = 0^{o}C$. The top and bottom edges are assumed to be insulated so that there is no flow of heat flux across them. A uniform arrangement of 1250 nodes along with six point Guass quadrature has been used to simulate the problem under plane strain conditions. The gradation of Young's modulus (E), Poisson's ratio (ν), thermal expansion coefficient (β) is defined by hyperbolic tangent function as follows:

$$E(X_1) = \frac{E^- + E^+}{2} + \frac{E^- - E^+}{2}\tanh\left[\tilde{\delta}\left(X_1 + d\right)\right] \tag{6.34}$$

$$\nu(X_1) = \frac{\nu^- + \nu^+}{2} + \frac{\nu^- - \nu^+}{2}\tanh\left[\tilde{\delta}\left(X_1 + d\right)\right] \tag{6.35}$$

$$\beta(X_1) = \frac{\beta^- + \beta^+}{2} + \frac{\beta^- - \beta^+}{2}\tanh\left[\hat{\delta}(X_1 + d)\right] \tag{6.36}$$

$$k(X_1) = \frac{k^- + k^+}{2} + \frac{k^- - k^+}{2}\tanh\left[\hat{\delta}(X_1 + d)\right] \tag{6.37}$$

where, $(E^-, E^+) = (1,3)$, $(\nu^-, \nu^+) = (0.3, 0.1)$, $(\beta^-, \beta^+) = (0.01, 0.03)$, $(k^-, k^+) = (1,3)$
$\tilde{\delta} = 15$, $\hat{\delta} = 5$, $d = 0$.

Figure 6.10b shows the temperature distribution over the domain under steady state condition. In order to visualize the gradation in material properties, Eq. (6.34) - Eq. (6.37) are plotted across the problem domain as shown in Fig. 6.11-6.12. The magnitude of material properties exhibits a sharp jump at the middle of domain.

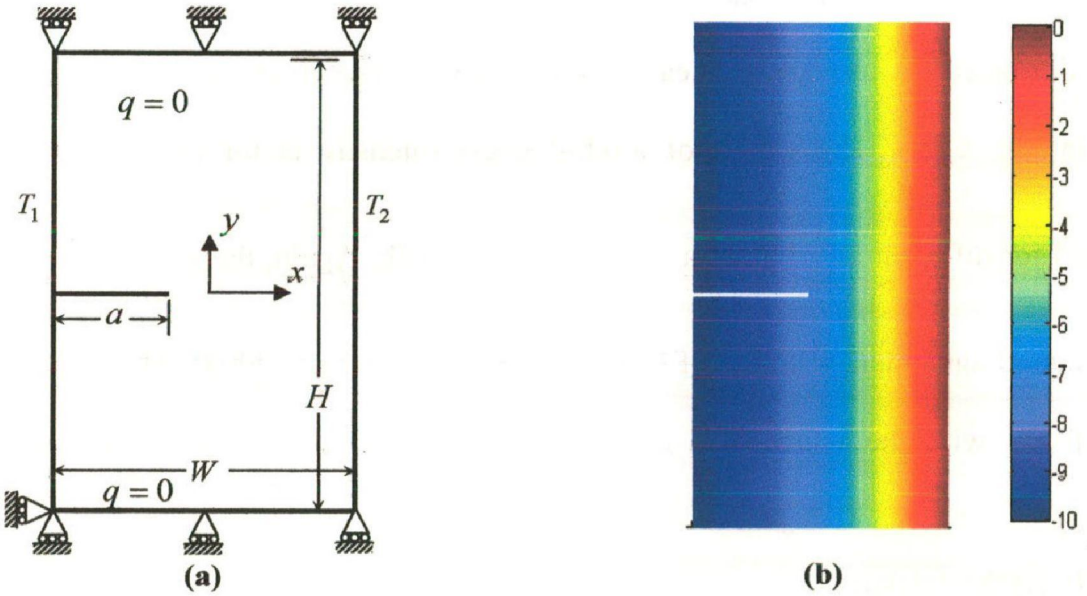

(a) (b)

Fig. 6.10: Problem geometry and temperature distribution over the domain

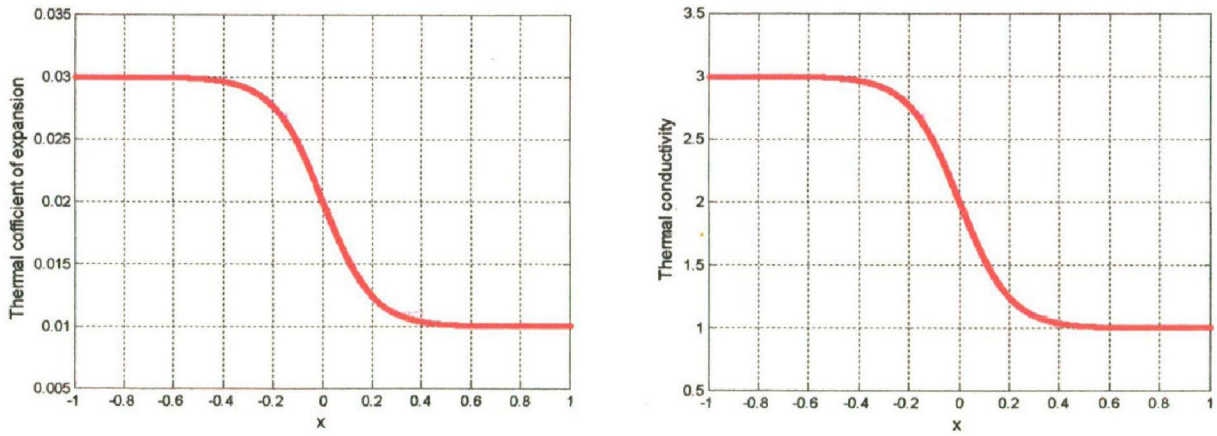

(a) (b)

Fig. 6.11: Gradation of coefficient of thermal expansion and condictivity

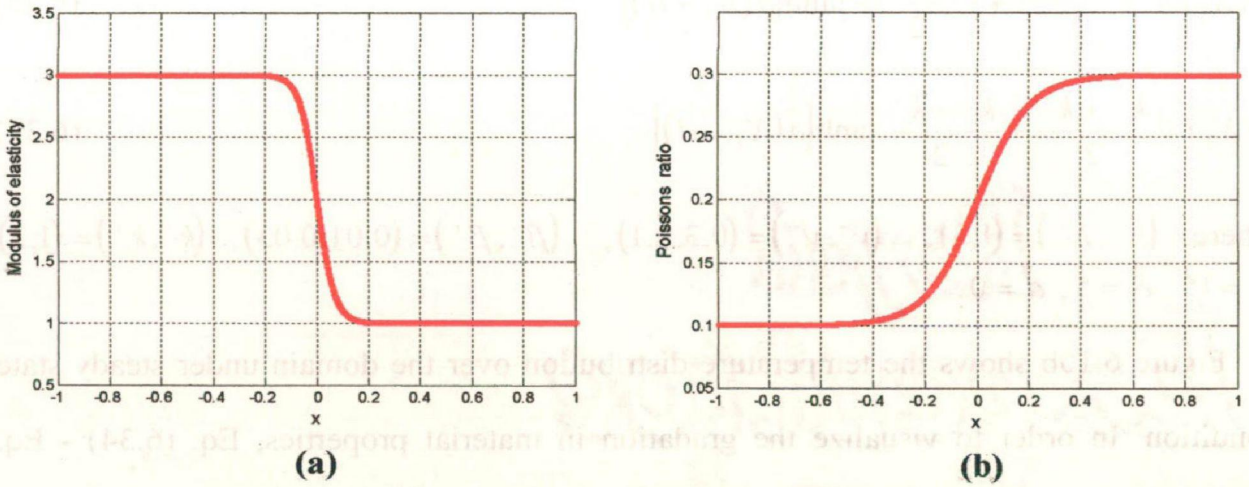

(a) (b)

Fig. 6.12: Gradation of modulus of elasticity and Poisson's ratio

Under the prescribed thermal loading and boundary conditions, the edge crack exhibits a mode-I displacement as can be clearly observed from the displaced nodal positions shown in Fig. 6.13a. The values of mode-I stress intensity factor i.e. K_I has been calculated for different $\left(\frac{a}{W}\right)$ ratio as shown in Fig. 6.13b. Again, the EFGM results are found in good agreement with the FEM solution (Amit and Kim, 2008). The decrease in value of K_I with the increase in crack length is due to the gradation in material properties.

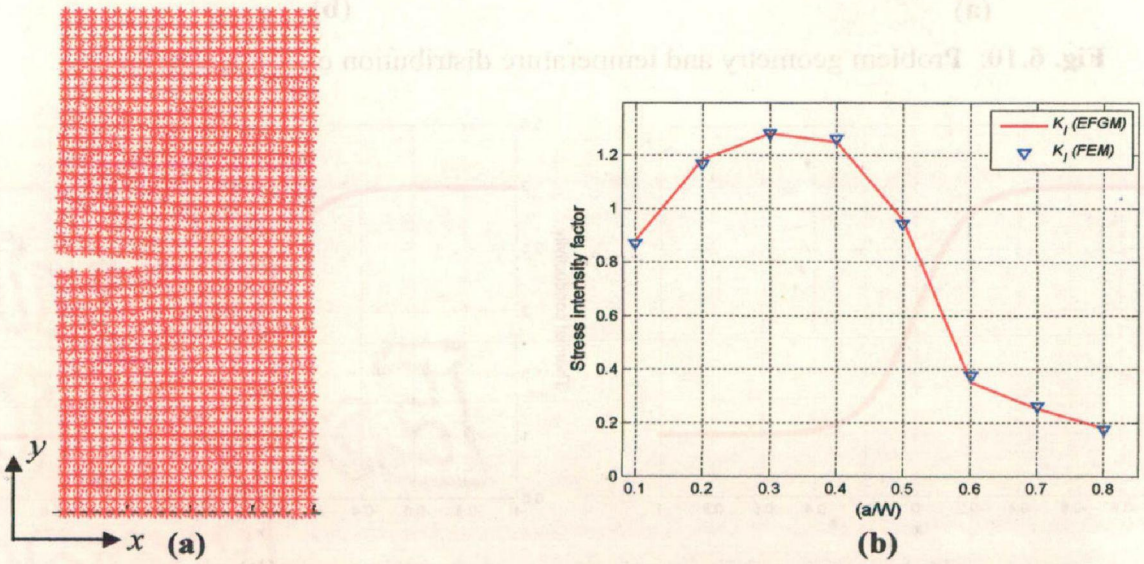

(a) (b)

Fig. 6.13: Displaced nodal positions and variation of stress intensity factor

6.5.3 Crack in Functionally Graded Thermal Barrier Coating (TBC)

Thermal barrier coating (TBC) can be defined as a highly advanced material system usually applied to metallic surfaces operating under elevated temperatures such as gas turbine blades, aero engines, ducting and nozzles, turbocharger casing, cutting tools etc. TBCs are characterized by their low thermal conductivity, bearing a large temperature gradient when exposed to heat flow. Modern engineering and industrial applications not only require a restriction on heat transfer but also prevent the surface from the damaging effect of oxidation and corrosion. Since, no single coating composition is able to satisfy all the desired requirements, the idea of coating system came into existence. Functionally graded thermal barrier coating (FTBC) introduces more reliability and reduces interfacial thermal stress between metallic and ceramic layers. FTBC provides less inter-layer thermal stress since the gradient will vary smoothly across the coating thickness. Discontinuities in thermal expansion coefficients between the bond coat and substrate also gets reduced. Each FTBC layer will act as a TBC layer with various material compositions thereby it gives more life cycles than that of TBC layers of same thickness under the same loading.

Applications of functionally graded thermal barrier coating at elevated temperature along with corrosive environment make them highly susceptible for crack initiation. In the present problem, an edge crack in FTBC under thermal loading has been modeled and analyzed using EFGM. Figure 6.14 shows a functionally graded thermal barrier coating deposited on the bond coat and the metallic substrate. The FGM coating consist of 100% Zirconium-Yttria at $X_1 = 0$ and 100% nickel-chromium-aluminum-Zirconium (NiCrAlY) bond coat at $X_1 = W_1$. The metallic substrate is made up of nickel based

super-alloy. The material properties of different constituents of thermal barrier coating are listed in Table 6.1. The dimensions of FGM thermal barrier coating along with thermal loading and boundary conditions are shown in Fig. 6.14. Initially the system is assumed to be at a uniform temperature ($T_o = 1000^oC$).

Table 6.1: Properties of TBC constituents

Material Property	**Zirconia-Yttria (FGM)**	**Bond Coat NiCrAlY**	**Metallic Substrate (Ni)**
$E(GPa)$	27.6	137.9	175.8
ν	0.25	0.27	0.25
$\beta(^oC^{-1})$	10.01×10^{-6}	15.16×10^{-6}	13.91×10^{-6}
$k(W/mK)$	1	25	7

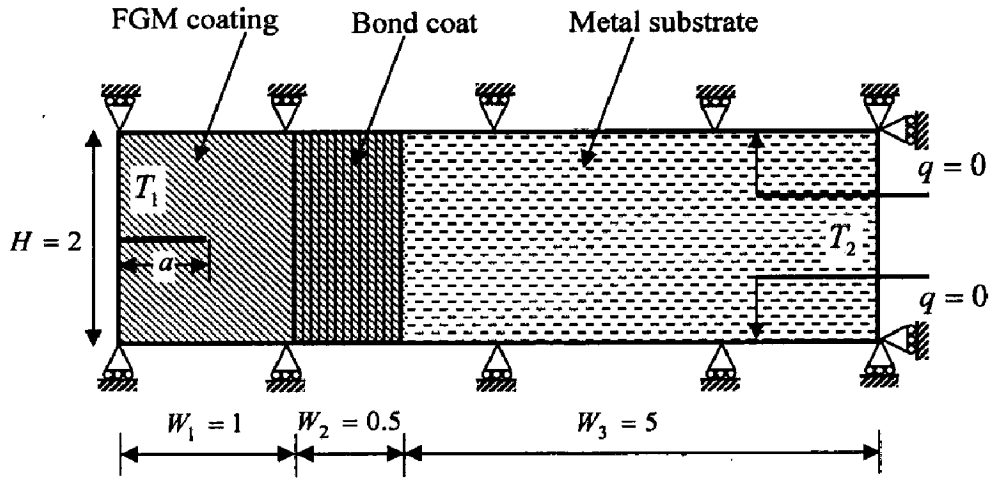

Fig. 6.14: A crack in a functionally graded thermal barrier coating

The top and bottom edges of the TBC system are assumed to be insulated. Application of temperature boundary conditions drives the system to a steady state condition with temperature $T_1 = 0.2T_o$ and $T_2 = 0.5T_o$ at left and right edges respectively. The gradation of Young's modulus (E), Poisson's ratio (ν) and thermal expansion coefficient (β) for the FGM coating region $(0 < X < 1)$ is defined by the relations given below:

$$E(X_1) = E_c + (E_{bc} - E_c)X^2 \tag{6.38}$$

$$\nu(X_1) = \nu_c + (\nu_{bc} - \nu_c)X \tag{6.39}$$

$$\beta(X_1) = \beta_c + (\beta_{bc} - \beta_c)X \tag{6.40}$$

$$k(X_1) = k_c + (k_{bc} - k_c)X^2 \tag{6.41}$$

where, subscript (c) symbolizes FGM coating and subscript (bc) denotes the bond coat. The gradation of material properties along the width of TBC has been shown in Fig. 6.15-6.16. Along the width of FGM coating i.e. W_1 the modulus of elasticity of the material exhibits a quadratic variation (Fig. 6.15a) while Poisson's ratio and coefficient of thermal expansion vary linearly, as shown in Fig. 6.15b and Fig. 6.16a respectively. The variation of thermal conductivity is plotted across the width (W) of the thermal barrier coating as shown in Fig. 6.16b. From Fig. 6.16b, it can be clearly observed that upto the thickness of FGM coating (W_1), the thermal conductivity follows a quadratic variation, and its value reaches to a maximum at the bond coat layer. At the interface of bond coat and metal substrate, there is a sharp decline in the magnitude of the thermal conductivity and further its value remains constant for the remaining thickness of metal substrate.

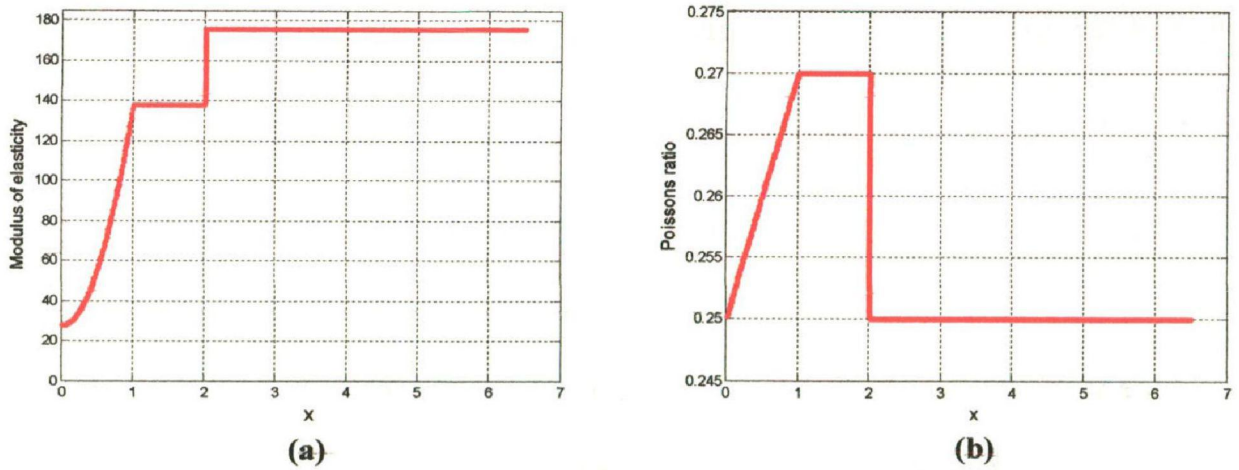

(a) (b)

Fig. 6.15: Gradation of modulus of elasticity and Poisson's ratio across the width (W) of the domain

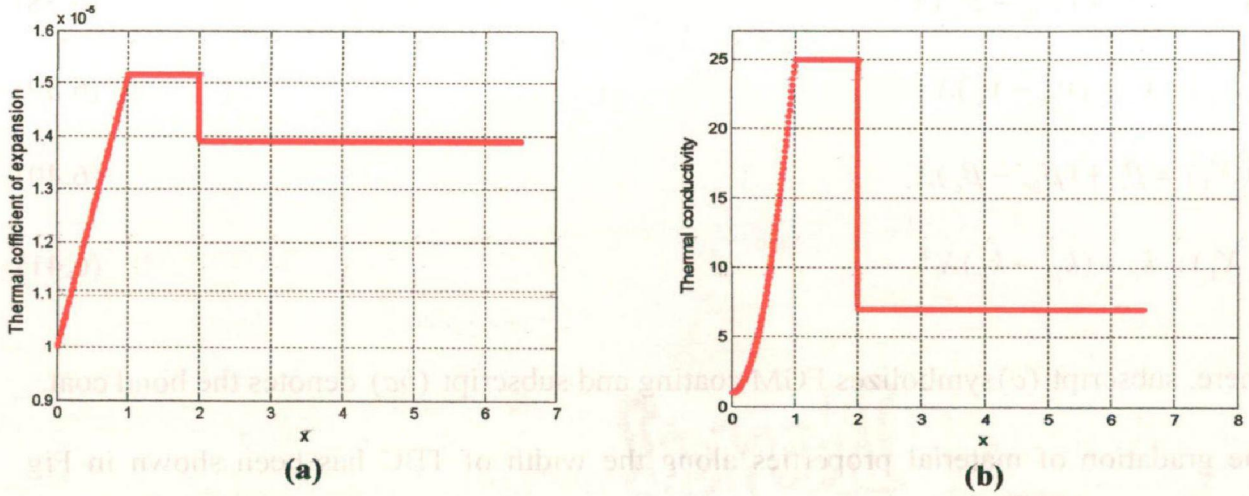

Fig. 6.16: Gradation of coefficient of thermal expansion and conductivity across the width (W) of the domain

A uniform nodal density of 1250 nodes along with six point Guass quadrature has been used to simulate the problem under plane strain conditions. Temperature field remains unaffected by the presence of crack as shown in Fig. 6.17 as the heat flux is parallel to the crack surface. Figure 6.18a shows the variation of normalized temperature i.e. $\left(\frac{T(X_1)}{T_o}\right)$ along the width of TBC assembly. A quadratic variation of thermal conductivity along the width of FGM layer is quite justified by a resulting quadratic variation of temperature as can be clearly seen from Fig. 6.18a. The values of mode-I stress intensity factor i.e. K_I is calculated for different $\left(\frac{a}{W}\right)$ ratio as shown in Fig. 6.18b. A good agreement in numerical results with the FEM solution (Amit and Kim, 2008) demonstrates the modeling capability of EFGM. In order to visualize the presence of crack, the stress/strain field contours have been generated for the functionally graded TBC assembly for a ratio of $a/W = 0.4$ as shown in Fig. 6.19-6.20.

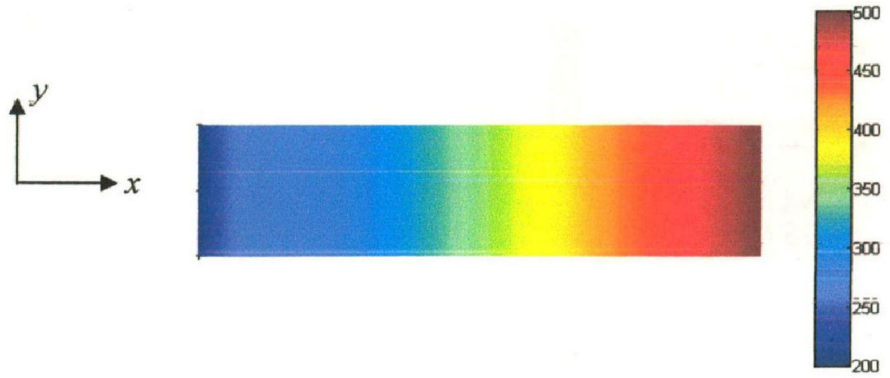

Fig. 6.17: Temperature distribution over the cracked TBC assembly

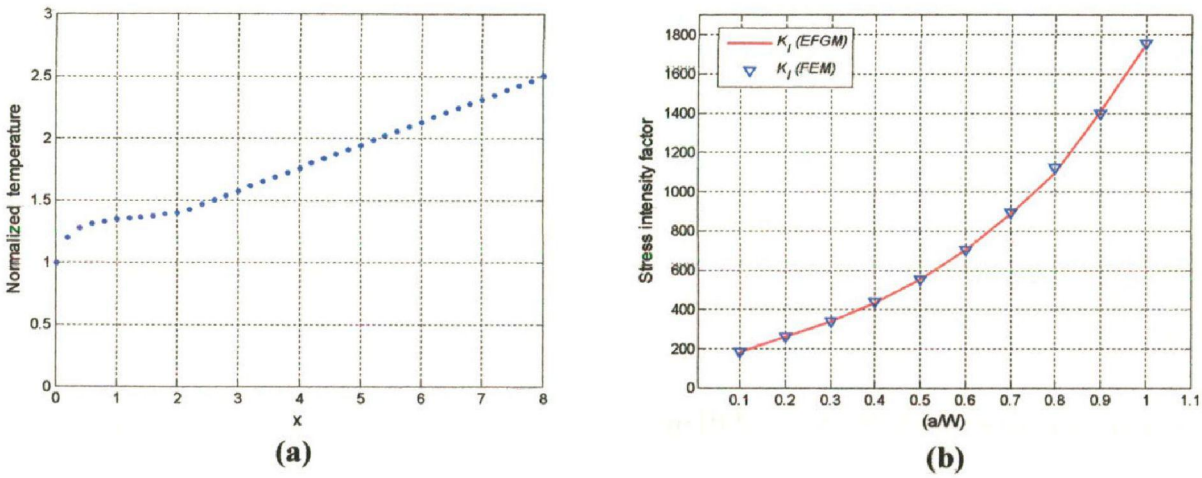

Fig. 6.18: Variation of normalized temperature and stress intensity factor

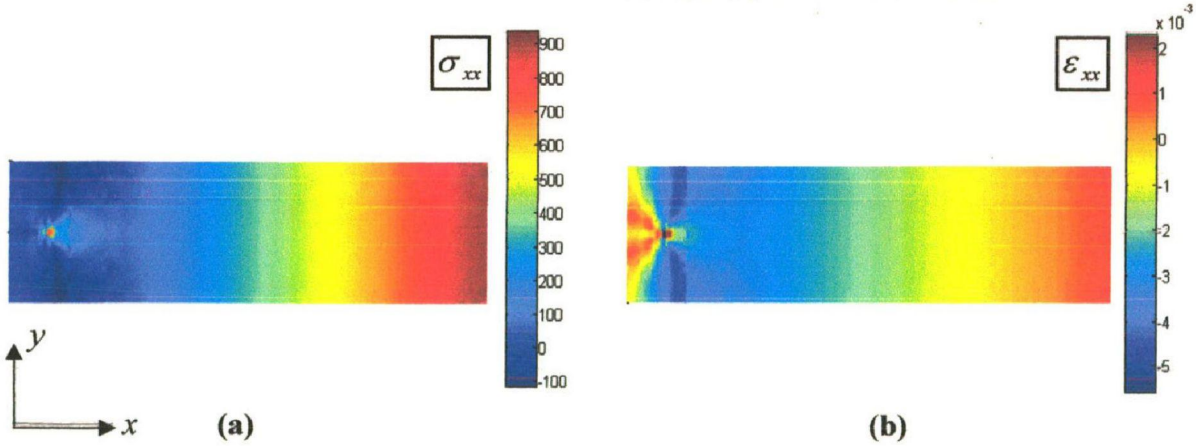

Fig. 6.19: Stress/strain contours along x-direction over the cracked TBC domain

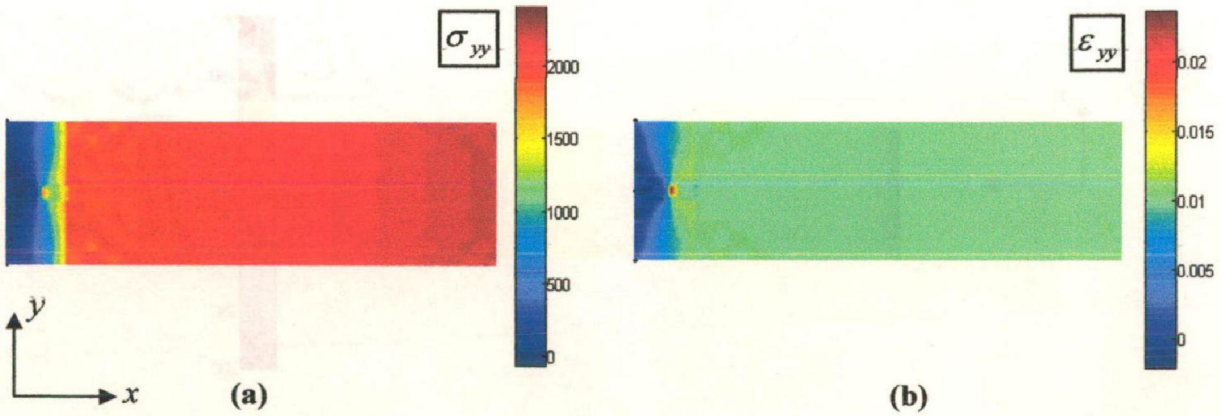

Fig. 6.20: Stress/strain contours along y-direction over the cracked TBC domain

6.6 CONCLUSION

The present chapter demonstrates the crack modeling capability of EFGM in functionally graded materials. The values of stress intensity factors were calculated using a modified form of interaction integral which accounts for the gradation of material properties in FGMs. The crack problems were modeled and analyzed under both mechanical and thermal loading conditions. A comparison has been made among the SIF values predicted by EFGM and available reference solutions generated analytically or numerically. On the basis of analysis performed in this chapter, it was found that the EFGM is an efficient method for modeling cracks in functionally graded materials, which reflects its potential to solve a variety of practical fracture problems.

Chapter 7

ELASTO-PLASTIC FRACTURE ANALYSIS

7.1 INTRODUCTION

The development of linear elastic fracture mechanics (LEFM) is associated with the study of crack growth and fracture under elastic conditions. Most of the early work on fracture was applicable only to linear elastic materials under quasi-static conditions. The basic assumption of LEFM is that the plastic zone is confined to a very small region surrounding the crack tip. However, such conditions are met only under plane strain fracture of high strength metallic materials and fracture of brittle materials such as ceramic, rocks, ice, etc. The theory of linear elastic fracture predicts a state of infinite stress at the crack tip which is not possible for a real material. Later on, subsequent advances in fracture research modeled other types of material behavior. Elastic-plastic fracture mechanics is applicable for materials that exhibit time-independent, non-linear behavior i.e. plastic deformation. The extension of theory of fracture mechanics to include elasto-plastic materials is based on deformation theory of plasticity. In the elastic-plastic materials, the size of plastic zone exceeds the small scale yielding approximation. In the present work, deformation theory of plasticity has been used to model the elasto-plastic material behavior by means of a generalized Ramberg-Osgood relation.

So far, the developments in meshfree methods have mainly focused on fracture of linear elastic materials. Research in elastoplastic materials using meshfree methods has not been widespread. It has been received some attention during last decade. Xu and Saigal (1998) proposed an EFGM based formulation for quasi-static and dynamic crack

growth in elastoplastic material undergoing small scale yielding. Rao and Rahman (2004) proposed an enriched meshfree EFGM for fracture analysis in two-dimensional solids. Kargarnovin *et al.* (2004) extended the EFGM for elasto-plastic stress analysis using incremental formulation of plastic deformation. Dynamic meshfree methods were formulated by Chen *et al.* (2002) using local and non-local field theories for the simulation of two crack problems. Liu *et al.* (2006) suggested an EFG-FE coupling procedure to simulate an elasto-plastic contact problem. Belinha and Dinis (2006) carried out the elasto-plastic analysis of plates using EFGM.

Motivated by the wide applicability of EFGM and to establish it as a robust tool for solving problems of fracture mechanics the present chapter focuses on simulating the elastoplastic analysis of a two dimensional cracked body. Rao and Rahman (2004) analyzed the cracks in non-linear elastic materials using enriched basis function. They employed the Newton-Raphson iterative scheme to solve the non-linear constitutive equations. In the present work, a constitutive relation for incremental plasticity have been used which accounts for non-linear material behavior using Ramberg-Osgood material model. For a material exhibiting power law hardening, the nature of dominant stress singularity near the crack tip is described by Hutchinson-Rice-Rosengren (HRR) relations. Enriched basis function (Rao and Rahman, 2004) is employed to capture the HRR stress singularity.

7.2 ELASTO-PLASTIC CONSTITUTIVE EQUATIONS

Consider a solid undergoing elastic-plastic deformation, then the plastic potential function can be treated as a function of stresses (σ_{ij}) and work hardening parameter $(\hat{k})$. Mathematically it can be expressed as (Hsu, 1986)

$$F = F(\sigma_{ij}, \hat{k}) \tag{7.1}$$

For a Von-Mises type material, the plastic potential (yield function) for an isotropic strain hardening material has the form

$$F = J_2 - \sigma_s^2 = J_2 - \frac{1}{3}\sigma_Y^2 \tag{7.2}$$

where, σ_s, σ_Y are respectively the yield strength of material in pure shear and uniaxial tension, J_2 is the second deviatoric stress invariant.

The second invariant of stress J_2 can also be expressed as

$$J_2 = \frac{1}{2}\sigma'_{ij}\,\sigma'_{ij} \tag{7.3}$$

where, σ'_{ij} represents the deviatoric stresses given by

$$\sigma'_{ij} = \sigma_{ij} - \sigma_m \delta_{ij} \tag{7.4}$$

$\sigma_m = \dfrac{\sigma_{11} + \sigma_{22} + \sigma_{33}}{3}$ is the mean stress, and δ_{ij} is the Kronecker delta.

Taking the partial derivative of deviatoric stress invariant (J_2), we get

$$\frac{\partial J_2}{\partial \sigma_{ij}} = \sigma'_{ij} \tag{7.5}$$

During small incremental plastic deformation in solids, equilibrium conditions requires that the plastic energy variation must be stationary $dF = 0$ (Hsu, 1986), hence differentiating Eq. (7.2) by chain rule of partial differentiation, we obtain

$$dF = \frac{\partial J_2}{\partial \sigma_{ij}} d\sigma_{ij} - \frac{2}{3}\sigma_Y \frac{\partial \sigma_Y}{\partial \hat{k}} d\hat{k} = 0 \tag{7.6}$$

or

$$\sigma'_{ij} d\sigma_{ij} - \frac{2}{3}\sigma_Y \frac{\partial \sigma_Y}{\partial \hat{k}} d\hat{k} = 0 \tag{7.7}$$

For a plane stress problem, $\sigma_{xz} = \sigma_{yz} = \sigma_{zz} = 0$ and Eq. (7.7) reduces to

$$\sigma'_x d\sigma_x + \sigma'_y d\sigma_y + 2\sigma_{xy} d\sigma_{xy} = \frac{2}{3}\sigma_Y \frac{\partial \sigma_Y}{\partial \hat{k}} d\hat{k} \tag{7.8}$$

Let us assume that

$$\sigma'_x d\sigma_x + \sigma'_y d\sigma_y + 2\sigma_{xy} d\sigma_{xy} = A d\lambda \tag{7.9}$$

where, $A d\lambda = \frac{2}{3}\sigma_Y \frac{\partial \sigma_Y}{\partial \hat{k}} d\hat{k}$, $d\lambda$ being a proportionality factor (7.10)

According to the additive decomposition of strains, the total strain may be written as

$$d\varepsilon_{ij} = d\varepsilon_{ij}^e + d\varepsilon_{ij}^p \tag{7.11}$$

where, $d\varepsilon_{ij}^e$ is the increment in elastic strain, and $d\varepsilon_{ij}^p$ is the increment in plastic strain.

$d\varepsilon_{ij}^p$ is proportional to the corresponding deviotric stress component, i.e.

$$d\varepsilon_{ij}^p = \sigma'_{ij} d\lambda \tag{7.12}$$

hence, for a plane stress problem

$$d\varepsilon_x = \frac{1}{E}\left(d\sigma_x - \nu\, d\sigma_y\right) + \sigma'_x\, d\lambda \tag{7.13}$$

$$d\varepsilon_y = \frac{1}{E}\left(d\sigma_y - \nu\, d\sigma_x\right) + \sigma'_y\, d\lambda \tag{7.14}$$

$$d\gamma_{xy} = \frac{2(1+\nu)}{E} d\sigma_{xy} + 2\sigma'_{xy} d\lambda \tag{7.15}$$

Rearranging Eq. (7.13) and Eq. (7.14), we have

$$d\varepsilon_x + \nu d\varepsilon_y = \frac{1-\nu^2}{E} d\sigma_x + \left(\sigma'_x + \nu\sigma'_y\right) d\lambda \tag{7.16}$$

$$d\varepsilon_y + \nu d\varepsilon_x = \frac{1-\nu^2}{E} d\sigma_y + \left(\sigma'_y + \nu\sigma'_x\right) d\lambda \tag{7.17}$$

Simplifying and rearranging Eq. (7.15) — Eq. (7.17), we get

$$d\sigma_x = \left(\frac{E}{1-\nu^2}\right)\left(d\varepsilon_x + \nu d\varepsilon_y\right) - S_1 d\lambda \tag{7.18}$$

$$d\sigma_y = \left(\frac{E}{1-\nu^2}\right)\left(d\varepsilon_y + \nu d\varepsilon_x\right) - S_2 d\lambda \tag{7.19}$$

$$d\sigma_{xy} = \frac{E}{2(1+\nu)} d\gamma_{xy} - S_3 d\lambda \tag{7.20}$$

where,

$$S_1 = \frac{E}{1-\nu^2}\left(\sigma'_x + \nu\sigma'_y\right) \tag{7.21}$$

$$S_2 = \frac{E}{1-\nu^2}\left(\sigma'_y + \nu\sigma'_x\right) \tag{7.22}$$

$$S_3 = \frac{E}{1+\nu}\sigma'_{xy} \tag{7.23}$$

Substituting the values of $d\sigma_x$, $d\sigma_y$ and $d\sigma_{xy}$ from Eq. (7.18) — Eq. (7.20) into Eq. (7.9), we get

$$Ad\lambda = \frac{E}{1-\nu^2}\sigma'_x\left(d\varepsilon_x + \nu\, d\varepsilon_y\right) + \frac{E}{1-\nu^2}\sigma'_y\left(d\varepsilon_y + \nu\, d\varepsilon_x\right) - \left(\sigma'_x S_1 + \sigma'_y S_2 + 2\sigma_{xy} S_3\right)d\lambda + \frac{E}{1+\nu}\sigma_{xy} d\gamma_{xy} \tag{7.24}$$

$$\left(A + \sigma'_x S_1 + \sigma'_y S_2 + 2\sigma_{xy} S_3\right)d\lambda = S_1 d\varepsilon_x + S_2 d\varepsilon_y + S_3 d\gamma_{xy} \tag{7.25}$$

$$d\lambda = \frac{S_1 d\varepsilon_x + S_2 d\varepsilon_y + S_3 d\gamma_{xy}}{S_o} \tag{7.26}$$

where, $S_o = A + \sigma'_x S_1 + \sigma'_y S_2 + 2\sigma_{xy} S_3$ (7.27)

Substituting the value of $d\lambda$ from Eq. (7.26) into Eq. (7.18), Eq. (7.19) and Eq. (7.20), we get

$$d\sigma_x = \frac{E}{1-\nu^2}\left(d\varepsilon_x + \nu d\varepsilon_y\right) - \frac{S_1^2 d\varepsilon_x + S_1 S_2 d\varepsilon_y + S_1 S_3 d\gamma_{xy}}{S_o} \tag{7.28}$$

$$d\sigma_y = \frac{E}{1-\nu^2}\left(d\varepsilon_y + \nu d\varepsilon_x\right) - \frac{S_1 S_2 d\varepsilon_x + S_2^2 d\varepsilon_y + S_2 S_3 d\gamma_{xy}}{S_o} \tag{7.29}$$

$$d\sigma_{xy} = \frac{E}{2(1+\nu)} d\gamma_{xy} - \frac{S_1 S_3 d\varepsilon_x + S_2 S_3 d\varepsilon_y + S_3^2 d\gamma_{xy}}{S_o} \tag{7.30}$$

Eq. (7.28), Eq. (7.29), and Eq. (7.30) can be further written in matrix form as

$$\begin{bmatrix} d\sigma_x \\ d\sigma_y \\ d\sigma_{xy} \end{bmatrix} = \frac{E}{1-\nu^2}\begin{bmatrix} 1 & \nu & 0 \\ \nu & 1 & 0 \\ 0 & 0 & \frac{1-\nu}{2} \end{bmatrix}\begin{bmatrix} d\varepsilon_x \\ d\varepsilon_y \\ d\gamma_{xy} \end{bmatrix} - \frac{1}{S_o}\begin{bmatrix} S_1^2 & S_1S_2 & S_1S_3 \\ - & S_2^2 & S_2S_3 \\ \text{SYM} & - & S_3^2 \end{bmatrix}\begin{bmatrix} d\varepsilon_x \\ d\varepsilon_y \\ d\gamma_{xy} \end{bmatrix} \tag{7.31}$$

$$\begin{bmatrix} d\sigma_x \\ d\sigma_y \\ d\sigma_{xy} \end{bmatrix} = C_{ep}\begin{bmatrix} d\varepsilon_x \\ d\varepsilon_y \\ d\gamma_{xy} \end{bmatrix} \tag{7.32}$$

where, C_{ep} denotes the elastoplastic stiffness matrix and is given by

$$C_{ep} = \frac{E}{1-\nu^2}\begin{bmatrix} 1 & \nu & 0 \\ \nu & 1 & 0 \\ 0 & 0 & \frac{1-\nu}{2} \end{bmatrix} - \frac{1}{S_o}\begin{bmatrix} S_1^2 & S_1S_2 & S_1S_3 \\ - & S_2^2 & S_2S_3 \\ \text{SYM} & - & S_3^2 \end{bmatrix} \tag{7.33}$$

In the elasto-plastic stiffness matrix C_{ep}, S_1, S_2 and S_3 are known in terms of σ'_{ij}. S_o contains an yet undetermined term A. From Eq. (7.10),

$$A = \frac{1}{d\lambda}\frac{2}{3}\sigma_Y \frac{\partial \sigma_Y}{\partial \hat{k}} d\hat{k} \tag{7.34}$$

The work hardening parameter $d\hat{k}$ may be expressed as (Hsu, 1986)

$$d\hat{k} = \sigma'_{ij}\, d\varepsilon^p_{ij} \tag{7.35}$$

Using Eq. (7.12),

$$d\hat{k} = \sigma_{ij}\sigma'_{ij}\, d\lambda = \sigma'_{ij}\sigma'_{ij} d\lambda = 2J_2 d\lambda \tag{7.36}$$

Hence, $A = \frac{4}{3}\sigma_Y J_2 \frac{\partial \sigma_Y}{\partial \hat{k}}$ (7.37)

For uniaxial loading in the plastic regime, the stress is σ_Y and the strain increment is the direction of the applied stress $d\varepsilon_p$ then, $d\hat{k} = \sigma_Y d\varepsilon_p$ and $J_2 = \frac{\sigma_Y^2}{3}$. Substituting these values in Eq. (7.37),

$$A = \frac{4}{9}\sigma_Y{}^2 \frac{d\sigma_Y}{d\varepsilon_p} \tag{7.38}$$

$\frac{d\sigma_Y}{d\varepsilon_p}$ is the plastic modulus(H') of the stress-strain curve in uniaxial tension. Hence,

$$A = \frac{4}{9}\sigma_Y{}^2 H' \tag{7.39}$$

H' can be measured experimentally. However, H' can be obtained using Ramberg-Osgood relation, which may be written as

$$\frac{\varepsilon}{\varepsilon_o} = \frac{\sigma}{\sigma_Y} + \alpha'\left(\frac{\sigma}{\sigma_Y}\right)^{n'} \tag{7.40}$$

where, σ_Y denotes the yield strength, α' and n' are the Ramberg-Osgood material constants. From Eq. (7.40), we get

$$\frac{d\varepsilon}{d\sigma} = \frac{1}{E} + \frac{n'\alpha'\sigma_Y^{(1-n')}\sigma^{(n'-1)}}{E} \tag{7.41}$$

$$\text{Hence, } H' = \frac{E}{n'\alpha'\sigma_Y^{(1-n')}\sigma^{(n'-1)}} \tag{7.42}$$

7.3 EVALUATION OF J- INTEGRAL

For a homogenous cracked body, the path independent *J*-integral is given as (Wilson and Yu, 1979)

$$J = \int_\Gamma \left(\tilde{W}\delta_{1j} - \sigma_{ij}\frac{\partial u_i}{\partial x_1}\right) n_j d\Gamma \tag{7.43}$$

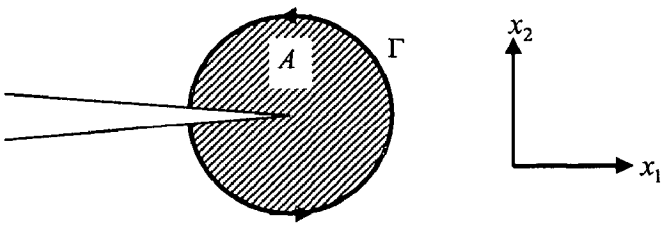

Fig. 7.1: Path Γ surrounding a crack with an enclosed area *A*

where, $\widetilde{W}$ is the strain energy density and n_j is the j-th component of the outward unit vector normal to an arbitrary contour Γ enclosing the crack tip (Fig. 7.1). The Ramberg-Osgood power law describing the non-linear uniaxial stress-strain curve is given by

$$\frac{\varepsilon}{\varepsilon_o} = \frac{\sigma}{\sigma_Y} + \alpha' \left(\frac{\sigma}{\sigma_Y} \right)^{n'} \tag{7.44}$$

where σ_Y is the reference stress (yield strength), $\varepsilon_o = \sigma_Y / E$ is the reference strain, E is the Young's modulus, α' is a material constant and n' the hardening exponent. For $n' = 1$ Eq. (7.44) represents a linear elastic material. For multiaxial stress state, the Ramberg-Osgood law can be generalized with respect to strain rate partition as

$$\dot{\varepsilon}_{ij} = \dot{\varepsilon}_{ij}^e + \dot{\varepsilon}_{ij}^p \tag{7.45}$$

$$\text{where } \dot{\varepsilon}_{ij}^e = \frac{1+\nu}{E} \dot{s}_{ij} + \frac{1-2\nu}{3E} \dot{\sigma}_{kk} \delta_{ij} \tag{7.46}$$

$$\text{and } \dot{\varepsilon}_{ij}^p = \frac{3}{2E} \alpha' \left(\frac{\sigma_e}{\sigma_Y} \right)^{n'-1} \dot{s}_{ij} \tag{7.47}$$

are the elastic and plastic components of strain rate, ν is the Poisson ratio, $\dot{s}_{ij} = \dot{\sigma}_{ij} - \dot{\sigma}_{kk}\, \delta_{ij}/3$ is the deviatoric stress rate, $\sigma_e = \sqrt{3 s_{ij} s_{ij}/2}$ is the Von-Mises stress and δ_{ij} is the Kronecker delta. If elastic strain rates are negligible compared with plastic strain rates (i.e., $\dot{\varepsilon}_{ij} \approx \dot{\varepsilon}_{ij}^p$) then the asymptotic crack tip fields under mode-I loading are (Hutchinson, 1968; Rice and Rosengren 1968)

$$\sigma_{ij} = \sigma_o \left(\frac{J}{\alpha' \sigma_Y \varepsilon_o I_n r} \right)^{1/(n'+1)} \widetilde{\sigma}_{ij}(\theta, n') \tag{7.48}$$

$$\varepsilon_{ij} = \alpha' \varepsilon_o \left(\frac{J}{\alpha' \sigma_Y \varepsilon_o I_n r} \right)^{n'/(n'+1)} \widetilde{\varepsilon}_{ij}(\theta, n') \tag{7.49}$$

$$u_i = \alpha' \varepsilon_o r \left(\frac{J}{\alpha' \sigma_Y \varepsilon_o I_n r} \right)^{n'/(n'+1)} \tilde{u}_i(\theta, n') \tag{7.50}$$

where, r and θ are polar coordinates with origin at the crack tip, I_n is a dimensionless constant that depends on n'. $\tilde{\sigma}_{ij}$, $\tilde{\varepsilon}_{ij}$ and $\tilde{u}_i$ are dimensionless angular function of θ and n'. Eq. (7.48) — Eq. (7.50) represents the well known HRR field under mode-I loading conditions. The same HRR field also exists in mixed-mode fracture but in that case the dimensionless angular functions also depend on the magnitude of mode-mixity (Pan and Shih, 1992).

7.4 ENRICHED BASIS FUNCTION FOR ELASTO-PLASTIC FRACTURE

The enrichment of basis function in EFGM is a convenient way of capturing the stress singularity at the crack tip. The basis function used to study the cracks under linear elastic fracture mechanics (LEFM) regime are not appropriate for the simulation of cracks under elasto-plastic conditions as the singularity of crack-tip fields is different than in LEFM. As HRR displacement and stress fields are known for elasto-plastic simulation, thereby enriched basis function can be developed for elasto-plastic fracture problems by enriching the standard basis function using information from elasto-plastic HRR solution. The enriched basis function developed by Rao and Rahman (2004) is used in the present study, which is given as

$$\mathbf{P}^T(\mathbf{x}) = \left[\underbrace{1,\ x,\ y}_{\text{Standard basis}} \ , \underbrace{r^{\frac{1}{n'+1}} \cos\frac{\theta}{2}, r^{\frac{1}{n'+1}} \sin\frac{\theta}{2}, r^{\frac{1}{n'+1}} \sin\frac{\theta}{2}\sin\theta, r^{\frac{1}{n'+1}} \cos\frac{\theta}{2}\sin\theta}_{\text{Enrichment terms}} \right] \tag{7.51}$$

where r and θ are the local crack tip parameters of evaluation point having (x, y) the spatial coordinates and n' is the Ramberg-Osgood parameter for the material. It should be noted that the linear terms in the basis function are not related to crack tip fields, but are required for linear completeness of EFGM solution.

7.5 RESULTS AND DISCUSSIONS

A two dimensional edge crack body along with its geometry and boundary conditions is shown in Fig. 7.2. The dimensions of the cracked body used in the present study are taken as $H = 200$ mm, $W = 100$ mm, $a = 40$ mm. The bottom edge has been constrained along y-direction, and an external far field stress is applied at the top edge. A regular nodal distribution of 648 nodes has been considered in all simulations. Six point Gauss quadrature has been used for the numerical integration of the Galerkin weak form. A plane stress condition has been assumed.

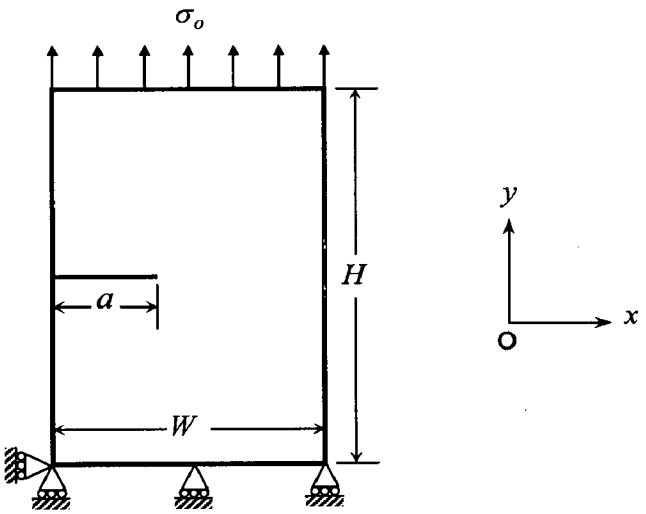

Fig. 7.2: Problem geometry along with boundary conditions

The material selected for the present study has a modulus of elasticity (E) = 206 GPa, Yield strength (σ_Y)=154 MPa. Poisson's ratio (ν) = 0.3. A far field stress, (σ_o) = 100 MPa is applied as an external load. Fifty load steps are taken with each load step of size 2 MPa. J-integral has been calculated for different values of Ramberg-Osgood parameters (n', α') along with the enriched basis function. Figure 7.3 shows the variation of J- integral with applied stress. In order to validate the formulation, results have been simulated for different values of Ramberg-Osgood parameter (n', α'). The EFGM results were found in good agreement with FEM solutions obtained using ABAQUS software.

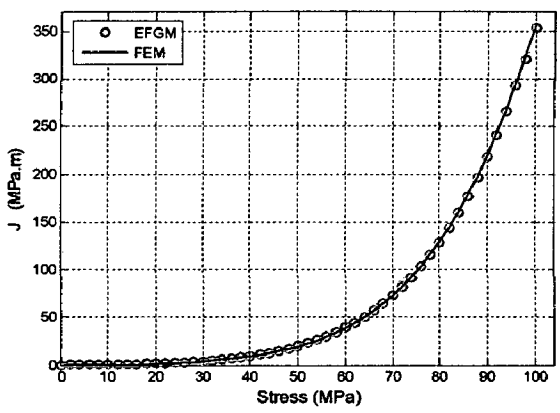

(a) $(n' = 4, \alpha' = 3)$

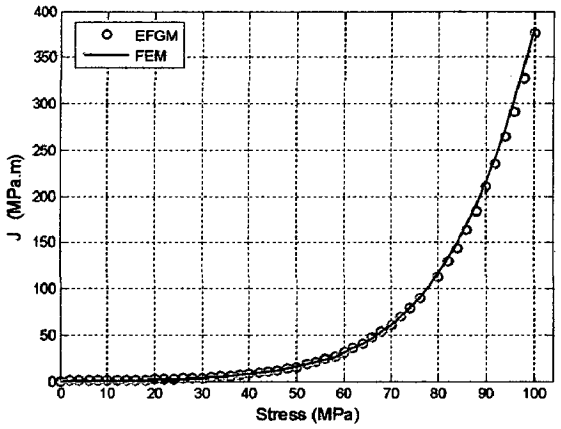

(b) $(n' = 5, \alpha' = 2)$

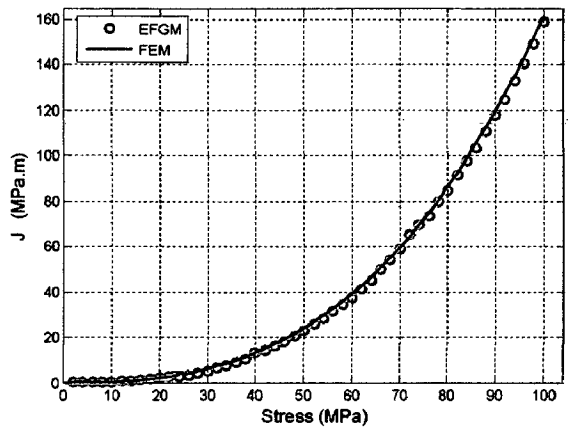

(c) $(n' = 2, \alpha' = 3)$

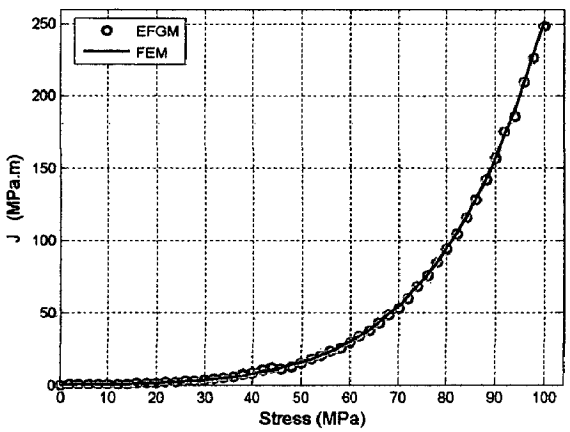

(d) $(n' = 4, \alpha' = 2)$

Fig. 7.3: *J vs.* stress plots for different values of n' and α'

The present elasto-plastic analysis is found to be quiet sensitive to the domain scaling parameter $(d_{\max})$. Initially the results were obtained with the scaling parameter $d_{\max}$=1.5. For linear elastic analysis $d_{\max}$=1.5 was giving accurate results. For elasto-plastic problems $d_{\max}$=1.5 was not adequate and the results did not match with the FEM results. Hence in order to optimize the value of the scaling parameter, a sensitivity analysis is also carried out as discussed in next subsection.

7.5.1 Sensitivity Analysis for scaling parameter $(d_{\max})$

In order to optimize the value of scaling parameter $(d_{\max})$ for elasto-plastic simulations, a sensitivity analysis is performed. An edge crack problem (as shown in Fig. 7.2) is

considered having same material properties and boundary conditions as discussed in previous section. The value of Ramberg-Osgood parameter for this study is taken as $n' = 4$ and $\alpha' = 3$. Figure 7.4a shows the variation of J-integral values for different magnitude of scaling parameter d_{max}. For $d_{max} < 2.5$, the EFGM results shows quite large deviation from the FEM results. Similarly, Fig. 7.4b shows the variation of nodal displacement (of a specific node) for different values of scaling parameter d_{max}. On the basis of results presented in Fig. 7.4a and Fig. 7.4b, an optimum value of d_{max} is found to be 2.75 by taking into consideration both convergence and computational time. The results presented in Fig. 7.3 have been obtained for $d_{max} = 2.75$ only.

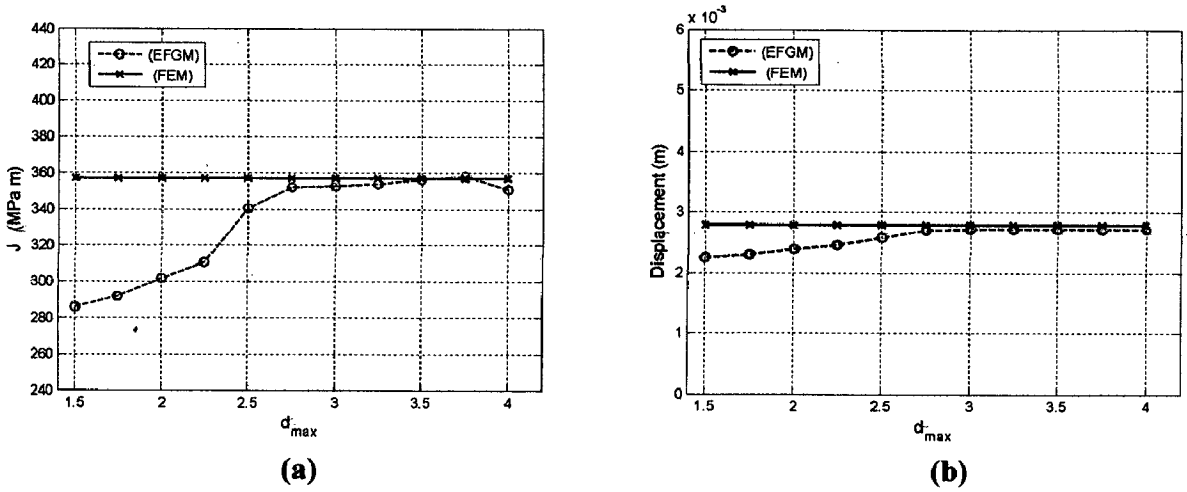

Fig. 7.4: Variation of J and displacement with scaling parameter d_{max}

7.6 CONCLUSION

In this chapter, EFGM has been employed for the simulation of elasto-plastic fracture problem. A new formulation based on incremental plasticity has been suggested and implemented in order to model the non-linear material response. The enriched basis function successfully captured the Hutchinson-Rice-Rosengren (HRR) stress singularity at the crack tip and the results were found in good agreement with the FEM solutions. It is concluded that scaling parameter d_{max} should be larger in the elasto-plastic analysis as compared to elastic analysis.

Chapter 8

QUASI-STATIC CRACK GROWTH MODELING

8.1 INTRODUCTION

The modeling of crack growth in a general direction plays an important role in predicting the life of engineering components and structures. Crack growth modeling remains one of the most challenging and interesting problem for computational mechanics. In the past, finite element method and boundary element method were mostly used for the modeling of crack growth. The limitations and disadvantages associated with these two methods restricted their application to a variety of problems.

The major drawback associated with finite element method is the remeshing scheme which must ensure the coincidence of element boundaries with moving discontinuities. The remeshing process requires a considerable amount of human effort and can be a source of numerical error. Moreover, the remeshing process involves interpolation of field variable such as displacement, stresses and strains to a new set of nodes and quadrature points. The use of various projection techniques for this interpolation process may further add to computational error.

The boundary element method has reduced the meshing process to a minimum as only the crack surface needs to be remeshed. However, the requirement of Green's function (Rice, 1968) for the underlying partial differential equation restricts the scope of boundary element method for solving a wide variety of problems. In addition to this drawback, the equations resulting from boundary element method are not sparse or banded, and tend to become ill-conditioned for large systems. This further hinders its application to engineering problems.

Meshfree methods have proven to be a powerful alternative in simulating growing cracks. A common feature of all these meshfree methods is that they do not require any fixed nodal connectivity information i.e. mesh. The ability of meshfree methods to simulate arbitrary crack growth without any remeshing makes them a promising alternative to the traditional approaches. Belytschko *et al.* (1995a) implemented EFGM for the modeling of crack growth in static problems. Xu and Saigal (1998a) further improved the formulation for stable crack growth in elastic solids. Tabbara and Stone (1998) developed a computational EFGM for quasi-static mixed-mode fracture problem. Ventura *et al.* (2001) proposed a new level set method for the description of a propagating crack in EFGM. Duflot (2006) proposed a meshfree method with enriched weight function for three-dimensional crack propagation. Li and Simonsen (2007) used the EFGM to simulate ductile crack growth and propagation under finite deformation and large scale yielding conditions. In general, the crack grows in an arbitrary direction under mixed-mode loading so a numerical method must be able to track the crack trajectory at each step. Since, the basis function used in the intrinsic enriched EFGM is capable of modeling the discontinuity along a straight crack only, some suitable techniques are required to model the crack growth for a kinked crack. Various methods have been proposed for the modeling of kinked cracks (Fleming *et al.,* 1997; Belytschko and Black, 1999; Duflot, 2006).

In the present Chapter, a new intrinsic enriched EFGM criterion for the modeling of kinked cracks has been proposed and implemented. In order to validate the proposed criterion, some kinked cracks problems in two-dimensional domain have been modeled. Next, the proposed criterion is employed for simulating the quasi-static crack growth in two-dimensional domain subjected to mixed-mode loading.

8.2 MODELING OF KINKED CRACKS

In intrinsic enriched EFGM, functions from the near-tip asymptotic displacement fields are included in the basis for the simulation of fracture mechanics problems. An enriched basis used in the present work is given as

$$\mathbf{P}^T(\mathbf{x}) = \left[1, x, y, \sqrt{r}\cos\frac{\theta}{2}, \sqrt{r}\sin\frac{\theta}{2}, \sqrt{r}\sin\frac{\theta}{2}\sin\theta, \sqrt{r}\cos\frac{\theta}{2}\sin\theta\right] \tag{8.1}$$

where, r denote the distance of an evaluation point from the crack tip, and θ is the angle measured in local coordinate system as shown in Fig. 8.1.

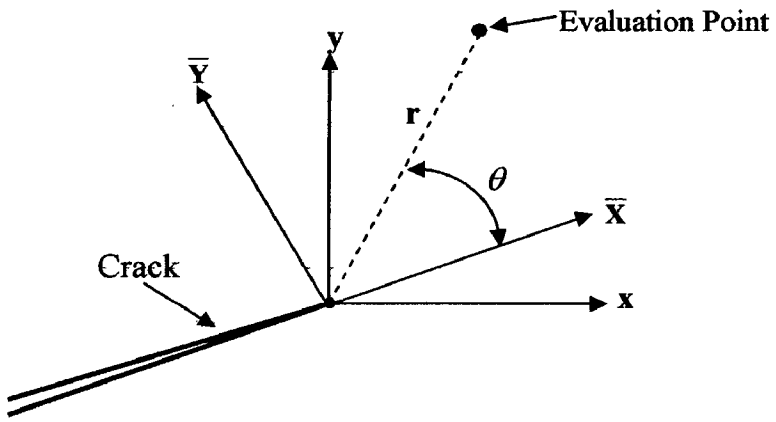

Fig. 8.1: Local coordinate system ($\bar{x}, \bar{y}$) at crack

The basis function given by Eq. (8.1) predicts a discontinuity along $\theta = \pm\pi$ from the crack line. However, for a kinked crack modeling, mapping is required to align the field discontinuity with actual crack segments. The proposed criterion for modeling a kinked crack is based on the modification in angular position of an evaluation point/node. The angular position of an evaluation point/node is modified in such a way that all points in the vicinity of the crack segments approximate the discontinuity along $\theta = \pm\pi$. Figure 8.2 shows a kinked crack with segments AB and BC. The local coordinate system is aligned along the leading segment i.e. BC with the origin at the tip. Consider an evaluation point P located in the vicinity of crack. Let, the angular orientation of point P

be α. In order to represent the discontinuity along the crack line, the angular orientation α should be mapped to a new coordinate system such that $\alpha \to \pm\pi$. The angular orientation of all the evaluation points are mapped to a new coordinate system in such a way that the evaluation points lying near the crack line exhibits a discontinuity in displacement fields.

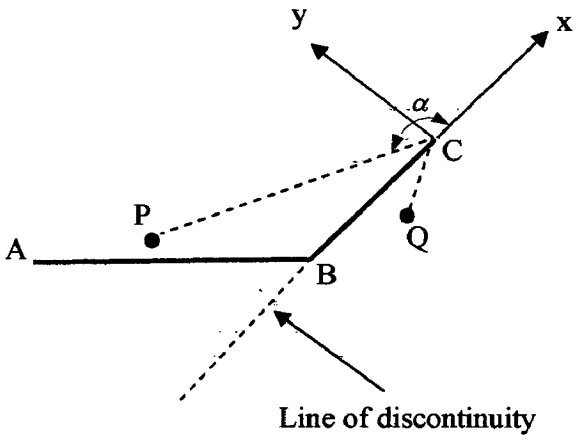

Fig. 8.2: Mapping scheme for kinked crack

The first step involved in the process of angular mapping is the division of domain into different regions. Figure 8.3 shows a kinked crack having segments *AB*, *BC* where C is the crack tip of the leading crack segment. A local coordinate system is fixed at the tip of leading crack. Normals are drawn at a common point to both crack segments, i.e. point B, so as to discretize the region above the crack. Thus, BQ and BP become normal to crack segments *AB* and *BC* respectively. Another normal is drawn at the tip of leading crack *BC*. The bisector of angle ABC is drawn so that the region below the crack gets divided into two parts. In this way, the entire region near the crack segments gets divided into six different regions. A similar process is involved for cracks having multiple kinks. The next step involves mapped new location of an evaluation point. This is done by some geometrical and mathematical calculations. Finally, a suitable mathematical mapping (for angular orientation) is applied depending upon the spatial location of an evaluation point.

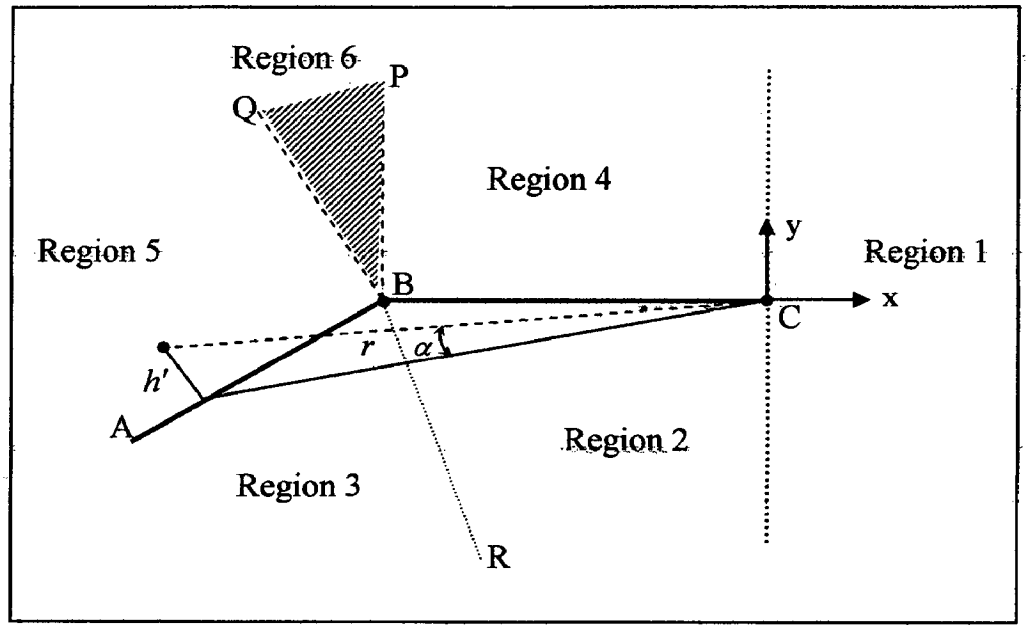

Fig. 8.3: Domain description for modeling kinked crack

For the region in front of the tip of leading crack i.e. region 1, all the angular measurements are made with respect to local coordinate axis in such a way that

$$\theta' = \theta \quad \text{for } -\frac{\pi}{2} \le \theta \le \frac{\pi}{2}. \tag{8.2}$$

For regions 2,3,4,5 the angle is modified as given below

$$\theta' = \begin{Bmatrix} \pi - Sin^{-1}\left(\frac{h'}{r}\right) & \text{above the crack} \\ -\pi + Sin^{-1}\left(\frac{h'}{r}\right) & \text{above the crack} \end{Bmatrix} \tag{8.3}$$

where, h' is the normal distance between the evaluation point/node and the crack segment lying in that region, r is the distance between an evaluation point and the tip of leading crack i.e. point C. For the points lying in shaded region QBP, the distance h' is measured between an evaluation point and the point representing kink i.e. point B. In

doing so, a transformation is made as the point approaches to the crack line, $h' \to 0$ then $\theta' \to \pm\pi$, and thus a clear discontinuity is obtained along the crack line.

Finally, the standard enriched basis function is written in terms of modified angle θ' as follows

$$\mathbf{P}^T(\mathbf{x}) = \left[\underbrace{1,\ x,\ y}_{\text{standard basis}},\ \underbrace{\sqrt{r}\cos\frac{\theta'}{2}, \sqrt{r}\sin\frac{\theta'}{2}, \sqrt{r}\sin\frac{\theta'}{2}\sin\theta', \sqrt{r}\cos\frac{\theta'}{2}\sin\theta'}_{\text{enrichment terms}} \right] \tag{8.4}$$

where, the first three terms represent the standard basis function $(1,\ x,\ y)$ while remaining four terms make the enrichment part for a kinked crack.

8.3 QUASI-STATIC FRACTURE

Quasi-static fracture and fatigue are two forms of crack growth. Fatigue refers to crack propagation under cyclic loading in cracked bodies where the SIF is below the fracture toughness, while in case of quasi-static fracture the crack propagation takes place when SIF is above the fracture toughness. Crack growth may be classified as stable and unstable depending upon the variation of stress intensity factor with crack growth. In stable fracture, the stress intensity factor decreases as the crack propagates and finally a crack is arrested when the SIF falls below the fracture toughness whereas in case of unstable fracture, the stress intensity factor increases with the crack length and crack continue to propagate until final failure occurs.

The simulation of quasi-static crack growth consists of evaluating equivalent stress intensity factor, and if it exceeds the fracture toughness of the material then the crack is extended by some finite length Δa in a particular direction found out by a suitable crack growth criterion. The step size Δa is a user defined parameter, and should be chosen

small enough to get an accurate crack growth path. The stress intensity factors are recalculated for the new crack geometry, and the crack is again extended in a new direction. This phenomenon continues until either the crack gets arrested or final failure takes place.

8.3.1 Crack Growth Direction

The propagation of crack requires a suitable criterion for a crack growth. The commonly used criteria are: the maximum principle stress criterion, the maximum energy release rate criterion, and the minimum strain energy density criterion. In the present work, the maximum principle stress criterion (Erdogan and Sih, 1963) is used which states that a crack will grow in a direction normal to the maximum stress $(\sigma_{\theta\theta})$. For a general mixed-mode state of stress, the stresses at the crack tip are given by (Wang, 1996).

$$\begin{Bmatrix} \sigma_{\theta\theta} \\ \sigma_{r\theta} \end{Bmatrix} = \frac{1}{\sqrt{2\pi r}} \cos\left(\frac{\theta}{2}\right) \begin{Bmatrix} K_I \cos^2\frac{\theta}{2} - \frac{3}{2} K_{II} \sin\theta \\ \frac{1}{2} K_I \sin\theta + \frac{1}{2} K_{II} (3\cos\theta - 1) \end{Bmatrix} \tag{8.5}$$

The direction of maximum hoop stress is the orientation for which the shear stress vanishes (Erdogan and Sih, 1963), i.e.

$$\sigma_{r\theta} = \frac{1}{\sqrt{2\pi r}} \cos\left(\frac{\theta}{2}\right)\left[\frac{1}{2} K_I \sin\theta + \frac{1}{2} K_{II} (3\cos\theta - 1)\right] = 0 \tag{8.6}$$

The solution of Eq. (8.6) leads to the condition

$$K_I \sin\theta_m + K_{II} (3\cos\theta_m - 1) = 0 \tag{8.7}$$

which can be solved to get the crack propagation angle (θ_m)

$$\theta_m = 2\tan^{-1}\frac{1}{4}\left[\frac{K_I}{K_{II}} \pm \sqrt{\left(\frac{K_I}{K_{II}}\right)^2 + 8}\right] \tag{8.8}$$

For this value of θ_m, $\sigma_{\theta\theta}$ is a principle stress field thus, $\sigma_{\theta\theta}$ may be written in terms of equivalent mode-I stress intensity factor (K_{Ieq}) which provides a single measure of the mixed-mode stress field.

$$\sigma_{\theta\theta} = \frac{1}{\sqrt{2\pi r}}\cos\left(\frac{\theta}{2}\right)\left[K_I\cos^2\left(\frac{\theta}{2}\right) - \frac{3}{2}K_{II}\sin\theta\right] = \frac{K_{Ieq}}{\sqrt{2\pi r}} \tag{8.9}$$

where,

$$K_{Ieq} = K_I\cos^3\left(\frac{\theta_m}{2}\right) - 3K_{II}\cos^2\left(\frac{\theta_m}{2}\right)\sin\left(\frac{\theta_m}{2}\right) \tag{8.10}$$

8.4 RESULTS AND DISCUSSIONS

8.4.1 Kinked Crack Modeling

In order to justify the modeling capability and effectiveness of the proposed criterion, few kinked crack problems are simulated. Figure 8.4 shows the dimensions of the cracked body having H = 200 mm, W = 100 mm. The bottom edge has been constrained along y-direction, and an external far field stress is applied at the top edge. A regular nodal distribution of 648 nodes has been considered in all simulations. Six point Gauss quadrature has been used for the numerical integration of the Galerkin weak form. A plane stress condition has been assumed. The material properties for this study are taken as: modulus of elasticity (E) = 200 GPa, Poisson's ratio (ν) = 0.3. A far field stress, (σ_o) = 100 MPa is applied at the top edge. Three different crack configurations having two, three and four kinked segments have been modeled as shown in Fig. 8.4a, b, c respectively. In order to have a clear visualization of near tip stress fields, stress contours

have been generated for different crack configurations as shown in Figs. 8.5-8.8. The modeling capability of proposed criterion has been verified for different crack configurations with different spatial and angular orientation.

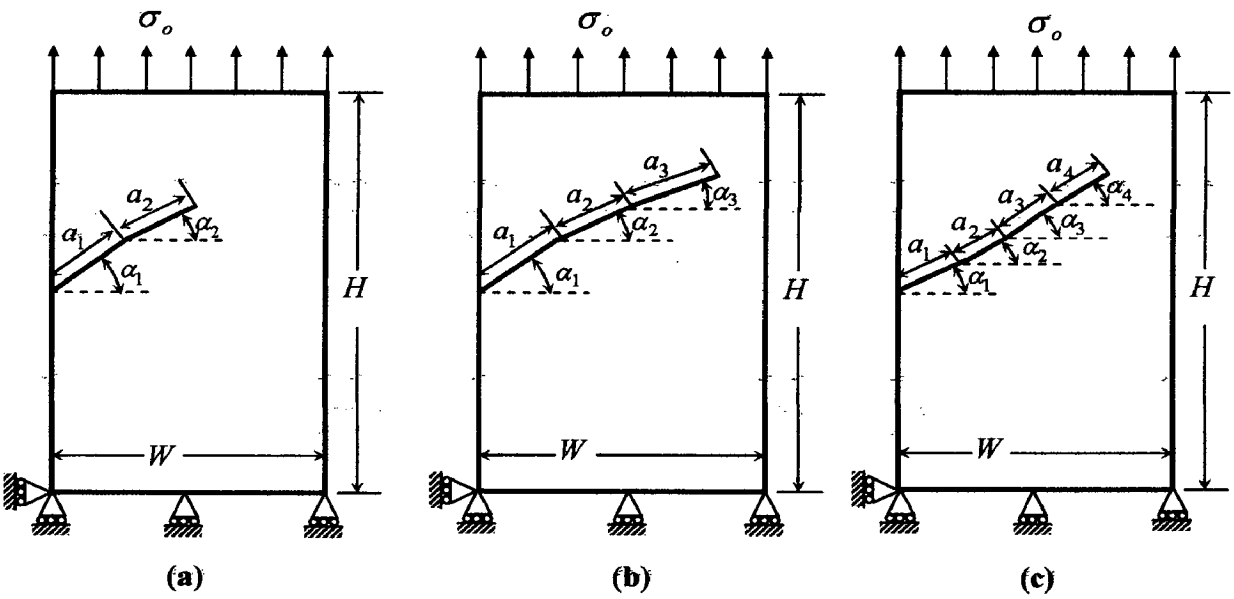

Fig. 8.4: Kinked crack geometry along with boundary conditions

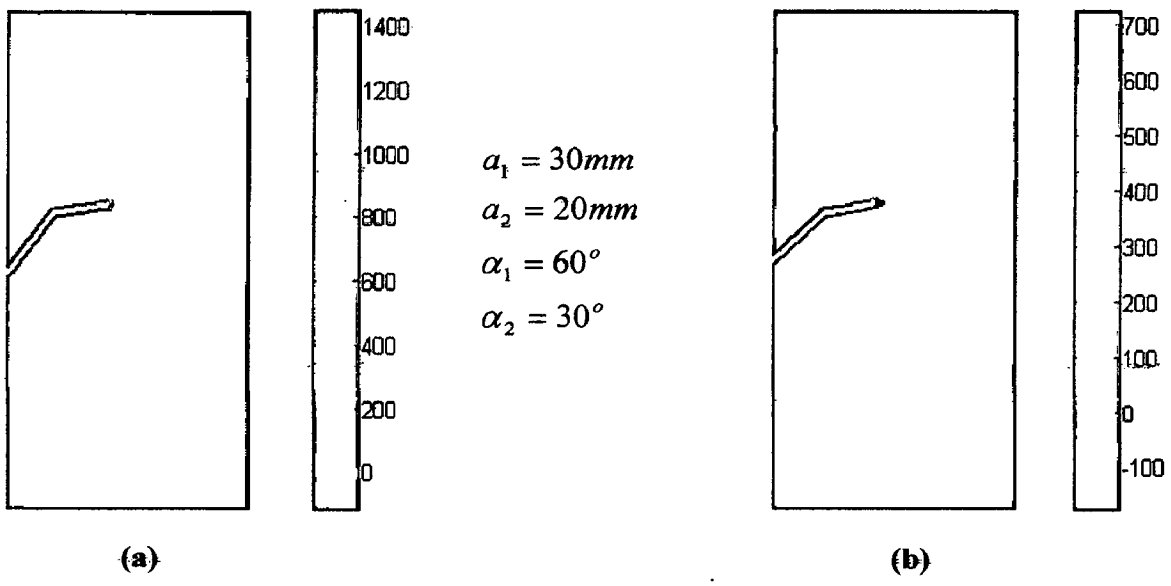

Fig. 8.5: Stress contours for kinked cracks: **(a)** σ_{yy}; **(b)** σ_{xx}

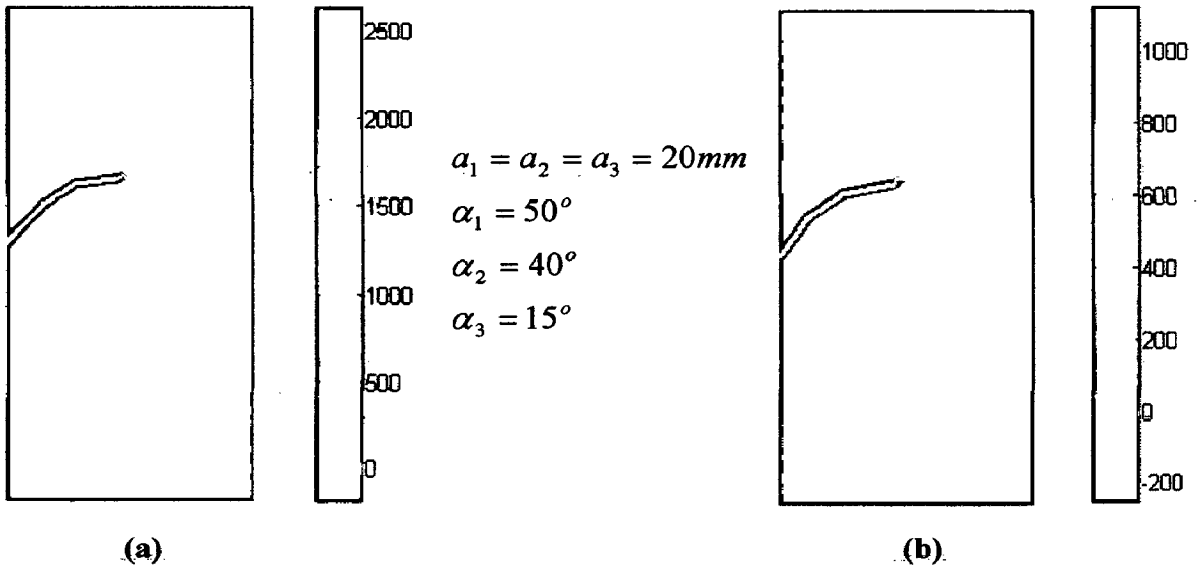

Fig. 8.6: Stress contours for kinked cracks: **(a)** σ_{yy}; **(b)** σ_{xx}

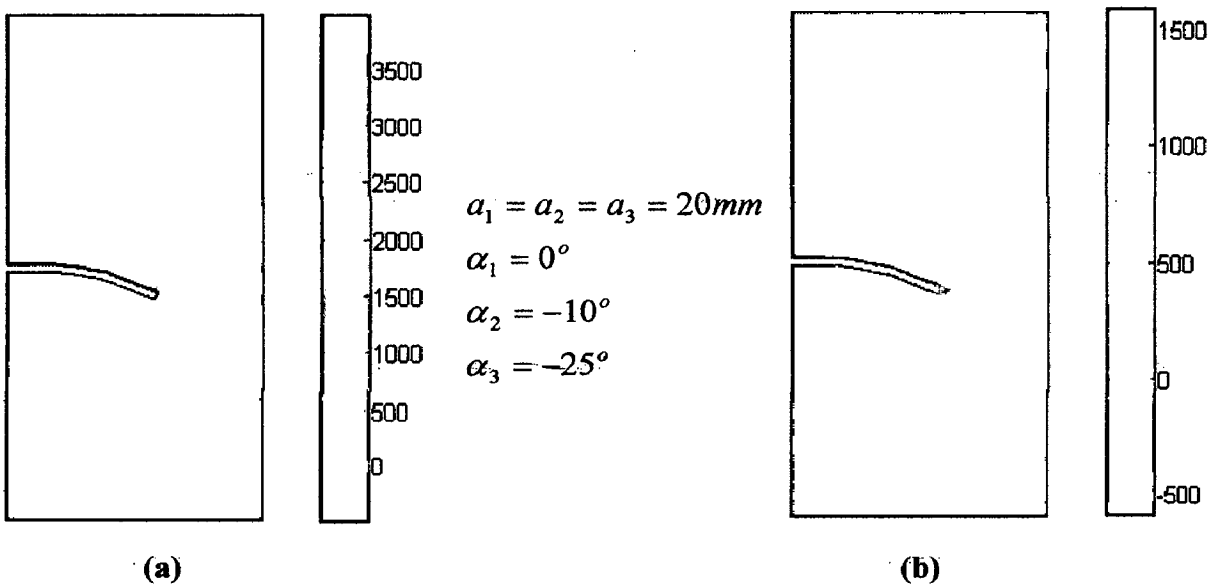

Fig. 8.7: Stress contours for kinked cracks: **(a)** σ_{yy}; **(b)** σ_{xx}

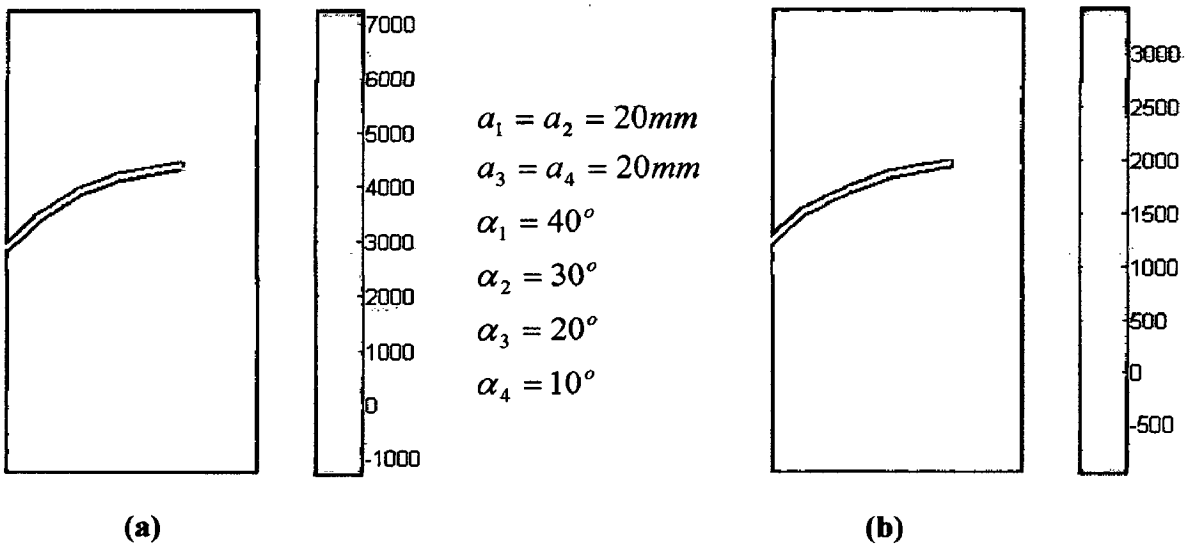

Fig. 8.8: Stress contours for kinked cracks: **(a)** σ_{yy}; **(b)** σ_{xx}

The stress contours generated for different kinked crack configurations reveal the effective modeling capability of the proposed criterion. In the next section the proposed criterion is used for modeling quasi-static crack propagation in two dimensional domains subjected to mixed-mode loading conditions.

8.4.2 Quasi-Static Crack Growth

In this sub-section, five different model problems of quasi-static crack growth have been simulated by the proposed criterion for modeling the kinked cracks. All problems are subjected to mixed-mode loading either due to crack orientation or applied loading. Although, small crack segments predict a crack path more accurately than larger ones but we have taken crack segment of 10 mm for quasi-static crack growth with initial crack length of 20 mm. The crack propagation angle θ_m and equivalent mode-I stress intensity factor K_{Ieq} are calculated using Eq. (8.8) and Eq. (8.10) respectively.

Figure 8.9a shows the geometrical configuration of a plate with an inclined crack subjected to tensile stress of 100 MPa at the top edge. The crack located on the left edge

has an initial inclination of 40° with the horizontal. The crack propagation path obtained for this case is shown in Fig. 8.9a, and the variation of equivalent mode-I stress intensity factor (K_{Ieq}) with crack length is plotted in Fig. 8.9b. From the crack growth path shown in Fig. 8.9a, it is observed that although initially the crack is under mixed mode loading but it propagates in such a way that it attains a mode-I loading condition. Another problem with same loading and boundary condition is shown in Fig. 8.10a. The geometry of this model problem is similar to that of Fig. 8.9a except an additional crack is introduced on the right edge. The crack path looks quite similar to previous model except some minor change in the crack growth direction due to the presence of the right edge crack. A similar trend in the values of equivalent mode-I SIF is observed in Fig. 8.10b. From the results presented in Fig. 8.9b and 8.10b, it is seen that the value of equivalent stress intensity factor keeps on increasing with the increase in crack length.

Figure 8.11a shows the geometrical configuration of a plate having zero degree crack inclination with the horizontal. The plate is subjected to mixed mode loading as shown in Fig. 8.11a with a tensile stress (σ_o) of 50 MPa and shear stress (τ_o) of 25 MPa at the top edge. Figure 8.11a shows that as crack grows, it deviates from its initial path, and tries to come under mode-I loading. The variation of equivalent mode-I intensity factor with crack length is plotted in Fig. 8.11b. Another model problem with same loading and boundary condition is shown in Fig. 8.12a. The only difference is that a right edge crack is introduced. The crack path nearly remains same except minor change in crack growth direction due to the presence of right edge crack. The trend of equivalent mode-I SIF as shown in Fig. 8.12b is found to be almost similar to that of Fig. 8.11b. However, a significant difference in the values of equivalent SIF is noticed. From the results

presented in Fig. 8.11b and 8.12b, it is seen that the values of equivalent stress intensity factor keeps on increasing with the increase in crack length.

Finally, the crack growth of an edge crack in the presence of a hole is investigated. The geometry of the plate along with loading and boundary conditions is shown in Fig. 8.13a. The crack is located on the left edge with an inclination of 40° with the horizontal. The crack propagation path for this problem is shown in Fig. 8.13a. From the crack growth path, it can be seen that the crack propagates in such a way that it gets arrested at the hole. From Fig. 8.13b, it is seen that the equivalent mode-I SIF keeps on increasing with the increase in crack length, and a sudden rise in the value of SIF is found near the hole.

On the basis of these simulations, it can be seen that the crack growth problems in a general direction under mixed-mode loading can also be easily simulated by the proposed criterion.

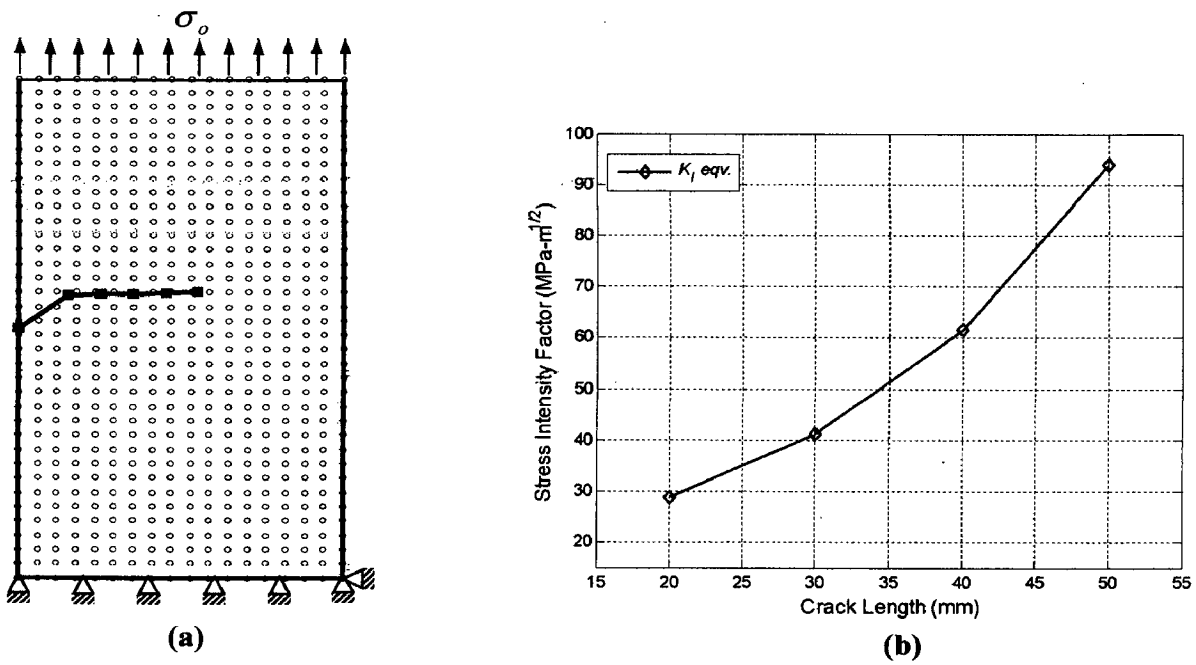

(a) (b)

Fig. 8.9: (a) Crack growth path (b) Equivalent mode-I stress intensity factor *vs.* crack length

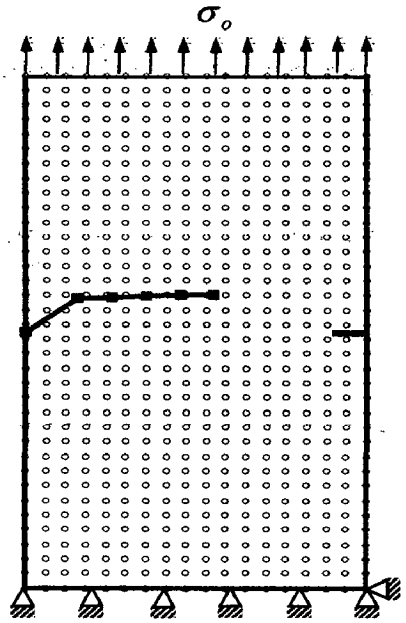

(a)

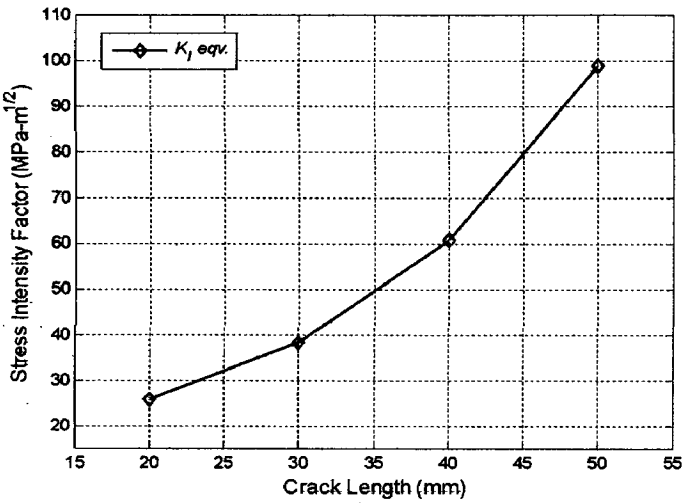

(b)

Fig. 8.10: (a) Crack growth path (b) Equivalent mode-I stress intensity factor *vs.* crack length

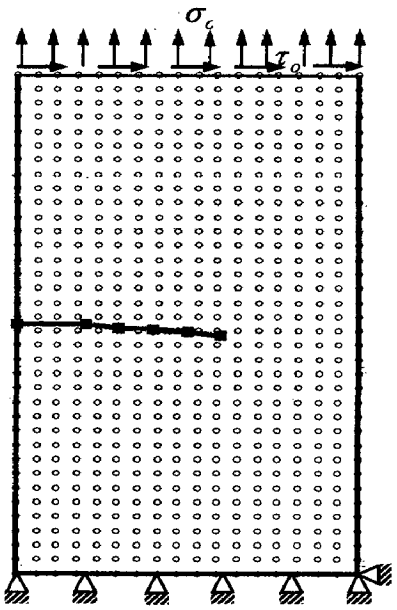

(a)

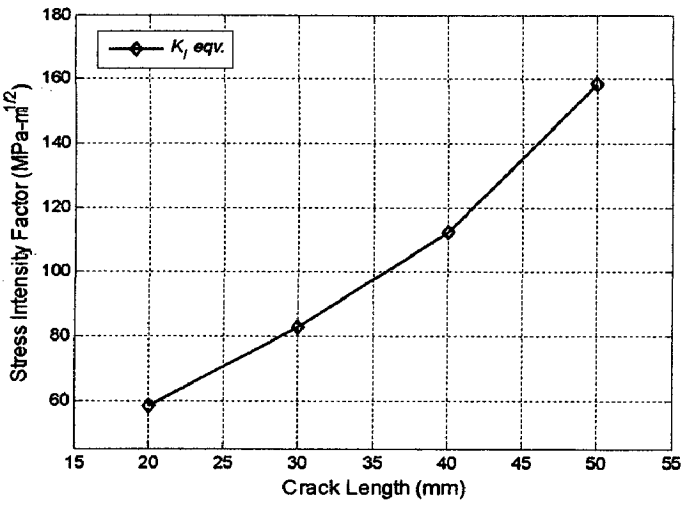

(b)

Fig. 8.11: (a) Crack growth path (b) Equivalent mode-I stress intensity factor *vs.* crack length

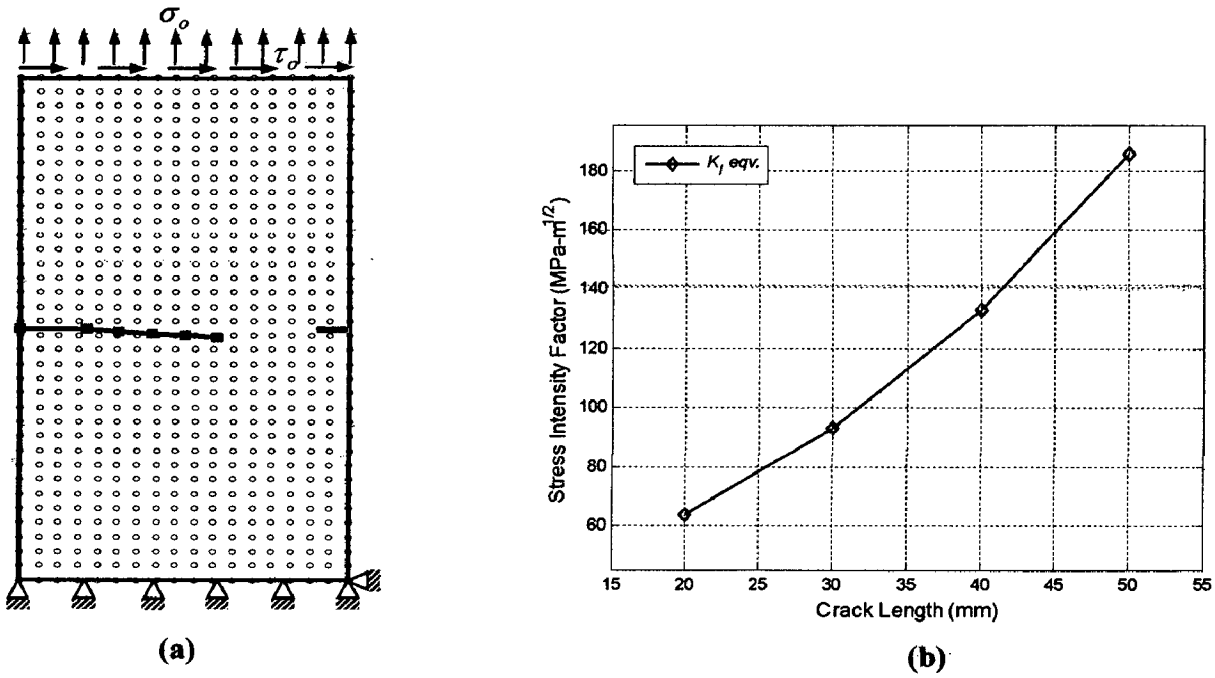

Fig. 8.12: (a) Crack growth path (b) Equivalent mode-I stress intensity factor *vs.* crack length

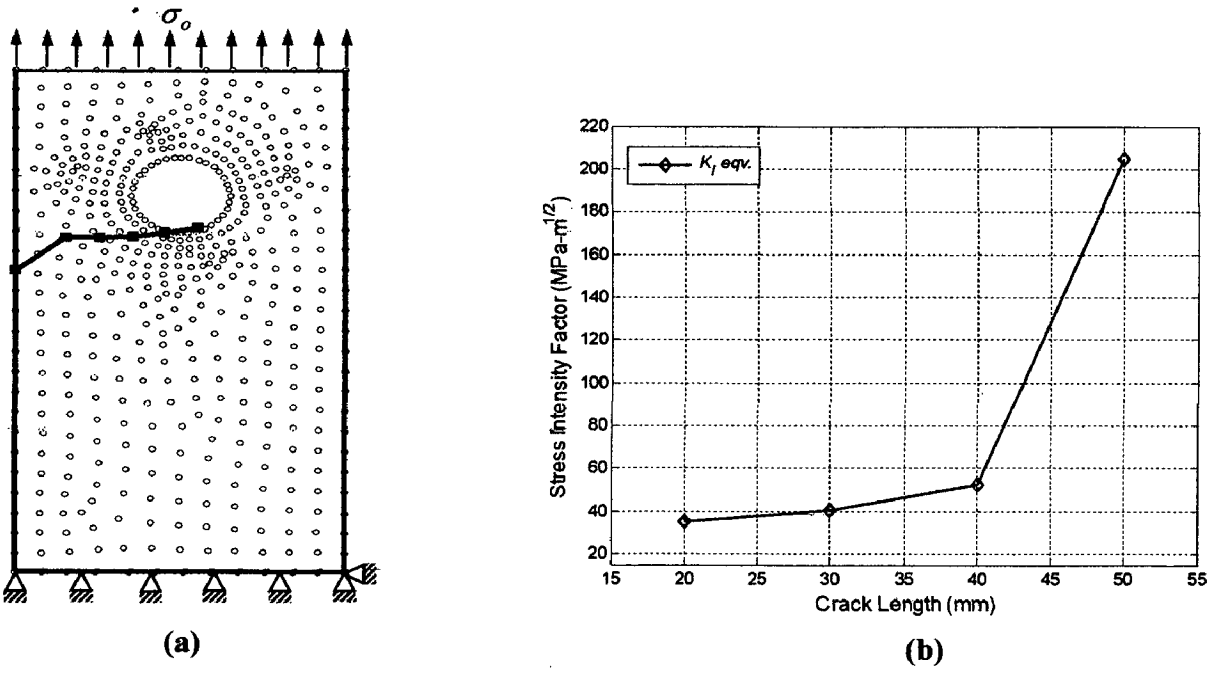

Fig. 8.13: (a) Crack growth path (b) Equivalent mode-I stress intensity factor *vs.* crack length

8.5 CONCLUSION

This Chapter presents the application of EFGM in quasi-static crack growth under mixed-mode loading. Since, the modeling of quasi-static crack growth requires crack tracking at each incremental step hence a new criterion for modeling the kinked cracks has been proposed. The proposed criterion has been used to simulate quasi-static crack growth in two-dimensional domains subjected to mixed-mode loading. The modeling capability of the proposed criterion has been demonstrated by simulating kinked crack problems. The ease of modeling quasi-static crack growth highlights the value of proposed criterion. Moreover, the crack growth simulation also demonstrates the modeling capability of EFGM without any requirement of re-meshing.

Chapter 9

CONCLUSIONS AND FUTURE SCOPE

9.1 CONCLUSIONS

A review of literature indicates that the meshfree methods are interesting complement to the traditional finite element method. The advantages of meshfree methods include the requirement of nodal data for geometry description, smooth shape functions for higher order approximations, various choices for the enrichment such as weight function, basis function and approximation function, and simple integration schemes. These characteristics together proffer the potential of meshfree methods in simplifying adaptive analysis, and crack growth modeling.

In the present work, a widely used meshfree method known as EFGM was employed and extended to study and analyze a variety of fracture mechanics problems under thermal/mechanical loads.

A comparison of various crack modeling techniques unveiled the advantages of intrinsic enrichment criterion. Owing to its accuracy, convergence, implementation issues and ease in modifications, it was further exploited to accomplish the present research work.

Weak discontinuities in EFGM were modeled using various criteria. The analysis shows that the Jump function approach is the best among the available techniques for the modeling of material discontinuities. A new criterion for modeling bi-material interfacial cracks using Jump function has been proposed. The proposed criterion involves only four enrichment functions in the basis instead of the usual twelve. This reduces the computational cost of the method significantly.

For modeling multiple interacting cracks, a new intrinsic enrichment criterion has been proposed and implemented. The proposed criterion performed well for nearly equal size cracks. However, most of the practical situations demand modeling unequal size multiple cracks; hence a new weighted enrichment criterion was further established to accomplish this task.

The existing intrinsic enrichment criterion failed to simulate the cracks lying in non-convex domains so a partial domain enrichment criterion was used to solve such problems. This criterion was found to be quiet effective in simulating the cracks lying in non-convex domains. Moreover, it also reduces the computational cost of EFGM.

The EFGM was extended further for the simulation of two-dimensional thermo-elastic fracture problems in isotropic materials. Both temperature and mechanical fields were enriched intrinsically in order to represent the discontinuous temperature and displacement fields across the crack surface. Some example problems of fracture in functionally graded materials were solved by EFGM under thermal/mechanical loads.

The simulation of elastoplastic fracture mechanics was carried out using EFGM. A new formulation based on incremental plasticity has been proposed and implemented in order to model the non-linear material response. The enriched basis functions were used in order to capture the HRR (Hutchinson-Rice-Rosengren) singularity. The values of *J*-integral were found to be in good agreement with the FEM solution.

Finally, EFGM was employed for the modeling of quasi-static crack growth under mixed-mode loading. A new criterion for modeling of kinked cracks was proposed. The ease of modeling quasi-static crack growth showcases the strength of the proposed criterion. Moreover, crack growth simulation by EFGM demonstrates its capability without a need of remeshing.

Thus the significant contribution of the present research work lies in its exploration of intrinsic enrichment criterion for solving a variety of fracture mechanics problems under thermal/mechanical loading. Development of some new criteria for the problems of multiple interacting cracks, bi-material interfacial cracks, cracks lying in non-convex domains and quasi-static crack growth further enhances the capability of intrinsic enrichment criterion. The suggested modifications are also justified on the basis of reduction in computational time and the associated computational complexities. Moreover, the application of intrinsic enrichment criterion was extended to fracture problems in functionally graded materials, cracks subjected to thermoelastic loading and elastoplastic fracture problems.

To sum up, it is concluded that the present research work establishes EFGM as an accurate, robust and indispensable method for solving a wide variety of fracture mechanics problems under thermal/mechanical loads. Moreover, the proposed modifications add to the proficiency of EFGM.

9.2 FUTURE SCOPE

The present study is generalized in nature and it establishes the capability of EFGM in tackling a wide variety of frcature mechanics problems. The objective of the present work was to employ and extend EFGM as an effective and efficient tool for modeling a variety of fracture mechanics problems. The present work can be extended further in many directions. Some of the recommendations for future work are listed below

- Crack interactions under coupled thermo-mechanical loading may be explored.
- Simulation of bi-metallic interfacial cracks under thermo-elastic loading may be performed.
- Intrinsic enrichment criterion is computationally expensive so a suitable technique may be developed to reduce the computational time.

- ❖ Elasto-plastic analysis may be extended to incorporate temperature dependent material non-linearity.
- ❖ These fracture simulations may be performed by using extrinsic PU based EFGM.
- ❖ EFGM may be further extended to simulate multifield and multiscale problems.
- ❖ EFGM may be extended to simulate crack growth involving large deformations.
- ❖ EFGM may be used to simulate cracks in piezoelectric materials.
- ❖ EFGM may be extended for three-dimensional fracture mechanics problems.

REFERENCES

Adrov, V. (1993): A new damage parameter for fatigue life predictions under local strain analysis, *International Journal of Fatigue*, Vol. 15, pp. 451–453.

Agarwal, B.D., Kumar, P. and Khanna, S.K. (1986): Determination of the fracture toughness of fabric reinforced composites by the *J*-integral approach, *Composites Science and Technology*, Vol. 25, pp. 311–323.

Aluru, N.R. (1998): A reproducing kernel particle method for meshless analysis of micro electromechanical systems, *Computational Mechanics*, Vol. 22, pp. 174–186.

Amit, K.C. and Kim, J.H. (2008): Interaction integrals for thermal fracture of functionally graded materials, *Engineering Fracture Mechanics*, Vol. 75, pp. 2542–2565.

Anderson, T.L. (2005): *Fracture Mechanics: Fundamentals and Applications*, Taylor and Francis, CRC Press.

Andreev, K. and Harmuth, H. (2003): FEM simulation of the thermo-mechanical behaviour and failure of refractories: A case study, *Journal of Materials Processing Technology*, Vol. 143-144, pp. 72–77.

Ang, W.T. and Clements, D.L. (1999): Hypersingular integral equations for a thermo-elastic problem of multiple planar cracks in an anisotropic medium, *Engineering Analysis with Boundary Elements*, Vol. 23, pp. 713–720.

Ang, W.T. and Gumel, A.B. (1996): Multiple interacting planar cracks in an anisotropic multilayered medium under an antiplane shear stress: a hypersingular integral approach, *Engineering Analysis with Boundary Elements,* Vol. 18, pp. 297–303.

Ang, W.T. and Park, Y.S. (1996): Stresses around a periodic array of planar cracks in an anisotropic bi-material, *International Journal of Engineering Science,* Vol. 34, pp. 1457–1466.

Anlas, G., Santare, M.H. and Lambros, J. (2000): Numerical calculation of stress intensity factors in functionally graded materials, *International Journal of Fracture*, Vol. 104, pp. 131–43.

Arfken, G. and Weber, H. (1985): "Gibbs Phenomenon", *Mathematical Methods for Physicists*, 3rd Edition Orlando, FL: Academic Press, pp. 783–787.

Armentani, E. and Citarella, R. (2006): DBEM and FEM analysis on non-linear multiple crack propagation in an aeronautic doubler-skin assembly, *International Journal of Fatigue*, Vol. 28, pp. 598–608.

Ashkenazi, D. (1999): *Determination of critical interface energy release rates for bonded elastic materials*, PhD Thesis, Tel-Aviv University, Israel.

Atkinson, C. and List, R.D. (1978): Steady state crack propagation into media with spatially varying elastic properties, *International Journal of Engineering Science*, Vol. 16, pp. 717–730.

Atluri, S.N. and Zhu, T. (1998): A new meshless local Petrov-Galerkin (MLPG) approach in computational mechanics, *Computational Mechanics*, Vol. 22, pp. 117–127.

Atluri, S.N., Sladek, J., Sladek, V. and T. Zhu (2000): The local boundary integral equation (LBIE) and its meshless implementation for linear elasticity, *Computational Mechanics*, Vol. 25, pp. 180–198.

Atluiri, S.N. and Shen, S. (2002): The meshless local Petrov-Galerkin (MLPG) method: A simple & less costly alternative to the finite element and boundary element methods, *Computer Modeling in Engineering and Sciences*, Vol. 3, pp. 11–51.

Babuska, I. and Melenk, J.M. (1997): The partition of unity method, *International Journal for Numerical Methods in Engineering*, Vol. 40, pp. 727–758.

Barry, W. and Saigal, S. (1999): A three-dimensional element free Gelarkin elastic and elasto-plastic formulation, *International Journal of Numerical Methods in Engineering*, Vol. 46, pp. 671–693.

Batra, R.C., Porfiri, M. and Spinello, D. (2004): Treatment of material discontinuity in two meshless local Petrov–Galerkin (MLPG) formulations of axisymmetric transient heat conduction, *International Journal for Numerical Methods in Engineering*, Vol. 61, pp. 2461–2479.

Beer, P., Johnston, E. and DeWolf, T. (2002): Mechanics of Materials, *Mc Graw-Hill*, International Edition, pp. 747.

Beissel, S. and Rahman, S. (1996): Nodal integration of the element free Galerkin method, *Computer Methods in Applied Mechanics and Engineering*, vol. 139, pp. 49–74.

Belinha, J. and Dinis, L.M.J.S. (2006): Elasto-plastic analysis of plates by the element free Galerkin method, *Engineering Computations*, Vol. 23, pp. 525–551.

Belytschko, T. and Black, T. (1999): Elastic crack growth in finite elements with minimal remeshing, *International Journal for Numerical Methods in Engineering*, Vol. 45, pp. 601–620.

Belytschko, T. and Fleming, M. (1999): Smoothing, enrichment and contact in element free Gelarkin method, *Computers and Structures*, Vol. 71, pp. 173–195.

Belytschko, T. and Gracie, R. (2007): On XFEM applications to dislocations and interfaces, *International Journal of Plasticity*, Vol. 23, pp. 1721–1738.

Belytschko, T., Organ, D. and Gerlach, C. (2000): Element free Gelarkin methods for dynamic fracture in concrete, *Computer Methods in Applied Mechanics and Engineering*, Vol. 187, pp. 385–399.

Belytschko T. and Tabbara M. (1996a): Dynamic fracture using element-free Galerkin methods, *International Journal for Numerical Methods in Engineering*, Vol. 39, pp. 923–938.

Belytschko T., Organ D. and Krongauz Y. (1996a): A coupled finite element-element free Galerkin method, *Computational Mechanics*, Vol. 17, pp. 186–195.

Belytschko, T., Krongauz, Y., Fleming, M., Organ, D. (1996b): Smoothing and accelerated computations in element-free Galerkin method, *Journal of Computational and Applied Mathematics*, Vol. 74, pp. 111–126

Belytschko, T., Krongauz, Y., Organ, D.J., Fleming, M. and Krysl, P. (1996c): Meshless methods: An overview and recent developments, *Computer Methods in Applied Mechanics in Engineering*, Vol. 139, pp. 3–47.

Belytschko T., Lu Y.Y. and Gu, L. (1994): Element-free Galerkin methods, *International Journal for Numerical Methods in Engineering*, Vol. 37, pp. 229–256.

Belytschko, T., Organ D. and Tabbara, M. (1995b): Numerical solutions of mixed mode dynamic fracture in concrete using element-free-Galerkin-methods, *ICES Conference Proceedings*.

Benzley, S.E. (1974): Representation of singularities with isoparametric finite elements, *International Journal for Numerical Methods in Engineering*, Vol. 8, pp. 537–545.

Bonet, J., Kulasegaram, S. (2002): A simplified approach to enhance the performance of smooth particle hydrodynamics methods, *Applied Mathematics & Computation*, Vol. 126, pp. 133–155.

Bouillard, Ph. and Suleau, S. (1998): Element-free Galerkin solutions for Helmholtz problems: formulation and numerical assessment of the pollution effect, *Computer Methods in Applied Mechanics and Engineering*, Vol. 162, pp. 317–335.

Brighenti, R. (2005): Application of the element-free Galerkin meshless method to 3-D fracture mechanics problems, *Engineering Fracture Mechanics*, Vol. 72, pp. 2808–2820.

Brown, E.J. and Erdogan, F. (1968): Thermal stresses in bonded materials containing cuts on the interface, *International Journal of Engineering sciences*, Vol. 6, pp. 517–529.

Budyn, E., Zi, G., Moes, N. and Belytschko, T. (2004): A method for multiple crack growth in brittle materials without re-meshing, *International Journal for Numerical Methods in Engineering,* Vol. 61, pp. 1741-1770.

Cardoso, R.P.R. and Yoon, J.W. (2007): One point quadrature shell elements: A study on convergence and patch tests, *Computational Mechanics*, Vol. 40, pp. 871–883.

Cardoso, R.P.R., Yoon, J.W., and Valente, R.A.F. (2007): Enhanced one point quadrature shell element for nonlinear applications, *International Journal for Numerical Methods in Engineering*, Vol. 69, pp. 627–663.

Chattopadhyay, J., Pavankumar, T.V., Dutta, B.K. and Kushwaha, H.S. (2005): Fracture experiments on throughwall cracked elbows under in-plane bending moment: Test results and theoretical/numerical analyses, *Engineering Fracture Mechanics*, Vol. 72, pp. 1461–1497.

Chell, G. G., and Ewing, D.J.F. (1976): The role of thermal and residual stresses in linear elastic and post yield fracture mechanics, *International Journal of Fracture*, Vol. 13, pp. 467–479.

Chen, J., Wu, L. and Du, S. (2000): Element free Galerkin methods for fracture of functionally graded materials, *Key Engineering Materials*, Vol. 183–187, pp. 487–492.

Chen, Y.P., Lee, J.D. and Eskandarian, A. (2002): Dynamic meshless method applied to non-local crack problems, *Theoretical and Applied Fracture Mechanics*, Vol. 38, pp. 293–300.

Chen, Y.Q. and Kulasegaram, S. (2009): Numerical modeling of fracture of particulate composites using SPH method, *Computational Material Science*, Vol. 47, pp. 60–70.

Chen, J. (2005): Determination of thermal stress intensity factors for an interface crack in a graded orthotropic coating-substrate structure, *International Journal of Fracture*, Vol. 133, pp. 303–328.

Chen, Y.Z. (1984): General case of multiple crack problems in an infinite body, *Engineering Fracture Mechanics*, Vol. 20, pp. 591–597.

Chen, Y. Eskandarian, A., Oskard, M., Lee, J.D. (2004): Meshless analysis of plasticity with application to crack growth problems, *Theoretical and Applied Fracture Mechanics*, Vol. 41, pp. 83–94.

Chen, J.S., Pan, C. and Wu, C.T. (1997): Large deformation analysis of rubber based on a reproducing kernel particle method, *Computational Mechanics*, Vol. 19, pp. 211–227.

Cheung, Y., Wang, Y. and Woo, C. (1992): A general method for multiple crack problems in a finite plate, *Computational Mechanics*, Vol. 10, pp.335–343.

Cho, J.Y. and Atluri, S.N. (2001): Analysis of shear flexible beams using the meshless local Petrov-Galerkin method, based on a locking-free formulation, *Engineering Computations*, Vol. 18, pp. 215–240.

Choubey, A., Sehgal, D.K. and Tandon, N. (2006): Finite element analysis of vessels to study changes in natural frequencies due to cracks, *Pressure Vessels and Piping*, Vol. 83, pp. 181–187.

Chowdhury, S.R. and Narasimhan, R. (2000): A finite element analysis of quasistatic crack growth in a pressure sensitive constrained ductile layer, *Engineering Fracture Mechanics*, Vol. 66, pp. 551–571.

Coda, H.B. (2009): A solid-like FEM for geometrically non-linear 3D frames, *Computer Methods in Applied Mechanics and Engineering,* Vol. 198, pp. 3712–3722.

Combe, U. and Korn, C. (1998): An adaptive approach with the element free Gelarkin method, *Computer Methods in Applied Mechanics and Engineering*, Vol. 162, pp. 203–222

Corvi, A. (1990): A preliminary approach to composite beam design using FEM analysis, *Composite Structures*, Vol. 16, pp. 259–275.

Cordes, L.W. and Moran, B. (1996): Treatment of material discontinuity in the element free Galerkin method, *Computer Methods in Applied Mechanics and Engineering*, Vol. 139, pp. 75–89.

Dag, S. (2006): Thermal fracture analysis of orthotropic functionally graded materials using an equivalent domain integral approach, *Engineering Fracture Mechanics*, Vol. 73, pp. 2802–2828.

Dai, K.Y., Liu, G.R., Han, X. and Lim, K.M. (2005): Thermo-mechanical analysis of functionally graded material (FGM) plates using element-free Galerkin method, *Computers and Structures*, Vol. 83, pp. 1487–1502.

De, S. and Bathe, K.J. (2000): The method of finite spheres, *Computational Mechanics*, Vol. 25, pp. 329–345.

De, S. and Bathe, K.J. (2001a): Towards an efficient meshless computational technique: the method of finite spheres, *Engineering Computations*, Vol. 18, pp. 170–192.

De, S. and Bathe, K.J. (2001b): The method of finite spheres with improved numerical integration, *Computers and Structures*, Vol. 79, pp. 2183–2196.

Delale, F. and Erdogan, F. (1983): The crack problem for a non-homogeneous plane, *Journal of Applied Mechanics*, Vol. 50, pp. 609–614.

Denda, M. and Dong, Y.F. (1997): Complex variable approach to the BEM for multiple crack problems" *Computer Methods in Applied Mechanics and Engineering*, Vol. 141, pp. 247–264.

Deodatis, G. (1989): Stochastic FEM sensitivity analysis for non-linear dynamic problems, *Probabilistic Engineering Mechanics*, Vol. 4, pp. 135–141.

Dhaliwal, R.S. and Singh, B.M. (1978): On the theory of elasticity of a non-homogeneous medium, *International Journal of Elasticity*, Vol. 8, pp. 211–219.

Dias, A.M.P.G., Kuilen, J.W.V.D., Lopes, S. and Cruz, H. (2007): A non-linear 3D FEM model to simulate timber–concrete joints, *Advances in Engineering Software*, Vol. 38, pp. 522–530.

Dolbow, J. and Belytschko, T. (1999): Numerical integration of Galerkin weak form in meshfree methods, *Computational Mechanics*, Vol. 23, pp. 219–230.

Dolbow, J. and Belytschko, T. (1998): An introduction to programming the meshless element free Galerkin method, *Archives in Computational Mechanics*, Vol. 5, pp. 207–241.

Duflot, M. (2006): A meshless method with enriched weight functions for three-dimensional crack propagation, *International Journal of Numerical Methods in Engineering*, Vol. 65, pp. 1970–2006.

Duflot, M. (2008): The extended finite element method in thermo-elastic fracture mechanics, *International Journal for Numerical Methods in Engineering*, Vol. 74, pp. 827–847.

Duflot, M. and Dang, H. (2002): A truly meshless Galerkin method based on a moving least squares quadrature, *Communications In Numerical Methods In Engineering*, Vol. 18, pp. 441–449.

Duflot, M. and Dang, H. (2004): A meshless method with enriched weight functions for fatigue crack growth, *International Journal of Numerical Methods in Engineering*, Vol. 59, pp. 1945–1961.

Durate, C.A. and Oden, J.T. (1996): An H-p adaptive method using clouds, *Computer Methods in Applied Mechanics and Engineering*, Vol. 139, pp. 237–262.

Emery, A.F., Neighbors, P.K., Kobayashi, A.S. and Love, W.J. (1977): Stress intensity factors in edge cracked plates subjected to transient thermal singularities, *Journal of Pressure Vessel Technology*, Vol. 99, pp. 100–105.

Erdogan, F. and Sih, G.C. (1963): On the crack extension in plates under plane loading and transverse shear, *Journal of Basic Engineering*, Vol. 85, pp. 519–527.

Erdogan, F. and Wu, B.H. (1997): The surface crack problem for a plate with functionally graded properties, *Journal of Applied Mechanics*, Vol. 64, pp. 449–456.

Fleming, M, Chu, Y.A., Moran, B. and Belytschko, T. (1997): Enriched element free Galerkin methods for crack tip fields, *International Journal of Numerical Methods in Engineering*, Vol. 40, pp. 1483–1504.

Fleming, M. (1997): *The element-free Galerkin method for fatigue and quasi-static fracture*, Ph.D. Thesis, Northwestern University, IL, USA.

Gavete, L., Falcon, S., Bellido J.C. (2000): Dirichlet boundary conditions in element free Galerkin methods, *European Congress on Computational Methods in Applied Sciences and Engineering*.

Gavete, L., Falcon, S., Ruiz, A. (2001): An error indicator for the element free Galerkin method, *European Journal of Mechanics and Solid*, Vol. 20, pp. 327–341.

Gdoutos, E.E. (2005): *Fracture Mechanics: An Introduction*, Springer.

Gibson R.E. (1967): Some results concerning displacements and stresses in a non homogeneous elastic half space, *Geotechnique*, Vol. 17, pp. 58–67.

Gingold, R.A. and Monaghan, J.J. (1982): Kernel estimates as a basis for general particle methods in hydrodynamics, *Journal of Computational Physics*, Vol. 46, pp. 429–453.

Giudice, S.D., Comini, G. and Mikhailov, M.D. (1978): Finite element analysis of combined free and forced convection, *International Journal of Heat Mass Transfer*, Vol. 21, pp. 1619–1621.

Goo, B.C., Lim, C.H. and Kwon, S.J. (2006): Finite element analysis of an induced current potential drop method for the defect detection of railway axles, *Key Engineering Materials*, Vol. 321-323, pp. 20–23.

Goo, B.C. and Seo, J.W. (2008a): Finite element analysis of the rolling contact fatigue life of rail-car wheels, *Materials Science Forum*, Vol. 575-578, pp. 1461–1466.

Goo, B.C. and Yang, S.Y. (2008b): Finite element analysis of the effect of residual stress on mechanical behavior of welded plates, *Materials Science Forum*, Vol. 580–582, pp. 605–608.

Gope P.C. (1999): Determination of sample size for estimation of fatigue life by using Weibull and log normal distribution, *International Journal of Fatigue*, Vol. 21, pp. 745–752.

Gu, P. and Asaro, R.J. (1997): Cracks in functionally graded materials, *International Journal of Solids Structures*, Vol. 34, pp. 1–17.

Gu, P., Dao, M. and Asaro, R.J. (1999): A simplified method for calculating the crack tip field of functionally graded materials using the domain integral, *Journal Applied Mechanics*, Vol. 66, pp. 101–108.

Gu, Y.T. and Zhang, L.C. (2008): Coupling of the meshfree and finite element methods for determination of the crack tip fields, *Engineering Fracture Mechanics*, Vol. 75, pp. 986–1004.

Gu, Y.T. and Liu, G.R. (2001): A local point interpolation method for static and dynamic analysis of thin beams, *Computer Methods in Applied Mechanics in Engineering*, Vol. 190, pp. 5515–5528.

Guagliano, M., Sangirardi, M., and Vergani, L. (2006): Photoelastic methods to determine K_{I}, K_{II} and K_{III} of internal cracks subjected to mixed mode loading, *International Journal of Fatigue*, Vol. 28, pp. 576–582.

Hagihara, S., Tsunori, M., Ikeda, T., Miyazaki, N. (2003): Element-free Galerkin method using directed graph and its application to creep problems, *Computational Mechanics*, Vol. 31, pp. 489–495.

Hazama, O., Okuda, H., Wakatsuchi, K. (2001): A digital systematization of meshfree method and its application to elasto-plastic infinitesimal deformation analysis, *Advances in Engineering Software*, Vol. 32, pp. 647–664.

Hegen, D. (1997): *An element free Galerkin method for crack propagation in brittle materials*, Ph. D. Thesis, Eindhoven University of Technology.

Hellen, T.K., Cesari, F. and Maitan, A. (1982): The application of fracture mechanics in thermally stressed structures, *International Journal of Pressure Vessels and Piping*, Vol. 10, pp. 181-204.

Hori, H. and Nemat-Nasser, S. (1983): Estimate of stress intensity factors for interacting cracks, *Advances in Aerospace Structures, Materials and Dynamics, ASME*, pp. 111-117.

Hsu, T.R. (1986): *The finite element method in thermomechanics*, Allen and Unwin Inc., London, U.K.

Huang, Z.M. (2007): Failure analysis of laminated structures by FEM based on nonlinear constitutive relationship, *Composite Structures*, Vol. 77, pp. 270–279.

Hutchinson, J.W. (1968) :Singular behavior at the end of a tensile crack in a hardening material, *Journal of the Mechanics and Physics of Solids*, Vol. 16, pp. 13–31.

Ikeda, T. and Sun, C.T. (2001): Stress intensity factor analysis for an interface crack between dissimilar isotropic materials under thermal stress, *International Journal of Fracture*, Vol. 111, pp. 229–249.

Jin, Z.H. and Noda, N. (1993): An internal crack parallel to the boundary of a non-homogeneous half plane under thermal loading, *International Journal of Engineering Science*, Vol. 31, pp. 793–806.

Jun, S., Liu, W.K. and Belytschko, T. (1998): Explicit reproducing kernel particle methods for large deformation problems, *International Journal for Numerical Methods in Engineering*, Vol. 41, pp. 137–166.

Kachanov, M. (1985): A simple technique of stress analysis in elastic solids with many cracks, *International Journal of Fracture*, Vol. 28, pp. R11–R19.

Kachanov, M. and Laures, J.P. (1989): Three- dimensional problem of strongly interaction arbitrarily located penny shaped cracks, *International Journal of Solids Structures*, Vol. 23, pp. 11–21.

Kant, T., Arora, C.P., Varaiya, J.H. (1992): Finite element transient analysis of composite and sandwich plates based on a refined theory and a mode superposition method, *Composite Structures*, Vol. 22, pp. 109–120.

Kant, T., Menon, M.P. (1993): A finite element-difference computational model for stress analysis of layered composite cylindrical shells, *Finite Elements in Analysis and Design*, Vol. 14, pp 55–71.

Kant, T., Pendhari, S.S., Desai, Y.M.. (2007): A new partial finite element model for statics of sandwich plates, *Journal of Sandwich Structures and Materials*, Vol. 9, pp 487–520.

Kargarnovin, M.H., Toussi, H.E., Fariborz, S.J. (2004): Elasto-plastic element-free Galerkin method, *Computational Mechanics*, Vol. 33, pp. 206–214.

Khandelwal, R. and Chandra Kishen J.M. (2007): The use of conservative integral in bi-material interface crack problems subjected to thermal loads, *International Journal of Solids and Structures*, Vol. 45, pp. 2976–2992.

Khanna, S.K. and Shukla, A. (1995): On the use of strain gages in dynamic fracture mechanics, *Engineering Fracture Mechanics*, Vol. 51, pp. 933–948.

Khanna, S.K. and Shukla, A. (1993): Energy absorption mechanisms during dynamic fracturing of fiber-reinforced composites, *Journal of Materials Science*, Vol. 28, pp. 3722–3730.

Kikuchi, F. and Liu, X. (2007): Estimation of interpolation error constants for the P_0 and P_1 triangular finite elements, *Computer Methods in Applied Mechanics and Engineering*, Vol. 196, pp. 3750–3758.

Kim, J.H. and Paulino, G.H. (2002): Finite element evaluation of mixed mode stress intensity factors in functionally graded materials, *International Journal for Numerical Methods in Engineering*, Vol. 53, pp. 1903–1935.

Krongauz, Y. and Belytschko, T. (1996): Enforcement of essential boundary conditions in meshless approximations using finite elements, *Computer Methods in Applied Mechanics and Engineering*, Vol. 131, pp. 133–145.

Krongauz, Y. (1996): *Applications of meshless methods to solid mechanics*, Ph.D. Thesis, Northwestern University, IL, USA.

Krongauz, Y. and Belytschko, T. (1998): EFG approximation with discontinuous derivatives, *International Journal for Numerical Methods in Engineering*, Vol. 41, pp. 1215–1233.

Krysl, P. and Belytschko (1999): The element free Gelarkin method for dynamic propagation of arbitrary 3-D cracks, *International Journal of Numerical Methods in Engineering*, Vol. 44, pp. 767–800.

Kulasegaram, S., Bonet, J., Lewis R.W. and Profit, M. (2004): A variational formulation based contact algorithm for SPH applications, *Computational Mechanics*, Vol. 33, pp. 316–325.

Lam, H.F. and Ng, C.T. (2008): A probabilistic method for the detection of obstructed cracks of beam-type structures using spatial wavelet transform, *Probabilistic Engineering Mechanics*, Vol. 23, pp. 237–245.

Lam, K.Y., Cao, W., and Zhuang, T. (1993): Interaction between micro-cracks and main crack in a semi-infinite medium, *Engineering Fracture Mechanics*, Vol. 44, pp. 753–761.

Lam, K.Y., Tay, T.E., and Yuan, W.G. (1992): Stress intensity factors of cracks in finite plates subjected to thermal loads, *Engineering Fracture Mechanics*, Vol. 43, pp. 641–650.

Lancaster, P. and Salkauskas, K. (1981): Surfaces generated by moving least squares methods, *Mathematics of Computation*, Vol. 37, pp. 141–158.

Lee, G.H., Chung, H.J. and Choi, C.K. (2003): Adaptive crack propagation analysis with the element-free Galerkin method, *International Journal of Numerical Methods in Engineering*, Vol. 56, pp. 331–350.

Li, S. and Simonsen, C.B. (2007): Meshfree simulations of ductile crack propagations, *International Journal for Computational Methods in Engineering Science and Mechanics*, Vol. 6, pp. 1–19.

Lee, S.H. and Yoon, Y.C. (2003): An improved crack analysis technique by element-free Galerkin method with auxiliary supports, *International Journal of Numerical Methods in Engineering*, Vol. 56, pp. 1291–1314.

Lee, S.H. and Yoon, Y.C. (2004): Numerical prediction of crack propagation by an enhanced element-free Galerkin method, *Nuclear Engineering and Design*, Vol. 227, pp. 257–271.

Liu, G.R. (2003): *Mesh Free Methods-Moving Beyond the Finite Element Method*, CRC Press, USA.

Liu, G.R. and Gu, Y.T. (2001a): A point interpolation method for two-dimensional solids, *International Journal for Numerical Methods in Engineering*, Vol. 50, pp. 937–951.

Liu, G.R. and Gu, Y.T. (2001b): A local radial point interpolation method (LRPIM) for free vibration analysis of 2-D solids, *Journal of Sound and Vibration*, Vol. 246, pp. 29–46.

Liu, T., Liu, G. and Wang, Q. (2006): An element-free Galerkin-finite element coupling method for elasto-plastic contact problems, *ASME Journal of Tribology*, Vol. 128, pp 1-9.

Liu, W.K., Jun, S. and Zhang, Y.F. (1995a): Reproducing kernel particle methods, *International Journal for Numerical Methods in Engineering*, Vol. 20, pp. 1081–1106.

Liu, W.K., Jun, S., Li, S., Adee, J. and Belytschko, T. (1995b): Reproducing kernel particle methods for structural dynamics, *International Journal for Numerical Methods in Engineering*, Vol. 38, pp. 1655–1679.

Liu, W.K., Chen, Y., Jun, S., Chen, J.S., Belytschko, T., Pan, C., Uras, R.A. and Chang, C.T. (1996): Overview and applications of the reproducing kernel particle methods, *Archives of Computational Methods in Engineering*, Vol. 3, pp. 3–80.

Liu, X.Y., Xiao, Q.Z. and Karihaloo, B.L. (2004): XFEM for direct evaluation of mixed mode SIFs in homogeneous and bi-materials, *International Journal for Numerical Methods in Engineering*, Vol. 59, pp. 1103–1118.

Liu, Y. and Mahadevan, S. (2005): Multiaxial high-cycle fatigue criterion and life prediction for metals, *International Journal of Fatigue*, Vol. 27, pp. 790–800.

Loehnert, S. and Belytschko, T. (2007): Crack shielding and amplification due to multiple micro-cracks interacting with a macro-crack, *International Journal of Fracture*, Vol. 145, pp.1–8.

Long, S. and Zhang, Q. (2002): Analysis of thin plates by the local boundary integral equation (LBIE) method, *Engineering Analysis with Boundary Elements*, Vol. 26, pp. 707–718.

Lu, Y.Y., Belytschko, T. and Gu, L. (1994): A new implementation of the element element-free Galerkin method, *Computer Methods in Applied Mechanics and Engineering*, Vol. 113, pp. 397–414.

Lu, Y.Y., Belytschko, T. and Tabbara, M. (1995): Element-free Galerkin method for wave propagation and dynamic fracture, *Computer Methods in Applied Mechanics and Engineering*, Vol. 113, pp. 131–153.

Lucy, L.B. (1977): A numerical approach to the testing of the fission hypothesis, *The Astronomical Journal*, Vol. 82, pp. 1013–1024.

MacKinnon, R.J. and Carey, G.F. (1987): Treatment of material discontinuities in finite element Computations, *International Journal for Numerical Methods in Engineering*, Vol. 24, pp. 393–417.

Maiti, S.K. and Patil, D.P. (2003): Detection of multiple cracks using frequency measurements, *Engineering Fracture Mechanics*, Vol. 70, pp. 1553–1572.

Marechal, Y., Coulomb, J.L. and Meunier, G. (1993): Use of the diffuse element method for electromagnetic field computations, *IEEE Transactions on Magnetics*, Vol. 29, pp. 1475–1478.

Marur, P.R. and Tippur, H.V. (2000): Numerical analysis of crack tip fields in functionally graded materials with a crack normal to the elastic gradient, *International Journal of Solids Structures*, Vol. 37, pp. 5353–5370.

Matos, P.P.L., Mc Meeking, R.M., Charalambides, P.G. and Drory, M.D. (1989): A method for calculating stress intensities in bimetal fracture, *International Journal of Fracture*, Vol. 40, pp. 235–254.

Matsumoto, T., Tanaka, M. and Obara, R. (2000): Computation of stress intensity factors of interface cracks based on interaction energy release rates and BEM sensitivity analysis, *Engineering Fracture Mechanics*, Vol. 65, pp. 683–702.

Melenk, J.M. and Babuska, I. (1996): The partition of unity finite element method: Basic theory and applications, *Computer Methods in Applied Mechanics and Engineering*, Vol. 139, pp. 289–314.

Meric, R.A. (2001): Gradient weighted residuals for error indicators in FEM and BEM, *Engineering Analysis with Boundary Elements*, Vol. 25, pp. 593–606.

Miyakazi, N., Ikeda, T., Soda, T. and Munakata, T. (1993): Stress intensity factor analysis of interface crack using boundary element method (application of virtual crack extension method), *JSME International Journal: Series A*, Vol. 36, pp. 36–42.

Miyakazi, N., Ikeda, T., Soda, T. and Munakata, T. (1993): Stress intensity factor analysis of interface crack using boundary element method (application of contour integral method), Engineering *Fracture Mechanics*, Vol. 45, pp. 599–610.

Moes N., Dolbow J. and Belytschko T. (1999): A finite element method for crack growth without remeshing, *International Journal for Numerical Methods in Engineering*, Vol. 46, pp. 131–150.

Monaghan, J.J. (1988): An introduction to SPH, *Computer Physics Communications*, Vol. 48, pp. 89–96.

Monaghan, J.J. (1992): Smoothed particle hydrodynamics, *Annual Review of Astronomy and Astrophysics*, Vol. 30, pp. 543–574.

Moran, B. and Shih, C.F. (1987): Crack tip and associated domain integrals from momentum and energy balance, *Engineering Fracture Mechanics*, Vol. 27, pp. 615-641.

Mukherjee, Y.X. and Mukherjee, S. (1997): The boundary node method for potential problems, *International Journal for Numerical Methods in Engineering*, Vol. 40, pp. 797–815.

Muravin, B. (2003): *The application of element-free Galerkin method in the investigation of crack interaction*, Ph.D. Thesis, Tel-Aviv University, Israel.

Muravin, B. and Turkel, A. (2006a): Multiple crack weight for solution of multiple interacting cracks by meshless numerical methods, *International Journal of Numerical Methods in Engineering*, Vol. 67, pp. 1146–1159.

Muravin, B. and Turkel, A. (2006b): Spiral weight for modeling cracks in meshless numerical methods, *Computational Mechanics*, Vol. 38, pp. 101–111.

Nagashima, T., Omoto, Y. and Tani, S. (2003): Stress intensity factor analysis of interface cracks using XFEM, *International Journal for Numerical Methods in Engineering*, Vol. 56, pp. 1151–1173.

Nahta, R. and Moran, B. (1993): Domain integrals for axisymmetric interface crack problems, *International Journal of Solids and Structures*, Vol. 30, pp. 2027–2040.

Nayroles, B., Touzot, G. and Villon, P. (1992): Generalizing the finite element method: diffuse approximation and diffuse elements, *Computational Mechanics*, Vol. 10, pp. 307–318.

Nguyen, P., Rabczuk, T., Bordas, S. and Duflot, M. (2008): Meshless methods: A review and computer implementation aspects, *Mathematics and Computers in Simulation*, Vol. 79, pp. 763–813.

Nurse, A.D. and Patterson, E.A. (1990): A photoelastic technique to predict the direction of edge crack extension using blunt cracks, *International Journal of Mechanical Sciences*, Vol. 32, pp. 253–264.

Onate, E., Perazzo, F. and Miquel, J. (2001): A finite point method for elasticity problems, *Computers and Structures*, Vol. 79, pp. 2151–2163.

Organ D.J. (1996): *Numerical solutions to dynamic fracture problems using the element-free Galerkin method*, Ph.D. Thesis, Northwestern University, IL, USA.

Organ D.J., Fleming, M. and Belytschko, T. (1996): Continuous meshless approximation for non-convex bodies by diffraction and transparency, *Computational Mechanics*, Vol. 18, pp. 225–235.

Ottosen, N. S. and Petersson, H. (1992): Introduction to finite element methods, *Prentice Hall*, London, U.K.

Pan, J. and Shih, C.F. (1992): Elastic plastic analysis of combined mode-I , II and III crack-tip fields under small scale yielding conditions, *International journal of solids and structures*, Vol. 29, pp. 2795–2814.

Pannachet, T. and Askes, H. (2000): Some observations on the enforcement of constraint equations in the EFG method, *Communications in Numerical Methods in Engineering*, Vol. 16, pp. 819–830.

Partheepan, G., Sehgal, D.K. and Pandey, R.K. (2008): Fracture toughness evaluation using miniature specimen test and neural network , *Computational Materials Science*, Vol. 44, pp. 523–530.

Paulino, G. H. and Kim, J. H. (2004): On the Poisson's ratio effect on mixed-mode stress intensity factors and T-stress in functionally graded materials, *International Journal of Computational Engineering Science*, Vol. 5, pp. 833–861.

Ponthot, J.P. and Belytschko, T. (1998): Arbitrary Lagrangian-Eulerian formulation for element free Gelarkin method, *Computer Methods in Applied Mechanics and Engineering*, Vol. 152, pp. 19–46.

Prasad, N.N.V. and Aliabadi, M.H. (1994): Incremental crack growth in thermo-elastic problems, *International Journal of Fracture*, Vol. 66, pp. R45–R50.

Prasad N.N.V., Aliabadi, M.H. and Rooke, D. P. (1994); The dual boundary element method for thermo-elastic crack problems, *International Journal of Fracture*, Vol. 66, pp. 255-272.

Prasad, N.N.V., Aliabadi, M.H. and Rooke, D.P. (1996): Effect of thermal singularities on stress intensity factors: edge crack in rectangular and circular plates, *Theoretical and Applied Fracture Mechanics*, Vol. 24, pp. 203–215.

Prathap, G. (1999): A priori error estimation of finite element models from first principles, *Sadhna*, Vol. 24, pp. 199–214.

Rabczuk, T. and Belytschko, T. (2004): Cracking particles: a simplified meshfree method for arbitrary evolving cracks, *International Journal of Numerical Methods in Engineering*, Vol. 61, pp. 2316–2343.

Rabczuk, T. and Belytschko, T. (2007): A three-dimensional large deformation meshfree method for arbitrary evolving cracks, *Computer Methods in Applied Mechanics and Engineering*, Vol. 196, pp. 2777–2799.

Rabczuk, T., Bordas, S. and Zi, G. (2007): A three-dimensional meshfree method for continuous multiple-crack initiation, propagation and junction in statics and dynamics, *Computational Mechanics*, Vol. 40, pp. 473–495.

Rao, B.N. and Rahman, S. (2000): An efficient meshless method for fracture analysis of cracks, *Computational Mechanics*, Vol. 26, pp. 398–408.

Rao, B.N. and Rahman, S. (2002): Probabilistic fracture mechanics by Galerkin meshless methods–part I: rates of stress intensity factors, *Computational Mechanics*, Vol. 28, pp. 351–364.

Rao, B.N. and Rahman, S. (2003): Mesh-free analysis of cracks in isotropic functionally graded materials, *Engineering Fracture Mechanics*, Vol. 70, pp. 1–27.

Rao, B.N. and Rahman, S. (2001): A coupled meshless-finite element method for fracture analysis of cracks, *International Journal of Pressure Vessels and Piping*, Vol. 78, pp. 647–657.

Rao, B.N. and Rahman, S. (2004): An enriched meshless method for non-linear fracture mechanics, *International Journal of Numerical Methods in Engineering*, Vol. 59, pp. 197–223.

Rao, M.N.B. (1976): Thermal stresses around an insulated crack in an infinite plate subjected to uniform heat flow, *International Journal of Fracture*, Vol. 12, pp. 777–779.

Raveendra, S.T. and Banerjee, P.K. (1992): Boundary element analysis of cracks in thermally stresses planar structures, *International Journal of Solids and Structures*, Vol. 29, pp. 2301–2317.

Reddy, J.N. and Chao, W.C. (1980): Finite element analysis of laminated bi-modulus composite- material plates, *Computers and Structures*, Vol. 12, pp. 245–251.

Rice, J.R. (1968): A path independent integral and the approximate analysis of strain concentration by notches and cracks, *Journal of Applied Mechanics*, Vol. 35, pp. 379–386.

Rice, J.R. and Rosengren, G.F. (1968): Plane strain deformation near a crack tip in a power hardening material, *Journal of the Mechanics and Physics* of *Solids*, Vol. 16, pp. 1–13.

Sasikala, G. and Ray, S.K. (2008): Evaluation of quasi-static fracture toughness of a modified 9Cr-1Mo (P 91) steel, *Materials Science and Engineering A*, Vol. 479, pp. 105–111.

Sekine, H. (1974): Thermal stress singularities at tips of a crack in a semi-infinite medium under uniform heat flow, *Engineering Fracture Mechanics*, Vol. 10, pp.713–729.

Shang, D.G., Wang, D.K., Li, M. and Yao, W.X. (2001): Local stress–strain field intensity approach to fatigue life prediction under random cyclic loading, *International Journal of Fatigue*, Vol. 23, pp. 903–910.

Sih G.C. (1962): On singular character of thermal stress near a crack tip, *Journal of Applied Mechanics*, Vol. 51, pp. 587.

Sills, B.L. and Dolev, O. (2004): The conservative M-Integral for thermal-elastic problems, *International Journal of Fracture*, Vol. 125, pp. 149–170.

Simkins, D.C. and Li, S. (2005): Meshfree simulations of thermo-mechanical ductile fracture, *Computational Mechanics*, Vol. 38, pp. 235–249.

Singh, A., Singh, I.V. and Prakash, R. (2006): Meshless analysis of unsteady-state heat transfer in semi-infinite solid with temperature dependent thermal conductivity, *International Communications in Heat and Mass Transfer*, Vol. 33, pp. 231–239.

Singh, I.V., Sandeep, K. and Prakash, R. (2003): Heat transfer analysis of two-dimensional fins using meshless element-free Galerkin method, *Numerical Heat Transfer*: *Part A*, Vol. 44, pp. 73–84.

Singh I.V. (2004): *Application of meshless element free Galerkin method in heat transfer problems*, Ph.D. Thesis, Birla Institute of Technology and Science, Pilani, India.

Singh, I.V., Sandeep, K. and Prakash, R. (2005): The effect of weight function and scaling parameter on meshless EFG results in heat transfer problems, *International Journal of Heat & Technology*, Vol. 23, pp. 13–20.

Singh, V.K, Gope, P.C. (2009): Photo-elastic determination of mixed mode stress intensity factors, *Journal of Solid Mechanics*, Vol. 1, pp. 233–244.

Sladek, J. and Sladek, V. (1997): Evaluation of T-stresses and stress intensity factors in stationary thermoelasticity by the conservation integral method, *International Journal of Fracture*, Vol. 86, pp.199–219

Sladek, J., Sladek, V. and Zhang, Ch. (2008a): Evaluation of the stress intensity factors for cracks in continuously non-homogeneous solids, part I: Interaction integral, *Mechanics of Advanced Materials and Structures*, Vol. 15, pp. 438–443.

Sladek, J., Sladek, V. and Zhang, Ch. (2008b): Evaluation of the stress intensity factors for cracks in continuously non-homogeneous solids, part I: Mshless method, *Mechanics of Advanced Materials and Structures*, Vol. 15, pp. 444–452.

Smelser, R. E. (1977): On the J-integral of bi-material bodies, *International Journal of Fracture*, Vol. 13, pp. 382–384.

Strern M. (1979): The numerical calculation of thermally induced stress intensity factor, *Journal of Elasticity*, Vol. 9, pp. 91–95.

Sukumar, N. (1998a): The natural element method in solid mechanics, *Ph.D. thesis, Theoretical and Applied Mechanics, Northwestern University, Evanston, IL, USA.*

Sukumar, N., Chopp, D.L., Moes, N. and Belytschko, T. (2001): Modeling holes and inclusions by level sets in the extended finite element method, *Computer Methods in Applied Mechanics in Engineering*, Vol. 190, pp. 6183–6200.

Sukumar, N., Huang, Z.Y., Prevost, J.H. and Suo, Z. (2004): Partition of unity enrichment for bi-material interface cracks, *International Journal for Numerical Methods in Engineering*, Vol. 59, pp. 1075–1102.

Sukumar, N., Moran, B. and Belytschko, T. (1998b): The natural element method in solid mechanics. *International Journal for Numerical Methods in Engineering*, Vol. 43, pp. 839–887.

Sukumar, N., Moran, B., Black, T. and Belytschko, T. (1997): An element-free Galerkin method for three-dimensional fracture mechanics, *Computational Mechanics*, Vol. 20, pp. 170–175.

Sumi, N. B. (1980): Thermal stress singularities at tips of a Griffith crack in a finite rectangular plate, *Nuclear Engineering Design*, Vol. 60, pp. 389–394.

Sze, K.Y., Wang, H.T. (2000): A simple finite element formulation for computing stress singularities at bi-material interfaces, *Finite Elements in Analysis and Design*, Vol. 35, pp. 97–118.

Tada, H., Paris, P.C. and Irwin, G.R. (1997): *The stress analysis of cracks Handbook*, 3rd Edition *ASME*, NewYork.

Tabbara, M.R. and Stone, C.M. (1998): A computational method for quasi-static fracture, *Computational Methods*, Vol. 22, pp. 203–210.

Tamuzs, V. P. and Petrova V. E. (2002): On macrocrack-microdefect interaction *International Applied Mechanics*, Vol. 38, pp. 1157–1177.

Terry T.G. (1994): *Fatigue crack propagation modeling using the element free Galerkin method*, Master's Thesis, Northwestern University.

Umar, A., Abbas, H., Qadeer, A. and Sehgal, D.K. (1996): Prediction of error in finite element results, *Computers and Structures*, Vol. 60, pp. 471–480.

Ventura, G., Xu, J. and Belytschko, T. (2001): Level set crack propagation modeling in the element free Galerkin method, *European Conference on Computational Mechanics*, Vol. 48, pp. 89–96.

Ventura, G., Xu, J.X. and Belytschko, T. (2002): A vector level set method and new discontinuity approximations for crack growth by EFG, *International Journal for Numerical Methods in Engineering*, Vol. 54, pp. 923–944.

Wang, C.H. (1996): Introduction to fracture mechanics, *DSTO Aeronautical and Maritime Research Laboratory*, DSTO-GD-0103.

Williams, M.L. (1957): On the stress distribution at the base of a stationary crack, *Journal of Applied Mechanics*, Vol. 24, pp.109–114.

Williams, M.L. (1959): The stress around a fault or crack in dissimilar media, *Bulletin of the Seismology Society of America*, Vol. 49, pp. 199–204.

Wilson, W.K. and Yu, I.W. (1979): The use of *J*-Integral in thermal stress crack problems, *International Journal of Fracture*, Vol. 15, pp. 377–387.

Wu, S. and Chudnovsky, A. (1993): Effect of micro-crack array on stress intensity factor of main crack, *International Journal of Fracture*, Vol. 59, pp. 41–52.

Xiao, J.R. and McCarthy, M.A. (2003): Meshless analysis of the obstacle problem for beams by the MLPG method and sub-domain variational formulations, *European Journal of Mechanics-A/Solids*, Vol. 22, pp. 385–399.

Xu, Y. and Saigal, S. (1998a): An element free Galerkin formulation for stable crack growth in an elastic solid, *Computer Methods in Applied Mechanics and Engineering*, Vol. 154, pp. 331–343.

Xu, Y. and Saigal, S. (1998b): Element free Galerkin study of steady quasi static crack growth in plane strain tension in elastic-plastic materials, *Computational Mechanics*, Vol. 22, pp. 255–265.

Xu, Y. and Saigal, S. (1999): An element free Galerkin analysis of steady dynamic growth of a mode-I crack in elastic-plastic materials, *International Journal of Solids and Structures*, Vol. 36, pp. 1045–1079.

Xuan, L., Zeng, Z., Shanker, B. and Udpa, L. (2002): Meshless element-free Galerkin method in NDT applications, *Quantitative Nondestructive Evaluation, AIP Conference Proceedings*, Vol. 615, pp. 1960–1967.

Yagawa, G. and Furukawa, T. (2000): Recent developments of free mesh method, *International Journal for Numerical Methods in Engineering*, Vol. 47, pp. 1419–1443.

Yagawa, G. and Yamada, T. (1996): Free mesh method, a new meshless finite element method, *Computational Mechanics*, Vol. 18, pp. 383–386.

Yau, J.F. and Wang, S.S. (1984): An analysis of interface cracks between dissimilar isotropic materials using conservation integral in elasticity, *Engineering Fracture Mechanics*, Vol. 20, pp. 423–432.

Yau, J.F., Wang, S.S. and Corten, H.T. (1980): A mixed-mode crack analysis of isotropic solids using conservation laws of elasticity, *Journal of Applied Mechanics*, Vol. 47, pp. 335–341.

Yavari, A., Kaveh, A., Sarkani, S., and Bondarabady, A. (2001): Topological aspects of meshless methods and nodal ordering for meshless discretizations, *International Journal of Numerical Methods in Engineering*, Vol. 52, pp. 921–938.

Yoon, J.W., Yang, D.Y., Chung, K. (1999): Elasto-plastic finite element method based on incremental deformation theory and continuum based shell elements for planar anisotropic sheet materials, *Computer Methods in Applied Mechanics and Engineering*, Vol. 174, pp. 23–56.

Yoon, J.W., Cardoso, R.P.R. and Dick, R.E. (2010): Puncture fracture in an aluminum beverage can, *International Journal of Impact Engineering*, Vol. 37, pp. 150–160.

Yosibash Zohar (1998): Thermal generalized stress intensity factors in 2-D domains, *Computer Methods in Applied Mechanics and Engineering*, Vol. 157, pp. 365–385.

Zhang, J., Tanaka, M., Matsumoto, T. (2004): The meshless regular hybrid boundary node method for 2-D linear elasticity, *Computer Methods in Applied Mechanics and Engineering*, Vol. 193, pp. 5597–5609.

Zhang, J. and Yao, Z. (2004): The regular hybrid boundary node method for three-dimensional linear elasticity, *Engineering Analysis with Boundary Elements,* Vol. 28, pp. 525–534.

Zhang, J., Yao, Z. and Tanaka, M. (2003): The meshless regular hybrid boundary node method for 2-D linear elasticity, *Engineering Analysis with Boundary Elements*, Vol. 27, pp. 259–268.

Zhang, Z., Liew K.M., Cheng, Y. and Lee, Y.Y. (2008a): Analyzing 2-D fracture problems with the improved element-free Galerkin method, *Engineering Analysis with Boundary Elements*, Vol. 32, pp. 241–250.

Zhang, Z., Liu, G. and Liu, T. (2008b): An adaptive EFG-FE computational model for thermal elasto-plastic frictional contact problems, *Advanced Materials Research*, Vol. 33, pp. 821–826.

Zhong, S. and Oyadiji S.O. (2007): Crack detection in simply supported beams without baseline modal parameters by stationary wavelet transform, *Mechanical Systems and Signal Processing*, Vol. 21, pp. 1853–1884.

Zhu, T., Zhang, J.D. and Atluri, S.N. (1998a): A local boundary integral equation (LBIE) method in computational mechanics and a meshless discretization approach, *Computational Mechanics*, Vol. 21, pp. 223–235.

Zhu, T., Zhang, J.D. and Atluri, S.N. (1998b): A meshless local boundary integral equation (LBIE) method for solving nonlinear problems, *Computational Mechanics*, Vol. 22, pp. 174–186.

Zi G., Rabczuk T. and Wall W. (2007): Extended meshfree methods with the branch enrichment for cracks, *Computational Mechanics*, Vol. 40, pp. 367–382.

Zi. G., Song J.H., Budyn, E., Lee, S.H. and Belytschko, T. (2004): A method for growing multiple cracks without re-meshing and its application to fatigue crack growth, *Modeling and Simulation in Materials Science and Engineering*, Vol. 12, pp. 901–915.

LIST OF PUBLICATIONS

Journal Publications

(1) **Mohit Pant**, I. V. Singh, B. K. Mishra, Numerical Simulation of Thermo Elastic Fracture Problems using Element Free Galerkin Method *International Journal of Mechanical Sciences*, Vol. 52 (12), pp. 1745–1755, 2010.

(2) **Mohit Pant**, I. V. Singh, B. K. Mishra, A Numerical Study of Crack Interactions under Thermo-Mechanical Load Using EFGM, *Journal of Mechanical Science and Technology (Accepted).*

(3) I. V. Singh, B. K. Mishra, **Mohit Pant**, An Enrichment based New Criterion for the Simulation of Multiple Interacting Cracks using Element Free Galerkin Method, *International Journal of Fracture* (*Available Online* DOI 10.1007/s10704-010-9536-z).

(4) **Mohit Pant**, I. V. Singh, B. K. Mishra, Vivek Bhasin, Kamal Sharma, I.A. Khan, Meshfree Solution of 2-D Edge Crack Problems under Thermo-Mechanical Load, *Journal of ASTM International* Vol. 7(5), pp. 12, 2010.

(5) I. V. Singh, B. K. Mishra, **Mohit Pant**, A Modified Intrinsic Enriched EFGM for Multiple Cracks Simulation, *Materials and Design*, Vol. 31 (1), pp. 628–632, 2010.

(6) **Mohit Pant**, I. V. Singh, B. K. Mishra, Vivek Bhasin, Kamal Sharma, I.A. Khan, A Comparative Study of Meshfree Techniques for Material Discontinuities, *JP Journal of Solids and Structures*, Vol. 3 (3), pp. 197–212, 2009.

(7) **Mohit Pant**, I.V. Singh, B.K. Mishra, Evaluation of Mixed Mode Stress Intensity Factors for Interface Cracks using EFGM, *Applied Mathematical Modeling* (in review).

(8) I. V. Singh, B. K. Mishra, **Mohit Pant**, An Efficient Partial Domain Enriched EFGM Criterion for the Simulation of Cracks in Non-Convex Domains, *Acta Mechanica* (in review).

Conference/Symposium Publications

(1) I. V. Singh, **Mohit Pant**, B. K. Mishra, A Comparative Study of EFGM Weight Functions in Linear Elastic Fracture Mechanics, *Interquadrennial Conference of the International Congress of Fracture (IQICF-2008), IISc Bangalore*, India, pp. 114-116, August 3-7, 2008.

(2) **Mohit Pant**, I. V. Singh, B. K. Mishra, Crack Interactions under Thermo-mechanical loading Using EFGM, *Proceedings of The 53rd Congress of Indian Society of Theoretical and Applied Mechanics (ISTAM)*, Osmania University, Hyderabad, India, pp. 20-26, December 27-29, 2008.

(3) Ch.Raghuveer, **Mohit Pant**, I.V. Singh, B.K. Mishra, V. Bhasin, Kamal Sharma, I.A. Khan, Application of Element Free Galerkin Method for the Simulation of Bi-Materials, *Proceedings of National Conference on Advances in Mechanical Engineering, RJIT, Mumbai*, India, pp. 104-108, January 15- 16, 2009.

(4) **Mohit Pant**, I.V. Singh, B.K. Mishra, Vivek Bhasin, Kamal Sharma and I.A. Khan Numerical Simulation of 2-D Crack Problems Under Mode-I Loading Using Mesh-Free Method, *Proceedings of National Conference on Recent Advances in Mechanical and Production Engineering*, G. B. Pant University of Agriculture & Technology, Pantnagar, India, pp. 19-25, February 12-14, 2009.

(5) **Mohit Pant**, I.V. Singh, B.K. Mishra, A Numerical Study of Centre Crack under Thermo-Mechanical Load Using EFGM, *International Conference on Computational & Experimental Engineering and Sciences (ICCES,09)*, Phuket, Thiland, Vol. 12 (1), pp. 13-21, April 8-13, 2009.

(6) Ch.Raghuveer, **Mohit Pant**, I.V. Singh, B.K. Mishra, V. Bhasin, Kamal Sharma, I.A. Khan, Numerical Simulation of Bi-Material Problems Using EFGM, *International Conference on Computational & Experimental Engineering and Sciences (ICCES,09)*, Phuket, Thiland, Vol. 12 (1), pp. 23-31, April 8-13, 2009.

(7) **Mohit Pant**, I. V. Singh, B. K. Mishra, Vivek Bhasin, Kamal Sharma, I.A. Khan, Meshfree Solution of 2-D Edge Crack Problems under Thermo-Mechanical Load, *Ninth International ASTM/ESIS Symposium on Fatigue and Fracture Mechanics (37th ASTM National Symposium on Fatigue and Fracture Mechanics)*, Vancouver, Canada, May 20-22, 2009.

(8) **Mohit Pant**, I. V. Singh, B. K. Mishra, Vivek Bhasin, Kamal Sharma, I.A. Khan, A numerical Comparison of Weak Discontinuities in Meshfree Methods, *3rd International Congress on Computational Mechanics and Simulations (ICCMS-09)*, IIT Bombay, Powai, India, pp. 197-198, Dec 1-5, 2009.

(9) **Mohit Pant**, I.V. Singh, B.K. Mishra, A Numerical Solution of Multiple Cracks using Enriched EFGM, *54th Congress of Indian Society of Theoretical and Applied Mechanics (ISTAM)*, NSIT Delhi, India, pp. 8-14, December 18-21, 2009.